Mesure de la section efficace de capture neutronique et determination des parametres de resonances de I-127 et I-129

G. Noguere

Numéro d'ordre : 4432

Université Louis Pasteur – Strasbourg I

Thèse

Présentée pour obtenir le grade de

Docteur en Sciences de l'Université Louis Pasteur
(spécialité : Physique Nucléaire)

par

Gilles NOGUERE

Mesures et analyses des sections efficaces neutroniques totales et de captures radiatives des iodes 127 et 129 de 0.5 eV à 100 keV ;

Effets expérimentaux et études de sensibilité

Soutenue publiquement le 2 décembre 2003 devant la commission d'examen :

Mme.	N.M . LARSON	Rapporteur
MM.	J.C. SENS	Président et Rapporteur
	G. RUDOLF	Directeur de thèse
	C. WAGEMANS	Rapporteur
	O. BOULAND	Examinateur
	F. KAEPPELER	Examinateur
	A. LEPRETRE	Examinateur

Ce travail a été réalisé dans le cadre du programme de mesures de données nucléaires n-TOF, en collaboration avec l'Institut des Matériaux et des Mesures de Références de Geel (IRMM), le Laboratoire d'Etudes Physiques du CEA-Cadarache (SPRC/LEPh), du Service de Physique Nucléaire du CEA-Saclay (SPhN) et de la Direction des Etudes et Recherches d'EDF (DER, Clamart).

Cette étude n'aurait jamais pu aboutir sans l'aide précieuse de Messieurs Alfred Leprêtre et Antonio Brusegan. Je les remercie chaleureusement de m'avoir guidé tout au long de cette thèse. Ils ont su me communiquer leur passion en m'enseignant les techniques de mesures par temps de vol. Je tiens à exprimer ma profonde gratitude pour leur soutien et leur disponibilité.

Je tiens également à adresser mes plus vifs remerciements à Monsieur Olivier Bouland pour son aide et ses nombreux conseils tout au long de l'analyse des données. Je lui suis reconnaissant d'avoir partagé ses connaissances sur l'ensemble des codes d'analyses intervenant dans cette évaluation.

J'exprime ma gratitude à Madame Nancy Larson et Monsieur Mick Moxon, les auteurs des codes SAMMY et REFIT. Je les remercie pour l'attention qu'ils ont portée à mon travail et pour les précieux conseils qu'ils m'ont prodigués concernant l'utilisation de leur code et l'interprétation physique des résultats.

Je désire exprimer ma reconnaissance à Monsieur Gérard Rudolf qui a accepté d'encadrer ce travail de recherche. Je le remercie particulièrement pour ses conseils et ses remarques lors de la correction du manuscrit.

Je remercie Messieurs Cyriel Wagemans de l'Université de Gand, Franz Kaeppler de l'Institut des Transuraniens de Karlsruhe et Jean-Claude Sens de l'Institut de Recherche Subatomique de Strasbourg de l'intérêt qu'ils ont porté à ce travail en acceptant d'être rapporteurs de cette thèse. Je leur suis très reconnaissant des remarques et conseils qui ont contribué à l'amélioration de ce manuscrit.

Au cours de cette thèse, Messieurs Herman Weigmann, Peter Rullhunsen et Robert Jacqmin m'ont accueilli au sein de leur laboratoire et ont soutenu ce travail, qu'ils en soient remerciés.

Qu'il me soit permis d'adresser mes remerciements et ma reconnaissance à l'ensemble des membres de l'unité ND de l'IRMM, du SPhN et du LEPh. Je tiens particulièrement à exprimer ma reconnaissance à Franco Corvi, Paolo Mutti, Peter Schillebeeckx, Peter Siegler, George Lobo, Franck Gunsing, Gaelle Aerts, Arjan Plompen, Natalia Janeva, Arnaud Courcelle, Cyril de Saint Jean, Emeric Dupond et Olivier Sérot pour les précieux échanges qui ont contribué à valoriser ce travail.

Je ne saurais oublier Jorge Gonzales, Charles Nazareth et Egidio Macavero pour leur assistance au niveau du système d'acquisition. La réussite de ces expériences incombe également à Chris Ingelbrecht, Jacque Lupo et Thierry Lombard pour la préparation des échantillons. De même, je souhaiterais remercier chaleureusement l'équipe chargée du fonctionnement de GELINA.

Enfin, j'ai une pensée pour tous ceux qui ont rendu mon séjour en Belgique et à Cadarache agréable. La liste est longue, aussi je les remercie tous pour leur soutien amical.

Pour terminer, je souhaite dédier ce manuscrit à Laurence pour son soutien précieux, ses encouragements répétés et sa présence tout au long de ce travail.

Ce travail s'inscrit dans le cadre de la loi Bataille (1991) visant à explorer les possibilités de transmutation des déchets radioactifs à vie longue issus des réacteurs nucléaires. Les études menées sur la transmutation ont pour objectif le développement de systèmes capables de réduire la radiotoxicité des principaux actinides mineurs (^{237}Np, ^{241,243}Am, ^{243,244,245}Cm) et produits de fission à vie longue (^{99}Tc, ^{129}I, ^{135}Cs). L'évaluation du potentiel de transmutation de ces isotopes et l'optimisation des scénarios envisagés requièrent une bonne connaissance des sections efficaces neutroniques des corps mis en jeu. L'iode-129 a une période radioactive de 1.57×10^{7} ans. Après capture d'un neutron, il peut être transmuté en iode-130 dont la période n'est que de 12.36 h. La précision actuelle sur la section efficace neutronique de capture radiative de ^{129}I est de l'ordre de 10%. Cette précision insuffisante a suscité une demande officielle de nouvelles mesures microscopiques (NEA/NSC/DOC-97-4). Dans ce contexte, une campagne de mesures par temps de vol a été réalisée en 2001-2002 auprès de la source pulsée de neutron GELINA de l'Institut des Matériaux et des Mesures de Référence (IRMM) de Geel, laboratoire européen situé en Belgique. Deux types d'expériences ont été réalisées. Une série de mesures de capture d'une part, et de transmission d'autre part, nous ont permis d'obtenir respectivement la section efficace de capture radiative et la section efficace totale de l'iode-129 de 0.5 eV à 100 keV. Les résultats expérimentaux ont été analysés avec les codes REFIT et SAMMY. Les paramètres de résonance obtenus ont ensuite été convertis en format ENDF-6. Le code NJOY a finalement été utilisé afin de produire les bibliothèques des codes de calculs MCNP et ERANOS. Ce travail, qui fait partie du projet n-TOF, a été réalisé dans le cadre d'une collaboration entre l'IRMM, le CEA et EDF.

Les quatre étapes principales dans l'évaluation des sections efficaces neutroniques sont la préparation des échantillons, la réalisation des expériences, l'analyse des données et la conversion des paramètres en fichier de données nucléaires évaluées (ENDF). Parallèlement, des études de sensibilité ont été menées au cours de cette évaluation afin de déterminer les erreurs systématiques affectant la précision de nos résultats.

Peu de mesures microscopiques ont été réalisées sur l'iode-129 en raison des difficultés liées à la préparation en quantités suffisantes d'échantillons chimiquement stables. Les échantillons nécessaires à la réalisation de nos mesures ont été préparés à l'IRMM à partir de 200 litres d'une solution radioactive provenant de la Hague (COGEMA). A l'issue de 11 mois de travail, environ 140 g d'iode-129 ont été extraits sous forme de PbI_2. Ce dernier est principalement composé de ^{129}I (16.43%), ^{127}I (3.36%) et de plomb naturel (~53.4%). Afin de déterminer avec précision les sections efficaces des réactions ^{129}I(n,tot) et ^{129}I(n,γ), une étude complète des réactions ^{127}I(n,γ) et ^{127}I(n,tot) et une mesure de transmission du plomb ont également été menées dans les mêmes conditions expérimentales que celles de l'iode-129 auprès de l'installation GELINA.

La source blanche de neutron GELINA est constituée d'un accélérateur linéaire d'électrons et d'une cible d'uranium appauvri. Après accélération, les électrons sont ralentis dans la cible d'uranium et génèrent un rayonnement de freinage (Bremsstrahlung). Les neutrons, produits par photoréactions (γ,n) et (γ,fission), ont un spectre en énergie centré autour de 1 à 2 MeV. Afin d'étudier les sections efficaces au-dessous de quelques centaines de keV, les neutrons émis par la cible d'uranium sont modérés par 3.6 cm d'eau, puis collimatés vers les diverses aires expérimentales. La méthode de mesure par temps de vol consiste à mesurer l'intervalle de temps entre la production du paquet de neutrons et la détection d'un événement. Si le temps de vol est exprimé en μs, la distance de vol en m et l'énergie des neutrons en eV, la relation temps/énergie pour un neutron non relativiste est exprimée par :

$$E = \left(72.298 \frac{L}{T} \right)^2$$

Les résultats expérimentaux sont représentés sous forme de spectres en temps de vol. Le temps de vol maximal couvert par nos mesures varie de 1.25 ms à 10 ms. Les spectres sont ensuite convertis en énergie lors de la réduction des données.

Les mesures de capture permettent d'accéder au taux de capture $Y(E)$ défini comme le nombre de captures radiatives $N_c(E)$ par neutron incident $\Phi(E)$:

$$Y(E) \propto \frac{N_c(E)}{\Phi(E)}$$

Le dispositif expérimental est localisé à 28,6 m de la source de neutron. Il est composé d'une chambre à bore mesurant le flux de neutrons incidents et de deux scintillateurs (C_6D_6) placés à 90 degrés par rapport à la direction du faisceau de neutrons. La cible de capture de 80 mm de diamètre est placée entre les deux C_6D_6. La réponse en amplitude des scintillateurs est pondérée afin d'obtenir une efficacité de détection constante, ceci quelque soit le gamma détecté. Pour ce travail, nous avons utilisé la ″fonction poids″ expérimentale mesurée par Corvi et al., largement utilisée à Geel.

Les expériences de transmission consistent à mesurer le flux de neutrons incidents (Φ_{out}) et le flux transmis (Φ_{in}) par l'échantillon. La transmission de ce dernier est ainsi exprimée à l'aide de la relation suivante :

$$T(E) \propto \frac{\Phi_{in}(E)}{\Phi_{out}(E)}$$

L'échantillon de PbI_2 est placé sur un support mobile automatisé situé à 23,7 m de la source de neutrons. Celui-ci permet d'introduire ou de retirer

l'échantillon du faisceau de manière répétitive suivant des cycles de mesures pilotés par le système d'acquisition. Les neutrons sont ensuite détectés à 49.3 m par un verre au lithium (NE912).

Les données brutes obtenues par les différents systèmes d'acquisition se présentent sous forme d'histogrammes, de matrices bi-dimensionnelles, et de constantes mesurées par un ensemble complet d'échelles de comptage. La ″réduction″ des données brutes consiste à corriger les données des effets expérimentaux. Le système de réduction des données AGS (Analysis of Geel Spectra) a été utilisé afin d'obtenir les taux de capture et les spectres de transmission exploitables par les codes d'analyses. Le système AGS est un ensemble de commandes écrites par C. Bastian en langage C. Il permet de gérer notamment la pondération des spectres de capture, la correction de temps mort, la soustraction du bruit de fond et la normalisation. La propagation des erreurs statistiques et systématiques liées aux paramètres intervenant à chaque étape de la réduction est conservée sous forme d'une matrice de variance-covariance V :

$$V=GWG^t+D$$

La matrice G représente la matrice de sensibilité, dont les éléments sont les dérivés partielles en fonction des paramètres de la réduction des données. La matrice W contient l'information sur les erreurs associées à ces paramètres. La matrice D est une matrice diagonale dont les éléments sont calculés à partir des incertitudes statistiques des taux de comptage. La matrice V peut être ensuite utilisée par le code d'analyse SAMMY, afin de propager les incertitudes expérimentales lors de la détermination des paramètres de résonances.

Après réduction des données, 18 spectres ont été obtenus et analysés simultanément à l'aide des codes d'analyses de forme REFIT et SAMMY. Pour l'analyse, il convient de distinguer le domaine des résonances résolues en énergie et le domaine des résonances non résolues. Nous avons utilisé l'approximation Reich-Moore de la théorie de la Matrice-R afin de décrire les sections efficaces résonnantes sous forme de paramètres de résonance (énergie, largeurs neutroniques, largeurs radiatives, spin, parité et rayon de diffusion effectif). Le domaine non résolu est décrit statistiquement à l'aide de paramètres moyens (largeur radiative moyenne, fonctions densités neutroniques, espacement moyen des niveaux et rayon ″infini″). Les sections efficaces moyennes ont été analysées à l'aide du formalisme généralisé de la théorie de Hauser-Feshbach introduit dans l'option FITACS de SAMMY. Le rayon ″infini″ et le rayon effectif de diffusion décrivent la contribution de la section efficace potentielle. Afin de comparer les sections efficaces théoriques avec les données expérimentales, il convient de prendre en compte, dans les codes d'analyse, l'effet Doppler $D(E)$, la résolution en énergie de l'installation $R(E)$ et la diffusion multiple des neutrons dans les cibles de capture $\mu(E)$. La transmission T_{th} et le taux de capture Y_{th} théoriques sont calculés à partir des expressions suivantes :

$$T(E) = \int_0^\infty R(E,E')T_{th}(E')dE'$$

$$Y(E) = \int_0^\infty R(E,E')Y_{th}(E')dE'$$

$$T_{th}(E) = e^{-nD(E)\otimes\sigma_t(E)}$$

$$Y_{th}(E) = \mu(E)\left(1 - T_{th}(E)\right)\frac{D(E)\otimes\sigma_\gamma(E)}{D(E)\otimes\sigma_t(E)}$$

La section efficace de capture $\sigma_\gamma(E)$ et la section efficace totale $\sigma_t(E)$ sont élargies par effet Doppler selon le modèle du gaz libre avec une température effective introduite par la théorie de Lamb. Celle-ci est déduite de la température de Debye du corps étudié et de la température de l'échantillon mesurée pendant les expériences. La fonction de résolution $R(E)$ de GELINA représente la distribution en temps (ou en distance) du temps de vol de neutrons monoénergétiques. Enfin, la correction $\mu(E)$ de la diffusion multiple des neutrons dans les cibles de capture est calculée analytiquement à l'aide d'un algorithme basé sur la probabilité de collision déterminée par Case et al. dans le cas d'un faisceau de neutrons parallèles incidents sur une cible mince cylindrique.

La limite entre les domaines des résonances résolues et non résolues est fonction de la résolution expérimentale de l'installation et de l'espacement moyen entre les résonances du corps étudié. Dans cette étude, le domaine résolu a été étendu jusqu'à 10 keV. Pour l'iode-127, nous avons identifié 719 résonances. L'étude statistique des paramètres de résonance nous a permis de déterminer un espacement moyen D_0 entre les résonances de type *s* de 12,5±0,3 eV, et une largeur radiative moyenne proche de 100 meV. Dans le domaine non résolu, la fonction densité S_0 a été estimée à $(0{,}78\pm0{,}01)\times10^{-4}$. De même pour l'iode-129, l'identification de 400 résonances nous a conduit à déterminer un espacement moyen D_0 de 27.3±0,9 eV et une largeur radiative moyenne de 106 meV. La fonction densité S_0 obtenue dans le domaine non résolu est de $(0{,}58\pm0{,}01)\times10^{-4}$. Les paramètres moyens obtenus dans ce travail sont en bon accord avec les systématiques expérimentales recommandées dans la librairie RIPL-2.

Les résultats obtenus ont été convertis en format ENDF-6. Nous avons utilisé le code NJOY afin de produire des sections efficaces multi-groupes ainsi que les librairies MCNP et ERANOS. L'un des paramètres clés en physique des réacteurs est ″l'intégrale de résonance″ définie comme :

$$I_0 = \int_{0.5}^\infty \sigma_\gamma(E)\frac{dE}{E}$$

Les valeurs de I_0 pour les iodes 129 et 127 déduites de cette étude sont respectivement égales à 28,8±1,7 barns et 153,7±4,8 barns. Ces résultats

intégraux sont cohérents avec les évaluations européennes (JEFF3.0) et japonaises (JENDL3.3).

Une étude de sensibilité a par ailleurs été menée afin de déterminer les erreurs systématiques affectant la précision de nos résultats. Nous avons particulièrement étudié :

- la ″fonction poids″ et son influence sur les résultats de capture,
- la description analytique du bruit de fond neutronique et photonique,
- la modélisation de la résolution expérimentale de GELINA,
- l'algorithme de transport des neutrons dans les cibles de capture.

La ″fonction poids″ intervient dans la réduction des données de capture. La méthode de pondération par les amplitudes permet d'obtenir une efficacité de détection (ε_c) indépendante du rayonnement gamma émis par le noyau composé après capture d'un neutron. La probabilité de détecter un événement de capture devient proportionnelle à l'énergie d'excitation (E^*) du noyau composé (neutron capturé + noyau cible) :

$$\varepsilon_c = k\, E^*$$

Si la forme de la ″fonction poids″ dépend notamment du détecteur, de son environnement et de l'échantillon étudié, son impact sur les paramètres de résonance dépend principalement de la dureté du spectre gamma émis par le noyau composé. Dans le cas de l'iode, une étude a montré que le choix de la ″fonction poids″ avait une faible influence sur la section efficace de capture radiative. L'erreur systématique maximale attendue est de l'ordre de 1,3%.

La détermination du bruit de fond (BDF) sur les spectres de temps de vol utilise la méthode des ″résonances noires″. Des filtres épais sont placés dans le faisceau de neutron afin d'obtenir une transmission presque nulle au niveau d'une ou de plusieurs résonances. Le signal mesuré sous ces résonances noires est attribué au BDF. En combinant différents filtres, il est possible d'obtenir plusieurs points de BDF et d'extrapoler son allure sur l'ensemble du domaine en énergie étudié. Le BDF est défini comme la somme d'une contribution constante et d'une fonction dépendant du temps :

$$B(t) = \alpha + \beta(t)$$

La modélisation de la fonction $\beta(t)$ a été améliorée sur la base de travaux réalisés par M.Moxon et A.Leprêtre. Ces derniers ont démontré la présence de structures dans le bruit de fond correspondant à la détection de neutrons diffusés hors du faisceau incident. Notre nouvelle étude a permis de confirmer que l'environnement du détecteur était la source la plus probable du bruit de fond neutronique, et que la capture des neutrons par l'hydrogène contenu dans les modérateurs était responsable du flux photonique détecté dans les mesures de

capture et de transmission. Dans le domaine des résonances résolues, le choix de la fonction $\beta(t)$ conduit à une erreur systématique de 2.4% sur les résultats de la transmission, et est négligeable dans les mesures de capture.

Le troisième effet expérimental étudié au cours de notre analyse est la résolution expérimentale de l'installation GELINA. La résolution en énergie $R(E)$ a pour effet d'élargir les résonances et d'atténuer leur amplitude. Dans le code d'analyse REFIT, sa description analytique résulte de la convolution de sept contributions associées au paquet d'électrons (I_p), à la cible d'uranium (I_t), aux modérateurs (I_m), à l'angle de la base de vol (I_θ), au détecteur (I_d) - transmission seulement -, au codage en temps des événements (I_c) et à la dispersion due à l'instabilité de l'électronique (I_e) :

$$R(E) = I_p(E) \otimes I_t(E) \otimes I_m(E) \otimes I_\theta(E) \otimes I_d(E) \otimes I_c(E) \otimes I_e(E)$$

L'utilisation de simulations Monte-Carlo réalisées par C.Coceva a permis d'améliorer la modélisation disponible dans REFIT. Parallèlement, nous avons également proposé le développement de l'option UDR dans SAMMY afin d'introduire la fonction de résolution de GELINA sous forme de distributions ponctuelles. L'étude de sensibilité, associée à la description de la fonction de résolution, montre que l'erreur systématique moyenne affectant la précision des paramètres de résonance de l'iode reste inférieure à 2%.

Enfin le dernier effet expérimental étudié concerne la correction due à la diffusion multiple calculée par SAMMY et REFIT. Les résultats de l'algorithme de transport des neutrons ont été comparés à ceux obtenus par simulations Monte-carlo réalisées avec MCNP et SAMSMC. Les résultats obtenus ont permis de mettre en lumière un biais systématique limitant l'application de la correction à des cibles de quelques millimètres d'épaisseur. Pour l'iode, l'erreur systématique est négligeable dans le cas de cibles minces (h<10 mm).

L'ensemble des informations collectées au cours des études systématiques des différents effets expérimentaux (fonction de pondération, bruit de fond, résolution expérimentale, correction due à la diffusion multiple, normalisation et composition de l'échantillon) a conduit à une estimation réaliste des erreurs introduites dans l'analyse. L'erreur systématique moyenne affectant les sections efficaces de capture de l'iode-127 et 129 reste inférieure à 5% dans le domaine des résonances résolues et non résolues. Cette évaluation représente une amélioration significative de la section efficace de capture pour les futures études dédiées à la transmutation de l'iode-129.

La suite de ce travail consistera à valider les résultats obtenus en les comparant à ceux provenant de mesures intégrales réalisées en réacteur, notamment avec les résultats de l'expérience PROFIL actuellement en cours auprès du réacteur PHENIX.

Contents

List of Tables

List of Figures

Chapter 1

Introduction

Historically, most of the experimental work conducted on neutron interactions with matter has focused on materials which were of prior importance in the field of reactor physics and reactor structures. By comparison, the corresponding data for minor actinides (MA) or long-lived fission products (LLFP) are poor. Recently, a significant demand for improved neutron cross-section data on these little-studied nuclides has developed due to the surge of interest in the transmutation of nuclear waste. Partitioning and Transmutation (P-T) of long-lived nuclides is a potential complement to the reference concept of the closed nuclear fuel cycle: fuel fabrication, energy generation, intermediate storage of spent fuel, reprocessing, plutonium use in fuel and disposal of solidified high-level waste (HLW) in a deep geologic depository. *Partitioning* is another word for the reprocessing of spent nuclear fuel. The world *transmutation* defines the transformation of long-lived nuclides into short-lived or stable nuclides through irradiation with neutrons in order to reduce the long-term radiological effects of storage of HLW. The main objective of P-T studies is to develop the technology to transmute from one hand minor actinides with serious toxicity such as ^{237}Np, ^{241,243}Am and ^{244,245}Cm and on the other hand some long-lived fission products such as ^{99}Tc, ^{129}I and ^{135}Cs using reactors (fast or thermal) or hybrid systems (ADS). Inventory of the irradiated nuclear fuel is given in Table 1.1.

For P-T studies, the most important characteristics of radioactive waste are radioactive half-life and mobility in the environment rather than quantity. With 400 kg of ^{129}I produced yearly in the EU countries reactors and a very long β^- half-life of 1.57×10^7 years, iodine requires disposal strategies that will isolate this isotope from the environment for very long periods of time. However, iodine is considered difficult to isolate as it readly dissolves into ground-water and easily move throughout the ecosystem [2]. It has the ability to migrate in any kind of material, including storage glasses [3], which could, in a worst-case scenario, leads to its leaking in the environment during its long-term storage. Thereby, ^{129}I is potentially a key long-lived fission product for P-T applications since ^{129}I transmutes in ^{130}I after one single neutron capture and decays to the noble gas ^{130}Xe with a 12.36 h half-life. The schematic ^{129}I transmutation process is shown on the left half of Figure 1.1. As it is known, the fission iodine contains ^{129}I and ^{127}I. The yields of radioactive and natural iodine per fission of ^{235}U by thermal neutrons are respectively close to $83.0 \pm 2.2\%$ and $17.0 \pm 2.2\%$. In addition, the ^{127}I neutron capture cross section is about five time higher than the ^{129}I(n,γ) cross section. Therefore, the ^{127}I contribution cannot be neglected and has to be introduced in nuclear reactor and fuel cycle calculations. The ^{127}I(n,γ) reaction is presented in the right half of Figure 1.1.

Experimental studies have shown that the effective transmutation rate of ^{129}I can potentially be achieved in special assemblies in thermal and fast reactors or in ADS facilities. The

Table 1.1: Inventory of the irradiated nuclear fuel (3.5% enriched ^{235}U) in a 900 MW PWR for a burn-up of 33000 MWday/t [1]

		mass (g/y)	half-life (y)
Uranium		954.7	
Plutonium		9.75	
Minor Actinides	^{237}Np	430	2 140 000
	^{241}Am	220	432.2
	^{243}Am	100	7380
	^{244}Cm	24	18.1
	^{245}Cm	3	8500
Fission Products	^{79}Se	4.7	70000
	^{90}Sr	500	28
	^{93}Zr	710	1 500 000
	^{99}Tc	810	210 000
	^{107}Pd	200	6 500 000
	^{126}Sn	20	100 000
	^{129}I	170	15 700 000
	^{135}Cs	360	2 300 000
	^{137}Cs	1100	30
	^{151}Sm	20	93
	others (stable)	30.7	

transmutation of iodine has been first demonstrated after neutron irradiation of milligram-sized NaI samples in the Fast Flux Test Facility located on the Hanford site in Richland, Washington [4]. The TARC experiment conducted at CERN has also shown the possibility of using the Adiabatic Resonance Crossing (ARC) to transmute ^{129}I in Accelerator Driven Systems [5]. The ARC principle is based on the lead properties. Neutrons produced by spallation into a large lead volume are slowed down quasi adiabatically (small energy loss per collision), with almost flat isolethargic energy distribution which allows to take full advantage of the resonant cross section in the transmutation process. More recently, the ^{129}I transmutation rate was investigated at the VVR-M water-cooled water-moderated reactor of the St. Petersburg Nuclear Physics Institute by using fission iodine in the form of KI [6]. The transmutation rate per year obtained in these scenarii typically ranges from 4% to 15%.

However, some serious problems are still encountered in the technical feasibility. The transmutation of ^{129}I in thermal reactors will be difficult because of the impractical low transmutation rate and the large inventories required. Better results could be obtained in moderated subassemblies [7] of fast reactors or, presumably, in future Accelerator-Driven Systems [8, 9]. The next step in exploring the feasibility of full-scale ^{129}I transmutation consists in evaluating material behaviour issues. Such studies are currently conducted by the EFTTRA collaboration which is the acronym for Experimental Feasibility of Targets for TRAnsmutation. The conclusion of irradiation tests carried out in the High Flux Reactor at Petten, Netherlands, is that sodium iodide is the best target material to transmute iodine [10].

On the basis of these technical outlines, the lack of reliable and sufficient data on neutron cross sections of LLFP and MA is one of the major problems faced in evaluating the transmutation

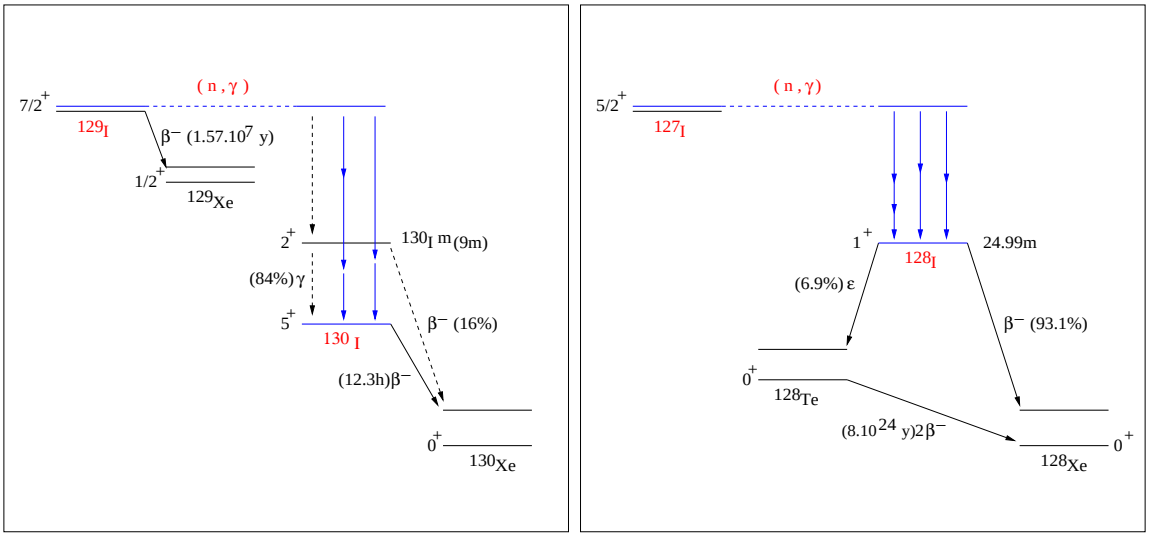

Figure 1.1: Schematic ^{129}I and ^{127}I radiative neutron capture processes.

potential of long-lived waste in appropriate reactor configurations. Within this context, an official request has been presented demanding neutron thermal and fast spectra measurements focusing on capture cross section data (NEA/NSC/DOC-97-4).

In order to improve the knowledge of the cross-sections of the various nuclei involved in the transmutation chains, the irradiation experiments PROFIL aim at collecting integral data. They contain rods with a large number of MA and LLFP separated into small quantities of several milligrams. Two designs can be distinguished, namely PROFIL-R and PROFIL-M. The PROFIL-R experiment is in progress in PHENIX. It consists in standard fuel subassemblies located in the fast flux of the internal core. The PROFIL-M experiment will use $^{11}B_4C$ moderated subassemblies located inside the core. The physical variables of interest for the PROFIL experiments are the concentration (n_i) and (n_f) of the isotopes at the beginning and at the end of the irradiation period. In order to reach an optimal exploitation of the results with a reliable uncertainty analysis, the sensitivity coefficients of the concentration according to cross sections must be known. In a first approximation, the evaluation of the sensitivities may be seen as the first derivative of a given concentration at a given time with respect to the cross sections of interest [11]. For ^{129}I, the variation of the concentration with respect to the capture cross section (σ_γ) in a given energy group (g) may be expressed as follows:

$$\frac{\Delta n}{n_i} \equiv \sum_{g=1}^{n} S_g \frac{\delta\sigma_{\gamma,g}}{\sigma_{\gamma,g}} \tag{1.1}$$

The sensitivity coefficients (S_g) calculated by C. De Saint Jean [7] are presented in Figure 1.2 in a 15 group energy mesh together with the ^{129}I capture cross section data from JEFF3. PROFIL-M will be sensitive to the [20 eV-2 keV] energy range, while PROFIL-R will give fundamental information in a broad [500 eV-100 keV] energy range. These sensitivity calculations demonstrate the need for accurate capture cross section in the resolved and unresolved energy range. Improvements of the capture cross section within these energy ranges, would help to reduce uncertainties in waste management concepts.

Very little experimental works have been performed on ^{129}I neutron cross section because of

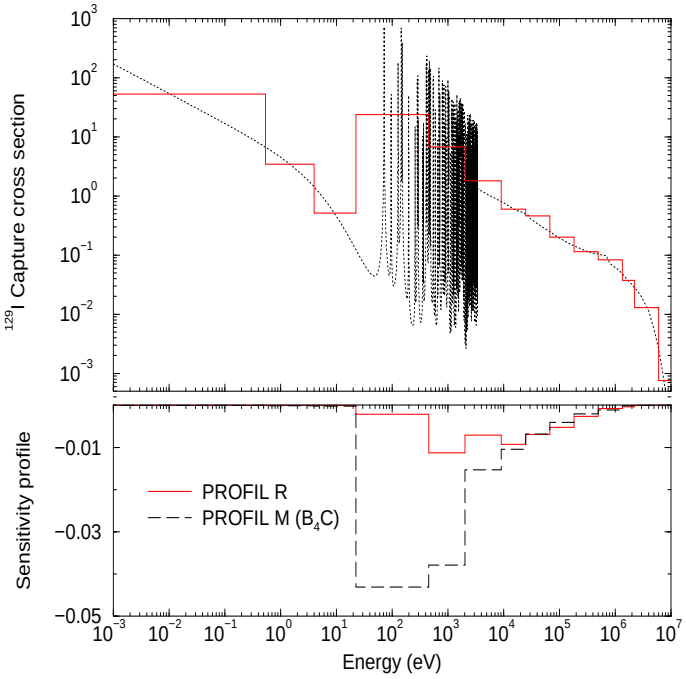

Figure 1.2: ^{129}I point-wise and multigroup capture cross sections data from JEFF3 together with the sensitivity profile calculated for the PROFIL-R and PROFIL-M experiments [7]. The results are presented in a 15 energy group mesh.

sample procurement and handling problems. From Table 1.2, large discrepancies are observed on the measured thermal capture cross section values. The spread between the Pattenden and Friedmann values reaches 21%. The resonance energy range has been investigated with transmission and capture measurements, which are respectively related to total and capture neutron cross sections. The recommended resonance parameters in the American neutron data base (ENDF/B-VI) come from the Pattenden's results. Those available in the European (JEFF3), Japanese (JENDL3.3) and Russian (BROND2.2) libraries were generated from the resonance areas given by Macklin. In the BROND2.2 data base only 66 resonances are listed below 2.1 keV, while the JEFF3 and JENDL3.3 data bases contain respectively parameters for 126 resonances and 127 resonances up to 3 keV. In each evaluation, the resonances are assumed to be s-waves. Owing to the need for more accurate evaluations, new microscopic measurements have been required in the High Priority Nuclear Data Request List.

For that purpose a series of capture and transmission Time-Of-Flight measurements covering the [0.5 eV-100 keV] energy range were carried out at the 150 MeV pulsed neutron source GELINA of the Institute for Reference Materials and Measurements (IRMM, Belgium). This work was part of the CEA-IRMM collaboration and of the n-TOF project. In transmission measurements, the neutrons, produced in the uranium target of the GELINA facility and moderated by water in a Be canning, came across a filter set-up and the sample at 23.7 m. They have been detected at 49.3 m with a Li-glass detector (NE912). The capture measurement consisted in measuring the prompt γ-rays emitted following a neutron capture in the sample. The capture set-up was located at 28.6 m from the neutron source. A ^{10}B ionisation chamber was located in the neutron beam line to measure the incident neutron flux, while the γ-rays were detected by two C_6D_6 liquid scintillators (NE230) to which a weighting method is applied. The fission iodine (^{127}I + ^{129}I) used in this work was extracted from 210 l of waste solution provided by

Table 1.2: ^{129}I thermal cross sections and resonance parameters available in the literature. σ_γ^{th} and σ_t^{th} stand respectively for the capture and total thermal cross sections. Pattenden deduced σ_γ^{th} from the total thermal cross section by subtracting the scattering contribution. From the information available in its work, we guess a σ_t^{th} close to 34.8 barns. The resonance energy range was investigated with the help of two experiments, namely transmission and capture measurements. The transmission gives the total cross section ($\sigma_t(E)$), and the capture is related to the radiative capture cross section ($\sigma_\gamma(E)$). Both experiments used the Time-Of-Flight technique.

Author	Ref.	Year	Measurements	Energy range	Results
Block	[12]	1958	σ_t^{th}	0.025 eV	35.0±4.0 barns
Pattenden	[13]	1963	σ_γ^{th}	0.025 eV	28.0±2.0 barns
Friedmann et al.	[14]	1983	σ_γ^{th}	0.025 eV	33.9±1.9 barns
Nakamura et al.	[15]	1996	σ_γ^{th}	0.025 eV	30.3±1.2 barns
Pattenden	[13]	1963	transmission	$<$ 170 eV	5 resonances
Macklin	[16]	1983	capture	$<$ 500 keV	125 resonances

COGEMA. The procedure for the separation of the iodine from the mother solution into PbI_2 samples was developed and optimised at the IRMM. Since the PbI_2 samples contained natural and radioactive iodine together with large amount of natural lead, a transmission measurement of a thick lead sample and some extensive measurements of the ^{127}I total and capture cross sections have been carried out under the same experimental conditions as for the ^{129}I. The data reduction process was performed with the AGS system, and the resonance parameters were finally extracted with the SAMMY and REFIT shape analysis codes. The parameters have been converted into ENDF-6 format and processed with the NJOY code to produce point-wise and multigroup cross sections, as well as preliminary MCNP and ERANOS libraries.

This PhD manuscript is structured as follows. The 2^{nd} Chapter will sum up some notions about the neutron cross section theory. In our analysis, we used the Reich Moore approximation of the R-matrix theory to describe the Resolved Resonance Range (RRR) in terms of resonance parameters. The Unresolved Energy Range (URR) was treated within a statistical description of the compound nucleus based on the generalised Hauser-Feshbach formalism. Chapter 3 will then deal with the target preparation and its characterisation methods, while the GELINA facility and the experimental set-up will be described in Chapter 4. In Chapter 5, special care will be given to the weighting function applied to our capture detectors, to the time dependent background and to the normalisation technique together with the uncertainty propagation in AGS. In Chapter 6, we will compare the results from the REFIT and SAMMY codes, with emphasis on the Doppler effect, on the experimental resolution of the GELINA facility and on the multiple scattering corrections. Finally, we will present in Chapter 7 the ^{127}I(n,γ), ^{127}I(n,tot), ^{129}I(n,γ) and ^{129}I(n,tot) cross sections obtained in this work. The overall conclusions will be presented in Chapter 8.

Chapter 2

Neutron cross section theory

Whenever the nuclei of a given species are bombarded with neutrons, nuclear reactions can be observed with probabilities expressed as cross sections in units of barn (1 b = 10^{-24} cm^2). In the range of neutron reactions from thermal to MeV energies, two distinct processes can be distinguished: the compound nucleus reactions and the direct reactions (Table 2.1).

Table 2.1: Main neutron reactions below 20 MeV of interest for this work.

total reaction (n, tot) σ_t	• *direct reaction* (*potential scattering* σ_p)		
	• *compound nucleus reaction*	• *elastic scattering* (n, n)	σ_s
		• *inelastic scattering* (n, n')	$\sigma_{s'}$
		• *radiative capture* (n, γ)	σ_γ
		• *fission* (n, f)	σ_f
		• *others* (n, xn), (n, p), (n, α)	

When neutrons collide with a nucleus, they may form compound states of very high complexity, decaying usually via particle production, γ-decay or fission. They are called the *compound nucleus reactions*. In some events, the incident neutron may be directly absorbed without intermediate state. The *direct reaction* such as the direct capture is a one-step reaction in which the nucleons which do not participate to the reaction are left undisturbed. The non-resonant potential scattering is a direct reaction whose cross section is close to the geometrical cross section of the nucleus. Its contribution to the total cross section is included in the compound nucleus theory.

Direct reactions play a dominant role at neutron energies higher than about 1 MeV. Within the frame of the present work, only compound nucleus reactions and potential scattering are investigated. The total, capture, elastic and inelastic cross sections of the ^{127}I and ^{129}I available in the JEFF3 neutron data base are shown in Figure 2.1. The compound nucleus reaction cross sections are characterised by resonance structures arising from the existence of long-lived nuclear states in the compound nucleus. At intermediate energies, the resonances are not fully resolved owing to the limitation of the experimental resolution of the facility. Thus, two resonance regions can be distinguished, that of the resolved resonances (RRR), and that of the unresolved resonances (URR). The RRR is parametrised in terms of the R-matrix resonance parameters [17], while the URR is analysed on the basis of the statistical properties of the average resonance

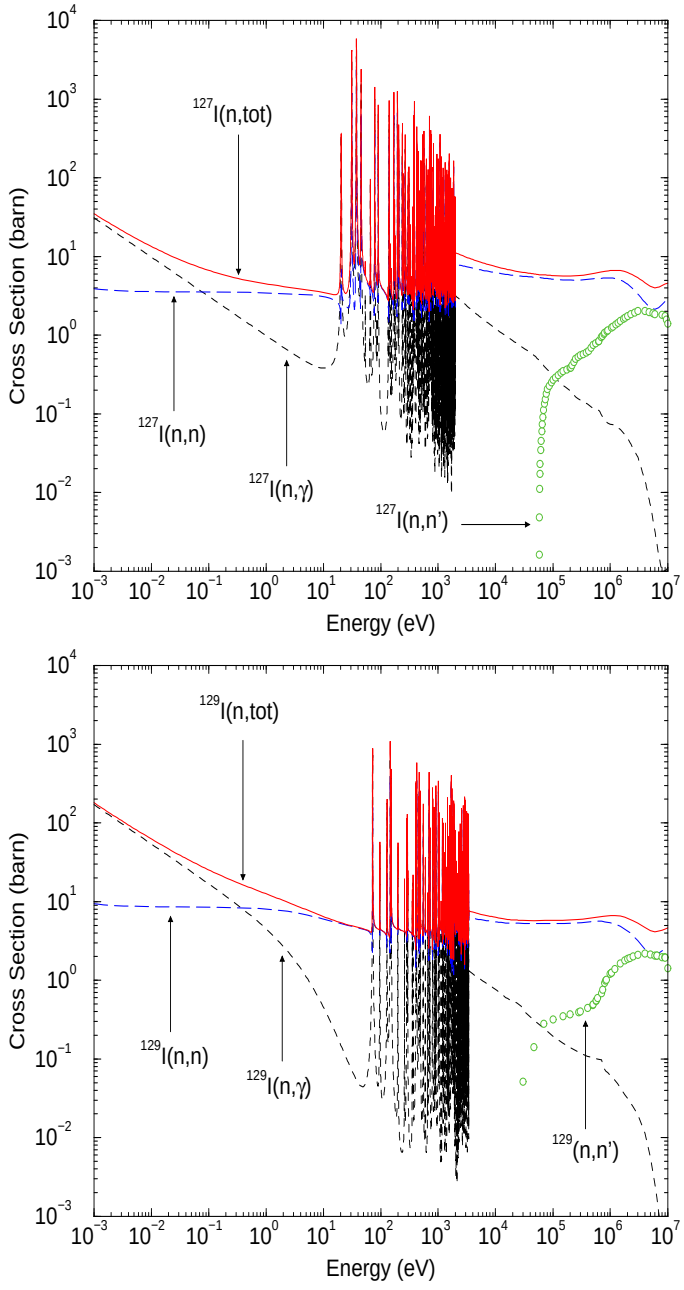

Figure 2.1: ^{127}I and ^{129}I neutron cross sections from the JEFF3 neutron database.

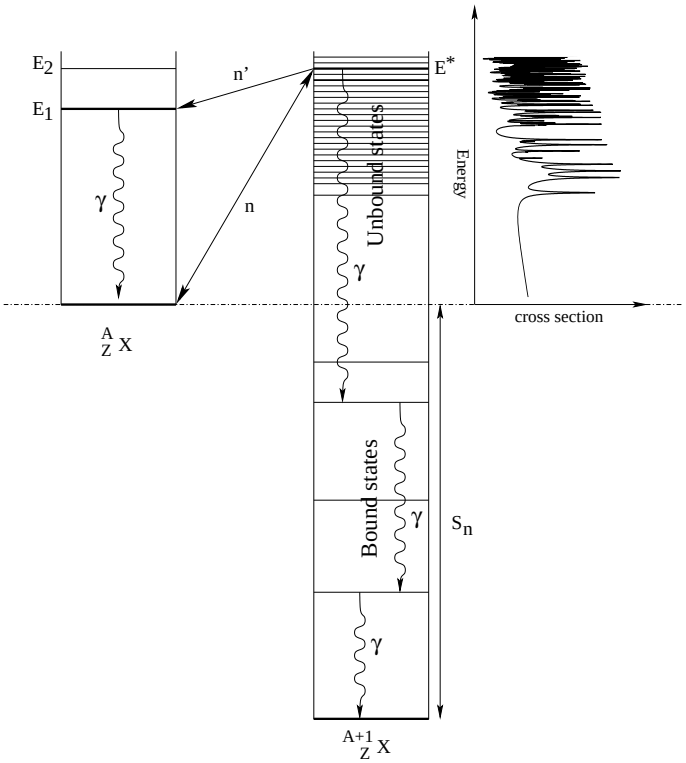

Figure 2.2: Neutron capture, elastic and inelastic level scheme. The excited resonances decay by γ-rays emission to lower energy states. Inelastic scattering reactions occur when the energy in the center of mass exceeds the energy of the first excited state in the target nucleus [21].

parameters. The Hauser-Feshbach theory [19] is the most popular formalism for the analysis of average cross sections.

2.1 Compound nucleus reactions

In the framework of the Bohr compound nucleus theory [18], a neutron induced reaction is considered as a two-step process (Figure 2.2):

$$\underbrace{{}^{A}_{Z}X + n}_{\text{entrance channel c}} \longrightarrow {}^{A+1}_{Z}X^{*} \longrightarrow \underbrace{Y + i}_{\text{exit channel c'}}$$

Since it is almost impossible to describe a nucleus and its excited states in terms of wave functions, the Bohr's compound nucleus model provides an adequate description of the interactions through the statistical properties of the nuclear system. The complex interactions between the $A + 1$ nucleons lead to the independence hypothesis according to which the formation and the decay of the compound nucleus are independent from one another. In this model, the absorption of the neutron is followed by a rapid distribution of the available energy among the other nucleons. The lifetime is about $10^{-16} - 10^{-18}$ s. The total excitation energy (E^*) of the nuclear system is determined by the neutron separation energy (S_n) of the compound nucleus plus the kinetic energy of the incident neutron (E) in the center of mass system:

$$E^* = S_n + E \tag{2.1}$$

When the energy of the compound system corresponds to that of an excited state, a resonance (λ) is observed at the laboratory energy (E_λ). The relationship between (E_λ) and (E) is expressed as follows:

$$E = \left(\frac{A}{A+1}\right) E_\lambda \tag{2.2}$$

It is to be noted that the difference between (E) and (E_λ) is negligible when $A >> 1$. Considering the unbound states (ie $E^* > S_n$) of the compound nucleus helps explaining the presence of neutron resonances. Their lifetime (τ_λ) is correlated to the total width of the resonance (Γ_λ) thanks to the Heisenberg uncertainty principle:

$$\Gamma_\lambda \, \tau_\lambda \simeq \hbar \tag{2.3}$$

The total width of a level is the sum of the partial widths ($\Gamma_{\lambda c}$) corresponding to the decay possibilities of the excited compound nucleus. Iodine is a non-fissile nucleus. Only elastic and capture reactions occur in the resolved resonance range (below 10 keV). The total width is defined as:

$$\Gamma_\lambda = \Gamma_{\lambda n} + \Gamma_{\lambda\gamma} \tag{2.4}$$

in which $\Gamma_{\lambda n}$ is the neutron width and $\Gamma_{\lambda\gamma}$ is the total radiation width. The latter results from the contribution of the partial radiation widths:

$$\Gamma_{\lambda\gamma} = \sum_{c' \in \gamma} \Gamma_{\lambda c'} \tag{2.5}$$

The resonances have a definite angular momentum and parity J^π. The possible values depend (1) on the spin I and parity π_I of the target nucleus, (2) on the spin i and parity π_i of the incident particle and (3) on the orbital momentum l of the incident particle. Their vectorial combinations lead to the channel spin (s), and to the total angular momentum (J) and parity (π) of the compound state [20]:

$$\begin{aligned} |I - i| &\leq s \leq I + i \\ |l - s| &\leq J \leq l + s \\ \pi &= (-1)^l \; \pi_I \; \pi_i \end{aligned}$$

The possible J^π values for the iodine resonances below 10 keV are given in Table 2.2. The statistical spin factor (g_J) gives out the probability of getting the allowed total angular momentum J from the intrinsic spins of the target nucleus and of the incident particle:

$$g_J = \frac{2J+1}{(2i+1)(2I+1)} \tag{2.6}$$

Finally, an interaction may occur if the $J'^{\pi'}$ value of the exit channel $c' = \{\alpha', l', s', J'\}$ is equal to the J^π value of the entrance channel $c = \{\alpha, l, s, J\}$. The α (or α') index labels the nature and the number of nucleons of the entrance (or outgoing) pair.

Table 2.2: ^{127}I and ^{129}I spin configuration for the s- and p-wave iodine resonances.

	l	s	J^π			g_J			wave
^{127}I $(5/2^+)$	0	2	2^+			5/12			s
		3	3^+			7/12			
	1	2	1^-	2^-	3^-	1/4	5/12	7/12	p
		3	2^-	3^-	4^-	5/12	7/12	3/4	
^{129}I $(7/2^+)$	0	3	3^+			7/16			s
		4	4^+			9/16			
	1	3	2^-	3^-	4^-	5/16	7/16	9/16	p
		4	3^-	4^-	5^-	7/16	9/16	11/16	

2.2 Resolved Resonance Region (RRR)

2.2.1 R-matrix formalism

The resolved resonance range is described by the R-matrix theory [22, 23]. The principle of the R-matrix formalism consists of assuming both incident particles as well as both emerging reaction products as an in-going and an out-going wave function. Since the nuclear forces are short-ranged, the configuration space is divided into an external and an internal regions separated by an imaginary closed surface of radius a_c. Ideally, the direct interactions take place predominantly outside the internal region while the compound nucleus mechanisms are confined inside. A reasonable choice for the channel radius a_c is:

$$a_c \simeq 1.35\ (A+1)^{1/3} \quad \text{(fm)} \tag{2.7}$$

in which A stands for the number of nucleons in the target nucleus. In the external region the nuclear forces are negligible. Therefore, the asymptotic wave function governing the dynamic of the free interacting particles may be known analytically. On the contrary, in the internal region the nuclear forces predominate. The neutron and the nucleus are merged together to form a system of $A+1$ nucleons in interaction which increases the complexity of the wave function of the nuclear system. Although the internal wave function is unknown, the internal domain may be treated in terms of the collision matrix U which describes the nuclear interaction. For a given ingoing wave c, all outgoing wave functions c' (or partial cross sections $\sigma^J_{cc'}$) may be expressed under the following simplified way:

$$\sigma^J_{cc'} = \pi\,\lambda\!\!\!^{-2}\, g_J |\delta_{cc'} - U_{cc'}|^2 \tag{2.8}$$

with

$$U_{cc'} = U^J_{\alpha ls,\alpha' l' s'} \qquad \text{and} \qquad \delta_{cc'} = \delta_{\alpha\alpha'}\delta_{ll'}\delta_{ss'} \tag{2.9}$$

where $|U_{cc'}|^2$ is the probability of a transition from channel c to channel c', and $\delta_{cc'}$ occurs because the in-going and the out-going particles cannot be distinguished if $c = c'$. The elastic cross section is then expressed as follows:

$$\sigma_{\alpha\alpha} = \pi\lambda\!\!\!^{-2} \sum_J g_J \sum_{l,s} |1 - U_{cc}|^2 \tag{2.10}$$

The expression of the reaction cross section ($\alpha \neq \alpha'$) quadratically depends on the $U_{cc'}$:

$$\sigma_{\alpha\alpha'} = \pi\lambda^2 \sum_J g_J \sum_{l,s} \sum_{l',s'} |U_{cc'}|^2 \tag{2.11}$$

By contrast, the total cross section is a linear function of U_{cc}:

$$\sigma_\alpha = 2\,\pi\,\lambda^2 \sum_J g_J \sum_{l,s} (1 - \mathcal{R}e(U_{cc})) \tag{2.12}$$

In order to describe all cross sections with the parameters of the nuclear system, the R-matrix theory allows U to be expressed in terms of the matrix R:

$$U_{cc'} = \mathrm{e}^{-i(\varphi_c+\varphi'_c)} \left\{ \delta_{cc'} + 2\,i\,P_c^{1/2} \left[(1 - R\,L^o)^{-1} R \right]_{cc'} P_{c'}^{1/2} \right\} \tag{2.13}$$

$$L^o_{cc'} = (S_c \;+\; iP_c \;-\; B_c)\,\delta_{cc'} \tag{2.14}$$

where φ_c stands for the phase shift of hard-sphere scattering, S_c is called the shift factor, P_c represents the penetration factor and B_c is a free choice quantity (boundary condition). For neutral projectiles ($c = n$), φ_n, S_n and P_n for s-, p- and d-waves are defined as follows:

$$\begin{array}{lllll}
\varphi_n^{(l=0)} = \rho & ; & \varphi_n^{(l=1)} = \rho - \arctan(\rho) & ; & \varphi_n^{(l=2)} = \rho - \arctan\left(\frac{3\rho}{3-\rho^2}\right) \quad ; \quad \cdots \\
S_n^{(l=0)} = 0 & ; & S_n^{(l=1)} = \frac{-1}{1+\rho^2} & ; & S_n^{(l=2)} = \frac{-3(\rho^2+6)}{9+3\rho^2+\rho^4} \quad ; \quad \cdots \\
P_n^{(l=0)} = \rho & ; & P_n^{(l=1)} = \frac{\rho^3}{1+\rho^2} & ; & P_n^{(l=2)} = \frac{\rho^5}{9+3\rho^2+\rho^4} \quad ; \quad \cdots
\end{array} \tag{2.15}$$

in which $\rho = ka_c$ stands for a function of the channel radius a_c and of the wave number defined as:

$$k \;=\; \frac{1}{\lambda} \;=\; \frac{\sqrt{2m_n E_n}}{\hbar} \;=\; 2.1968 \times 10^{-3} \left(\frac{A}{A+1}\right) \sqrt{E} \tag{2.16}$$

Figure 2.3 shows the behaviour of P_n for $l = 0, 1, 2, 3$. At 1 keV, s-wave levels dominate, p-wave levels contribute to 1% and contribution of the higher order partial waves are negligible.

The collision matrix contains also the R-matrix elements $R_{cc'}$ defined as:

$$R_{cc'} \;=\; \sum_\lambda \frac{\gamma_{\lambda c}\;\gamma_{\lambda c'}}{E_\lambda \;-\; E} \tag{2.17}$$

The parameters of the problem can be identified with the energy E_λ and with the reduced width amplitudes $\gamma_{\lambda c}$ and $\gamma_{\lambda c'}$ of the resonance λ. $\gamma_{\lambda c}$ is the probability amplitude for the formation of compound state λ via the entrance channel c, and $\gamma_{\lambda c'}$ is the probability amplitude for the decay of compound state via the exit channel c'. According to the fundamental assumptions of the statistical model, $\gamma_{\lambda c}$ and $\gamma_{\lambda c'}$ are independent, uncorrelated and have random signs. These assumptions imply that the statistical properties of the exit channel c' contain no memory of the entrance channel. Besides, the treatment of $\gamma_{\lambda c}$ as a random variable is consistent with the complicated wave function of the nuclear states.

Cross sections formulae are usually written in terms of partial widths $\Gamma_{\lambda c}$ rather than decay amplitudes. The partial width is related to the square of the amplitude via the penetration factor P_c:

$$\Gamma_{\lambda c} \;=\; 2\,\gamma_{\lambda c}^2\,P_c \tag{2.18}$$

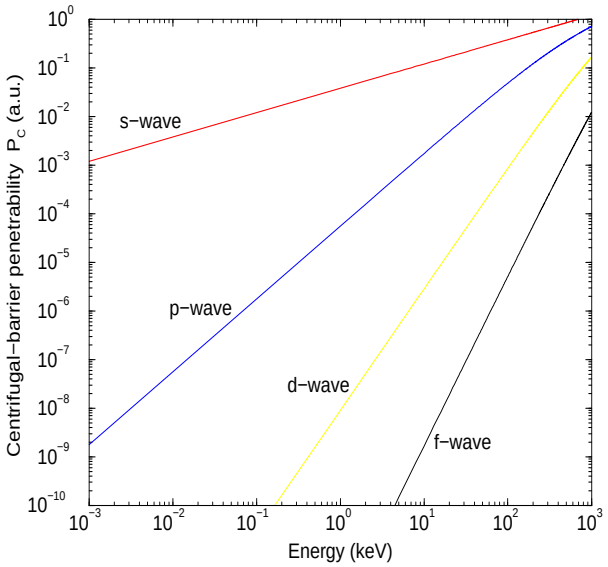

Figure 2.3: Penetration factor (P_c) calculated for ^{129}I neutron induced reactions.

E_λ and the partial widths depend on the nuclear interaction. In typical application of the R-matrix theory, they just serve as fit parameters adjustable to experimental data. The full derivation of the R-matrix theory is so formidable, that its numerical implementation in a computer program is hardly applicable. The practically important variants of the R-matrix formalism presented in this work are the Reich-Moore approximation [24] and the Single Level Breit-Wigner formalism (SLBW) [25].

2.2.2 Reich-Moore approximation

The Reich-Moore approximation consists of neglecting the off-diagonal contribution of photon channels in the R-matrix. This approximation is valid, because there are usually very many channels where decay amplitudes have comparable magnitude and random signs. Therefore, their contribution to the sum over the channel ($c \in \gamma$) tend to cancel for $\lambda \neq \mu$:

$$\sum_{c\in\gamma} \gamma_{\lambda c}\, \gamma_{\mu c} \;\simeq\; 0 \tag{2.19}$$

The resulting collision matrix becomes a function of a reduced R-matrix:

$$R_{cc'} \;=\; \sum_{\lambda} \frac{\gamma_{\lambda c}\, \gamma_{\lambda c'}}{E_\lambda \;-\; E - i\Gamma_{\lambda\gamma}/2} \qquad (c, c' \notin \gamma) \tag{2.20}$$

It is a reduced matrix in the sense that $R_{cc'}$ is only defined over the non-photonic channels. The photon channels are explicitly taken into account through the total radiation width defined as:

$$\Gamma_{\lambda\gamma} = \sum_{c\in\gamma} \Gamma_{\lambda c} \tag{2.21}$$

At low neutron energy, the reduced R-matrix dimension for fissile target nuclei is usually a 3×3 matrix (1 elastic plus 2 fission channels). For non-fissile nuclei, the only energetically

allowed processes are elastic scattering ($c = n$) and radiative capture ($c = \gamma$), for which the 1-channel Reich-Moore expression suffices. Consequently, the reduced R-matrix merely is an R function expressed as follows:

$$R_{nn} \;=\; \sum_{\lambda} \frac{\gamma^2_{\lambda n}}{E_\lambda \;-\; E - i\Gamma_{\lambda\gamma}/2} \tag{2.22}$$

The reduced collision matrix U_{nn} is obtained from Equation 2.13 with the arbitrary choice $B_n = S_n$. Equation 2.14 becomes:

$$L^o_{nn} \;=\; iP_n \tag{2.23}$$

and U_{nn} is given by:

$$U_{nn} \;=\; \mathrm{e}^{-2i\varphi_n} \frac{1 + i\; P_n\; R_{nn}}{1 - i\; P_n\; R_{nn}} \tag{2.24}$$

The elastic ($\sigma_s \equiv \sigma_{\alpha\alpha}$) and total ($\sigma_t \equiv \sigma_\alpha$) cross sections are respectively obtained from Equations 2.10 and 2.12. The capture cross section (σ_γ) may alternatively be obtained as the following difference:

$$\sigma_\gamma(E) \;=\; \sigma_t(E) \;-\; \sigma_s(E) \tag{2.25}$$

The iodine capture and total cross sections were analysed with the Reich-Moore approximation of the R-matrix theory as implemented in the REFIT [26] and SAMMY [27] shape analysis programs.

2.2.3 External levels

In practice, using the R-function expressed in Equation 2.22 doesn't allow a satisfactory fit of the experimental data. The R-matrix theory shows that the cross sections in a limited energy range depend not only on the *internal* levels in that range, but also on the *external* levels outside. Typically, some difficulties arise in resonance analysis whenever compound levels below the neutron separation energy ($E < 0$) happen to be omitted. Although these external levels are unobservable and therefore unknown, they must be introduced in the R-matrix formalism. A convenient approximation consists of accounting for the effect of such distant levels by the tails of broad resonances having negative energies [23, 28]. The correct nuclear parameters of the negative resonances are those which reproduce accurately the thermal cross section as well as the $1/v$ behaviour of the capture cross section (Figure 2.4). Dealing with this approach, the reduced R function may be split into a sum over the external (ext) and internal (int) levels:

$$R_{nn} \;\equiv\; R^\infty_n \;+ \sum_{\mu=1}^{\mu_{ext}} \frac{\gamma^2_{\mu n}}{E_\mu \;-\; E - i\Gamma_{\mu\gamma}/2} \;+ \sum_{\lambda=1}^{\lambda_{int}} \frac{\gamma^2_{\lambda n}}{E_\lambda \;-\; E - i\Gamma_{\lambda\gamma}/2} \tag{2.26}$$

The first term in Equation 2.26 is the so-called distant level parameter. In applied neutron resonance field the effective potential scattering length or radius R' for s-wave channels is explicitly defined as [29]:

$$R' \;=\; a_n\;(1 - R^\infty_n) \tag{2.27}$$

The radius R' is connected to the potential scattering cross section. In the absence of resonances, the scattering cross section at low neutron energies is reduced to the potential scattering cross section:

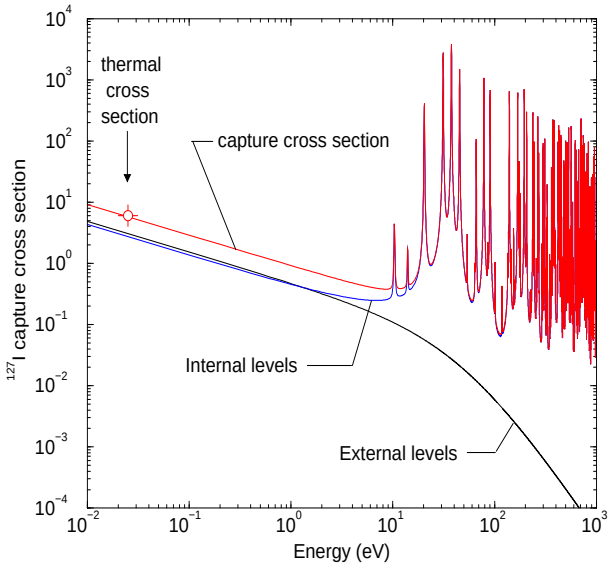

Figure 2.4: Contribution of the external levels in the ^{127}I capture cross section.

$$\sigma_p \;=\; 4\,\pi\,R'^2 \tag{2.28}$$

In the R-matrix shape analysis programs, R' (in SAMMY) or R_n^{∞} (in REFIT) are free parameters determined from the fit of the total cross section.

2.2.4 Single-level Breit-Wigner approximation

Earlier versions of the various evaluated data libraries, as well as earlier resonance analysis made very heavy use of the Single Level Breit-Wigner (SLBW) approach before introducing the Reich-Moore approximation. The SLBW may be seen as an efficient approximation of the R-matrix formalism, which consists of taking into account each level separately. It may give reasonable nuclear parameters in the case of isolated resonances that are virtually unaffected by multi-level interference.

According to the R-matrix formalism, the single level collision matrix for s-wave is defined as follows [23]:

$$U_{cc'} \;\equiv\; \mathrm{e}^{-2ikR'}\left(\delta_{cc'} + \frac{i\sqrt{\Gamma_{\lambda c}\Gamma_{\lambda c'}}}{(E_\lambda - E) - \Gamma_\lambda/2}\right) \tag{2.29}$$

where $\Gamma_\lambda = \sum_c \Gamma_{\lambda c}$ represents the total width. The resulting total and partial cross section are expressed as follows:

$$\sigma_c^J = 4\pi g_J R'^2 + 4\pi\lambda\!\!\!^{-2}\frac{g_J\Gamma_{\lambda c}\Gamma_\lambda}{\Gamma_\lambda^2 + 4(E_\lambda - E)^2} + 4\pi\lambda\!\!\!^{-2}R'\frac{g_J\Gamma_{\lambda c}(E_\lambda - E)}{\Gamma_\lambda^2 + 4(E_\lambda - E)^2} \tag{2.30}$$

$$\sigma_{cc'}^J = 4\pi\lambda\!\!\!^{-2}\frac{g_J\Gamma_{\lambda c}\Gamma_{\lambda c'}}{\Gamma_\lambda^2 + 4(E_\lambda - E)^2} \tag{2.31}$$

The total cross section is a sum of three terms: (1) the constant potential scattering cross section, (2) a symmetric resonance term, (3) and an asymmetric term arising from interference between hard-sphere potential and resonance scattering.

The SLBW formalism may be a relevant alternative to get prior information about resonance parameters. At low energy, the resonances are usually so narrow compared with resonance spacing that the experimental resolution will separate resonances over a large energy range. Prior estimate can be extracted from a transmission $T(E)$ (see Equation 4.2) or a capture yield $Y(E)$ (see Equation 4.3) using the *area analysis* method [30, 31]. In transmission, the area function for an isolated resonance is defined as the integral between the transmission curve and unity:

$$A_\lambda = \int_0^{+\infty} (1 - T(E))\,\mathrm{d}E \simeq \int_0^{+\infty} \left(1 - \mathrm{e}^{-n\sigma_t(E)}\right)\mathrm{d}E \tag{2.32}$$

Similarly, the capture area is expressed as:

$$A_{\lambda\gamma} = \int_0^{+\infty} Y(E)\mathrm{d}E \simeq \int_0^{+\infty} (1 - T(E))\,\frac{n\sigma_\gamma(E)}{n\sigma_t(E)}\mathrm{d}E \tag{2.33}$$

in which n represents the sample thickness in at/b, σ_γ stands for the capture cross section and σ_t is the total cross section. The asymptotic forms of Equations 2.32 and 2.33 can be evaluated analytically for a thin and thick sample using the Breit-Wigner formulae. The potential term in the total cross section and the Doppler effect are neglected to get the expressions:

$$A_{\lambda\gamma}(thin) \;\simeq\; \frac{1}{2}\pi n\sigma_o\Gamma_{\lambda\gamma} \;=\; 2n\pi^2\lambda\!\!\!^{-2} g_J \frac{\Gamma_{\lambda n}\Gamma_{\lambda\gamma}}{\Gamma_\lambda} \tag{2.34}$$

$$A_\lambda(thin) \;\simeq\; \frac{1}{2}\pi n\sigma_o\Gamma_\lambda \;=\; 2n\pi^2\lambda\!\!\!^{-2} g_J \Gamma_{\lambda n} \tag{2.35}$$

$$A_\lambda(thick) \;\simeq\; \sqrt{\pi n\sigma_o}\Gamma_\lambda \;=\; 2\pi\lambda\!\!\!^{-}\sqrt{n g_J \Gamma_{\lambda n}\Gamma_\lambda} \tag{2.36}$$

in which $2\pi\lambda\!\!\!^{-}$ stands for the de Broglie wavelength of the relative motion of neutron and target nucleus, and σ_o is the peak total cross section of the resonance defined as:

$$\sigma_o = 4\pi\lambda\!\!\!^{-2} g_J \frac{\Gamma_{\lambda n}}{\Gamma_\lambda} \tag{2.37}$$

Figure 2.5 compares the experimental area ($A_{\lambda\gamma}$) extracted from a thin ^{129}I capture yield together with the values obtained from the thin sample form (Equation 2.34). The results are in reasonable agreement up to a capture area of about 0.1 eV. Within the condition $\Gamma_{\lambda\gamma} >> \Gamma_{\lambda n}$, data from a thin capture or transmission sample gives $\sigma_o\Gamma_{\lambda\gamma}$ directly and hence $g_J\Gamma_{\lambda n}$.

2.3 Average R-matrix parameters

The formalism dedicated to the URR analysis is widely based on the probabilistic treatment of the R-matrix parameters [23]. The parameters to be extracted from our iodine transmission and capture measurements are the neutron strength function (S_l), the average radiation width ($< \Gamma_{\lambda\gamma,l} >$) and the mean level spacing (D_l). The strength function yields the basic statistical properties of the compound states and has the property of being nearly independent of energy.

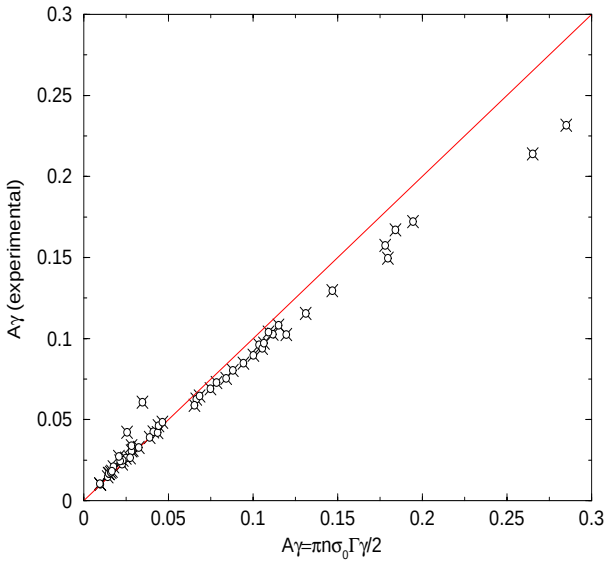

Figure 2.5: Experimental capture area $A_{\lambda\gamma}$ extracted from a thin ^{129}I sample capture yield compared with the results provided by the Single-Level Breit-Wigner approximation of the capture area (Equation 2.34).

The neutron strength function is closely related to the transmission coefficients (T_l) currently obtained from the optical model:

$$S_l \equiv \frac{ka_c}{2\pi}\frac{T_l}{P_l\sqrt{E}} \tag{2.38}$$

It is also defined as the ratio of the average reduced partial width to the mean level spacing:

$$S_l = \frac{1}{2l+1}\sum_J \frac{g_J < \Gamma^l_{\lambda c} >}{D_J} \tag{2.39}$$

For $c = n$, the reduced neutron width is defined as:

$$\Gamma^l_{\lambda n} = \frac{k\ a_c}{P_l}\frac{\Gamma_{\lambda n}}{\sqrt{E}} = \frac{2a_c\sqrt{2m_n}}{\hbar}\gamma^2_{\lambda n} \tag{2.40}$$

For s-wave resonances ($l = 0$), $\Gamma^o_{\lambda n}$ is simply given by:

$$\Gamma^0_{\lambda n} = \Gamma_{\lambda n}\sqrt{\frac{1\ eV}{E}} \tag{2.41}$$

The prediction of the mean level spacing is currently done with the *Gilbert and Cameron formula* [32], the distribution for the energy spacing between adjacent levels in a given J^π level sequence obeys *Wigner's surmise* [33], and the probability density function of the reduced width (or $\gamma^2_{\lambda c}$) is described by the *Porter-Thomas distribution* [38].

2.3.1 The Gilbert and Cameron level density formula

The description of the compound nucleus can be carried out within the framework of the statistical theory of nuclear reactions. The average level spacing serves as one of the required

parameters. The study of the spacing between the neutron resonances sharing the same l in an interval ΔE containing N resonances provides a direct way of determining D_l [35]:

$$D_l = \frac{\Delta E}{N-1} \tag{2.42}$$

Alternatively, one may define the observed level density ρ_l as the number of levels per unit of energy:

$$\rho_l = \frac{1}{D_l} \tag{2.43}$$

However, many sources of error may alter the level spacing deduced from neutron resonance data. Capture and transmission measurements are not precise enough to make sure that all resonances have been detected. Therefore, a semi-empirical formula was introduced to predict reliable estimates of the level density $\rho_J(E)$ of all levels with spin J, regardless of parity (+ or -). It was developed on the basis of the Bethe free gas model, which considers the nucleus as being a Fermi gas of free nucleons confined to the nuclear volume. Gilbert and Cameron proposed a formula to account for the dependence of the various parameter on the mass number A, the odd-even effect, the shell structure and the nuclear deformation [32]. The adopted formula may be written as follows [23]:

$$\rho_J(E) = \frac{1}{3}\frac{a\ \mathrm{e}^{\sqrt{4aU}}}{\sigma(4aU)^{5/4}}\left[\mathrm{e}^{-\frac{J^2}{2\sigma^2}} - \mathrm{e}^{-\frac{(J+1)^2}{2\sigma^2}}\right] \quad \text{if} \quad U > 2.5 + \frac{150}{A} \qquad (\mathrm{MeV}^{-1}) \tag{2.44}$$

in which (U) is the effective excitation energy, (σ) a spin-dependent parameter often called the spin cut-off, and (a) the fermion gas level density parameter. The effective excitation energy is the excitation energy E^* corrected for pairing energy $P(Z)$ and $P(N)$:

$$U = E^* - P(Z) - P(N) \tag{2.45}$$

The pairing energy is the energy required to pair two identical nucleons in the same orbit. $P(N)$ and $P(Z)$ are zero for odd values of N and Z. The spin cut-off parameter is calculated from the expression [37]:

$$\sigma^2 \simeq 0.1459\sqrt{a\,U}(A+1)^{2/3} \tag{2.46}$$

The level density parameter (a) can be deduced from the s-wave level density. In the analysis of neutron resonances, the relevant parameter is the observed level density ρ_l rather than $\rho_J(E)$ which involves both parities. Assuming equal probability for both parities, ρ_l may be defined as:

$$\rho_l = \frac{1}{2}\sum_J \rho_J(E) \tag{2.47}$$

For s-wave neutron resonances, and a target nucleus with a ground state spin I and parity π, the states of the compound nucleus exhibit a spin either of $J = I + 1/2$ or $J = |I - 1/2|$ and a parity π. The level density of s-wave resonance is therefore:

$$\rho_o = \frac{1}{2}\left(\rho_{|I-1/2|}(E) + \rho_{I+1/2}(E)\right) \tag{2.48}$$

2.3.2 The Wigner level spacing distribution

The so-called next-neighbour spacing distribution is the distribution of the energy spacings (S) between adjacent level in a given J^π level sequence. The most commonly used level statistic was introduced by Wigner [33]. In the framework of the Random Matrix Theory (RMT) [34], he suggested that the Hamiltonian of the nuclear system should be similar to a real symmetric matrix with random matrix elements that are Gaussian distributed. When the energy levels are eigenvalues of a random matrix, they are not independent. The RMT exhibits repulsion of energy levels, vanishing probability for zero level spacing. The Wigner's law follows from the assumption of a linear repulsion. He suggested that, at least for small S values, the probability of the level occurrence is proportional to the spacing S. Assuming proportionality also for large S values, the distribution of the level spacings can be adequately described with the so-called Wigner's surmise:

$$P(x)\mathrm{d}x \;=\; \frac{\pi}{2} x \mathrm{e}^{-\frac{\pi}{4}x^2}\mathrm{d}x \tag{2.49}$$

The distribution is expressed in terms of the dimensionless variable

$$x \;=\; \frac{S}{D_{l,J}} \tag{2.50}$$

where $D_{l,J}$ stands for the mean level spacing in a given J^π level sequence. The above expression is a good approximation of the exact s-wave level spacing distribution for zero-spin target nuclei. For non zero-spin target nuclei, the distribution is altered, since the s-wave resonances have two possible J values (J_1 and J_2). The complete expression that can be used for combining two Wigner distributions with mean spacing D_{0,J_1} and D_{0,J_2} has the following form [35, 70]:

$$\begin{aligned} P(x)\mathrm{d}x \;=\; \tfrac{\pi k}{2(k+1)^3} \Bigg[& x\, \mathrm{e}^{-\frac{\pi}{4(k+1)^2}x^2} \left(1 - \mathrm{erf}\left(\tfrac{\sqrt{\pi}k}{2(k+1)}x\right)\right) \\ & + 4\,\pi\,k\,(k+1)\, \mathrm{e}^{-\frac{\pi(k^2+1)}{4(k+1)^2}x^2} \\ & + \; k^2\, x\, \mathrm{e}^{-\frac{\pi k^2}{4(k+1)^2}x^2} \left(1 - \mathrm{erf}\left(\tfrac{\sqrt{\pi}}{2(k+1)}x\right)\right) \Bigg]\, \mathrm{d}x \end{aligned} \tag{2.51}$$

where x and k are defined as follows:

$$x \;=\; \frac{S}{\frac{1}{D_{0,J_1}} + \frac{1}{D_{0,J_2}}} \qquad \text{and} \qquad k \;=\; \frac{D_{0,J_1}}{D_{0,J_2}} \tag{2.52}$$

The above combined distribution gives the probability of obtaining any spacing regardless of the spin. P.Ribon has implemented the CALENDF code with similar expressions in order to get valuable information for spin assignment applications [36].

2.3.3 The Porter-Thomas reduced neutron width distribution

Within the framework of the statistical description of the compound nucleus, the probabilistic prediction of the unseen resonances as well as the probability distribution of their partial width is of central importance. The statistical distribution of the reduced width ($\Gamma^l_{\lambda c}$) was introduced by Porter and Thomas [38].

• **Reduced neutron width**

The neutron widths strongly fluctuate among resonances with the same total angular momentum and parity. According to Equation 2.18, the fluctuations must be attributed to the reduced width amplitude ($\gamma_{\lambda n}$) because of the smooth energy dependence of the penetration factor (P_c). On the basis of the compound nucleus theory, $\gamma_{\lambda n}$ have random signs which nearly cancel positive and negative contributions. Thus, their most objective probability distribution is a Gaussian with zero mean. This assumption leads to the reduced width distribution hypothesised by Porter and Thomas. The adequate distribution for the reduced neutron width is a chi-squared function with one degree of freedom:

$$P(x)\mathrm{d}x = \frac{\mathrm{e}^{-\frac{x}{2}}}{\sqrt{2\pi x}}\mathrm{d}x \qquad x \equiv \frac{\Gamma^l_{\lambda n}}{<\Gamma^l_{\lambda n}>} \tag{2.53}$$

• **Radiation width**

In the case of the total radiation width, the situation gets more complex as the distribution (2.53) is only valid for a single-transition photon width. The total radiation width is the sum of many partial radiation widths. Thus, $\Gamma_{\lambda\gamma}$ should obey the generalised Porter and Thomas distribution which is a chi-squared function with ν degrees of freedom (ν being the number of exit channels c):

$$P(x)\mathrm{d}x = \frac{\nu/2}{\Gamma\left(\frac{\nu}{2}\right)}\left(\frac{\nu}{2}x\right)^{\frac{\nu}{2}-1}\mathrm{e}^{-\frac{\nu}{2}x}\mathrm{d}x \qquad x \equiv \frac{\Gamma_{\lambda\gamma}}{<\Gamma_{\lambda\gamma}>} \tag{2.54}$$

in which $\Gamma(\nu/2)$ is a gamma function. A large number of freedom degree (ν) is expected in the case of heavy nuclei because of the usually large number of allowed radiative transitions. It is possible for $\Gamma_{\lambda\gamma}$ to have a nearly normal distribution, suggesting to have nearly constant radiation widths from level to level in a given nuclide. When no information is available a reasonable estimate of $\Gamma_{\lambda\gamma}$ for a particular resonance is often the average value of the total radiation width:

$$\Gamma_{\lambda\gamma} \simeq <\Gamma_\gamma> \tag{2.55}$$

2.3.4 Information from the Resolved Resonance Range

Before analysing the URR, prior average parameters must be determined from the resolved resonances. The calculation is performed with the computer code ESTIMA [39]. From a set of resolved resonance parameters, this code determines the average spacing (D_0) and the neutron strength function (S_0). The estimate procedure uses a method based on the Porter and Thomas distribution with one degree of freedom which accounts for the experimentally missed small resonances.

The results are sensitive to the contamination of p-wave resonances. The quantity usually measured from a capture or a transmission experiment is $g\Gamma_{\lambda n}$, instead of $\Gamma_{\lambda n}$, and no direct evidences are available to derive the parity of the resonances. A statistical test was implemented in ESTIMA in order to provide useful information about l assignment. The test is based on the Bayes' theorem. Following the conditional probability theory, the probability that any resonance with a certain value $g\Gamma_{\lambda n}$ is a l-wave resonance is expressed as:

$$P(l|g\Gamma_{\lambda n}) = \frac{P(g\Gamma_{\lambda n}|l)\ P(l)}{\sum_{l'} P(g\Gamma_{\lambda n}|l')\ P(l')} \tag{2.56}$$

$P(l)$ is the prior probability that a resonance is an l-wave and $P(g\Gamma_{\lambda n}|l)$ is the probability density function (pdf) of $g\Gamma_{\lambda n}$ of l-wave resonances. $P(l|g\Gamma_{\lambda n})$ is the posterior probability calculated by ESTIMA. In distinguishing p-wave from s-wave resonances, the posterior probability may be written as [40, 41]:

$$P(l=1|g\Gamma_{\lambda n}) \equiv \left[1+\frac{1}{G_1}\sqrt{\frac{S_1 P_n^{(l=1)}}{S_0 P_n^{(l=0)}}}\frac{\mathrm{e}^{\frac{k\ a_c\ g\Gamma_{\lambda n}}{2\ D_0\sqrt{E_\lambda}}\left(\frac{1}{S_1 P_n^{(l=1)}}-\frac{1}{S_0 P_n^{(l=0)}}\right)}}{\alpha_1+(1-\alpha_1)\sqrt{\frac{k\ a_c\ \pi g\Gamma_{\lambda n}}{2\ D_0 S_1\sqrt{E_\lambda}P_n^{(l=1)}}}}\right]^{-1} \tag{2.57}$$

The probability is expressed in terms of level spacing and neutron strength function. The α_1 and G_1 parameters depend on the target spin (for iodine nucleus, α_1 and G_1 are respectively equal to 1/2 and 2). ESTIMA provides a confident s-wave resonance sample according to a threshold probability (P_B) given by the user. Below P_B, the s- and p-wave probabilities become indistinctive. The P_B threshold is chosen in order to obtain a satisfactory agreement between the experimental and calculated Porther-Thomas distributions.

2.4 Unresolved Resonance Region

The URR analysis consists of calculating cross sections in an average energy range wide enough on the one hand to contain many unresolved resonance structures but on the other hand so narrow to allow the variations of level statistics and other weak energy dependence to be neglected. The average cross section are described in terms of level-statistical parameters (strength function S_l, mean level spacing D_l, mean radiation width $<\Gamma_\gamma>$ and distant level parameter R^∞). The appropriate cross section models are based on the average R-matrix theory. The original formalism was introduced by Hauser and Feshbach [19]. Its exact solution was proposed later over the Gaussian Orthogonal Ensemble triple integral [42]. More recently, an alternative approach was developed using the characteristic function of the R matrix elements [43, 44]. The formalism used in this work is based on an elaborate form of the Hauser-Feshbach formula proposed by Moldauer [45, 46] and implemented in the FITACS program [47].

The general average cross section may be defined as:

$$<\sigma_{cc'}^J>=\pi\lambda\!\!\!^{-2} g_J\overline{|\delta_{cc'}-U_{cc'}|} \tag{2.58}$$

In the same way as in Equation 2.12, the average total cross section for given spin, parity and incident channel c, may be written as:

$$<\sigma_c^J>=2\pi\lambda\!\!\!^{-2} g_J\left(1-\mathcal{R}e\ \overline{U_{cc}}\right) \tag{2.59}$$

According to the R-matrix theory, the average scattering matrix (or collision matrix) is given by:

$$\overline{U_{cc}}\equiv \mathrm{e}^{-2\varphi}\frac{1+i\,(R_c^\infty+i\pi\ s_c)}{1-i\,(R_c^\infty+i\pi\ s_c)} \tag{2.60}$$

where R_c^∞ is the distant level parameter related to the effective radius, and s_c is the pole strength function which may be expressed in term of strength function (S_l) or transmission coefficient (T_l):

$$s_c \;=\; \frac{S_l\,\sqrt{E}}{2\,k\,a_c} \;=\; \frac{T_l}{4\pi P_l} \tag{2.61}$$

Much effort has been devoted to derive an analytic and computationally simple average partial cross section on a basis of the Hauser-Feshbach theory. In FITACS, the total cross section is calculated with Equation 2.59, and the partial cross sections are written in terms of transmission coefficients as:

$$< \sigma^J_{cc'} >= \underbrace{\sigma_p \delta_{cc'}}_{\substack{\text{direct}\\ \text{reaction}}} + \underbrace{\pi \bar{\lambda}^2 g_J \frac{T_c T_{c'}}{\sum_c T_c}}_{\substack{\text{Hauser}\\ \text{Feshbach}}} \underbrace{\left(1 + \frac{2}{\bar{\nu}_c}\delta_{cc'}\right)}_{\substack{\text{elastic}\\ \text{enhancement}}} \underbrace{\int_0^\infty \prod_{c''} \left(1 + \frac{2T_{c''}}{\bar{\nu}_{c''}\sum_c T_c}x\right)^{-\delta_{cc''}-\delta_{c'c''}-\bar{\nu}_{c''}/2} \mathrm{d}x}_{\substack{\text{width fluctuation}\\ \text{correction}}} \tag{2.62}$$

where $\bar{\nu}_c$ is an effective degree of freedom for channel c. According to the Moldauer recommendation based on Monte-Carlo simulations, it is defined as [48]:

$$\bar{\nu}_c = \left[1.78 + \left(T_c^{1.218} - 0.78\right) \mathrm{e}^{-0.228 \sum_c T_c}\right] \nu_c \tag{2.63}$$

where ν_c is the degree of freedom assuming a generalised Porter-Thomas distribution for the partial width.

In the pure Hauser-Feshbach formula, the resonant structures are described in Single-Level Breit-Wigner approximation, under the restriction that all partial widths are smaller than the level spacing (isolated resonance), and assuming no correlation between the partial widths of different channels. The generalisation of the formalism for significant level overlap involves two extra factors. The *width fluctuation correction* (or *Dresner factor*) accounts for the multi-level interferences, while the *elastic enhancement* accounts for the channel-channel correlations [49]. The latter correction is of particular importance for the evaluation of elastic cross section ($c = c'$). Its value is expected to be limited to a factor ranging from 2 to 3. Its importance becomes negligible for non-elastic cross sections when there is a large number of open channels.

2.5 Conclusion

In the present study, the resonance analysis is performed with the shape analysis programs REFIT and SAMMY using the Reich-Moore approximation of the R-matrix theory. A least squares fit of the capture and transmission data yields the resonance energies (E_λ), the neutron widths ($\Gamma_n \equiv \Gamma_{\lambda n}$), the radiation widths ($\Gamma_\gamma \equiv \Gamma_{\lambda\gamma}$) and the distant level parameter ($R_n^\infty(l=0)$). An estimate of the s-wave level spacing (D_0) and strength function (S_0) is deduced from the resolved resonance parameters with the ESTIMA code. The average resonance parameters (D_l, S_l, $< \Gamma_\gamma >$, and R_n^∞) are then extracted from a fit of the average cross sections using the generalised Hauser-Feshbach formula implemented in the FITACS option of SAMMY.

Chapter 3

Sample preparation

The ideal target material would have been elemental iodine, but after a few tries this was considered not to be practical in view of the radiological hazard, volatility and reactivity of elemental I_2. The PbI_2 compound was considered a reasonable compromise, with no lead resonances in the energy range of interest. Besides, the lead has a low capture cross section and pressed PbI_2 is mechanically more stable. Two transmission targets (0.15 and 1.55 g/cm^2) with a 55 mm diameter, and two capture targets (0.16 and 0.78 g/cm^2) with a 80 mm diameter were prepared, together with five natural iodine samples.

3.1 Iodine separation

The starting material was 210 l of waste solution from the French fuel reprocessing facility of La Hague. The solution, containing 1.3 g/l iodine and other products (Table 3.1), had been made alkaline (Ph=14) using Na_2CO_3 in order to keep the iodine in solution. Though well documented, the chemistry of iodine remains complex. The nature of species formed during a reaction is not always predictable. Indeed, numerous oxidation states are possible and iodine may also form compounds with itself, oxygen and other elements. The procedure for the separation of the iodine from the mother solution was developed and optimised at the IRMM [50]. This procedure involved three steps: (1) acidification and oxidation of iodide (I^-) to iodine (I_2) with nitric acid and extraction of the I_2 into chloroform ($CHCL_3$); (2) reduction of iodine to iodide with sodium sulfite (Na_2SO_3) and extraction back into an aqueous phase; (3) precipitation of iodine as PbI_2 by the addition of $Pb(NO_3)_2$.

The oxidation of iodine to iodide cannot be carried out under alkaline conditions. It is also important to avoid precipitation of lead hydroxide, which occurs at pH$>$ 7. Thus, the first step consisted in dropping concentrated (14 M) nitric acid into the mother solution. The pH evolution of the mother solution is shown in Figure 3.1. I_2 vapor started to be released at a pH of 5-6 together with CO_2. Nitric acid was carefully added in order to avoid any loss of I_2 vapor dragged up by the CO_2 into a reflux column. Chloroform was then added to the

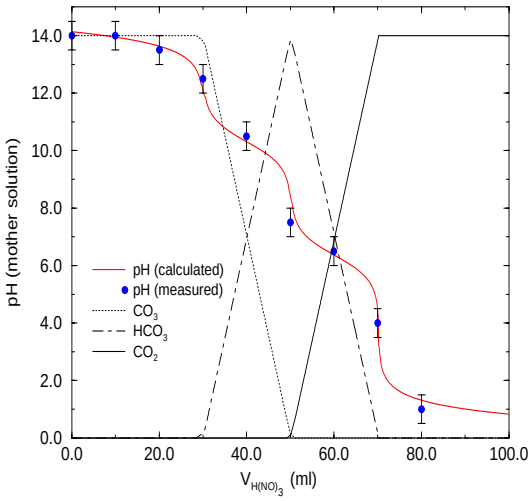

Figure 3.1: pH behaviour of the mother solution during the first step of the iodine separation process. I_2 vapour started to be released at a pH of 5-6 together with CO_2.

reaction vessel. After the organic and aqueous phases were separated, the second step consisted in reducing the I_2 contained in the organic phase. This reaction was rapid but reversible. It was necessary to add sodium sulfite in large excess to retain the iodide in the aqueous solution. That explains the small amount of ^{23}Na observed in our transmission TOF spectra. The final step was the precipitation of yellow PbI_2 together with $PbSO_4$ and various potentially insoluble oxo-, hydroxo- and iodohydroxo-complexes of the type $PbI_2{\cdot}PbO$, $PbI_2 \cdot 2PbO$, $PbI_2{\cdot}PbO{\cdot}I_3$, $PbIOH, \cdots$. Non negligible amounts of sulfur, hydrogen and oxygen are then expected in the final samples. Owing to the total amount of $Pb(NO_3)_2$ used in the final separation step, the lead mass fraction in the precipitate should be lower than 67.5%.

The total quantity of ^{129}I extracted was about 140 g. The samples were canned by compaction of the powder into cylindrical aluminum containers of different sizes.

Table 3.1: Composition of the mother solution provided by COGEMA.

Elements	Concentration ($mol.l^{-1}$)	Activity ($Bq.l^{-1}$)	Elements	Concentration ($mol.l^{-1}$)	Activity ($Bq.l^{-1}$)
Na^+	2.93		^{90}Sr	4×10^{-12}	1800
OH^-	1.37		^{106}Ru	2×10^{-13}	4800
CO_3^{2-}	0.916		^{154}Eu	6×10^{-14}	110
NO_2^-	0.355		^{125}Sb	4×10^{-14}	230
I	$\sim 10^{-2}$		^{60}Co	3×10^{-14}	100
^{14}C		2.9×10^7	^{144}Ce	3×10^{-14}	1440
^{3}H	4×10^{-9}	4.5×10^6	^{106}Rh	2×10^{-19}	4800
^{137}Cs	1×10^{-11}	5000			

3.2 Neutron Resonance Capture Analysis (NRCA)

The preparation and mass determination of the sample is a crucial step in the experimental procedure of any accurate cross section determination. Indeed, the uncertainty on the sample thickness in atom per barns is often the main source of errors. The characterisation of the sample was done by activation measurements, Neutron Resonance Capture Analysis (NRCA), ICP-MS and conventional chemical methods.

3.2.1 NRCA principle

Our radioactive PbI_2 samples have a complex elemental composition involving natural and radioactive iodine (^{127}I, ^{129}I) together with natural lead, sulfur, sodium, hydrogen, oxygen and nitrogen. The challenging task is to accurately determine their mass fraction within the sample. For this purpose, we have used a technique based on the so-called Neutron Resonance Capture Analysis method (NRCA). It is a non destructive method to analyse the elemental composition of materials, which consists of identifying isotopes via the occurrence of resonances at particular neutron energies in the TOF spectra (Figure 3.2). The NRCA technique has been recently explored at GELINA. Capture experiments have demonstrated its applicability for archaeological applications [51].

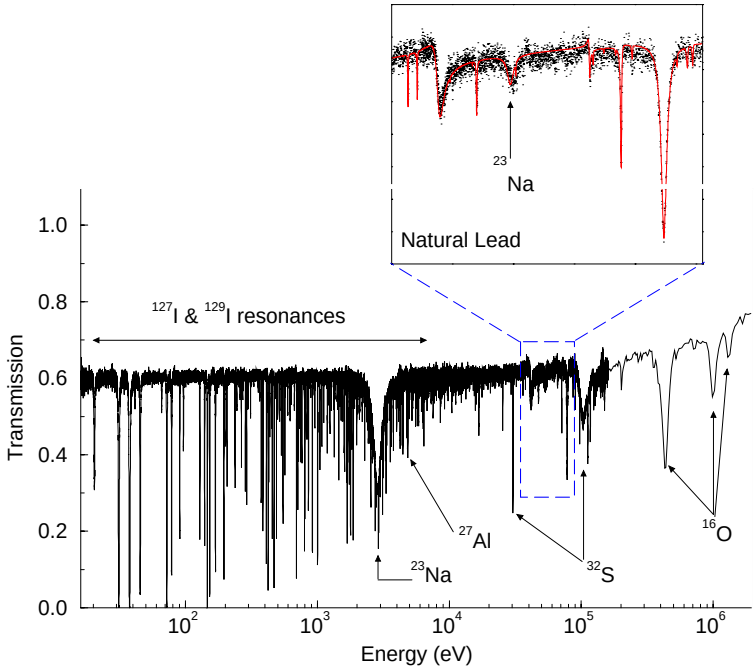

Figure 3.2: Transmission of the thick ^{129}I sample.

The TOF spectra are commonly analysed with the R-matrix shape fitting programs REFIT [26] or SAMMY [27]. Detailed descriptions of these codes are given in Chapter 6. The mass fraction of each isotope is adjusted so that the theoretical capture yield or transmission agrees with the observed data within the limit of the uncertainties. The accuracy of the NRCA results depends on the uncertainties of the resonance parameters recommended in the neutron data bases. The assessment of reliable uncertainties is achieved through the analysis of auxiliary measurements. For this purpose we have measured the transmission of thick natural lead and sodium samples. The characteristics of the samples under investigation are listed in Table 3.2.

Table 3.2: Samples characteristics. Four pressed PbI_2 samples containing a mixture of radioactive and natural iodine were prepared at the IRMM together with five ^{127}I samples. A 1 mm thick LiI liquid sample was designed to investigate the ^{127}I(n,tot) reaction at low neutron energies. The natural lead and sodium samples were used for studying the total cross sections. The transmission measurements were carried out under the same experimental conditions as for the iodine samples. The ^{206}Pb measurement was performed by A.Borella et al. at the GELINA facility [52]. The $^{207}Pb(n,\gamma)$ reaction was measured at the IRMM by P.Mutti and F.Corvi [53].

Experiment	Sample	mass (g)	thickness (mm)	Diameter (mm)
^{129}I Transmission	thin PbI_2	21.857 ± 0.001	3.40 ± 0.1	55.0 ± 0.1
	thick PbI_2	218.1 ± 0.1	28.3 ± 0.1	55.0 ± 0.1
^{129}I Capture	thin PbI_2	49.276 ± 0.001	2.83 ± 0.1	80.0 ± 0.1
	thick PbI_2	232.2 ± 0.1	14.8 ± 0.1	80.0 ± 0.1
^{127}I Transmission	thin PbI_2 (98.4%)	6.731 ± 0.001	5.6 ± 0.1	55.0 ± 0.1
		(+22.9123 g of Sulfur)		
	thick PbI_2 (99.99%)	218.5 ± 0.1	17.5 ± 0.1	55.0 ± 0.1
	LiI target	$(9.45 \pm 0.10) \times 10^{-4}$ at/b		
^{127}I Capture	thin PbI_2 (98.4%)	18.224 ± 0.001	8.5 ± 0.1	80.0 ± 0.1
		(+50.1402 g of Sulfur)		
	thick PbI_2 (98.4%)	93.115 ± 0.001	4.1 ± 0.1	80.0 ± 0.1
Transmission	Natural lead	1264.6 ± 0.1	14.1 ± 0.5	100.0 ± 1.0
	Sodium		100.0 ± 5.0	
Capture	^{206}Pb [52]	34.432 ± 0.001	1.14 ± 0.01	60.0 ± 0.1
	^{207}Pb [53]	$(4.3 \pm 0.1) \times 10^{-3}$ at/b		

The natural lead and sodium measurements have been carried out under the same experimental conditions as the ^{129}I and ^{127}I measurements, while ^{206}Pb and ^{207}Pb capture data were taken from References [52, 53]. Examples of TOF spectra are shown in Figure 3.3.

3.2.2 Sample composition

- **^{127}I mass fraction**

The PbI_2 separated from the mother solution contains natural iodine. In order to analyse the ^{129}I capture and total cross sections, accurate ^{127}I cross sections are required. Extensive ^{127}I capture and transmission measurements have been carried out over four natural PbI_2 samples. The low energy range was investigated with thin samples. For that purpose, a 1 mm thick LiI liquid sample was especially designed to achieve a high homogeneous sample. It is a crucial condition which cannot be achieved with thin samples in powder form. Detailed discussion of the experimental conditions and of the final available data are given in the following Chapters. The

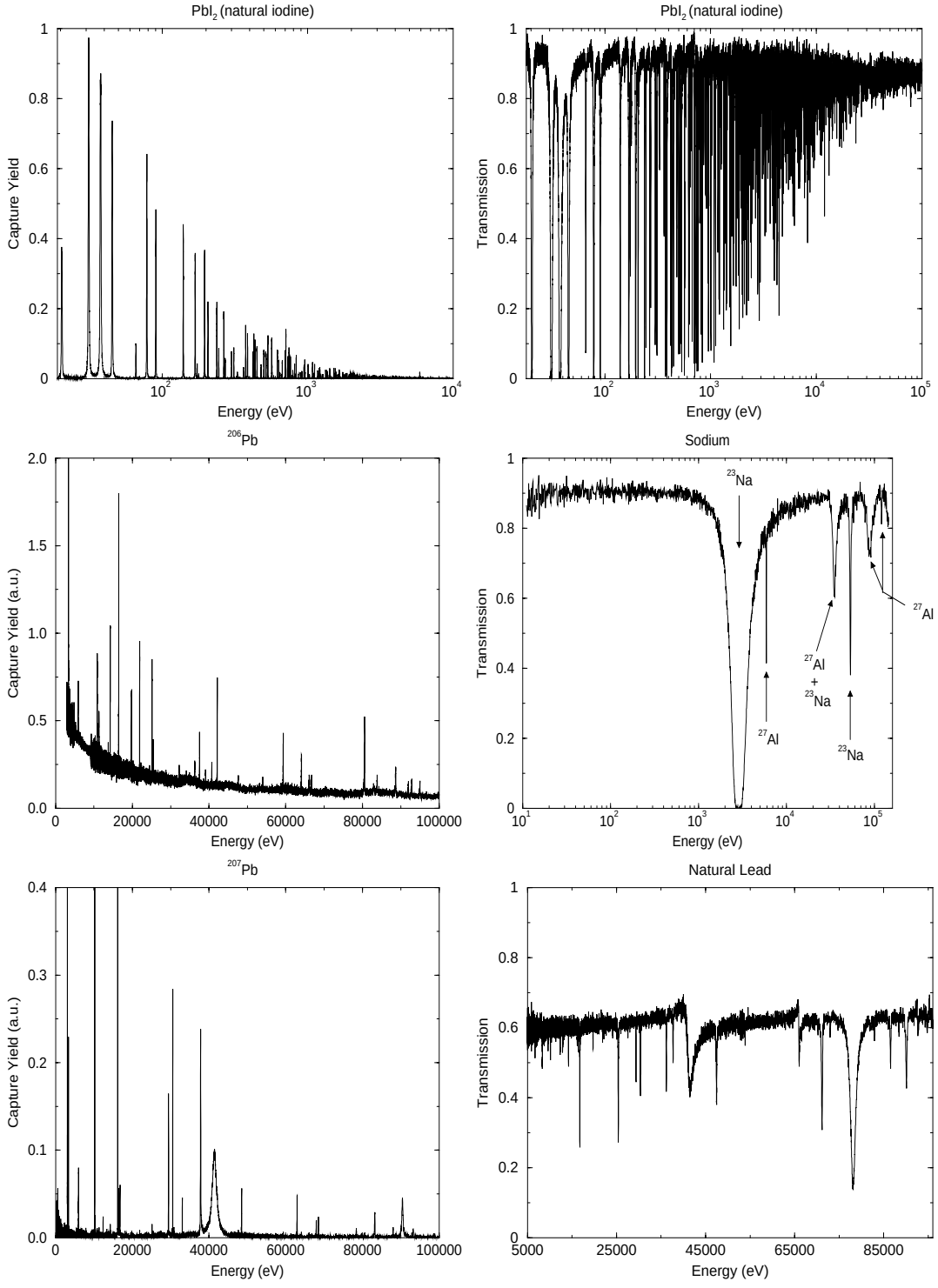

Figure 3.3: Examples of capture and transmission TOF spectra used in the NRCA analysis (a.u.=arbitrary unit).

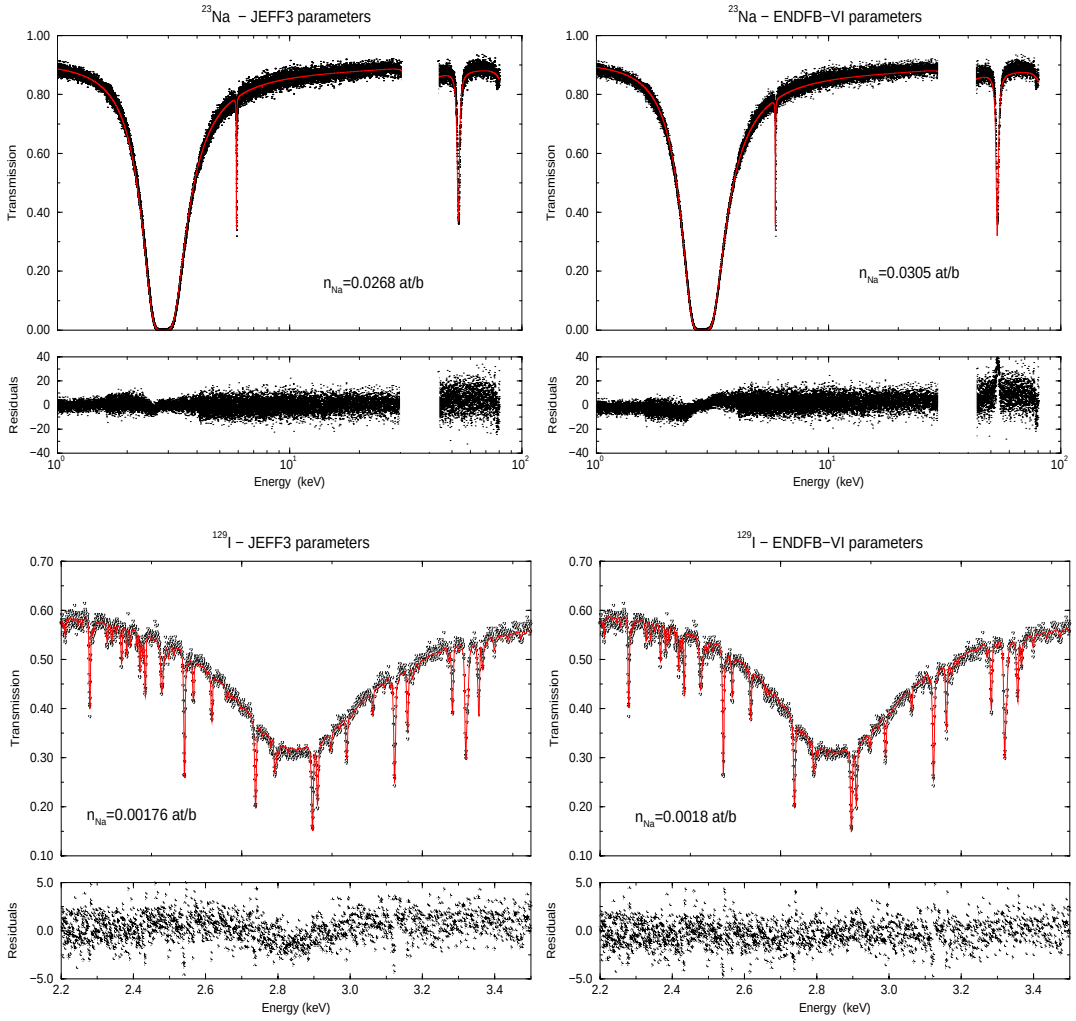

Figure 3.4: Transmission of the thick sodium and PbI_2 samples together with the theoretical curves obtained with SAMMY. The resonance parameters are those recommended in ENDF/B-VI and JEFF3.

Resolved Resonance Range of the ^{127}I cross sections have been analysed in terms of Reich-Moore parameters with the shape analysis code REFIT and SAMMY. The final resonance parameters obtained in this work are given in Chapter 7.

The new natural iodine resonance parameters were then introduced in the NRCA calculation in order to determine the ^{127}I mass fraction in the radioactive PbI_2 samples. From the shape fit of 36 resonances, we obtained a ^{127}I mass fraction of $(3.44 \pm 0.12)\%$. This accuracy is deduced from the standard deviation of the fitted mass fractions.

- **^{23}Na mass fraction**

We cannot extract accurate resonance parameters from the ^{23}Na transmission measurement. The accuracy of the sample thickness is about 5% and the broad s-wave resonance at 2.8 keV is black. The 2.8 keV resonance observed in the ^{23}Na and ^{129}I transmission data is shown in Figure 3.4 together with the theoretical curves calculated with SAMMY. The ^{23}Na starting parameters were those available in the American (ENDF/B-VI) and European (JEFF3) neutron data bases. The normalisation and the ^{23}Na thickness were adjusted to obtain the better agreement with

the data. The behaviour of the residuals (see definition Equation 6.12) gave out ambiguous results. The JEFF3 parameters provide a better description of the ^{23}Na transmission compared with those recommended in the ENDF/B-VI library. By contrast, the residuals obtained from the analysis of the ^{129}I transmission data suggests to adopt the ENDF/B-VI parameters. Up to now, we cannot confirm these discrepancies. A (0.75±0.04)% ^{23}Na average mass fraction was then assumed in this work.

• **Natural lead mass fraction**

The radioactive PbI_2 samples contain a large amount of natural lead which consists of a mixture of four isotopes. The respective natural abundance of ^{204}Pb, ^{206}Pb, ^{207}Pb and ^{208}Pb are 1.42%, 24.14%, 22.08% and 52.34% [55].

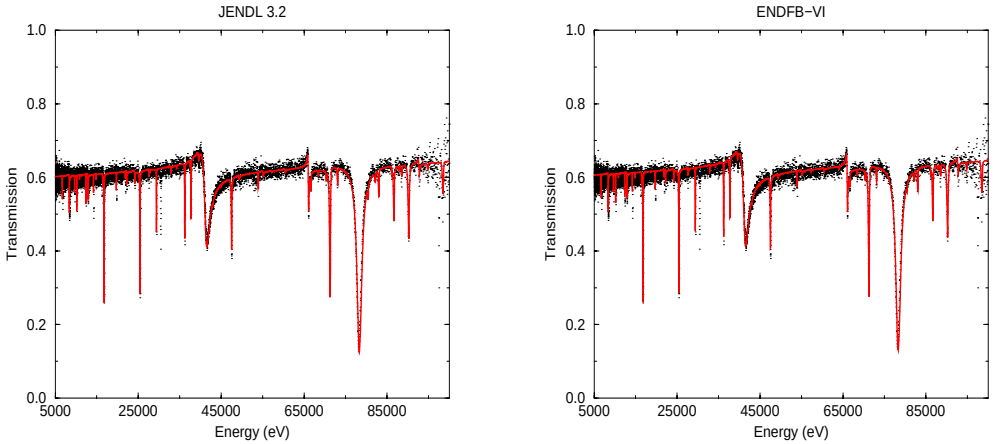

Figure 3.5: Natural lead transmission (16.11g/cm^2) compared with the theoretical curves calculated with the R-matrix fitting program SAMMY using the JENDL3.2 and ENDF/B-VI resonance parameters.

The lead resonant and non-resonant scattering have to be carefully taken into account in our iodine resonance analysis. Indeed, the effective scattering length or radius R' is an important parameter which is required in the determination of the total cross section. The effective scattering lengths of the lead isotopes (R'_i) available in the data bases and in the Brookhaven National Laboratory compilation (BNL) are given in Table 3.3. The natural lead radius reported by Mughabghab (i.e. BNL) comes from experimental techniques based on the wave properties of the neutron (interference, refraction, reflection and diffraction), while those for the ENDF/B-VI and JENDL3.3 neutron data bases are calculated as follows:

$$R'^2 = 0.0142\ R'^2_{204} + 0.2414\ R'^2_{206} + 0.2208\ R'^2_{207} + 0.5234\ R'^2_{208} \quad (3.1)$$

The inspection of the radii (R') recommended in the ENDF/B-VI and JENDL3.3 neutron libraries suggests a large discrepancy on the ^{206}Pb value, and no ^{204}Pb resonance parameters are reported in the American neutron data base. In order to verify the R' values, we have measured the transmission of a thick natural lead sample from 10 eV up to 150 keV. The data are shown in Figure 3.5 together with the theoretical curves calculated with SAMMY. The American and the Japanese evaluations are in a good agreement with our measurement. The agreement is improved with a correction of about 1.1% of the normalisation factor. This discrepancy suggests

Table 3.3: Effective scattering lengths of the lead given in the BNL compilation, and recommended in the Japanese and American neutron data bases, together with the accuracy ($\Delta R'$) deduced from our natural lead transmission data.

isotope	BNL [56]	ENDF/B-VI	JENDL3.3	$\Delta R'$ (this work)
^{204}Pb			8.50 fm	
^{206}Pb	9.46±0.15 fm	9.50 fm	8.042 fm	
^{207}Pb	9.3±0.5 fm	9.50 fm	9.53 fm	
^{208}Pb		9.69 fm	9.69 fm	
natural lead	9.4003±0.0014 fm	9.59 fm	9.26 fm	0.19 fm

Table 3.4: Resonance parameters of the lead isotopes extracted from the analysis of capture and transmission measurements. The quoted uncertainties are deduced from the results obtained over various TOF spectra. Results are compared with those recommended in the ENDF/B-VI and JENDL3.3 data bases.

		JENDL3.3		ENDF/B-VI		This work	
isotope	Energy (keV)	Γ_γ (meV)	Γ_n (eV)	Γ_γ (meV)	Γ_n (eV)	Γ_γ (meV)	Γ_n (eV)
^{206}Pb	25.407±0.013	330.0	51.0	330.0	51.0	261.9±5.7	52.0±0.5
	36.186±0.019	284.0	40.0	284.0	98.8	309.5±7.9	38.7±0.9
	47.459±0.024	250.0	89.0	250.0	85.2		
^{207}Pb	37.701±0.020	800.0	50.0	800.0	50.0	896.6±0.9	48.9±0.9
	41.281±0.023	5100.0	1220.0	3331.0	1220.0	4526.0±22.0	1153.0±5.4
	90.025±0.060	198.0	272.0	198.0	271.3		250.0±6.4
^{208}Pb	71.147±0.050	35.0	101.0	35.0	101.0	12.0±2.0†	101.0±5.0†
	78.150±0.052	538.0	958.0	538.0	958.0	125.0±30.0†	958.0±10.0†
	86.513±0.055	180.0	75.4	25.0	75.4	15.0±6.0†	75.4±3.0†

† from Reference [54].

to apply a small correction of about 0.11 fm on the effective scattering length of the natural lead. This correction together with the 3.5% sample thickness accuracy (see Table 3.2) involve a systematic error on the R' value close to 0.19 fm. Within the present uncertainty, the radii available in the ENDF/B-VI and JENDL3.3 libraries, given in Table 3.3, remain consistent with the accurate experimental value R'=9.4 fm recommended in the BNL compilation. The $\Delta R'$ accuracy obtained in this work, will be used for determining the hydrogen mass fraction uncertainty as well as for estimating the accuracy of the ^{129}I effective potential radius (see Chapter 7).

In order to extract the lead abundance from the thick ^{129}I transmission sample, we have investigated the parameters of five lead resonances at 25.4 keV, 36.2keV, 37.7 keV, 41.2 keV and 90.0 keV. The ^{206}Pb, ^{207}Pb and natural lead measurements have been analysed simultaneously with REFIT. The extracted resonance parameters are given in Table 3.4. The ^{208}Pb resonance parameters are taken from Reference [54]. The results are compared with those available in the data bases. The discrepancies between the neutron widths range from 2% to 40% depending on the isotopes and on the data bases. Similar discrepancies between the radiation widths are obtained.

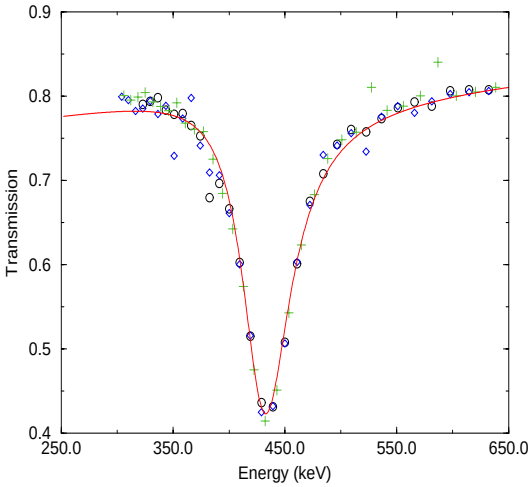

Figure 3.6: Fit of the 434 keV resonance of the ^{16}O(n,tot) reaction over three transmission data. The oxygen thickness in the thick ^{129}I transmission sample is about 0.053 at/b.

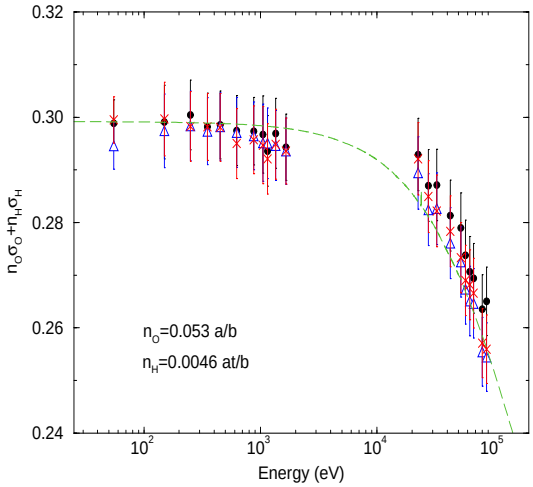

Figure 3.7: ln(1/N) values obtained from the analysis of three transmissions spectra (thick PbI_2 sample). The dash curve results from the least squares fit of the data with Equation 3.3.

From the resonances listed in Table 3.4, we get a lead mass fraction of $(53.4 \pm 3.0)\%$. The present accuracy is deduced from the standard deviation of the fitted values. The ^{206}Pb, ^{207}Pb and ^{208}Pb abundances in the lead contained in our PbI_2 samples are 23.9%, 22.6% and 52.0%. These features are consistent with their natural abundance of 24.14%, 22.08% and 52.3%. The ^{204}Pb mass fraction is deduced from its natural abundance of 1.42%.

- **Oxygen and Hydrogen mass fraction**

It was found that our samples contain a large amount of oxygen. The first oxygen resonance is at 434 keV. The oxygen mass fraction was deduced from three transmission data (Figure 3.6). The average result is (15.23±0.83)%, corresponding to a sample thickness of 0.053 atom/barns. The hydrogen mass fraction can only be determined via the normalisation factor ($N(E)$) obtained from the analysis of the transmission spectra. The transmission can be expressed as follows:

$$T(E) = \underbrace{e^{-n_O\sigma_{t_O}(E)-n_H\sigma_{t_H}(E)}}_{N(E)} \; e^{-\sum_{i\neq O,H} n_i\sigma_{t,i}(E)} \tag{3.2}$$

The relationship between $N(E)$, oxygen and hydrogen thicknesses and total cross sections is then given by:

$$\ln\left(\frac{1}{N(E)}\right) = n_O\sigma_{t_O}(E) + n_H\sigma_{t_H}(E) \tag{3.3}$$

The result of the least squares fit of the $\ln(1/N)$ values with Equation 3.3 is shown in Figure 3.7. The hydrogen mass fraction is about (0.087±0.012)%. The monotonous behaviour of the hydrogen cross section within the 10 eV to 100 keV energy range does not allow an accuracy better than 14%.

- **^{129}I mass fraction**

The NRCA technique is also a powerful tool for the ^{129}I mass fraction determination. Indeed, the area formalism (see Chapter 2) predicts the possibility of extracting a reliable mass fraction value from our measurements. According to the asymptotic forms of the capture and transmission area functions and under the condition $\Gamma_\gamma > \Gamma_n$, we obtain the following relationship:

$$\frac{A_\gamma}{n_\gamma} \simeq \frac{A}{n} \simeq 2\,\pi^2\,\lambda\!\!\!^{-2}\,g\Gamma_n \tag{3.4}$$

in which n_γ and n stand for the ^{129}I thicknesses in the capture and transmission samples. Therefore, the best ^{129}I resonance parameters and mass fraction can be achieved through the simultaneous analysis of thin and thick capture and transmission samples data. From the REFIT results, we deduce an average mass fraction of (17.1±0.7)%.

3.3 Inter-laboratory comparison

In Table 3.5, the NRCA results are compared with those resulting from conventional chemical methods and activation measurements.

3.3.1 The Paul Scherrer Institute (PSI)

The isotopic and wet analytical chemistry laboratory of the Paul Scherrer Institute (PSI) has determined the lead and iodine mass fractions, as well as the iodine isotope ratio, by inductively coupled plasma mass spectrometry (ICP-MS) and isotope dilution ICP-MS (ID-ICP-MS). The determination of hydrogen, oxygen and nitrogen contents was done by gas fusion method at high temperature ($T = 2300^o$C). A LECO RH-404 instrument was used for hydrogen, and a LECO TC-436 for nitrogen. A semi-quantitative elemental analysis by ICP-MS was used for determining trace elements (Table 3.6). PSI laboratories have no equipment for measuring sulfur.

The sample preparation for the detection of lead and iodine mass fractions consisted in dissolving PbI_2 with the help of a sodium hydroxide digestion step. Approximately 0.2 g of the sample was weighed into a 3-neck-flask. After closing the flask, 25 ml of a 4 M sodium hydroxide were added with a dropping funnel. Then the solution boiled under reflux and a small flow of compressed air (for 30 minutes). The excess pressure was led through two wash bottles that contained 20 ml sodium hydroxide (4 mol/l). The yellow color of the sample disappeared at the moment the sample was dissolved. After cooling in the flask it was transferred quantitatively into a Nalgene bottle. For the determination of lead, the solution was diluted to an approximate lead concentration of 80 μg/kg with 1% HNO_3 ultrapur and spiked with NIST SRM 983 (^{206}Pb enriched). For the determination of iodine, the solution was diluted to an approximate iodine concentration of 100 μg/kg with 0.5% NH_4OH and spiked with an ^{127}I iodine standard.

Concerning the detection of oxygen and hydrogen, some technical problems occurred owing to the high oxygen contents. Therefore, only a very small sample amount could be measured (about 10 mg). This experimental situation influenced the precision and accuracy of oxygen measurements and induced a 10% uncertainty on the final value. The determination of nitrogen and oxygen occurred simultaneously.

3.3.2 The Institute for Reference Materials and Measurements (IRMM)

Activation experiments were carried out at the Geel 7 MV van de Graaff accelerator in order to determine the ^{127}I and natural lead mass fraction [57]. A PbI_2 sample containing natural iodine was irradiated simultaneously with the PbI_2 extracted from the waste solution during 6 h with

Table 3.5: Composition of the PbI_2 sample (%). Results from the NRCA method are compared with those obtained at the IRMM by ICP-MS and activation measurements, and with results provided by the Paul Scherrer Institute (PSI).

Element		IRMM-Geel			PSI
		ICP-MS method	Activation technique	NRCA (this work)	
Iodine	^{127}I		3.35±0.10	3.44±0.12	3.36±0.08
	^{129}I			17.1±0.7	16.49±0.40
	total			20.54±0.85	19.85±0.47
Lead	^{204}Pb†			0.76	
	^{206}Pb			12.8±0.5	
	^{207}Pb			12.1±0.3	
	^{208}Pb			27.8±2.2	
	total		51.1±1.8	53.4±3.0	59.47±0.18
Sulfur	^{32}S			5.9±0.4	
	^{33}S†			0.046	
	^{34}S†			0.26	
	^{36}S†			0.0012	
	total			6.2±0.4	
Sodium				0.75±0.04	1.00±0.15
Oxygen				15.23±0.83	14.5±1.5
Hydrogen				0.087±0.012	0.02±0.002
Nitrogen					1.2±0.4
^{129}I/^{127}I		4.97±0.25		4.97±0.27	4.91±0.03
		4.79±0.24			

† mass fraction obtained from the natural abundance given in Reference [55].

Table 3.6: Trace elements analysed in the PbI_2 sample, and found beyond the detection limits.

Concentration	elements
< 100 mg/kg (ppm)	Cr Ni Cu Ag Cd In Cs Tl Bi U
< 500 mg/kg (ppm)	Au Ba Dy Eu Er Fe Gd Hf Hg Ho Li Lu Mg Nd Pt Re Sm Sr Ta Tb Tm
<1000 mg/kg (ppm)	Fe Zn

mono-energetic neutrons of 16 MeV. The iodine content was obtained by measuring the activity of the irradiated samples with a HPGe detector. The latter activity was measured 6 days after the irradiation, and determined via the 388 keV γ-rays of the ^{127}I(n,2n) reaction, where the activity has a half-life of 13 days. The lead mass fraction was assessed in a similar way via the ^{204}Pb(n,n') reaction (simultaneous irradiation of a PbI_2 sample together with a $Pb(NO_3)_2$ sample). The iodine isotope ratio (^{129}I/^{127}I) was also measured at Geel by the ICP-MS method. Two independent measurements were carried out with two different mass spectrometers using the same PbI_2 sample. Detailed procedures for determining isotope abundance ratio are given in Reference [58].

3.4 Conclusion

The NRCA is a suitable method to determine the full isotopic composition of our PbI_2 samples with an accuracy on the mass fractions ranging from 5% to 14%. According to the NRCA results, we confirm the oxygen mass fraction given by PSI. On the contrary, our analysis suggests to increase drastically the hydrogen content, and to decrease the lead mass fraction in accordance with the Geel values. The ^{127}I and ^{129}I mass fractions derived from the NRCA agree with the PSI results. Similarly, the natural iodine mass fraction from the activation measurement carried out at Geel is in excellent agreement with the latter. The average value of the iodine isotope ratio over the available values is consistent with the PSI result of 4.91 ± 0.03.

A final characterisation of the sample carried out at the guided cold neutron beam of the Budapest research reactor will be provided before the end of the year by Molnar et al. [59]. Therefore, in this work, we assume correct the iodine mass fractions from PSI and their associated uncertainties. The iodine thicknesses in atom per barns used in the calculations are given in Table 3.7.

Table 3.7: ^{127}I and ^{129}I thicknesses in atoms per barns (capture and transmission samples).

Experiment	Sample	^{127}I thickness (at/b)	^{129}I thickness (at/b)
^{127}I Transmission	thin sample	$(7.089 \pm 0.998) \times 10^{-4}$	
	LiI target	$(9.451 \pm 0.106) \times 10^{-4}$	
	thick sample	$(2.380 \pm 0.040) \times 10^{-2}$	
^{127} Capture	thin sample	$(9.476 \pm 0.223) \times 10^{-4}$	
	thick sample	$(4.764 \pm 0.086) \times 10^{-3}$	
^{129}I Transmission	thin sample	$(1.468 \pm 0.044) \times 10^{-4}$	$(7.091 \pm 0.174) \times 10^{-4}$
	thick sample	$(1.465 \pm 0.044) \times 10^{-3}$	$(7.076 \pm 0.173) \times 10^{-3}$
^{129}I Capture	thin sample	$(1.564 \pm 0.047) \times 10^{-4}$	$(7.556 \pm 0.184) \times 10^{-4}$
	thick sample	$(7.897 \pm 0.235) \times 10^{-4}$	$(3.814 \pm 0.091) \times 10^{-3}$

Chapter 4

Experimental techniques

Many relevant facilities and techniques are available to obtained differential neutron cross sections. Nuclear reactors are the most powerful facility to provide intense and efficient thermal neutron source. Accelerator-based monoenergetic neutron sources are useful to investigate the MeV energy range (see References [63, 64]). For measurements of nuclear reaction involving neutrons from subthermal energies up to several MeV, pulsed white neutron sources are the most suitable facility to achieve a high resolution neutron spectroscopy on a large energy range. Such a neutron beam is obtained by inducing nuclear reactions in a suited target bombarded by charged particles from an accelerator. The source is pulsed because the selection of the neutron energy is determined by the time-of-flight method. A comparison of the most productive facilities is given in Reference [62]. The experiments discussed in this thesis were performed at the Geel Electron Linear Accelerator (GELINA) of the Institute of Reference Materials and Measurements [65]. Short burst of neutrons are produced after collision of the accelerated electrons in a mercury cooled uranium target. The neutrons, emitted in all directions, are collimated in the direction of the transmission and capture experimental areas.

4.1 Principles of capture and transmission measurements

In transmission experiment, a beam of neutron with flux $\phi_{out}(E)$ going through a sample of thickness n atoms per barn is attenuated by interaction of the neutrons with the sample. The outgoing flux $\phi_{in}(E)$ is related to the incident flux $\phi_{out}(E)$ by the total neutron cross section $\sigma_t(E)$ as:

$$\phi_{in}(E) = \phi_{out}(E)\mathrm{e}^{-n\sigma_t(E)} \tag{4.1}$$

The *transmission* $T(E)$ is then defined as :

$$T(E) \;=\; N_T \,\frac{\phi_{in}(E)}{\phi_{out}(E)} \;\equiv\; \mathrm{e}^{-n\sigma_t(E)} \tag{4.2}$$

in which N_T stands for the normalisation factor.

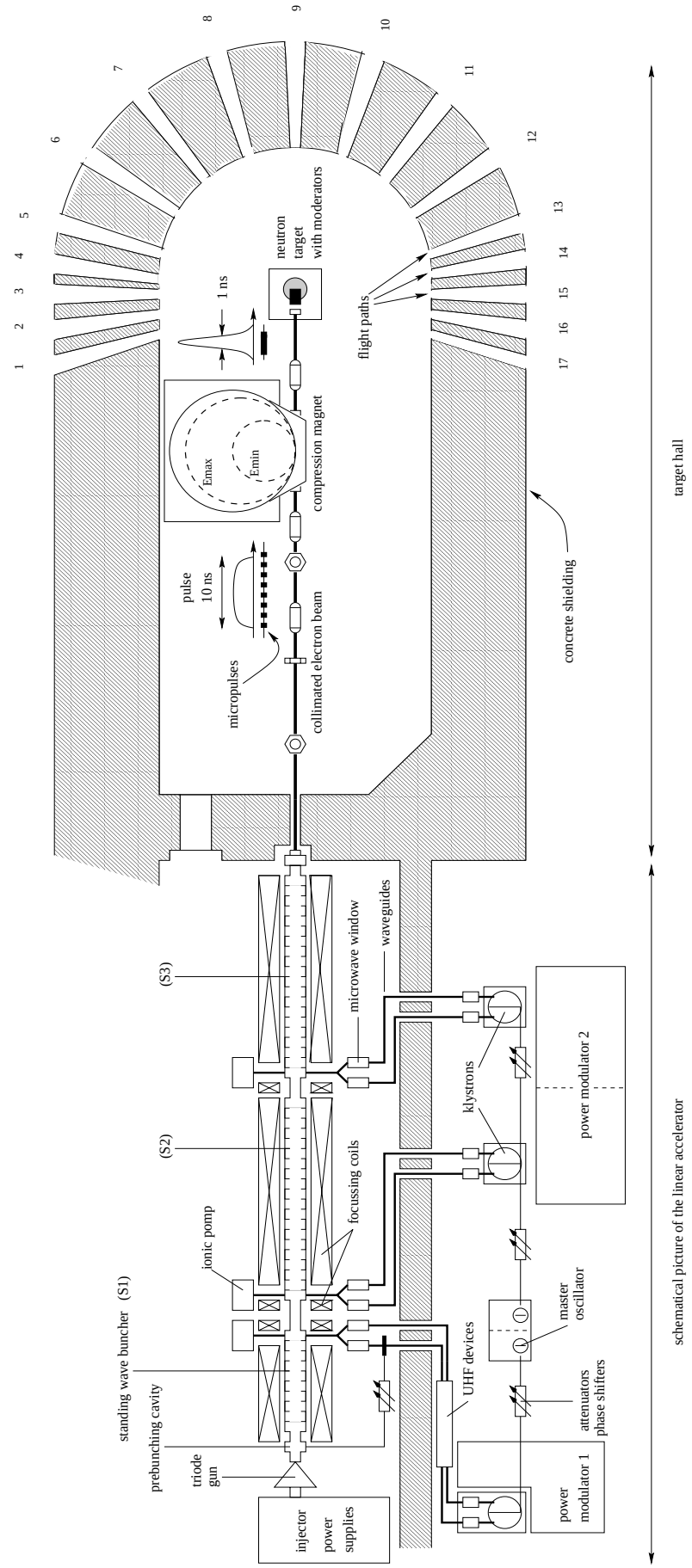

Figure 4.1: Scheme of the GELINA facility.

The capture measurement is related to the neutron capture cross section $\sigma_\gamma(E)$ via the so-called *capture yield* ($Y(E)$). $Y(E)$ is the number of capture events ($N_c(E)$) per incident neutron ($\phi(E)$) integrated over the sample thickness n. It is a reaction rate expressed as a function of the neutron capture probability times the neutron flux reduction in the sample. The capture yield may be defined in a simplified form as:

$$Y(E) \;=\; N_Y \,\frac{N_c(E)}{\phi(E)} \equiv (1+\alpha(E))(1-T(E))\frac{\sigma_\gamma(E)}{\sigma_t(E)} \tag{4.3}$$

where N_Y represents the normalisation factor and $(1+\alpha(E))$ stands for the multiple scattering correction. In practice, $N_c(E)$ and $\phi(E)$ are measured simultaneously with two C_6D_6 detectors and a boron chamber, while $\phi_{in}(E)$ and $\phi_{out}(E)$ are measured alternatively having the sample *in* the beam and *out* of the neutron beam with a Li-glass detector. In the following sections, the neutron production as well as the principles of the transmission and capture experiments are explained.

4.2 Time of Flight Method

Pulse white sources are founded on the time-of-flight method (TOF) to correlate detected events to the energy of the neutrons by measuring the time elapsed since the generation of the neutron burst. The neutron energy is given as a function of the flight time (T_n) and of the effective flight path length L_n it traveled from the production target to the detection system. The non-relativistic neutron energy is given by:

$$E_n = \frac{1}{2} m_n \left(\frac{L_n}{T_n}\right)^2 \tag{4.4}$$

where m_n is the neutron mass. If L_n is expressed in meters, T_n in μs and E_n in eV, Equation 4.4 can be rewritten numerically as:

$$E_n = \left(72.298 \frac{L_n}{T_n}\right)^2 \tag{4.5}$$

In TOF measurements, the experimental resolution of the spectrometer affects the accurate determination of the neutron energy. The definition of the resolution function in TOF experiments is given in Chapter 6.

4.3 The white neutron sources GELINA

The GELINA facility is an S-band linac which produces a 12-14 kW electron beam with a maximum energy of 140-150 MeV. It consists of a triode gun , a 2 m-long standing wave buncher and two 6 m-long traveling wave sections (Figure 4.1). Three klystrons produce electromagnetic waves, which are then injected in the accelerating sections. At the exit of the linac, before the uranium target, a unique compression system provides short bursts of electrons (1.5 ns).

The triode gun was especially designed to produce short bursts of electrons with an average energy range of about 100 keV. At the exit of the S-band accelerator, the electron pulses are about 10 ns width, and consist of a sequence of 30 bunches (micropulses) with energies progressively decreasing from 140 MeV to 70 MeV.

Through the first section S1, the original electron pulse, accelerated to an energy of 20 MeV, is chopped into a train of micropulses. The bunches are about 10 ps width and their time

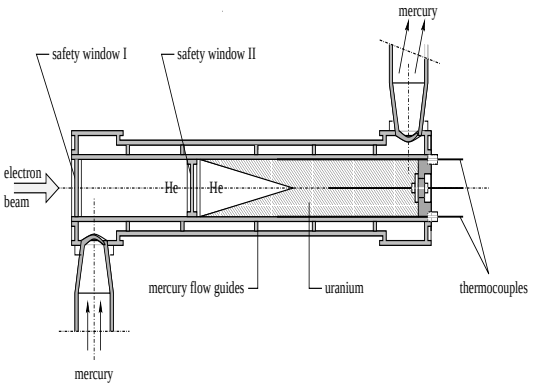

Figure 4.2: Scheme of the *stationary* target without slab moderators [65].

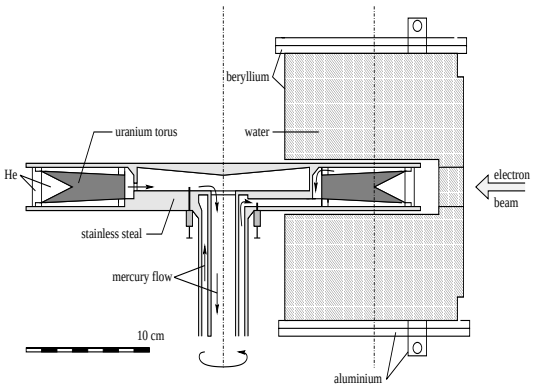

Figure 4.3: Scheme of the *rotary* target with a water moderator canned in a beryllium box [66].

distance is 333 ps, corresponding to a 3 GHz S-band frequency. In sections S2 and S3, the energy gain of the electrons is entirely obtained from the electromagnetic energy stored in the cavity of the sections. The first micropulse in the train sees the maximum accelerating field, and the next one gets slightly less acceleration since a part of the stored energy was consumed by the forerunner. So the energy of the electrons is reduced from the beginning to the end of the pulse.

This intrinsic feature of the relativistic electron beam at the exit of the linac is used for pulsed compression [67]. The post-acceleration bunching technique consists of a special 360^o deflection magnet (3.4 m $\times$ 3.1 m $\times$ 0.66 m), located in the target hall (Figure 4.1). This buncher compresses a 10 ns pulse (10 A maximum intensity) into a 1 ns pulse (100 A maximum intensity) with negligible beam loss. According to their energy and under the influence of an intense magnetic field ($\sim$ 0.37 Tesla), the incoming bunches are deflected along different trajectories. The first micropulse (having the highest energy) travels along the largest trajectory (6 m) and the last micropulse along the smallest one (3 m). After one lap inside the magnet, they leave the system at the same time toward the neutron source.

The neutron source of the GELINA facility consists of a cooled uranium target. Two types of targets are described in Reference [66]. The *stationary* and *rotary* targets are shown in Figures 4.2 and 4.3. Owing to technical problems with the latter, we used the *stationary* target at the beginning of our measurements. Both types of targets basically share the same design features and the same mercury cooling systems. The application of the *stationary* target is limited to a 7 kW beam power, while the *rotary* target can dissipate the heat source produced by a 14 kW electron beam.

Neutrons are produced in a two-step process [68]. The slowing down of fast electrons in a target material is dominated by radiation process above $E \simeq 800/(Z+1.2)$. In the case of heavy materials, such as uranium, this energy is about 9 MeV. Consequently, intense Bremsstrahlung radiation called γ-flash is generated. Fast neutrons are produced via (γ,n) reactions and, to a lesser extent of about 30%, via (γ,f) process. Heavy material is used because the probability that electrons loose energy by Bremsstrahlung is roughly proportional to Z^2. Uranium was originally chosen as its neutron yield per incident electron is more than a factor two larger than a tantalum

target, used at other laboratories [60, 61]. In a thick uranium target, bombarded with 100 MeV electrons, the electron to neutron conversion rate reaches about 9%. Fast neutrons emitted from the target have an energy distribution similar to a fission neutron spectrum. To enhance the neutron spectra intensity below a few hundred kilo-electron-volts, two 36 mm water slabs in a beryllium canning are placed as close as possible above and below the target. At thermal energy the distribution is characterised by a Maxwellian peak, and the partially moderated neutrons have an approximate 1/E energy dependence.

The accelerator status during our measurements are given in Table 4.1. The *stationary* target has been used at a 100 Hz repetition rate without compression. The main experiments have been carried out with the *rotary* target at 800 Hz in the compressed mode.

Table 4.1: Accelerator status during the measurements with the *stationary* and the *rotary* targets.

Neutron source	Repetition rate	pulse width	average current	average power
stationary target	100 Hz	10-12 ns	$\sim$ 10 μA	$\sim$ 7 kW
rotary target	800 Hz	1-2 ns	$\sim$ 70 μA	$\sim$ 12 kW

4.4 Flight path description

The neutrons emission from the target-moderator assembly is nearly isotropic. The neutron beam is led to the experimental areas along twelve 10 to 400 m-long neutron flight paths. Along them, the neutron beam is shaped by copper and lead collimators surrounded by boron-loaded wax containers.

The transmission and radiative capture experiments were carried out respectively on flight paths 4 and 15 at 50 m and 30 m from the neutron source (Figure 4.4). Shadow bars, composed of lead and copper, are introduced in the target hall to eliminate fast neutrons leaving the uranium target. Their design were optimised in order to prevent γ-flash from reaching the detectors directly. If the intensity of the huge amount of prompt γ-rays, which accompanies the neutrons production, is not reduced the detector is blinded for several μs [92]. For both experiments, we use a sample changer, monitored by the acquisition system, in order to expose different filters to the neutron beam in a repetitive way.

In transmission measurement, the neutrons cross a filter setup and the sample/dummy at a distance of 23.7 m. They are detected at 49.34 m with a Li-glass detector. The neutron beam diameter is 45 mm.

The filter setup of the capture experiment is placed close to the target hall, and the sample at 28.67 m from the neutron source. The experimental setup consists of three detectors. The neutron flux is measured with a ^{10}B ionisation chamber placed in the neutron beam, while capture γ-rays emitted from the sample are detected by two C_6D_6 liquid scintillators placed at the right angle to the beam axis. A series of collimators, placed at an appropriate distance, results in a neutron beam with a diameter of 75 mm. Its profile was measured with a Micromegas detector. Detailed descriptions are given in Reference [82].

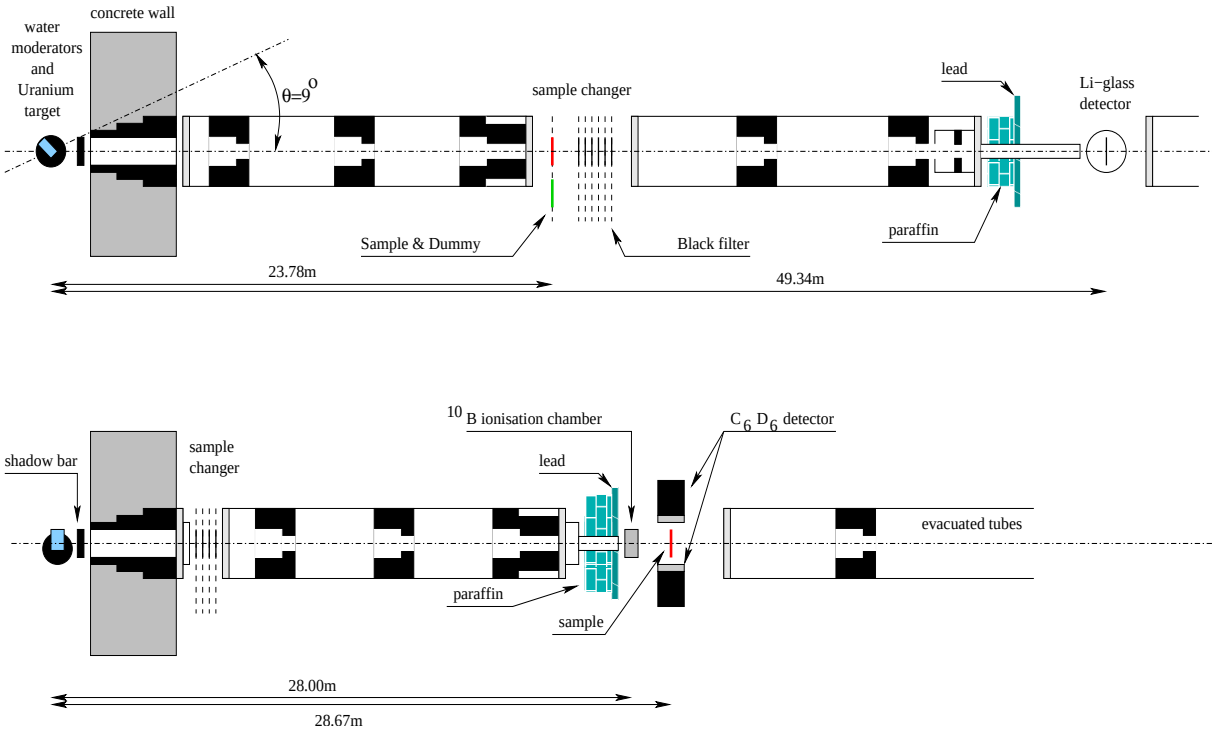

Figure 4.4: Schemes of the transmission and capture flight path.

4.5 Filter setup

Two kinds of filters can be distinguished in TOF measurements. Permanent anti-overlap filters eliminate slowest neutrons of each burst, while black resonance filters are used for determining the time dependent background.

Adequate thicknesses of W, Mo, Co, Na, S, Bi are placed in the neutron beam line in order to absorb nearly all the neutrons in a given energy region (Table 4.2). In that way, any count rate observed below a black resonance can unmistakably be attributed to the background. The energy dependent background is interpolated between the different black resonance regions.

Anti-overlap filters have a different goal. Without it, slow neutrons from one given burst get mixed up with neutrons from the next burst. For instance, a thermal neutron needs 13.7 ms and 22.8 ms to travel the respective distance of 30 m and 50 m, whereas the time interval between 2 bursts is 1.25 ms at a 800 Hz repetition rate and 10 ms at 100 Hz. In order to prevent overlap, boron or cadmium filters are placed in the neutron beam line. Figure 4.5 shows the boron and cadmium neutron total cross sections together with their transmission. At a 800Hz repetition rate, the perfect 1/v behaviour of the boron total cross section is suitable to investigate a large neutron energy range. At a 100Hz repetition rate, we take advantage of the so-called Cd cut-off at 0.2 eV to study the energy range below 10 eV. However, above 100 eV, information is partially lost because of the resonances induced by the Cd(n,tot) reaction.

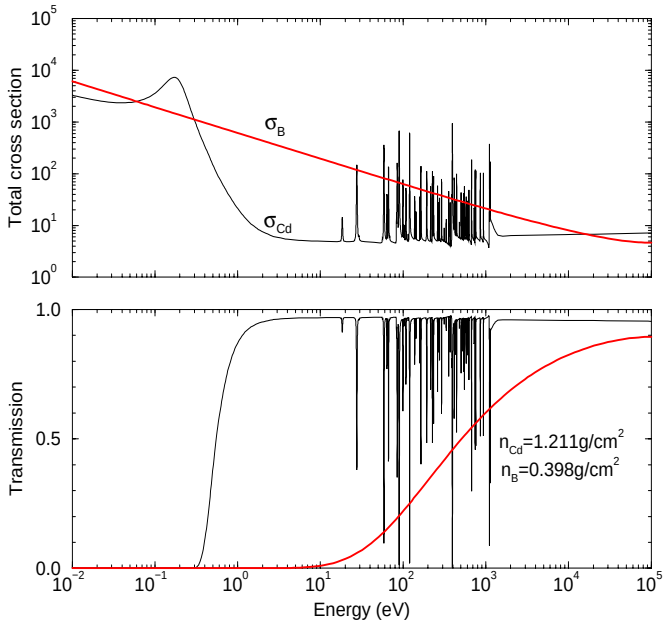

Figure 4.5: Boron and cadmium neutron total cross sections from JEFF3, together with the calculated transmissions of the anti-overlap filters.

Table 4.2: Energy and thickness of the black resonance filters used in transmission and capture experiments.

Element	Energy [56]	Capture	Transmission
W	18.8 eV	6.17×10^{-4} at/b	8.52×10^{-4} at/b
Mo	44.9 eV	5.60×10^{-3} at/b	
Ge	102.0 eV		1.85×10^{-2} at/b
Co	132.0 eV	2.60×10^{-3} at/b	1.82×10^{-3} at/b
Bi	800.0 eV	2.82×10^{-2} at/b	2.82×10^{-2} at/b
Na	2850.0 eV	3.20×10^{-2} at/b	2.31×10^{-2} a/b
S	102.7 keV	3.49×10^{-1} at/b	3.31×10^{-1} at/b

4.6 Neutron and γ-ray detectors

The transmission and capture yield are defined as:

$$T(E) = N_T \frac{\phi_{in}(E)}{\phi_{out}(E)} \tag{4.6}$$

$$Y(E) = N_Y \frac{N_c(E)}{\phi(E)} \tag{4.7}$$

Measurement of $T(E)$ involves neutron detectors. The neutron flux $\phi_{out}(E)$ incident upon the sample and the neutron flux $\phi_{in}(E)$ transmitted by the sample are measured with a Li-glass detector. The normalisation N_T of $T(E)$ is provided by four BF_3 neutron detectors, positioned in the target hall. In the capture experiment, the simultaneous measurement of the neutron flux $\phi(E)$ with the number of capture event $N_c(E)$ is achieved by using a boron ionisation chamber and a pair of C_6D_6 liquid scintillators. The normalisation technique is explained in Section 5.5.

4.6.1 Neutron flux measurement

Neutrons are detected through nuclear reactions resulting in energetic charged particles. The neutron detector used in our capture experiments, involves the combination of a ^{10}B target material designed to carry out the conversion together with a conventional double Frisch gridded ionisation chamber (Figure 4.6). The detector consists of a 11.5 cm-long cylindrical aluminium container with a 18.2 cm outer diameter. The windows, anodes and cathode are made of 30 μm-thick aluminium foils. The cathode holds a double back-to-back deposit of ^{10}B, each 40 μg/cm^2 thick. The Frisch grids consist of 0.1 mm thick steel wires, fixed parallely on a stainless steel ring. The cathode is at a negative voltage, the grids are at the earth potential and the anodes are at a positive voltage. Each grid creates two independent electric fields in the chamber to separate the drift space and the region of the so-called Townsen Avalanche. The chamber is filled with a gas flowing continuously at atmospheric pressure. This gas is a mixture of argon (90%) and methane (10%) for quenching purposes[84].

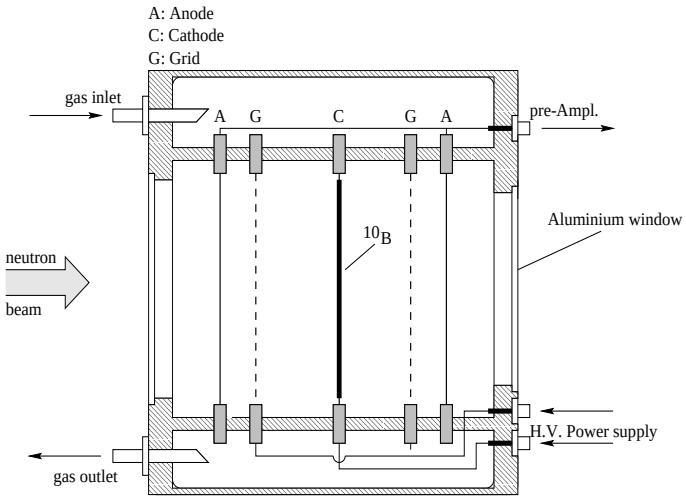

Figure 4.6: Drawing of the ^{10}B ionisation chamber used for flux measurement [71].

For the conversion of neutrons into directly detectable particles, the ^{10}B(n,α) reaction is considered as a standard structureless cross section from thermal energy up to 200 keV. The reaction may be written as:

$$^{10}B + n \longrightarrow \begin{cases} ^{7}Li + \alpha \quad Q = 2.792MeV & \text{(ground state)} \\ ^{7}Li^{*} + \alpha \quad Q = 2.310MeV & \text{(excited state)} \end{cases} \tag{4.8}$$

The reaction product (^{7}Li) may be left either in its ground state or mainly in its excited state with the emission of a 0.48 MeV gamma ray. Due to the large Q-value of the reaction compared to the kinetic energy of the neutrons, the reaction products are emitted at 180^o from each other with respective energy of $\frac{4}{11}Q$ and $\frac{7}{11}Q$ for lithium and alpha particles.

One of the reaction product is stopped in the cathode, and the particle emitted by the ^{10}B layer loses its energy by ionisation of the gas atoms. Under the influence of the electric field, the positive ions are accelerated toward the cathode and the electrons toward the anode. The gas multiplication process takes place between the grid and the anode. The signal pulse at the anode is proportional to the total number of ion-electron pairs formed along the track of the incident

particle, then becomes independent of their original position. The anode signal pulse height, shown in Figure 4.7, consists of four peaks corresponding to the lithium and alpha detection.

The observed count rate N_F is defined as the product of the incident neutron flux $\phi(E)$ with the detector efficiency ε. This efficiency depends only on the interaction cross section of the incident neutron with the detector, since the counting efficiency for any charged particle entering the active volume of the chamber is essentially 100%. Due to the negligible perturbation of the neutron flux by the detector materials, ε is simply given by the probability of an incident neutron interacting with a thin disk of ^{10}B [70]. The count rate N_F is given by:

$$N_F(E) = n_{^{10}B}\sigma_{n,\alpha}^{^{10}B}(E)\phi(E) + B_F(E) \tag{4.9}$$

where $\sigma_{n,\alpha}^{^{10}B}$ is the cross section of the ^{10}B(n,α) reaction, $n_{^{10}B}$ is the ^{10}B thickness in at/barns, and $B_F(E)$ is the background.

The neutron flux impinging the sample ($\phi'(E)$) is connected to the neutron flux ($\phi(E)$) measured by the ^{10}B ionisation chamber via the transmission $T_d(E)$ of the bodies between the cathode and the sample (aluminum, argon, methane, oxygen, hydrogen). Owing to the small variations of their macroscopic scattering cross sections, $T_d(E)$ may be assumed constant over a large energy range. Thus:

$$\phi'(E) \simeq \kappa\, \phi(E) \tag{4.10}$$

This assumption may involved an error lower than 0.5% on the neutron flux behaviour.

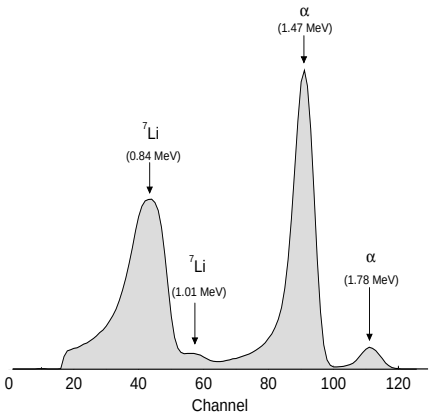

Figure 4.7: Anode signal pulse height of the boron chamber.

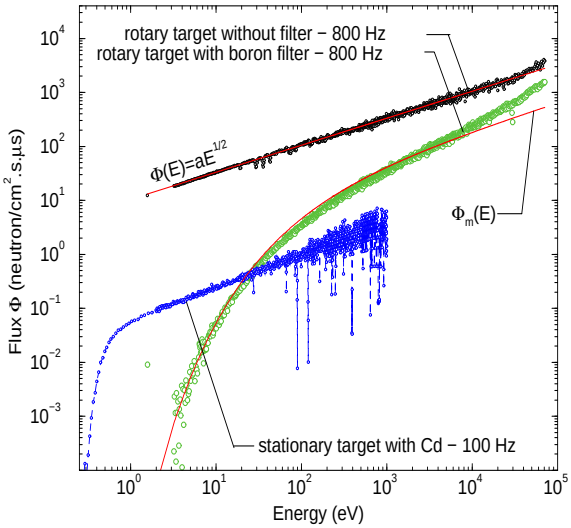

Figure 4.8: Neutron flux at 30 m flight distance.

The results of flux measurements performed at a 30 m flight distance are shown in Figure 4.8. Due to the electron beam intensity GELINA delivers (Table 4.1), the neutron flux available at a 100 Hz repetition rate is about seven times smaller than the neutron flux produced at 800 Hz. Black filters affect the count rate as well as the behaviour of the neutron flux spectrum. A flux reduction of about 50% is observed when all black filters are in the beam. Figure 4.8 shows the effects of permanent boron or cadmium anti-overlap filters.

A neutron flux measurement has been performed without filters. The resulting neutron flux is roughly proportional to $\sqrt{E}$. This energy dependence can be retrieved through the conventional theory of the neutron slowing down in an infinite homogeneous medium with constant scattering cross section and without absorption [85, 159]. These assumptions can be applied to describe the neutron flux emitted from the water moderator of GELINA. The absorption cross sections in the moderator slab are negligible compared to the hydrogen scattering cross section, whose value is about 20 barns on a large energy range from 1 eV to 10 keV. The neutron flux per energy unit (n/cm^2.s.eV) can thus be expressed by the Fermi formula as :

$$\Phi_E(E)\mathrm{d}E \propto \frac{\mathrm{d}E}{E} \tag{4.11}$$

It is convenient to define the flux per time interval unit (n/cm^2.s.μs). From the relationship $\Phi_E(E)dE = \Phi_t(t)dt$ and the time/energy relation (Equation 4.4), Equation 4.11 becomes :

$$\Phi_t(E)\mathrm{d}t \propto \sqrt{E}\mathrm{d}t \tag{4.12}$$

To account for the effect of the filters, their transmission $T_i(E)$ should be introduced. We should adopt the corrected equation:

$$\Phi_m(E)\mathrm{d}t = \Phi_t(E)\prod_i T_i(E)\mathrm{d}t \tag{4.13}$$

This equation doesn't allow an accurate description of the flux behaviour on a large energy range [1 eV - 100 keV]. A more realistic expression should account for the finite size of the moderator, the neutron absorption, and the energy dependence of the hydrogen and oxygen scattering cross sections. The flux description is improved if the following phenomenological formula is applied [54]:

$$\Phi_E(E)\mathrm{d}E \propto E^{\alpha(E)}\mathrm{d}E \tag{4.14}$$

The exponent $\alpha(E)$ being a function of the energy expressed as:

$$\alpha(E) = a_0 + a_1\sqrt{E} + a_2 E \tag{4.15}$$

4.6.2 Neutron capture detector

Neutron capture cross sections are measured by detecting γ-rays emitted when the compound nucleus de-xcites to its ground state. A review of currently used techniques can be found in Reference [74]. The essential requirement for a radiative neutron capture detector is that its efficiency be independent of the capture γ-ray spectrum (ε_c =cst). To achieve this goal, two classes of detector can be considered: the total absorption detector and the total energy detector.

The total absorption detector is a 4π-detector that surrounds the sample in order to absorb all the emitted γ-radiations. It is usually a liquid scintillator of large volume with nearly a 100% efficiency [75]. The main limiting factors depend on the background contributions. Nevertheless, similar results can be achieved by using a so-called total energy detector which has the property of making the γ-ray efficiency $\varepsilon\gamma_i$ proportional to its energy $E\gamma_i$.

$$\varepsilon\gamma_i = kE\gamma_i \tag{4.16}$$

For such a system, the efficiency ε_c of a neutron capture event can be expressed as:

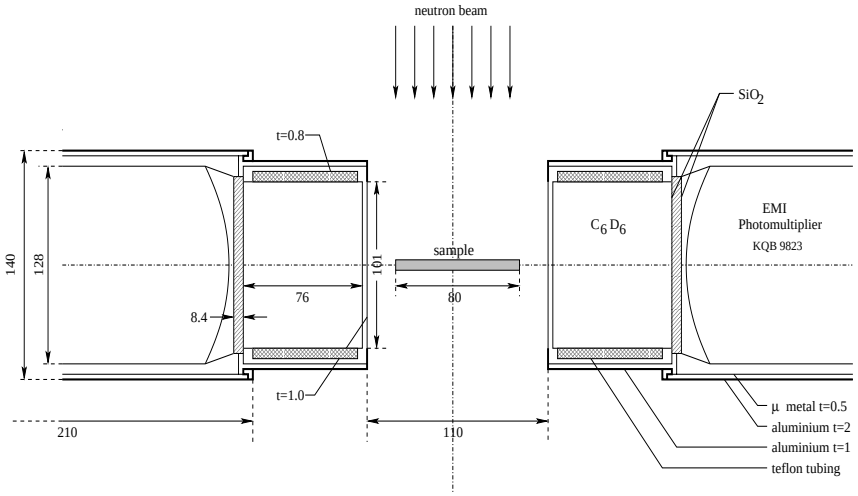

Figure 4.9: Top view of the neutron capture detection system. Dimensions are in millimeters [83].

$$\varepsilon_c = \sum_i \varepsilon\gamma_i + \sum_i \sum_j \varepsilon\gamma_{i,j} + ... \tag{4.17}$$

The smaller $\varepsilon\gamma_i$ is, the more negligible the probability $\varepsilon\gamma_{i,j}$ of observing more than one γ-ray from a cascade. Equation 4.17 becomes:

$$\varepsilon_c \simeq \sum_i \varepsilon\gamma_i = k \sum_i E\gamma_i = kE^* \tag{4.18}$$

The probability of detecting a capture event ε_c is then independent of the mode of decay. It depends only on the excitation energy E^* of the compound nucleus. This condition can be realised using a Moxon-Rae detector which can achieve such a response thanks to its design via the conversion of gamma rays into electrons [76]. However its efficiency is inherently low and non linear for γ-rays below 1 MeV.

The alternative system used at Geel, is based on the suggestion by Maier-Leibnitz [77]. Small hydrogen-free liquid scintillators achieve the same result as the Moxon-Rae detector by appropriately weighing their pulse amplitude response. The so-called pulse weighting technique was first applied to C_6F_6 liquid scintillators [78, 79] which was replaced later by the less neutron sensitive deuterate benzene C_6D_6 scintillators.

Our experimental setup is shown in Figure 4.9. The detection of γ-rays from capture events is performed using two 10.2 cm$\times$7.6 cm cylindrical C_6D_6 detectors NE230, placed at a 90^o angle to the neutron beam direction. The liquid is canned in a standard BA1 cell provided with a teflon expansion tube wrapped around the side. Each scintillator is viewed by a EMI 9823 KQB photomultiplier canned in aluminium. The flight path station is air conditioned in order to minimise the pulse-height variations due to the temperature. The energy calibration of the C_6D_6 spectra is adjusted to 25 keV/channel by using a ^{238}Pu+^{13}C γ-ray source ($E\gamma$ = 6.13 MeV). A hardware threshold of 150 keV for the pulse amplitude spectrum avoids the detection of any deuteron recoil below 1 MeV neutron energy. Figure 4.10 shows the pulse height spectrum of the calibration source. Owing to the low Z-value of the absorber, the compton scattering stands as

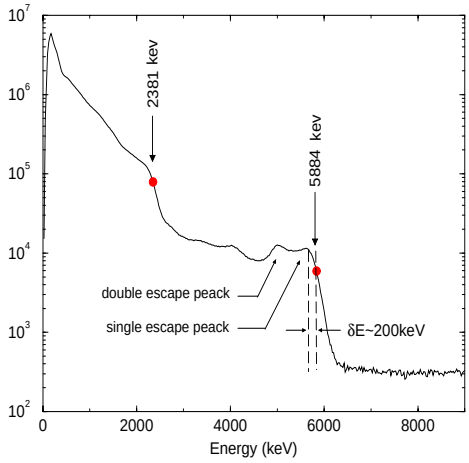

Figure 4.10: Pulse height amplitude of the calibration source (^{238}Pu+^{13}C).

the dominant γ-ray interaction process. Although the amplitude resolution is poor, it remains adequate to distinguish the compton edge of the calibration source at 5884 keV, plus the single and double escape peak. The compton edge at 2381 keV is due to the thorium decay.

A symmetric pair of detectors is used in order to get high-solid angle. Careful measurements of the coincidences between the detectors have to be performed to account for the detection of more than one γ-ray per capture. Indeed, because of the symmetry, the probability of detecting a γ-ray in each detector is equal to the probability of summing two γ-rays within a detector. During the experiment, the coincidence rate was lower than 1%. The mean overweight induced by this is disregarded, and the assumption given in equation 4.18 can be applied to the present measurements.

For a monochromatic γ-ray source (γ_i), the γ-ray detection efficiency $\varepsilon\gamma_i$ verifies the generic expression:

$$\varepsilon\gamma_i = \sum_I R_i(I) \tag{4.19}$$

where the response function $R_i(I)$ of the detector is the pulse height spectrum obtained from the monochromatic γ-ray source, and I is the energy of the pulse height spectrum. Thus $R_i(I)$ is the number of γ-rays $N_{\gamma_i}(I,E)$ observed at a given pulse height energy normalised to the number of capture event $N_c(E)$:

$$R_i(I) = \frac{N_{\gamma_i}(I,E)}{N_c(E)} \tag{4.20}$$

The detection efficiency is made proportional to $E\gamma_i$ (Eq. 4.16) by introducing in Equation 4.19 a weighting function $W(I)$:

$$\varepsilon_{\gamma_i} = \sum_I R_i(I)W(I) = kE\gamma_i \tag{4.21}$$

Neutron capture measurements of iodine involve a complex decay mode. Equation 4.21 then becomes a sum over γ_i:

$$\varepsilon_c = \sum_i \varepsilon_{\gamma_i} = \sum_i \sum_I R_i(I) W(I) = k \sum_i E\gamma_i = kE^* \tag{4.22}$$

Folding together equations 4.20 and 4.22 and introducing the background contribution, the number of capture event N_c is given by:

$$N_c(E) = \frac{N_\gamma^w(E) - B_\gamma(E)}{kE^*} \tag{4.23}$$

where $B_\gamma(E)$ is the background, and $N_\gamma^w(E)$ stands for the weighed count rate, defined as follows:

$$N_\gamma^w(E) = \sum_I N_\gamma(I, E) W(I) \tag{4.24}$$

It has been found that a fourth-degree polynomial adequately describes $W(I)$ [80, 83]. If I is in MeV, the weighting function is given by:

$$W(I) = 11.95 + 8.176I + 36.75I^2 - 7.142I^3 + 0.4669I^4 \tag{4.25}$$

The validity and the effects of the weighting function on the resonance parameters are discussed in Section 5.2.

4.6.3 Lithium glass detector

The lithium glass detector is an inorganic scintillator used as a fast neutron detector. Owing to their relatively poor light output and non linear response, these scintillators have evolved to record the arrival time of a neutron in TOF experiments. The lithium formulations have predominated in this application because they have a good timing resolution (typically 50-75 ns), and a low-background activity in thorium and potassium (less than 12 kB/kg [93]).

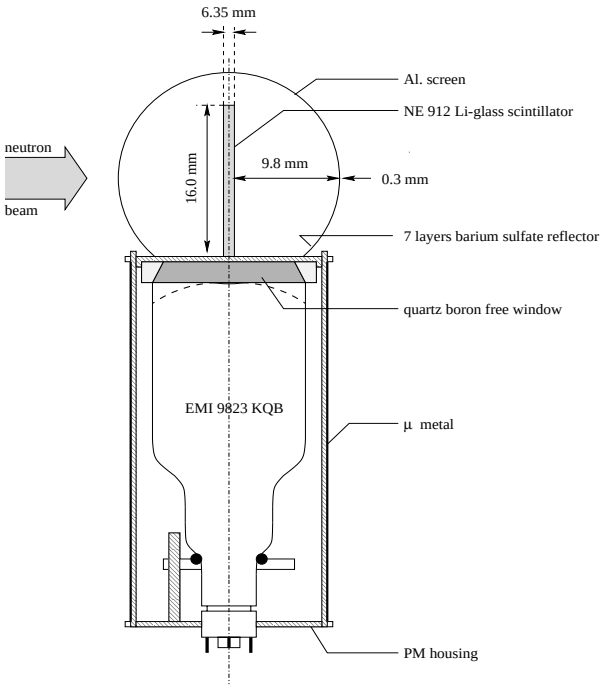

Figure 4.11: Drawing of the lithium glass detector used in transmission measurements.

In our transmission measurements, neutrons are detected with a 1/4" thick Li-glass (NE 912) placed in a Al. sphere and viewed by a 5" EMI 9823 KQB photomultiplier, placed at the right angle to the neutron beam axis (Figure 4.11). The detection of neutrons is based on the (n,α) reaction in ^{6}Li:

$$^6\text{Li+n} \longrightarrow \alpha +^3 \text{H} \qquad Q = 4.78 MeV \tag{4.26}$$

The lithium is enriched to 95% in ^{6}Li. Small amounts of cerium (Ce^+) are added to be used as a scintillation medium. Alpha particles going through the detector generate electron-hole pairs. The free electrons migrate through the crystal until they drop into an impurity site. The de-excitation of the cerium occurs very quickly with the emission of photons. The light aluminium sphere plated with barium sulfate is designed to reflect the light to the entrance window of the photomultiplier.

The anode pulse height signal provided by the photomultiplier is shown in Figure 4.12. The full energy peak of the (n,α) reaction is the neutron response of the detector. In order to measure the neutron flux incident upon the detector, a hardware window selects the events corresponding to the (n,α) reaction. The observed count rates $N_{in}(E)$ (sample in the beam) and $N_{out}(E)$ (sample out of the beam) are expressed as:

$$\begin{cases} N_{in}(E) &= \varepsilon(E)\phi_{in}(E) + B_{in}(E) \\ N_{out}(E) &= \varepsilon(E)\phi_{out}(E) + B_{out}(E) \end{cases} \tag{4.27}$$

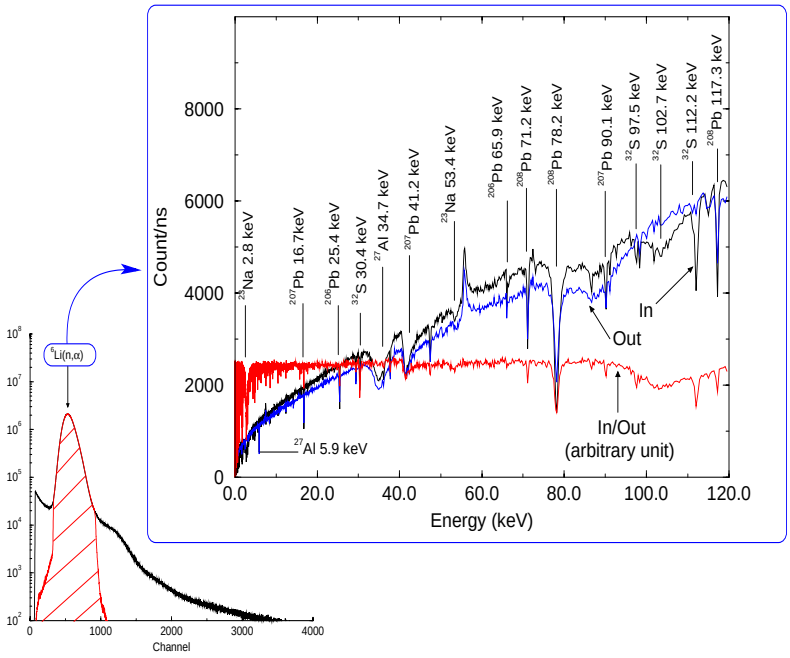

Figure 4.12: Anode signal pulse height and examples of count rate of the Li-glass detector together with the ratio N_{in}/N_{out}.

where B_{in} and B_{out} are the background count rates. An approximation of the neutron absolute detection efficiency in the $1/v$ region is given by [92]:

$$\varepsilon(E) \sim 0.007 \left(1 - e^{-l\Sigma_{n,\alpha}(E)}\right) \tag{4.28}$$

where $\Sigma_{n,\alpha}(E)$ is the macroscopic cross section of the ^{6}Li(n,α) reaction, and l is the thickness of the detector. A complete expression of $\varepsilon(E)$ is given in Reference [70]. In addition to ^{6}Li, the scintillator also contains significant quantities of silicon and oxygen whose resonance and neutron scattering cross section alter the efficiency of the scintillator. Nevertheless, a precise knowledge of the detection efficiency is not required because the transmission factor is obtained via the N_{in}/N_{out} ratio. Examples of count rates are shown in Figure 4.12 together with the N_{in}/N_{out} ratio.

4.6.4 Central Monitor

The normalisation of the transmission is provided by four BF_3 tubes (TGM 25) placed in the concrete wall above the uranium target. These detectors are called Central Monitors (CM). Each detector is a tube measuring 2.54 cm in diameter and 63.2 cm in length (Figure 4.13). They are filled at 1 atm with a gas highly enriched in ^{10}B. The boron trifluoride serves both as a target for neutron conversion into secondary particles and as proportional counter.

The neutron detection is based on the ^{10}B(n,α) reaction as described in section 4.6.1. The CM detects a fraction $\varphi(E)$ of the neutrons produced by the uranium target, and thus deliver a number proportional to the total neutron flux. The count rate during the time interval $\Delta_{t_{in}}$ and $\Delta_{t_{out}}$ is given by:

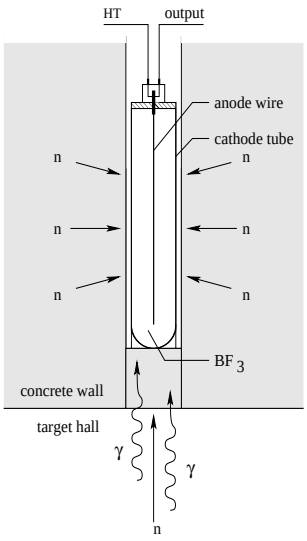

Figure 4.13: Drawing of the BF_3 tube used as Central Monitor (CM).

$$\begin{cases} M_{in} &= \int\int_{\Delta t_{in}} \varepsilon(E)\varphi(E,t)\mathrm{d}E\mathrm{d}t \\ M_{out} &= \int\int_{\Delta t_{out}} \varepsilon(E)\varphi(E,t)\mathrm{d}E\mathrm{d}t \end{cases} \tag{4.29}$$

The detection efficiency for a neutron incident along the axis of a BF_3 tube is approximately given by [93]:

$$\varepsilon(E) \sim 1 - e^{-l\Sigma_{n,\alpha}(E)} \tag{4.30}$$

where $\Sigma_{n,\alpha}(E)$ is the macroscopic absorption cross section of ^{10}B at energy E, and l is the active length of the tube. At thermal energy the detection efficiency is about 95%, and drops to 10% at 100 eV [70]. A BF_3 tube responds principally to the slow neutron component. To account for this feature, the neutrons emitted by the target-moderator assembly are partially moderated by the concrete before reaching the detector.

The background contribution is mainly due to γ-rays found together with the neutron flux. It is possible to separate gamma and neutron induced events, as most of γ-ray interactions result in low-amplitude pulses. A simple amplitude discrimination enables us to eliminate these contributions without sacrificing neutron efficiency.

4.6.5 Electronic setup

Each detector signal is divided along two different chains of electronics: one determines the pulse height according to the energy absorbed in the detector (slow signal) and the other consists of fast electronic which determines the arrival time (t_n) relative to the start time of the neutrons (T_0). After preamplification and amplification, the slow signal is sent to an Analogue to Digital Convertor (ADC). In the ADC the pulse heights are converted into channel numbers. The injection of a stabilised light pulse in the C_6D_6 and Li-glass detectors during the measurement provides an efficient tool to control to better than 1% the gain of the electronic (detector + preamplifier + amplifier + hight voltage and ADC).

A time coder [89] receives the time information t_n, the T_0 signal and the Pretrigger (P_{tr}). The T_0 is a signal which corresponds to the moment when the electrons leave the accelerator. It is generated as the electrons go through a ferrite pick up coil, just before their impact on the

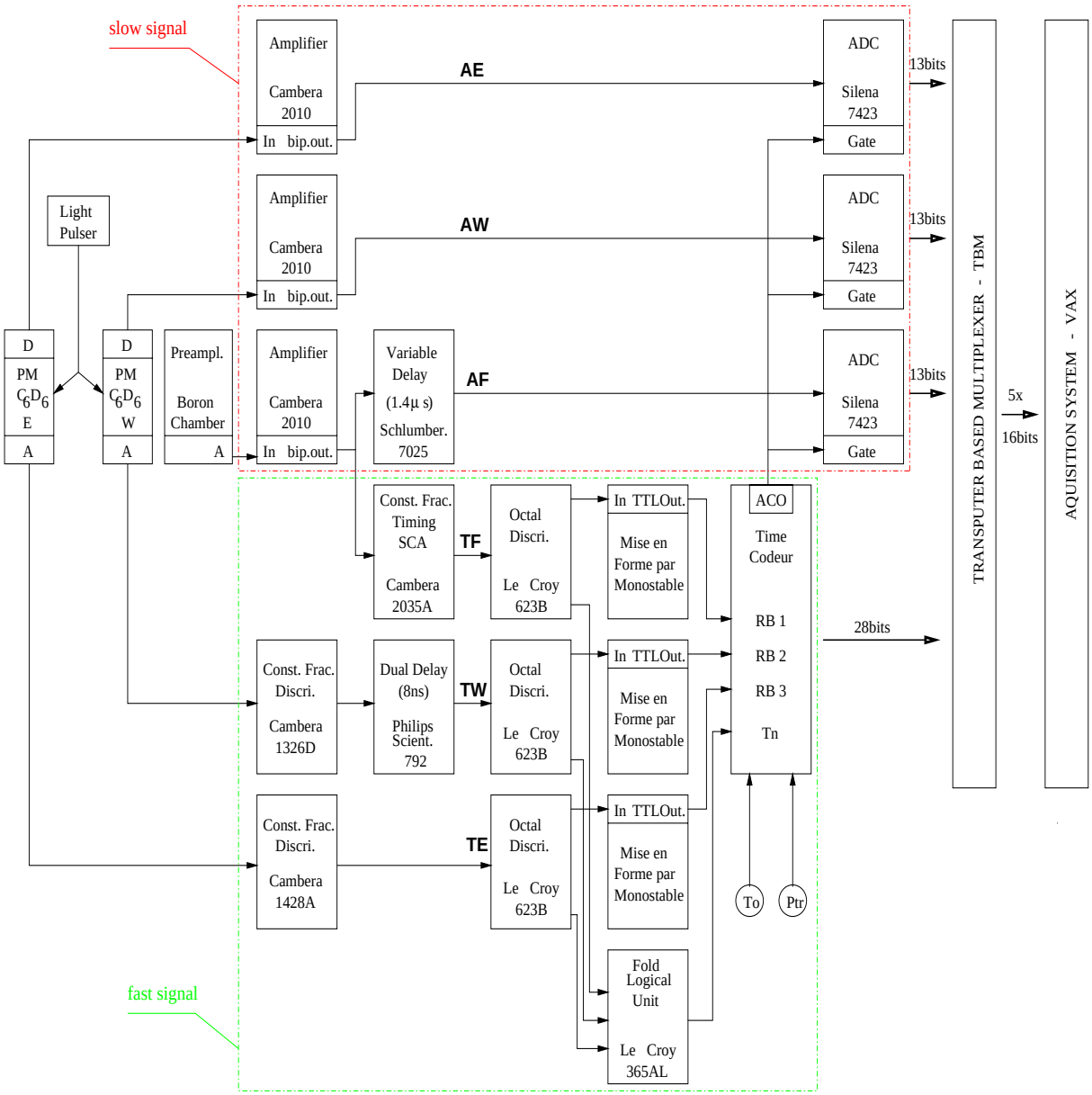

Figure 4.14: Block diagram of the capture electronic setup. AE, AW and AF are the slow signals delivered by the two C_6D_6 and the boron chamber. TE, TW, TF are the respective fast signals. They are mixed in a *fold logical* unit and sent to a single T_n input of the time coder. The *Variable Delay, Constant Fraction Timing* and *Dual Delay* units are used for timing applications. The *Octal Discriminator* distribute logical signals provided by the *Constant fraction* units.

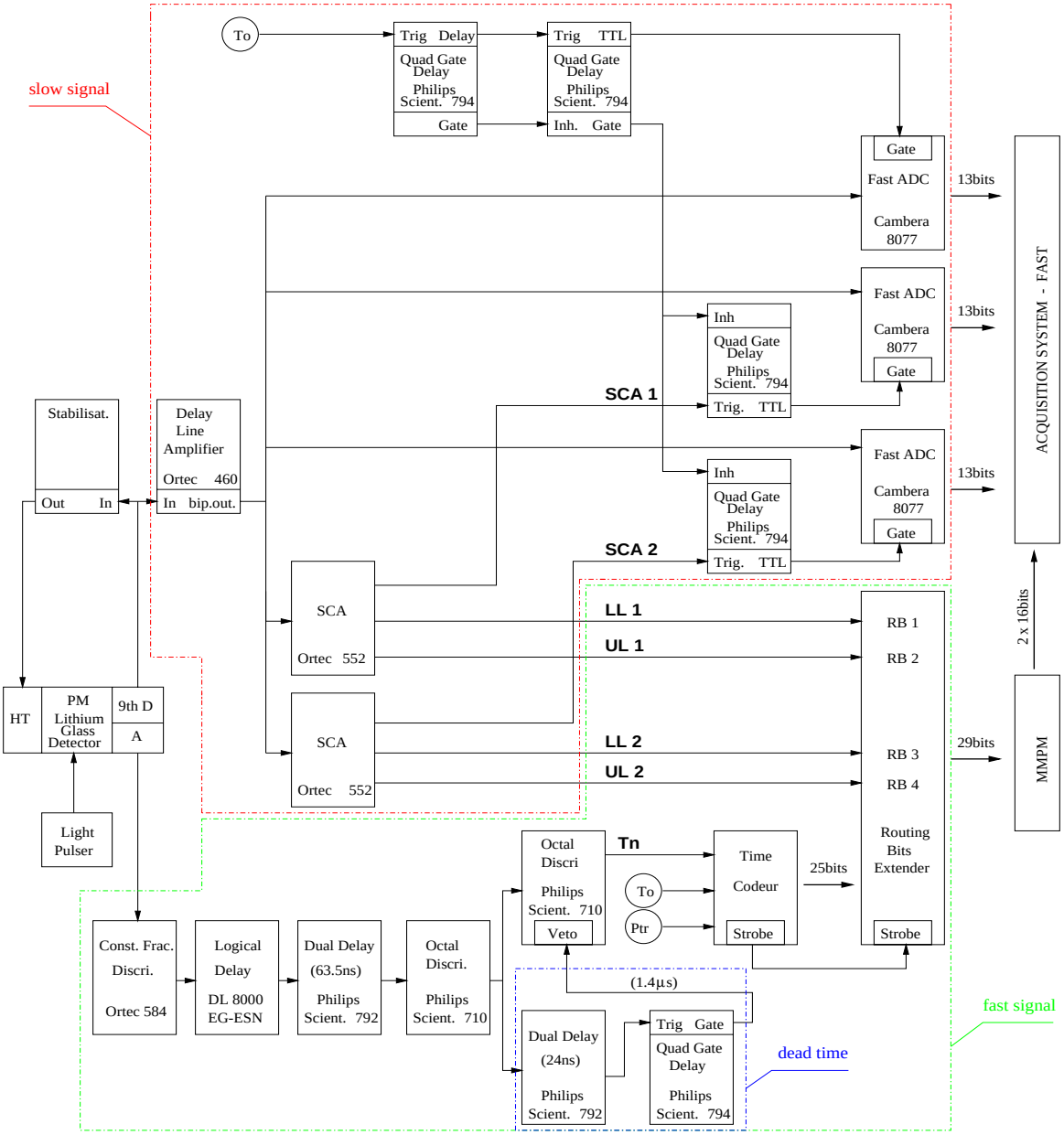

Figure 4.15: Block diagram of the transmission electronic setup. Two Single Channel Analysers (SCA) deliver three signals (LL, UL and SCA) used in the time dependent background determination (Appendix A). They define two fixed hardware windows with a *Lower Level* (LL1 and LL2) and an *Upper Level* (UL1 and UL2). The ADC are gated according to the SCA information (SCA1 and SCA2). After each T_n signal, a fixed dead time of 1.4 μs is imposed via a *Dual Delay* in association with a *Quad Gate Delay* unit.

uranium target. The P_{tr} is a signal which automatically resets the time coder according to the linac frequency. It is supplied by the accelerator and precedes the T_0 signal. The time difference between the T_0 and the t_n signals is converted into a channel number and sent to the data acquisition system via an interface (Modular Multi-Parameter Multiplexer [87] or Transputer Based Multiplexer [88]).

The time coder receives additional information provided by the so-called Routing-Bits (RB) [91]. A RB is a signal recorded together with the time information in order to identify the event.

• Capture experiment

For the capture experiment, we used the Multi-Parameter Acquisition system (MPA) developed at the IRMM and based on a VAX/VMS computer [90].

Fast as well as slow signals originating from the detection event are complementary and have to be related to each other in the data acquisition system. The time signal delivered by the C_6D_6 and the boron chamber are mixed in an OR logic function, and sent to a single t_n input of a time coder. In order to know from which detector a signal has been generated, a RB input on a time coder is associated to each detector. In that way, the time coder delivers the time value along with the RB information which identifies the detector.

The Time coder also provides a logical signal (ACO) to gate the ADC in order to ensure a coincidence. The event provided by the data acquisition system is formed by three RB, one TC and three ADC information (AE, AW and AF). Each event is then stored in a list-mode data file.

• Transmission experiment

For transmission measurement, we used a FAST data acquisition system upgraded at the IRMM, and based on a two personal computers [86].

The acquisition system operates in free mode. Fast and slow signals delivered by the Li-glass detector are recorded independently. Routing bits are also used, but for background measurement only. The slow signal is sent to three ADC. The events are selected according to their pulse height by using two Single Channel Analysers (SCA). For each event falling in a fixed hardware window (defined by a Lower Level LL and an Upper Level UL), four RB are created together with the time information. Several TOF spectra are generated by the acquisition system and incremented according to the RB signals. The effective 1.42 μs experimental dead time of the acquisition system is continuously monitored during the experiment. The TOF and amplitude spectra are being recorded as histogram in a binary file.

• Channel width and accordion

The maximum number of channels available for the coding of the flight time of a neutron is 32 K in the case of the FAST acquisition system and 24 K in the case of the MPA acquisition system. The maximum time resolution of the time coder is 0.5 ns. To cover the entire neutron energy region below 100 keV, the TOF spectrum has to be divided into several regions. This time discretisation is called *accordion*. In each of these regions, the channel width Δt_i shall be large enough to map the TOF spectrum with acceptable resolution. Therefore, the flight time t_n given by the acquisition system is defined as the time elapsed from the initial channel to the center of channel n:

$$t_n = \sum_{i=1}^{n-1} \Delta t_i + \frac{1}{2}\Delta t_n \tag{4.31}$$

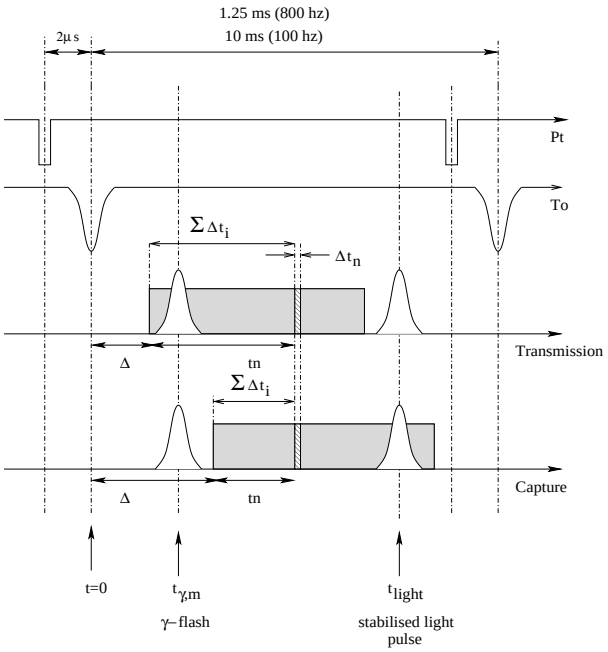

Figure 4.16: Schematic representation of the timing signals available in a Linac cycle. The time region of interest varies according to the Linac repetition rate.

For iodine measurements, the channel width typically varies from 256 ns ($E < 100$ eV) to 2 ns ($E > 40$ keV). For practical purposes, the number of regions and the channel widths have been chosen to map each resonance with at least 18 points.

• **Timing signal**

A timing signal sequence of the Linac is given in Figure 4.16. The time region varies from 1.25 ms to 10 ms at 800 hz and 100 hz repetition rates. An initial delay t_{ID} can be imposed on the time coder before accepting an event. It defines the upper energy limit of our energy range.

In transmission measurements, the value of this delay is chosen so as to continuously record the intense γ-flash generated by the neutron production. The position of the γ-flash peak $t_{\gamma,m}$ is observed in the TOF spectrum with a delay (t_{offset}) as regards with the true value $t_\gamma = L/c$. This additional delay is due to the time interval between T_o and the beam impact, the finite speed of light, the detection process and the cable lengths. The order of magnitude of t_{offset} is about 100-150 μs. The exact flight time (t) of a neutron detected by the acquisition system at time t_n is given by:

$$t = t_n + \Delta \qquad \text{with} \qquad \Delta = t_{ID} - t_{offset} \tag{4.32}$$

In transmission measurements the γ-flash is recorded in the TOF spectrum, therefore, t is simply given by:

$$t = t_n + t_\gamma - t_{\gamma,m} \tag{4.33}$$

This technique provides a definition of the zero time of the TOF spectrum with an accuracy nearly equal to 3 ns.

Chapter 5

Measuring sequence and data Reduction

The output of the MPA and FAST detection systems consists of a set of multichannel spectra and of scaler values. Raw data have to be corrected for the experimental effects and combined to obtain a capture yield ($Y(E)$) or a transmission spectrum ($T(E)$):

$$T(E) = N_T \frac{a_{in}(E)N_{in}(E) - B_{in}(E)}{a_{out}(E)N_{out}(E) - B_{out}(E)} \tag{5.1}$$

$$Y(E) = \frac{\kappa\, n_{^{10}B}}{k\, E^*} \frac{a(E)\sum_I N_\gamma(I,E)W(I) - B_\gamma(E)}{a(E)N_F(E) - B_F(E)} \sigma_{n,\alpha}^{^{10}B}(E) \tag{5.2}$$

where $a_{in}(E)$, $a_{out}(E)$ and $a(E)$ are the dead time corrections. The other terms stand for the count rate or constant parameters defined in Chapter 4.

The data reduction process is divided into several sequences of operation. C.Bastian wrote a set of commands for neutron data reduction [94]. It is dedicated to the Analysis of Geel Spectra (AGS). The AGS system concerns basic operations like spectrum addition or division, dead time correction, non linear fitting and several other involved operations, preserving all the steps in a single file with full uncertainty propagation. An exhaustive description of the complete data reduction procedure is given in References [70] and [71]. The present work shall only discuss the weighting function, the dead time correction, the time dependent background and the normalisation technique.

5.1 Measuring sequence and data sorting

Capture and transmission experiments consist of a sequence of sample changer position. Examples of sequences are given in Table 5.1. Black filters (Cd, W, Mo, Ge, Co, Bi, Na, S) are exposed in a repetitive way to the neutron beam. In addition, transmission experiments consist of a sequence of *in* (sample in the neutron beam) and *out* (sample out of the neutron beam) sample positions.

- **Transmission experiment:**

As the experiments took several weeks, the sequence has to be short enough to reduce the systematic uncertainties due to a possible instability of the accelerator and to any variations of the sample temperature. In transmission measurements, neutron flux fluctuations are continuously

Table 5.1: Measuring sequence used in capture and transmission at 800 Hz and 100 Hz repetition rates.

Capture measurements

Repetition rate	Sequence	Sample	Cd	W	Mo	Co	Bi	Na	S
800 Hz	1^{st}	×		×	×	×	×	×	×
	2^{nd}	×						×	
	3^{rd}	×							×
100 Hz	1^{st}	×	×			×	×		

Transmission measurements

Repetition rate	Sequence	Sample	Cd	W	Ge	Co	Bi	Na	S
800 Hz	1^{st}	IN		×	×	×	×	×	×
	2^{nd}	OUT		×	×	×	×	×	×
	3^{rd}	IN						×	
	4^{th}	OUT						×	
	5^{th}	IN							
	6^{th}	OUT							
100 Hz	1^{st}	IN	×			×		×	
	2^{nd}	OUT	×			×		×	

monitored during the experiment. Any given cycle with a ratio $\int N_{in}(t)/\int N_{out}(t)$ larger than 1.05 compared to the reference value taken at the beginning of the experiment is automatically rejected. Fewer than 1% of the cycles have been rejected during our measurements.

The output of the FAST acquisition system consists of several TOF spectra. The events selected to build the transmission spectrum are those corresponding to the full energy peak of the (n,α) reaction, which is the neutron response of the Li-glass detector. The other spectra are used for dead time and background corrections. These corrections are described in the following section together with the normalisation technique.

• **Capture experiment:**

In capture experiments, a software sorting of the cycle is used. The main criteria chosen to select the cycles are shown in Figure 5.1.

• The ratio of the central monitor values CM_1/CM_2 shows the neutron flux fluctuations in the target hall. These fluctuations are related to a small variation of the position of the electron beam impinging the uranium target [70, 71].

• The neutron flux impinging the sample is monitored with information provided by the ionisation chamber. ϕ_2 and ϕ_1 are neutron flux integrated over small time regions at the beginning and at the end of the flux spectrum. The ϕ_1/ϕ_2 ratio shows a possible variation of the amount of slow neutrons with respect to the number of high energy neutrons. Origins of the large fluctuations seen in Figure 5.1 are probably due to the variations of the energy spectrum of the electrons. At the start of the linac (beginning and middle of the week), the production of low energy electrons may explains the production of slow neutrons. The spurious behaviour around the 300^{th} run could be explained with strong variations of the temperature in the accelerating sections. Besides, one of the thyratrons had to be changed at the end of the 3^{rd} week. The

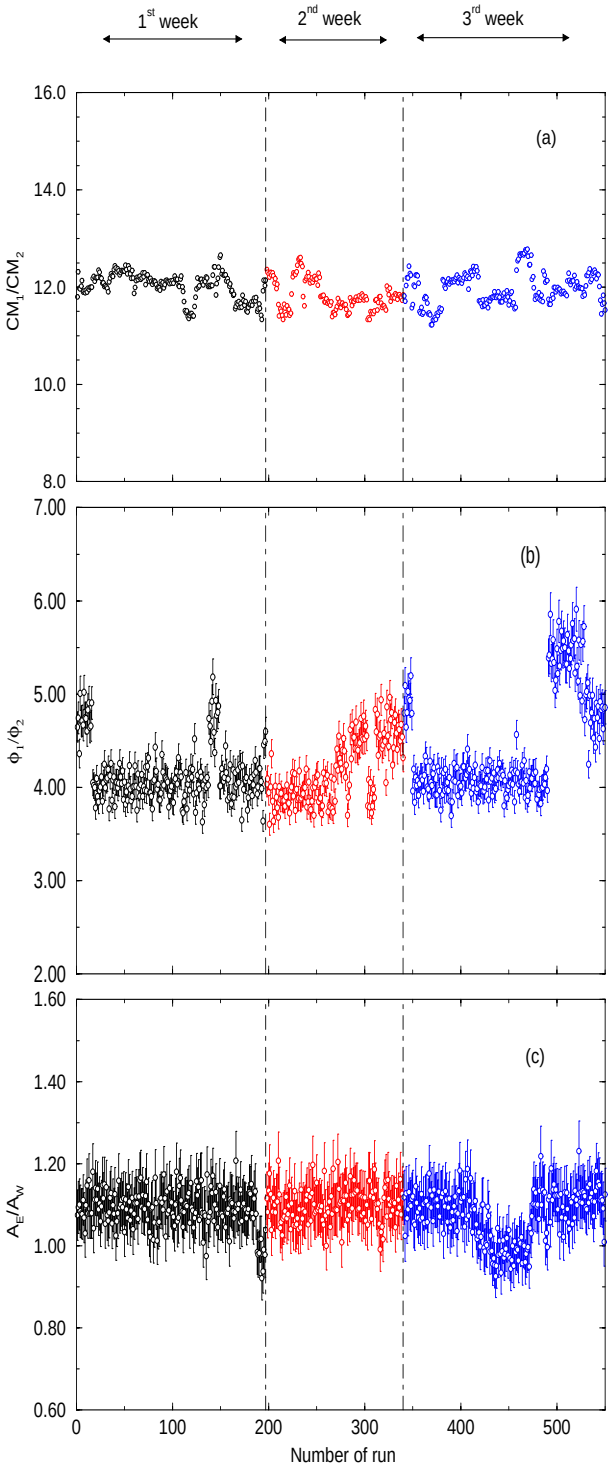

Figure 5.1: Example of fluctuations of the neutron flux produced in the target hall and detected by the ^{10}B ionisation chamber, together with the evolution of the C_6D_6 count rate: (a) CM_1 and CM_2 are the central monitor count rates; (b) ϕ_1 and ϕ_2 are neutron flux integrated over small time regions at the beginning and at the end of the flux spectrum; (c) A_E and A_W are the area of the same resonance seen by the two C_6D_6 detectors.

cycles connected to these spurious behaviours are rejected.

• The final criterion is applied to the control of the C_6D_6 information. In a first approximation, both detectors give out some information on the neutron beam position impinging the sample. The A_E and A_W values stand for the area of the same resonance seen in each γ-rays spectrum. The fluctuations of the ratio $R = A_E/A_W$ indicate a possible change in the average solid angle under which the detector is seen from the sample. It may be connected to a small variation of the neutron beam position. Indeed, a 2 mm variation may entail fluctuations larger than 10% on R [82]. In addition, a fraction of the capture area uncertainty depends on the behaviour of R. The relationship between $\Delta A_\gamma/A_\gamma$ and $\Delta R/R$ may be expressed as:

$$\frac{\Delta A_\gamma}{A_\gamma} = \frac{1}{2}\frac{\Delta R}{R} \tag{5.3}$$

After the data obtained around the 200^{th} and 450^{th} runs has been rejected, the $\Delta R/R$ value is about 3.1%. From the Equation 5.3, the associated systematic error on the capture area (A_γ) is about 1.5%.

The list-mode data from the data acquisition system consists of a large number of events. They are selected according to their Routing Bit information. The capture events are stored in a two-dimensional ADC×TOF grid, and the flux information is stored as a TOF spectrum. Three additional TOF spectra are built in order to calculate the dead time correction.

5.2 Weighting Function

The weighting function is applied at the beginning of the capture data reduction process. The time information provided by the C_6D_6 is weighted according to its pulse height amplitude in order to achieve a capture detector efficiency proportional only to the total γ-ray energy emitted. The procedure used to weight the raw data is shown in Figure 5.2. Each capture event defined by a time information (t) and a pulse height amplitude (I) is collected in a time×amplitude matrix. The matrix elements are weighted according to the $W(I)$ value of the weighting function (Equation 4.24). The weighted count rate as a function of the time t is given by:

$$N_\gamma^w(t) = \sum_I N_\gamma(I,t)W(I) \tag{5.4}$$

Extensive work was done to obtain a reliable description of the weighting function. In 1988, Corvi et al. [80, 83] developed a method for its experimental determination. It consists of measuring γ-ray transition from a (p,γ) reaction with a high resolution germanium detector in coincidence with two C_6D_6 scintillators, these being arranged in the same setup as used for our neutron capture cross section measurements (see Figure 4.9). The Germanium detector was placed at a 0^o angle to the beam direction. The (p,γ) measurements have been carried out at the Geel 7 MV Van de Graaff accelerator. In addition, the weighting function, the efficiencies and the response function of the detector for monochromatic incident γ-rays were obtained using a time-integrated coupled electron-photon Monte-Carlo transport code (ITS) [69]. Lately, increasing interest for reliable weighting functions has arisen from the n-TOF collaboration. New Monte-Carlo simulations were performed with GEANT4 [73] and MCNP4C [95]. A new experimental investigation of the weighting function was carried out at the 4 MV Van de Graaff accelerator of the Centre d'Etude Nucléaire de Bordeaux Gradignan (CENBG) [96].

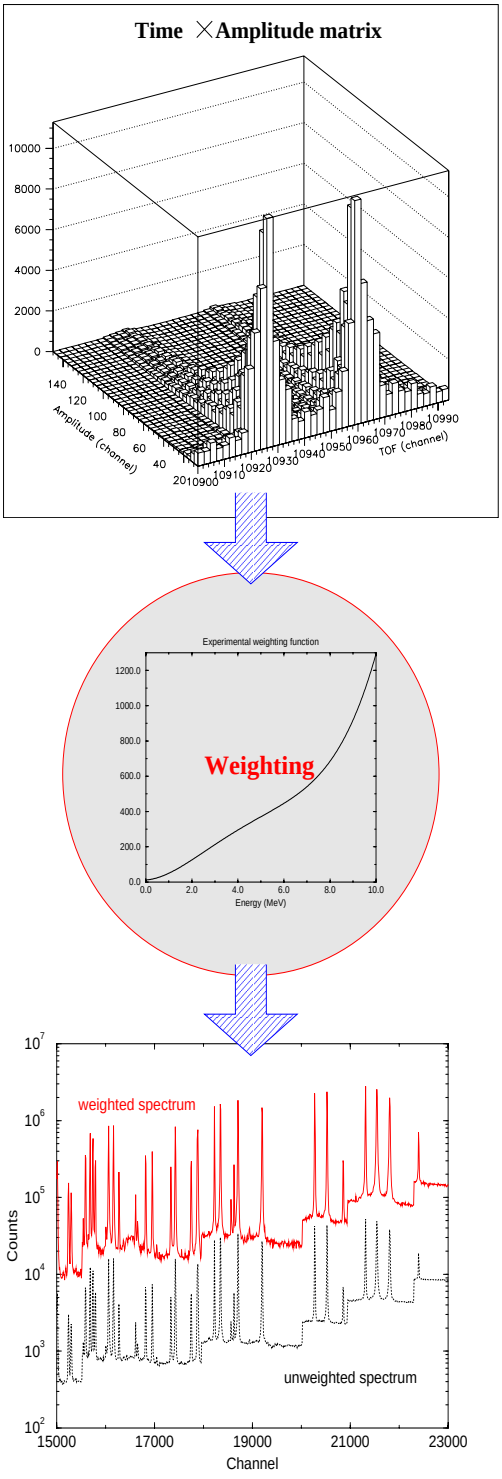

Figure 5.2: Weighting function applied on matrix *time* × *amplitude*.

The weighting functions related to our capture setup are shown in Figure 5.3. The calculated and experimental weighting functions have different shapes. However, the real effect of the weighting function on the resonance parameters cannot be achieved by a simple analysis of the differences in their form [69]. It strongly depends on the hardness of the γ-rays spectrum emitted by the compound nucleus.

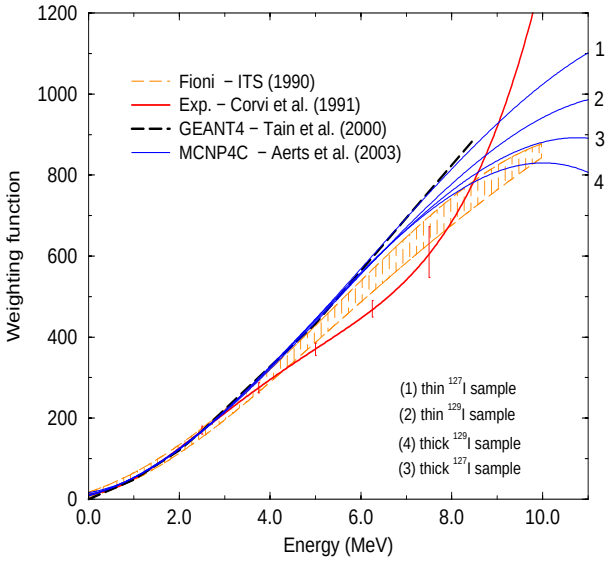

Figure 5.3: Experimental and calculated weighting functions available for our capture setup. The experimental weighting function from Corvi et al. [83] is currently in use at the IRMM.

The limitation on the validity of the experimental weighting function from Corvi et al. currently in use at the IRMM was studied over a considerable number of samples [69]. It follows that only samples not exceeding the thickness equivalent to 1 mm metallic iron (1 g/cm^2) can be used without introducing systematic error. Indeed, the experimental weighting function cannot deal with the degraded γ-ray and electron spectra from a thick sample. This problem was investigated in the case of the thick ^{127}I sample (4.1 mm) over several resonances up to 2 keV. For this exercise, weighted an unweighted capture yield have been built. The weighted area and the unweighted area of the resonances are then given by:

$$\begin{cases} A^w &= \int \sum_I N_\gamma(I,t) W(I) \mathrm{d}t \\ A &= \int \sum_I N_\gamma(I,t) \mathrm{d}t \end{cases} \tag{5.5}$$

The distribution of the A^w/A ratio obtained over a large number of resonances below 2 keV is shown in Figure 5.4. The mean value of the distribution can be interpreted as a mean weight ($\overline{W}(I) \simeq 56.5$) applied on our ^{127}I capture γ-rays spectrum. An estimate of the weighted and unweighted capture area ($A_\gamma \propto g\Gamma_n\Gamma_\gamma/\Gamma_{tot}$) for each resonance under investigation has been also extracted with the shape analysis program REFIT (see Chapter 6). The distribution of the ratio A^w_γ/A_γ is shown in Figure 5.5. The assymetry in the distribution is mainly due to the small s- and p-wave resonances. The mean value of the A^w_γ/A_γ distribution is about 1.013. These results suggest that the hardness of the γ-rays emitted by the compound nucleus (^{128}I) does not vary noticeably within the resonances.

A similar study has been conducted to investigate the effect of the weighting function over the unresolved energy range from 20 keV to 80 keV. Figure 5.6 shows the distributions of the

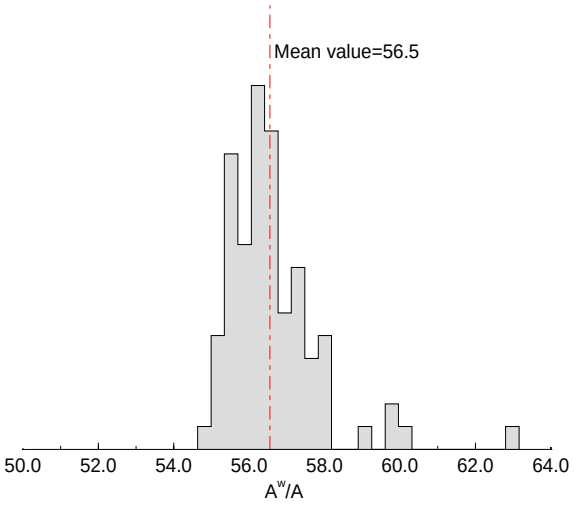

Figure 5.4: Distribution of the weighted and unweighted area ratio A^w/A (thick ^{127}I sample

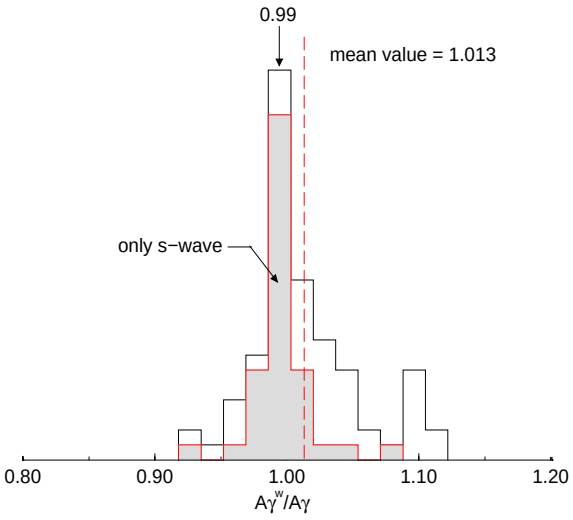

Figure 5.5: Distribution of the weighted and unweighted capture area A^w_γ/A_γ (thick ^{127}I sample).

ratio of the capture yield ($Y(E)/Y_{UW}(E)$) obtained after and before weighting in the cases of the thick ^{129}I and ^{127}I samples. The distribution related to the natural iodine is accurately described by a Gaussian with a mean value of 56.2 and a standard deviation of 0.8. The larger standard deviation as well as the asymmetry of the distribution related to the ^{129}I data suggest that such capture measurements must not be included in our analysis. Thick ^{129}I capture sample will be used only to derive the capture area of small resonances.

The mean value of the distribution related to ^{127}I is in excellent agreement with the mean weight ($\overline{W}(I)$) deduced from the resolved resonance range. Therefore, we may suppose negligible the variations of the γ-ray spectra over the neutron energy range under investigation. It follows, the final capture cross section will be not significantly affected by the choice of the weighting function.

5.3 Dead time correction

In a system with a short dead time, the relationship between the number of real events $N_{true}(t)$ and the number of counted pulses $N(t)$ is:

$$N_{true}(t) \;=\; a(t)\; N(t) \tag{5.6}$$

in which the $a(t)$ correction factor is expressed by:

$$a(t) = \frac{1}{1-\beta_o(t)} \qquad\qquad \beta_o(t) = \frac{1}{T_o}\sum_{k=1}^{n}\int_{t-\tau_k}^{t} N_{\tau_k}(t')\mathrm{d}t' \tag{5.7}$$

where τ_k (k=1...n) are the dead time per event, T_o is the number of cycles each producing a dead time and t is the time-of-flight. Count rate $N_{\tau_k}(t')$ is the total number of counts that are contributed to the dead time (τ_k). According to Monte-Carlo calculations carried out at Harwell, this algorithm underestimates the real count rate by approximately half the square of the correction [97]. For a 10% dead time correction, the true count rate is underestimated by at least 0.5%.

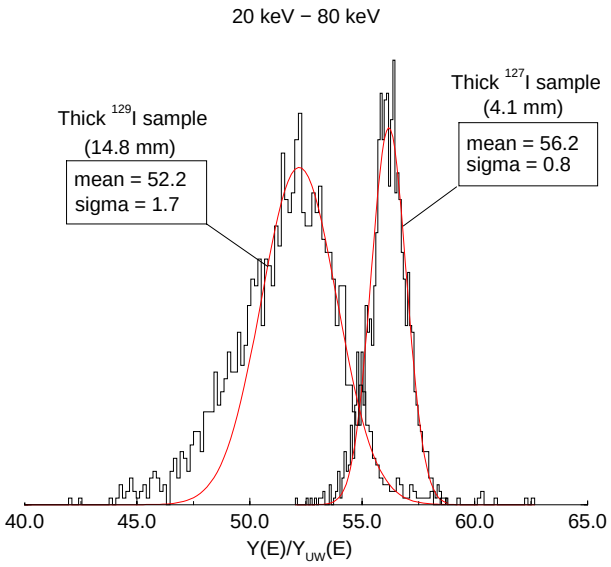

Figure 5.6: Distributions of the ratio of the capture yield obtained after ($Y(E)$) and before ($Y_{UW}(E)$) weighting in the case of thick ^{127}I and ^{129}I samples in the unresolved energy range.

5.3.1 Capture measurements

Three detectors and a single time coder are involved in capture measurements. Detector pulses are converted to digital values by Analog to Digital Converters (ADC). The output of all ADCs are then combined to a single stream of data words via the Transputer Based Multiplexer (TBM) [88]. The conversion time to be taken into account for dead time estimation is that of the slowest digitizer involved in the event. Thus, the dead time can differ from one event to another, depending on which digitizers are participating. In our case, three independent dead times are considered: (1) the events which involve the time coder alone induce a dead time of about 4.9 ± 0.1 μs, (2) the capture events which involve at least one ADC produce a dead time of about 6.84 ± 0.14 μs, and (3) the flux events introduce a dead time of about 7.8 ± 0.2 μs. In the first case the dead time is shorter since the conversion time of the time coder is shorter than the ADC's.

The TBM used in coincidence mode produces a large dead time. It acts as an event builder determining which inputs come in coincidence. The multiparameter acquisition system is busy (dead) from the time a t_n reaches the time coder to the end of the clear signal. During this period, the system is unable to accept any other event. After the end of the coincidence, the system records all the ADCs which have started a conversion. When all recorded ADCs have finished converting (4 μs), their data are stored with zero for the ADCs which are not participating in the event (0.3 μs). After the data have been written, all the digitizers are cleared (0.4 μs) and the system is ready to accept the next event. The maximum dead time per events depends on the length of the coincidence window.

Figure 5.7 shows the total dead time correction ($a(t)$) in the case of the thick ^{127}I sample. The flux events contribution can be discarded because of the low ionisation chamber count rate. The dead time produced by the events which involve the time coder alone is also negligible as this kind of events are minimised by a suitable electronic setup.

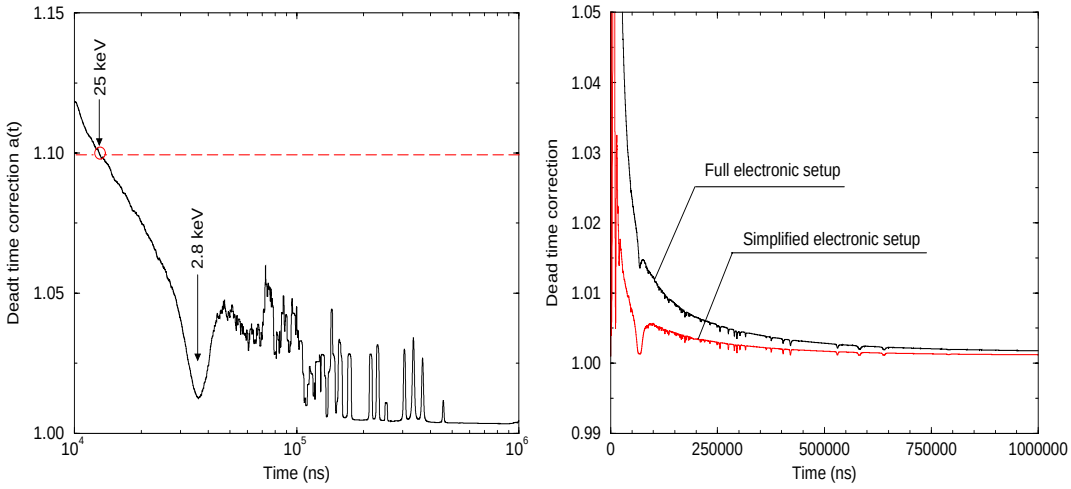

Figure 5.7: Dead time correction in capture and transmission measurements for data recorded with the thick ^{127}I sample. Two transmission measurements of the same sample were performed. The *Full electronic setup* consists of three ADCs, whereas the *simplified electronic setup* is based on one single ADC.

5.3.2 Transmission measurements

The dead time correction is the first operation to be applied in the transmission data reduction procedure. The full electronic setup consists of three ADCs and one time coder. A Modular MultiParameter Multiplexer (MMPM) [87] processes the information provided by each digitizer to build an event corresponding to the Routing Bit information. The MMPM is a recent version of the TBM. In transmission experiments, the MMPM operates in free mode: each ADC works independently from the others. When one ADC has finished a conversion, its data is stored together with a signature. A fixed 1.4 μs dead time per event is applied and continuously monitored by the acquisition system.

Figure 5.7 shows examples of dead time corrections ($a(t)$) for the thick ^{129}I transmission measurements. The correction due to the full electronic setup was too high in the unresolved resonance region. Additional transmission measurements were performed with a simplified electronic setup based on one single ADC without Routing Bits. The $a(t)$ correction decreases below 5% over the whole time range under investigation.

5.4 Time dependent background

The origin and the time dependence of the background is not well understood. A fraction of that background is produced by neutrons scattered in the target hall, in the tube guide and in the vicinity of the detector. Simple functions of time were used in the present data reduction to deduce the time dependent background. According to the results given in References [82, 98], the time dependence of the background involves structures connected to the incident neutron flux. Structured and smooth background are discussed in Appendix A.

5.4.1 Boron chamber

The time dependence of the background in the neutron flux spectrum given by the boron chamber is commonly estimated with the black resonance technique. This method consists of placing a

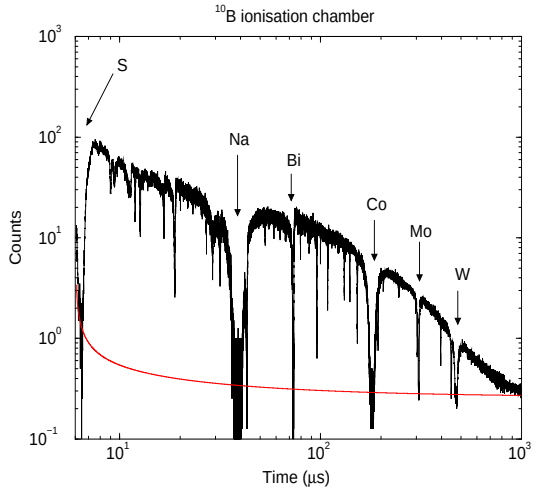

Figure 5.8: Neutron flux spectrum and its time dependent background ($\alpha + bt^c$).

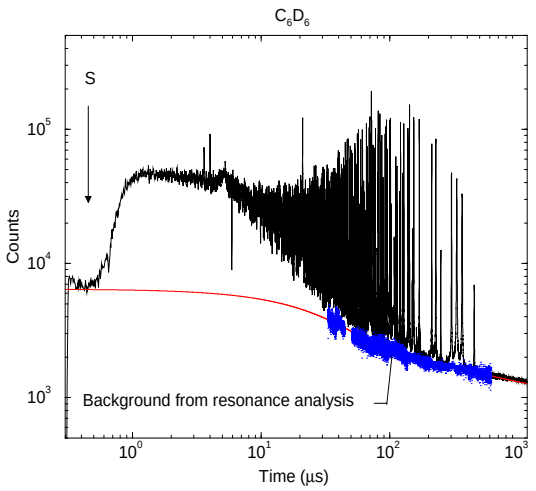

Figure 5.9: γ-ray spectrum and its time dependent background (Equation 5.12).

sufficiently thick resonance filter in the neutron beam, so that at least one of the resonances has "zero" transmission over several channels at the peak position. Interpolating between several black resonances over the entire energy range gives an approximation for the time dependent background. Black filters used in capture measurements are given in Table 4.2. In such approach it is convenient to define the background as a function of the incident neutron flux. According to the flux behaviour expressed in Equation 4.14, the background for the flux measurement over the whole time range was approximated by a power function including a constant term (Figure 5.8):

$$B_F(t) = \alpha + b\ t^c \tag{5.8}$$

5.4.2 C_6D_6 detector

In the resolved resonance region, it is recommended to derive the shape of the background together with the resonance parameters. For this purpose the capture yield becomes:

$$Y(t) = N_Y \frac{a(t)N_\gamma(t)}{a(t)N_F(t) - B_F(t)} \sigma_{n,\alpha}^{^{10}B}(t) - B_{Fit}(t) \tag{5.9}$$

in which B_{Fit} stands for the background obtained from the resonance analysis. Then, the background $B_\gamma(t)$ becomes a fraction of the incident neutron flux:

$$B_\gamma(t) = \frac{B_{Fit}(t)}{N_Y\ \sigma_{n,\alpha}^{^{10}B}(t)}\ (a(t)N_F(t) - B_F(t)) \tag{5.10}$$

In order to greatly simplify the analysis, the shape of the background is assumed to be linear in energy over small energy ranges. The expression of B_{Fit} as a function in time is:

$$B_{Fit}(t)\ =\ A\ +\ \frac{B}{t^2} \tag{5.11}$$

In the unresolved resonance range, the background can be measured by replacing the iodine sample with a sample with similar scattering properties and with negligible capture yield [99]. However, the complex composition of the iodine samples rules out this technique. Therefore, the time dependent background is interpolated between the information derived from the analysis of the resolved range and the bottom of the sulfur black resonance at 102 keV. The expected

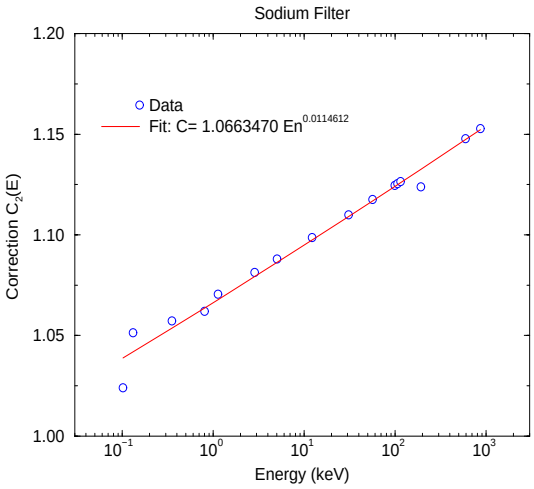

Figure 5.10: Correction $C_2(E)$ given as a function of the neutron energy.

time dependent background over the entire energy range is defined by a constant term plus two exponential decaying functions (Figure 5.9):

$$B_\gamma(t) = \alpha + a\mathrm{e}^{-b\,t} + c\mathrm{e}^{-d\,t} \tag{5.12}$$

5.4.3 Li-glass detector

The technique used to obtain the time dependent background is based on the black resonance method. However a closer inspection of the minima of the resonances shows that this method requires some improvement [70, 98].

In the present data reduction, the shape of the background is assumed to be a smooth function:

$$B(t) \;=\; \alpha \;+\; b\,t^c \tag{5.13}$$

At a 800 Hz repetition rate, α, b and c are obtained from measurements taken with all black filters (W, Ge, Co, Bi, Na, S). The flux attenuation by the filters is taken into account in order to deduce a correct background function for transmission data obtained with a sodium filter ($B_2(t)$) and without black filters ($B_3(t)$):

$$B_2(t) \;=\; \kappa_2\,\frac{B(t)}{C_2(t)} \qquad \text{and} \qquad B_3(t) \;=\; \kappa_3\,\frac{B(t)}{C_3(t)} \tag{5.14}$$

The κ_2 and κ_3 normalisation factors are respectively deduced from the bottom of the black resonance of the sodium filter at 2.8 keV, and from any black resonances of the body under investigation. We cannot found a reliable background $B_3(t)$ in the cases of transmission spectra without black resonances. $C_i(t)$ corrections have been obtained by A.Brusegan from accurate transmission measurements dedicated to background applications (Figure 5.10). He expressed the correction as a function of time or equivalently in neutron energy:

$$C_i(t) \;=\; b'\,t^{c'} \qquad C_i(E) \;=\; b''\,E^{c''} \tag{5.15}$$

Time dependent backgrounds $B(t)$, $B_2(t)$ and $B_3(t)$ are shown in Figure 5.11.

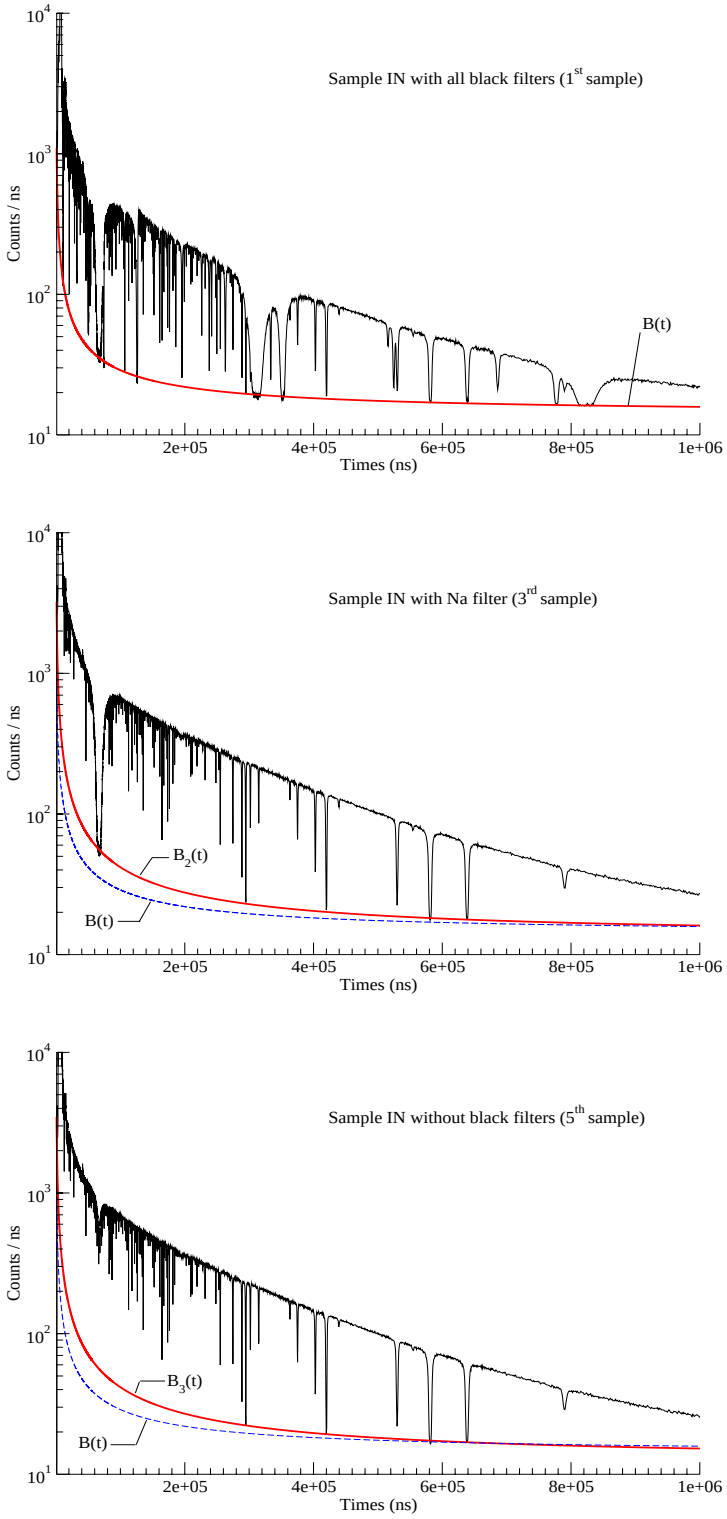

Figure 5.11: Examples of the time dependent background $B(t)$, $B_2(t)$, and $B_3(t)$ (thick PbI_2 sample containing natural iodine).

5.5 Normalisation technique

5.5.1 Capture yield calibration

The expression of the capture yield given in Equation 5.2 can be written as follows:

$$Y(E) = N_Y \frac{a(t)N_\gamma^w(E) - B_\gamma(E)}{a(t)N_F(E) - B_F(E)} \sigma_{n,\alpha}^{^{10}B}(E) \tag{5.16}$$

$$N_Y = \frac{\kappa \; n_{^{10}B}}{k \; E^*} \tag{5.17}$$

The calibration of the capture yield consists in determining κ and k as related to the boron chamber and the capture detector. Intercalibration of the detectors is achieved by using a saturated resonance of a standard element [100], or saturated resonances of the nucleus under investigation.

Here, the $E_o = 4.9$ eV resonance of the ^{197}Au(n,γ) reaction is a particularly useful resonance (Figure 5.12). At the peak capture cross section, the N_o factor may be defined as:

$$N_o = \frac{\kappa \; n_{^{10}B}}{k \; E_o^*} \tag{5.18}$$

Folding together Equations 5.17 and 5.18, the normalisation factor of the iodine capture yield becomes:

$$N_Y \; = \; N_o \frac{E_o^*}{E^*} \tag{5.19}$$

Accurate N_o value may be deduced from the analysis of measurements performed with a thin gold foil (0.01 mm). The first resonance has a much larger radiation width than the neutron width, and a large peak cross section (27×10^3 b). Almost all incident neutrons are absorbed over an energy range near E_o. The transmission and the capture yield tend respectively to zero and unity:

$$0.97 \; < \; Y(E_o) \; < \; 1.0 \tag{5.20}$$

The saturated resonance technique presents the advantage of being nearly independent from the resonance parameters. However, the intercalibration of the detectors with the gold resonance (Equation 5.19) assumes as correct the weighting function and unchanged all experimental conditions during the measurements. In order to avoid the possibility of large systematic errors, It is recommended to normalise the capture yield with the help of saturated iodine resonances. An example of fits performed with REFIT over three resonances at 31 eV, 37 eV and 45 eV is shown in Figure 5.13. This method cannot be used without saturated resonances in the capture γ-rays spectra. Therefore, for thin capture samples, the normalisation factor is deduced from the simultaneous analysis of transmission and capture data. The best fitted values are averaged over several resonances. Results are given in Table 5.2 and compared with those obtained from gold measurements.

5.5.2 Transmission calibration

The transmission is written as the ratio of the time-integrated incident neutron during the *in* and *out* measurement (Equation 5.1). The constant N_T is the normalisation factor that relates the time-integrated neutron flux for the *in* and *out* measurements. The count rate N_{in} and N_{out} are normalised to a constant total neutron flux which should not depends on the neutron energy. For the determination of N_T, the neutron flux is monitored by four BF_3 tubes (CM_1, CM_2, CM_3,

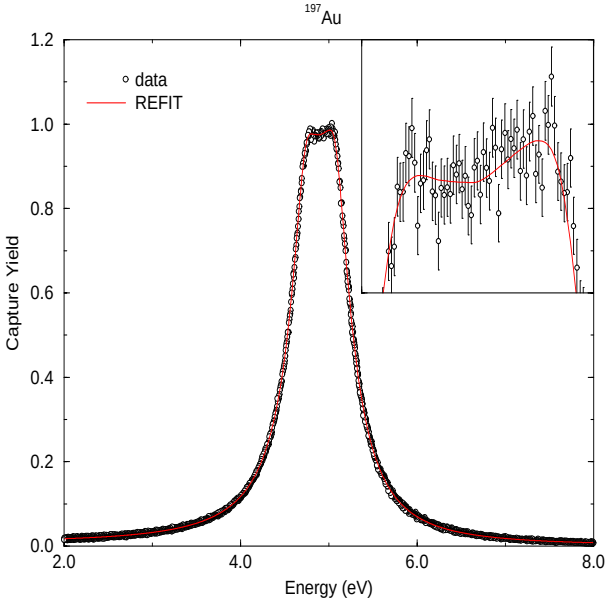

Figure 5.12: Saturated resonance of the ^{197}Au(n,γ) reaction. Theoretical curve was obtained with REFIT using resonance parameters recommended in the JEFF3 data base.

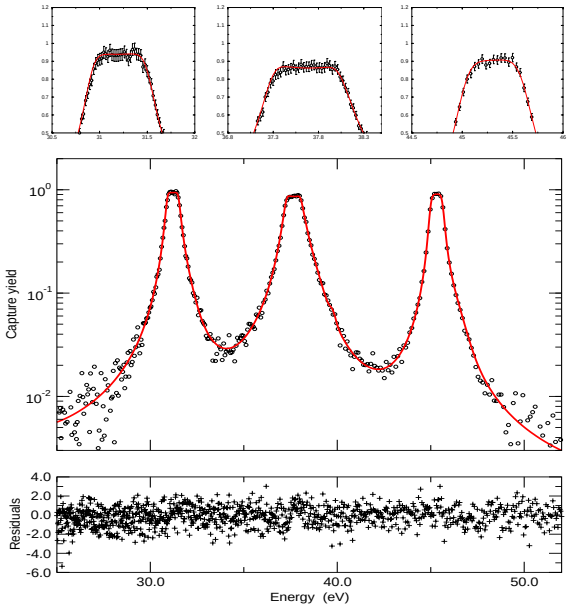

Figure 5.13: 31.2 eV, 37.6 eV and 45.3 eV saturated resonances of the ^{127}I(n,γ) reaction

Table 5.2: Calibration factors deduced from capture measurements carried out at 100 Hz and 800 Hz repetition rate.

Experiment	Repetition rate	Normalisation N
Gold	100 Hz	$0.547 \pm 0.001^*$
Gold	800 Hz	$0.566 \pm 0.002^*$
thick ^{127}I sample	800 Hz	0.578 ± 0.018
thin ^{127}I sample	800 Hz	0.575 ± 0.021
thin ^{127}I sample	100 Hz	0.573 ± 0.025
thin ^{129}I sample	800 Hz	0.527 ± 0.017

$*$ statistical uncertainty from REFIT.

and CM_{south}) placed in the target hall. The Central Monitors CM count all detected neutrons without distinction of the energy. Each of them detects a fraction of the neutrons produced in the uranium target, and gives an estimate of the normalisation factor:

$$\begin{aligned} \frac{1}{N_1} &= \frac{1}{n}\sum_{i=1}^{n}\frac{M_{1,i}^{in}}{M_{1,i}^{out}} \\ \frac{1}{N_2} &= \frac{1}{n}\sum_{i=1}^{n}\frac{M_{2,i}^{in}}{M_{2,i}^{out}} \\ \frac{1}{N_3} &= \frac{1}{n}\sum_{i=1}^{n}\frac{M_{3,i}^{in}}{M_{3,i}^{out}} \\ \frac{1}{N_{south}} &= \frac{1}{n}\sum_{i=1}^{n}\frac{M_{south,i}^{in}}{M_{south,i}^{out}} \end{aligned} \tag{5.21}$$

Then, the normalisation factor N_T is the average value defined as:

$$\frac{1}{N_T} = \frac{1}{4}\left(\frac{1}{N_1} + \frac{1}{N_2} + \frac{1}{N_3} + \frac{1}{N_{south}}\right) \tag{5.22}$$

Examples of the distributions of the M_j^{in}/M_j^{out} ratio are shown in Figure 5.14. The normalisation N_1, N_2, N_3 and N_{south} are consistent with the averaged value N_T, being equal to 1.163. The uncertainty is taken from the standard deviation of the distribution. The measure of the normalisation factor, provided by the Central Monitors, is roughly 0.5% precise.

5.6 Uncertainty propagation in AGS

Assigning uncertainties to TOF experimental data is a recurrent puzzle. It became apparent when uncertainty information (*covariance file*) had to be added to Evaluated Nuclear Data File in response to requests from users involved in fission and fusion reactor development programs. The need for reliable nuclear parameters and their quantitative uncertainties require the knowledge of the experimental covariance matrices, as the weights the evaluator attributes to the data obtained from different sources depend on the uncertainties. Most frequently, several data sets are available without adequate information on uncertainties and almost nothing at all on correlations. The problem of the evaluator is then to use empirical or semi-empirical methods in order to deduce experimental covariance matrices either from information given by the experimentalists or by comparison with results coming from all available experiments [101]. Many papers offer

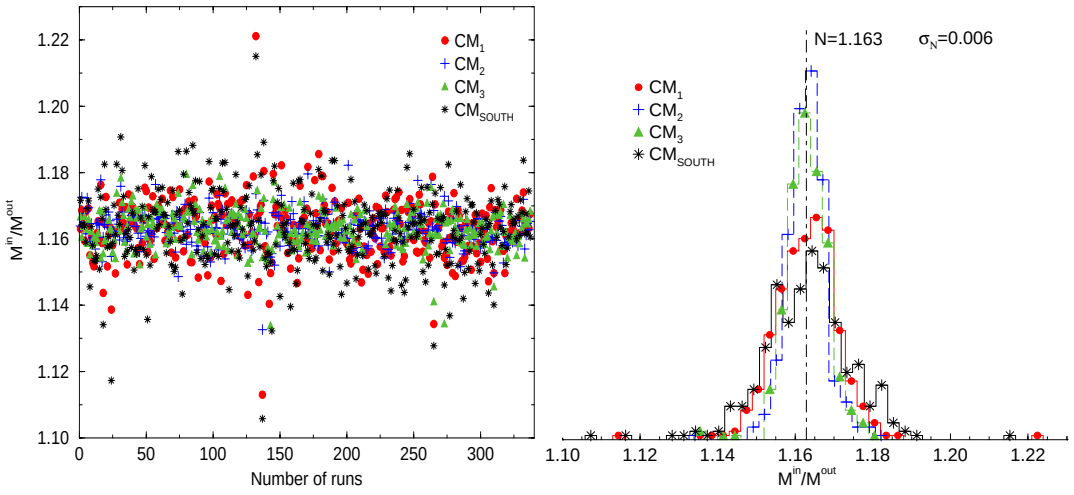

Figure 5.14: Example of normalisation (N_T) provided by four Central Monitors (CM_1, CM_2, CM_3, CM_{south}).

some perspective and address various issues related to the application of experimental covariance matrices for nuclear data [102, 103].

On the basis of these general remarks, a particular interest in reliable experimental covariance matrices has arisen since the rapid developments in the implementation of covariance matrix methodologies in the SAMMY code. In SAMMY, the classical approach makes it possible to include in the calculation an explicit experimental covariance matrix. Its determination is achieved in the AGS system through the conventional law of error propagation. A detailed description of the uncertainty propagation in AGS is given elsewhere [71, 104].

5.6.1 Covariance matrix

The original counting histograms (N_{in}, N_{out}, N_γ and N_F) are supposed to have independent uncertainties. The covariance matrix D_o of the histogram is a diagonal matrix. All the off-diagonal elements are zero. D_o may be defined as follows:

$$D_o = diag\left(\sigma_{o_1}^2 \cdots \sigma_{o_m}^2\right) \tag{5.23}$$

in which $\sigma_{o_i}^2$ are the variance of the channel content. The counting uncertainty is supposed to be due to a Poisson distribution. In that case the variance is equal to the channel content. Simple operations on the original counting histograms correlates all data points , making off-diagonal elements of the covariance matrix non-zero. In the AGS system, the experimental covariance matrix V for a spectrum is not stored as an $m \times m$ table. In practice, there are both independent and correlated errors, therefore, the matrix may be split into two parts:

$$V \;=\; G\,W\,G^t \;+\; D \tag{5.24}$$

The matrix G is the sensitivity matrix. The elements of G are the partial derivatives with respect to the parameters involved in the data reduction process. Matrix W contains information on the parameter uncertainties. Matrix D is a diagonal matrix whose elements σ_i^2 (uncorrelated uncertainties) are deduced from the uncertainty on the counting following the rules of elementary calculus.

A covariance matrix must be positive definite[1], with equal dimensions and rank, and positive eigenvalues. Physically, this means that the information are consistent and not redundant. According to this principle, if matrix W is symmetric and positive definite there is one lower triangular matrix L so that:

$$W \;=\; L\,L^t \tag{5.25}$$

This decomposition is known as the Cholesky factorisation. Matrix W is positive definite in the particular case of independent parameters. Equation 5.24 becomes:

$$V \;=\; S\,S^t \;+\; D \qquad \text{with} \qquad S \;=\; G\,L \tag{5.26}$$

where $S = (\mathrm{s}_1 \cdots \mathrm{s}_k)$ is a matrix composed of the lamination of k vectors s_i of length n, each vector consisting of elements s_{ij}. The number k depends on the number of operations applied to the originally uncorrelated spectrum. In capture and transmission measurements, k is often less than 10. After the data reduction procedure, the correlated uncertainties are the square root of the diagonal elements of the matrix V:

$$V_{jj} = \sum_{i=1}^{k} s_{ij}^2 \;+\; \sigma_i^2 \tag{5.27}$$

The off-elements V_{ij} of the matrix V are the covariance between the channel i and j, which measures the degree of sensibility of their content to the same sources of uncertainties. The correlation coefficient between two channels is defined as follows:

$$\rho_{ij} = \frac{V_{ij}}{\sqrt{V_{ii}V_{jj}}} \tag{5.28}$$

In practise, instead of storing the $m \times m$ elements of the covariance matrix V, only the diagonal of D has to be stored as a vector of length m together with the k vectors of the matrix S. According to the formalism implemented in AGS, the dead time correction, the background subtraction and the normalisation involve correlations between channels.

5.6.2 Weighting function

In capture measurements, the starting raw data provided by the γ-rays detectors is stored as a $TOF \times amplitude$ matrix. The weighted spectrum is obtained as follows:

$$\begin{pmatrix} N^w_{\gamma_1} \\ \vdots \\ N^w_{\gamma_m} \end{pmatrix} = \begin{pmatrix} N_{\gamma_{1,1}} & \cdots & N_{\gamma_{1,p}} \\ \vdots & \ddots & \vdots \\ N_{\gamma_{m,1}} & \cdots & N_{\gamma_{m,p}} \end{pmatrix} \begin{pmatrix} w_1 \\ \vdots \\ w_p \end{pmatrix} \tag{5.29}$$

where the elements w_i are the weighting factor deduced from Equation 4.25. The associated covariance matrix $V_{N^w_\gamma}$ is reduced to a diagonal matrix with the following elements:

$$D_{N^w_\gamma} = diag\left(\sum_{i=1}^{p} w_i^2\; N_{\gamma_{1,i}} \cdots \sum_{i=1}^{p} w_i^2\; N_{\gamma_{m,i}}\right) \tag{5.30}$$

[1] A square matrix V is *positive definite* if $X^t\;V\;X > 0$ for all non-zero column vector X

5.6.3 Dead time correction

The dead time correction can be expressed as:

$$\begin{pmatrix} N_{true_1} \\ \vdots \\ N_{true_m} \end{pmatrix} = \begin{pmatrix} a_1 & & 0 \\ & \ddots & \\ 0 & & a_m \end{pmatrix} \begin{pmatrix} N_1 \\ \vdots \\ N_m \end{pmatrix} \tag{5.31}$$

The correction a must be applied to a counting histogram N, having a diagonal covariance matrix D_N, before further transformation. The vector a has elements $a_i = (1 - \beta_{o_i})^{-1}$ (Equation 5.7) and a diagonal covariance matrix C_a defined as:

$$C_a = diag\left(a_1^4 \frac{\beta_{o_1}}{T_o} \cdots a_m^4 \frac{\beta_{o_m}}{T_o}\right) \tag{5.32}$$

The uncertainty propagation rules give the following covariance matrix $V_{N_{true}}$:

$$V_{N_{true}} = \left(\frac{\delta N_{true}}{\delta a}\right) C_a \left(\frac{\delta N_{true}}{\delta a}\right)^t + \left(\frac{\delta N_{true}}{\delta N}\right) D_N \left(\frac{\delta N_{true}}{\delta N}\right)^t \tag{5.33}$$

The matrix C_a is positive definite. According to the Cholesky factorisation, the matrix C_a may be written as $C_a = L_a\, L_a^t$. The matrix L_a is a lower triangular matrix. The Equation 5.33 becomes:

$$V_{N_{true}} = \underbrace{\left(\frac{\delta N_{true}}{\delta a}\right) L_a}_{S_{N_{true}}} \underbrace{L_a^t \left(\frac{\delta N_{true}}{\delta a}\right)^t}_{S_{N_{true}}^t} + \underbrace{\left(\frac{\delta N_{true}}{\delta N}\right) D_N \left(\frac{\delta N_{true}}{\delta N}\right)^t}_{D_{N_{true}}} \tag{5.34}$$

One part of the resulting covariance matrix is stored in the diagonal:

$$D_{N_{true}} = diag\left(a_1^2\, N_1 \cdots a_m^2\, N_m\right) \tag{5.35}$$

and the contribution due to the uncertainty of a_i is stored in the correlated part:

$$S_{N_{true}} = \left(N_1\, a_1^2 \sqrt{\frac{\beta_{o_1}}{T_o}} \cdots N_m\, a_m^2 \sqrt{\frac{\beta_{o_m}}{T_o}}\right)^t \tag{5.36}$$

5.6.4 Background correction

The background functions B_F, B_{in} and B_{out} (Equations 5.1 and 5.2) result from a non-linear fit of the data. The function used in our data reduction is a power function plus a constant term:

$$\left.\begin{matrix} B_F(t) \\ B_{in}(t) \\ B_{out}(t) \end{matrix}\right\} = \alpha + b\, t^c \tag{5.37}$$

The outcome of the fit is a set of parameters with covariance matrix $C_B = L_B L_B^t$. The AGS package contains routines for fitting non-linear models through user specified parts of the

spectrum. From the fitted parameters a spectrum B is constructed by applying the non-linear function over the time range under investigation. All elements of the constructed histogram are then fully correlated. The resulting covariance matrix V_B is stored entirely as a matrix $S_B S_B^t$. The matrix S_B is defined as:

$$\begin{aligned} S_B &= G_B\, L_B \\ &= \begin{pmatrix} \frac{\delta B_1}{\delta\alpha} & \frac{\delta B_1}{\delta b} & \frac{\delta B_1}{\delta c} \\ \vdots & \vdots & \vdots \\ \frac{\delta B_m}{\delta\alpha} & \frac{\delta B_m}{\delta b} & \frac{\delta B_m}{\delta c} \end{pmatrix} \begin{pmatrix} \sigma_\alpha & 0 & 0 \\ \sigma_{\alpha,b} & \sigma_b & 0 \\ \sigma_{\alpha,c} & \sigma_{b,c} & \sigma_c \end{pmatrix} \\ &= \begin{pmatrix} \frac{\delta B_1}{\delta\alpha}\sigma_\alpha + \frac{\delta B_1}{\sigma b}\sigma_{\alpha,b} + \frac{\delta B_1}{\delta c}\sigma_{\alpha,c} & \frac{\delta B_1}{\delta b}\sigma_b + \frac{\delta B_1}{\delta c}\sigma_{b,c} & \frac{\delta B_1}{\delta c}\sigma_c \\ \vdots & \vdots & \vdots \\ \frac{\delta B_m}{\delta\alpha}\sigma_\alpha + \frac{\delta B_m}{\delta b}\sigma_{\alpha,b} + \frac{\delta B_m}{\delta c}\sigma_{\alpha,c} & \frac{\delta B_m}{\delta b}\sigma_b + \frac{\delta B_m}{\delta c}\sigma_{b,c} & \frac{\delta B_m}{\delta c}\sigma_c \end{pmatrix} \end{aligned} \tag{5.38}$$

Matrix S_B is composed of the lamination of three vectors connected to the uncertainties of α, b and c.

5.6.5 Final covariance matrix

The final covariance matrix connected to a transmission (T) or a capture yield (Y) is $V = SS^t + D$ in which the matrix S may be defined as:

$$\begin{aligned} S &\equiv \left(\left(\tfrac{\delta Y}{\delta a_F}\right) L_{a_F} \;\; \left(\tfrac{\delta Y}{\delta a_E}\right) L_{a_E} \;\; \left(\tfrac{\delta Y}{\delta a_W}\right) L_{a_W} \;\; \left(\tfrac{\delta Y}{\delta B_F}\right) L_{B_F} \;\; \left(\tfrac{\delta Y}{\delta N}\right) L_N\right) \qquad \text{(Capture)} \\ S &\equiv \left(\left(\tfrac{\delta T}{\delta a_{in}}\right) L_{a_{in}} \;\; \left(\tfrac{\delta T}{\delta a_{out}}\right) L_{a_{out}} \;\; \left(\tfrac{\delta T}{\delta B_{in}}\right) L_{B_{in}} \;\; \left(\tfrac{\delta T}{\delta B_{out}}\right) L_{B_{out}} \;\; \left(\tfrac{\delta T}{\delta N}\right) L_N\right) \qquad \text{(Transmission)} \end{aligned} \tag{5.39}$$

in which the index F labels the flux spectrum, E and W represents the capture γ-rays spectra measured with the two C_6D_6 detectors, and *in* and *out* refer to the transmission spectra. The first vectors are connected to the dead time correction (a), the following vectors are due to the background subtraction (B) and the final vector is related to the normalisation factor (N). Examples of correlation matrices calculated with AGS are given in Tables 5.3 and 5.4. The matrices are given around the 72.1 eV resonance of the ^{129}I. The correlations between channels are mainly due to the normalisation and its uncertainty. The rules of elementary calculus used in the AGS formalism make the final covariance matrix questionable. The models themselves introduce a certain bias as they impose some simplifying assumptions (experimental weighting function, smooth background and dead time algorithm) [105]. The assessment of correct correlation coefficients needs the addition of larger uncertainties related to the validity of the models. A direct method may be applied to quantify such information [82]. For example, the direct comparison of two capture yields $Y_1(E)$ and $Y_2(E)$ obtained with two different weighting functions (wf), backgrounds (bkg) or dead time models (dt) may give reliable uncertainties. A crude estimate of the sensitivity may be defined as follows:

$$\begin{aligned}
\left(\frac{\delta Y_i}{\delta wf_i}\right) L_{wf_i} &\equiv \delta Y_{wf_i} \equiv Y_{1_{wf,i}} - Y_{2_{wf,i}} \\
\left(\frac{\delta Y_i}{\delta bkg_i}\right) L_{bkf_i} &\equiv \delta Y_{bkg_i} \equiv Y_{1_{bkg,i}} - Y_{2_{bkg,i}} \\
\left(\frac{\delta Y_i}{\delta dt_i}\right) L_{dt_i} &\equiv \delta Y_{dt_i} \equiv Y_{1_{dt,i}} - Y_{2_{dt,i}}
\end{aligned} \tag{5.40}$$

According to the definition of S, additional vector s_{wf}, s_{bkg} or s_{dt} may be implemented as follows:

$$S = (\mathrm{s}_1 \cdots \mathrm{s}_k \ \mathrm{s}_{wf} \ \mathrm{s}_{bkg} \ \mathrm{s}_{dt}) \tag{5.41}$$

with

$$\begin{aligned}
\mathrm{s}_{wf} &= (\delta Y_{wf_i} \ \cdots \ \delta Y_{wf_m})^t \\
\mathrm{s}_{bkg} &= (\delta Y_{bkg_i} \ \cdots \ \delta Y_{bkg_m})^t \\
\mathrm{s}_{dt} &= (\delta Y_{dt_i} \ \cdots \ \delta Y_{dt_m})^t
\end{aligned} \tag{5.42}$$

A new option in SAMMY was recently implemented in order to introduce these vectors instead of an explicit very large experimental covariance matrix. This option is numerically more stable, not only because of the problems associated to storing and inverting very large matrices, but also to avoid round-off errors. When the covariance matrices are written into ascii format, many significant digits are needed to avoid artificial singularities or to keep the program from crashing [27]. The use of this option applied to our iodine measurements is available in the SAMMY test case *Tr140*.

| Energy (eV) | Transmission | | |

Energy (eV)	Capture Yield																				
71.46	0.0143 ± 0.0009	100																			
71.50	0.0159 ± 0.0009	20	100																		
71.54	0.0190 ± 0.0011	19	19	100																	
71.58	0.0240 ± 0.0013	18	17	16	100																
71.61	0.0294 ± 0.0015	16	16	15	15	100															
71.65	0.0383 ± 0.0019	14	14	14	14	13	100														
71.69	0.0461 ± 0.0022	13	13	13	13	13	12	100													
71.73	0.0615 ± 0.0029	12	12	12	12	12	11	11	100												
71.76	0.0827 ± 0.0039	11	11	11	11	11	11	11	11	100											
71.80	0.1007 ± 0.0045	10	11	11	11	11	11	11	10	10	100										
71.84	0.1231 ± 0.0054	10	10	10	10	11	11	11	11	11	10	11	100								
71.88	0.1583 ± 0.0070	9	10	10	10	10	10	10	10	10	10	11	100								
71.91	0.1946 ± 0.0086	9	9	9	10	10	10	10	10	10	10	10	10	100							
71.95	0.2255 ± 0.0097	9	9	9	10	10	10	10	10	10	11	11	11	11	100						
71.99	0.2698 ± 0.0117	9	9	9	9	10	10	10	10	10	11	10	10	11	11	100					
72.03	0.3087 ± 0.0135	8	9	9	9	10	10	10	10	10	10	10	10	11	10	100					
72.06	0.3492 ± 0.0154	8	9	9	9	10	10	10	10	10	10	10	10	10	10	10	100				
72.10	0.3878 ± 0.0174	8	8	9	9	9	10	10	10	10	10	10	10	10	10	10	10	100			
72.14	0.3739 ± 0.0162	8	9	9	9	10	10	10	10	10	10	10	11	11	10	10	10	10	100		
72.18	0.3757 ± 0.0161	8	9	9	9	10	10	10	10	10	11	10	11	11	11	10	10	11	100		
72.22	0.3872 ± 0.0171	8	8	9	9	10	10	10	10	10	10	10	10	10	10	10	10	10	10	100	
72.25	0.3759 ± 0.0167	8	8	9	9	10	10	10	10	10	10	10	10	10	10	10	10	10	10	10	100
72.29	0.3390 ± 0.0148	8	9	9	9	10	10	10	10	10	10	10	11	10	10	10	11	11	10	10	100
72.33	0.2780 ± 0.0116	9	9	9	10	10	10	10	10	10	11	11	11	11	11	11	11	11	11	11	100
72.37	0.2493 ± 0.0105	9	9	9	10	10	10	10	10	10	11	11	11	11	11	11	11	11	11	11	100
72.41	0.2282 ± 0.0100	9	9	9	10	10	10	10	10	10	11	10	10	11	11	10	10	10	11	11	100
72.44	0.1865 ± 0.0081	9	9	10	10	10	10	10	10	10	11	10	10	11	11	10	10	10	11	11	100
72.48	0.1502 ± 0.0066	9	10	10	10	10	11	10	10	10	11	10	10	11	10	10	10	10	11	10	100
72.52	0.1203 ± 0.0054	10	10	10	11	11	11	10	10	11	10	10	11	10	10	10	10	10	10	10	100
72.56	0.0935 ± 0.0042	11	11	11	11	11	11	10	11	11	10	11	10	10	11	10	10	10	10	10	100
72.60	0.0704 ± 0.0031	12	12	12	12	11	11	11	11	11	11	10	11	10	10	10	10	10	10	10	100
72.63	0.0540 ± 0.0024	13	13	12	12	12	12	11	11	11	11	10	11	10	10	10	10	10	10	10	100
72.67	0.0459 ± 0.0022	13	13	13	12	12	12	11	11	11	11	10	10	10	10	10	10	10	10	10	100
72.71	0.0350 ± 0.0017	15	15	14	14	13	13	12	12	11	11	11	10	10	10	10	10	10	10	10	100
72.75	0.0270 ± 0.0013	17	16	16	15	14	13	13	12	11	11	11	10	10	10	10	10	9	10	10	100
72.79	0.0225 ± 0.0012	18	17	17	16	15	14	13	12	11	11	11	10	10	10	10	9	9	9	9	100
72.83	0.0202 ± 0.0011	19	18	17	16	15	14	13	12	11	11	10	10	10	9	9	9	9	9	9	100
72.86	0.0187 ± 0.0011	19	19	18	17	15	14	13	12	11	11	10	10	9	9	9	9	9	9	9	100
72.90	0.0160 ± 0.0009	20	20	19	17	16	14	13	12	11	10	10	9	9	9	9	8	8	8	9	100

Table 5.4: Experimental correlation matrix around the 72.1 eV resonance of ^{129}I (thin capture sample).

5.7 Conclusion

A large number of data sets covering the energy range [0.5 eV-150 keV] were obtained, together with their covariance matrices (Table 5.5). Examples of capture yields and transmissions are given in Figures 5.15 and 5.16. The systematic errors involved by the choice of the weighting function, of the dead time algorithm and of the background model are not included in the covariance matrices. Thus, the final errors on the nuclear parameters provided by the shape analysis codes should account for additional uncertainties. According to the derivation proposed in Reference [102], the addition of the statistical and systematic errors in quadrature may get the total error.

On the basis of the sensitivity study conducted in section 5.2, the results extracted from our iodine capture measurements are not significantly affected by the accuracy of the weighting function. Therefore, the additional uncertainties involved by the latter can be neglected in the uncertainty propagation process. Similarly, the bias introduced by the dead time algorithm may be neglected over the Resolved Resonance Range. Only the experimental data in the unresolved energy range should be slightly corrected. A correction below 1% is expected. The background function is a more complicated problem which cannot be solved yet.

Table 5.5: ^{127}I and ^{129}I capture and transmission data obtained at the GELINA facility.

Experiment	Sample	Repetition rate	Filters set-up	Time
^{127}I Transmission	thin PbI_2	800 Hz	B + W + Mo + Co + Bi + Na + S	24 h
		800 Hz	B + Na	27 h
	thick PbI_2	100 Hz	Cd + Co + Na	118 h
		800 Hz	B + W + Mo + Co + Bi + Na + S	42 h
		800 Hz	B + Na	49 h
		800 Hz	B	45 h
	LiI target	100 Hz	Cd + Co + Na	82 h
^{127}I Capture	thin PbI_2	100 Hz	Cd + Co + Na	19 h
		800 Hz	B + Na	37 h
		800 Hz	B + S	37 h
	thick PbI_2	800 Hz	B + Na + S	78 h
^{129}I Transmission	thin PbI_2	100 Hz	Cd + Co + Na	74 h
	thick PbI_2	100 Hz	Cd + Co + Na	43 h
		800 Hz	B + W + Mo + Co + Bi + Na + S	86 h
		800 Hz	B + Na	77 h
		800 Hz	B	70 h
		800 Hz	B + W + Mo + Co + Bi + Na + S	74 h
		800 Hz	B + Na + S	86 h
^{129}I Capture	thin PbI_2	800 Hz	B + Na	79 h
		800 Hz	B + S	79 h
	thick PbI_2	100 Hz	Cd + Co + Bi	41 h
		800 Hz	B + Na	25 h
		800 Hz	B + S	25 h

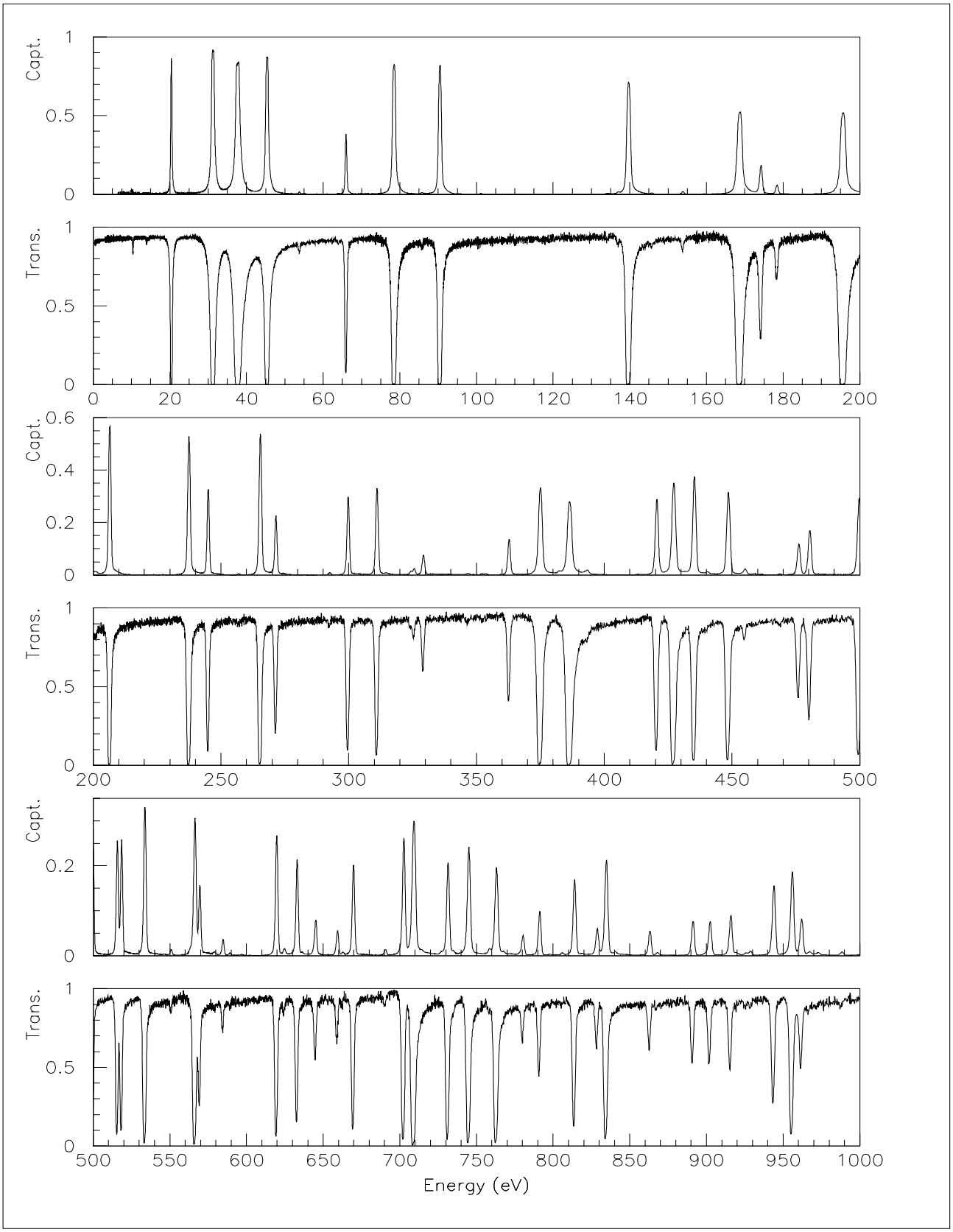

Figure 5.15: Thick ^{127}I capture yield and transmission up to 1 keV.

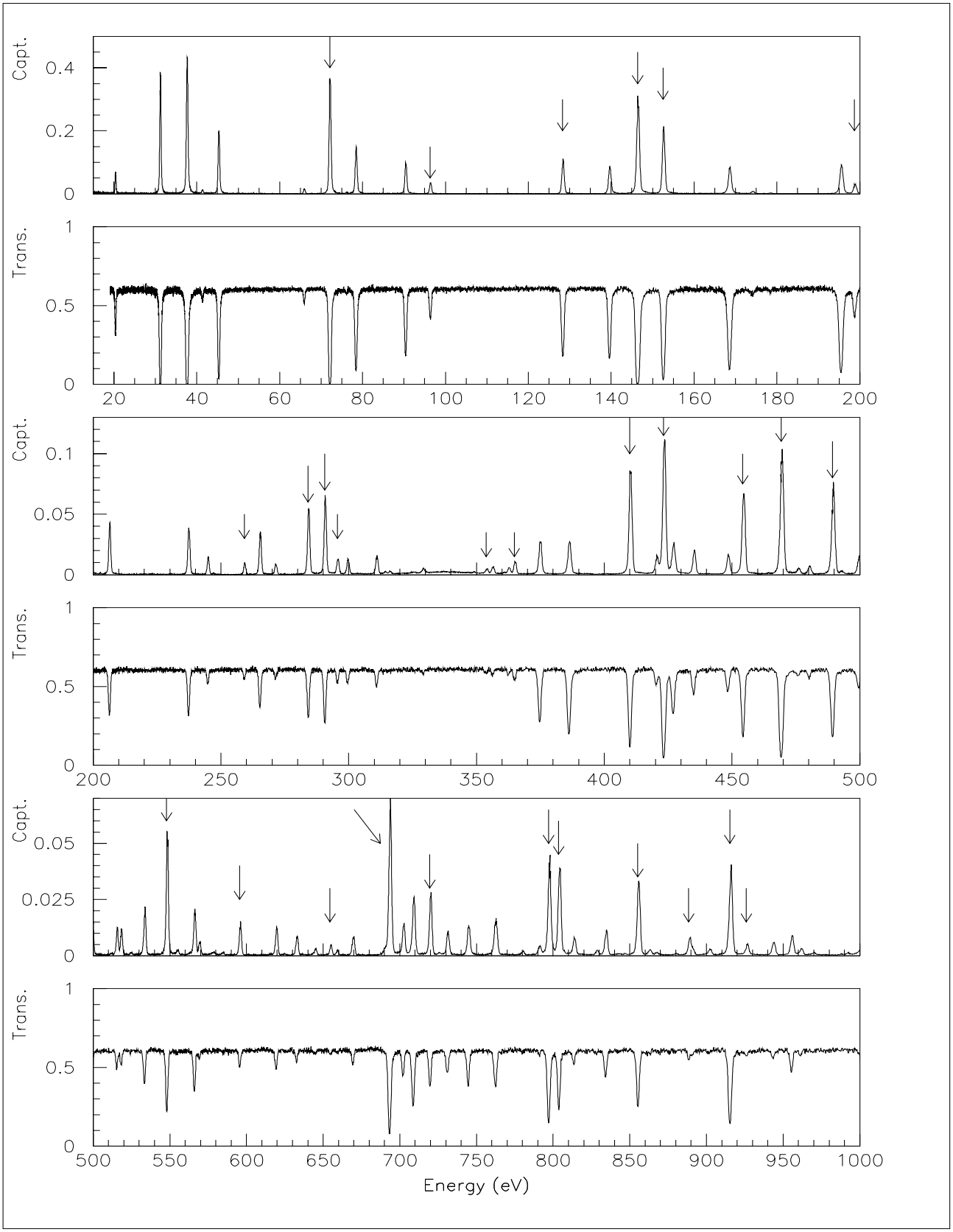

Figure 5.16: Thin ^{129}I capture yield and thick ^{129}I transmission up to 1 keV (the arrows indicate the ^{129}I resonances).

Chapter 6

REFIT-IRMM and SAMMY-M6 shape analysis codes

Shape analysis programs like REFIT [26] and SAMMY [27] adjust nuclear parameters so that the theoretical curve agrees with the observed data within the limit of the uncertainties. In the Resolved Resonance Range, the nuclear parameters are the energies (E_o), the partial widths and the effective radii (R'). Theoretical curves are calculated from the sample thickness (n) and the cross section (σ). The cross sections are generated with the Reich-Moore approximation of the R-Matrix formalism and Doppler broadened using the ideal Free Gas Model with a given effective temperature (T_{eff}) or the Lamb Crystal Lattice Model. Theoretical transmission and yield are folded with the experimental resolution ($R(E)$) which is calculated from analytic models or point-wise distributions provided by Monte-Carlo simulations. The theoretical capture yield includes the effect of the self-shielding and of the multiple scattering ($(1+\alpha(E))$). Theoretical curves are given by:

$$T_R(E) = \int_0^\infty R(E,E')\, T_{th}(E')\, \mathrm{d}E' \tag{6.1}$$

$$Y_R(E) = \int_0^\infty R(E,E')\, Y_{th}(E')\, \mathrm{d}E' \tag{6.2}$$

$$T_{th}(E) = \mathrm{e}^{-\sum_i n_i D(E) \star \sigma_{T,i}(E)} \tag{6.3}$$

$$Y_{th}(E) = (1+\alpha(E))\,(1-T_{th}(E))\,\frac{\sum_i n_i\, D(E)\star\sigma_{\gamma,i}(E)}{\sum_i n_i D(E)\star\sigma_{T,i}(E)} \tag{6.4}$$

in which $(D(E)\star\sigma_{T,i})$ and $(D(E)\star\sigma_{\gamma,i})$ stand for the total and capture Doppler broadened cross sections.

6.1 Least-squares fitting procedure

The values for nuclear parameters and data-related parameters (such as background, normalisation, effective temperature, sample thickness, resolution parameters) can be determined via fits from the experimental data. The REFIT code uses the familiar least-squares method, whereas SAMMY uses the so-called generalised least-squares fitting procedure. The latter relies on Bayes' Theorem. Therefore, SAMMY is able to find the best parameters values and the associated covariance matrix by solving Bayes' Equations. Bayes' Theorem is a statistical method for improving prior knowledge through the acquisition of new information. Suppose that

$X = x_1, ..., x_n$ is the vector of the unknown parameters, and $Y = y_1, ..., y_m$ is the data vector. The posterior conditional probability density function (pdf) that the observation of Y justifies the choice X, is then given by the formula [106]:

$$P(X|Y) \;=\; \frac{P(Y|X)\;P(X)}{\int P(Y|X')\;P(X')\mathrm{d}X'} \tag{6.5}$$

According to the Bayesian approach, the probability for the value of the parameter (X) given the data (Y) is obtained from the pdf for observing the data (Y) given that the parameter (X) is correct times the pdf for the values of the parameter (X). The prior information consists of an initial estimate X_o of X. According to the factorisation property of the conditional probability, Equation 6.5 becomes:

$$P(X|Y, X_o) \;\propto\; P(Y|X, X_o)\;P(X|X_o) \tag{6.6}$$

The prior estimate X_o and its associated covariance matrix M are assumed to imply a Gaussian error distribution [27, 102]:

$$P(X|X_o) = \frac{1}{2\pi^{n/2}}\frac{1}{\sqrt{\det M}}e^{-\frac{1}{2}(X-X_o)^t M^{-1}(X-X_o)} \tag{6.7}$$

where n stands for the number of unknown parameters. Similarly, any given data vector Y with a covariance matrix V implies a Gaussian likelihood function:

$$P(Y|X, X_o) = \frac{1}{2\pi^{m/2}}\frac{1}{\sqrt{\det V}}e^{-\frac{1}{2}(Y-Y_{th})^t V^{-1}(Y-Y_{th})} \tag{6.8}$$

in which $Y_{th} = Y_{th}(X)$ represents the theory, and m stands for the number of data points in Y. Combining Equations 6.7 and 6.8, the posterior pdf becomes :

$$P(X|Y, X_o) \propto e^{-\frac{1}{2}\left((X-X_o)^t M^{-1}(X-X_o)+(Y-Y_{th})^t V^{-1}(Y-Y_{th})\right)} \tag{6.9}$$

A suitable approximation consists of reducing the theory $Y_{th}(X)$ down to a linear function of the parameters (see Reference [27]). According to this assumption, the posterior pdf becomes a normal distribution and may be expressed as:

$$P(X|Y, X_o) \propto e^{-\frac{1}{2}\left(X-\bar{X}\right)^t C^{-1}\left(X-\bar{X}\right)} \tag{6.10}$$

The best estimate of the parameters consists of the mean vector and the covariance of this distribution, which are found iteratively by solving Bayes'Equations[1]. The best fit minimises the exponent of Equation 6.10 (generalised least-squares fit). Within the limit in which the matrix V is diagonal and without prior information on the parameter uncertainties, this approach becomes the familiar least-squares method:

$$\chi^2 = (Y - Y_{th})^t\, V^{-1}\, (Y - Y_{th}) \tag{6.11}$$

Explicitly, the fitting code REFIT minimises the sum of the weighed squares of the residuals R_i for all the data. Equation 6.11 may be written as:

$$\sum_{i=1}^{m} R_i^2 = \sum_{i=1}^{m}\left(\frac{y_i - y_{th,i}}{\sigma_{y_i}}\right)^2 \tag{6.12}$$

Agreement between the results from SAMMY and REFIT is subject to linearity restriction. In the case of data with modest accuracies, local discrepancies higher than 5% are expected.

[1] Derivation of Bayes' Equations from the exponent of Equation 6.10 are given in Reference [27].

6.2 Broadening effect

It is not possible to proceed to a direct comparison of the cross sections generated via the Reich-Moore formalism with the capture and transmission data. To confront the experiment with the theory, the latter must be broadened with the so-called Doppler effect and with the experimental resolution function of the facility. The resolution function is the distribution in time (or in distance) of the neutron flight time. This, together with the Doppler effect, broadens the natural width (Γ_{tot}) and attenuates the amplitude of the nuclear resonances (Figure 6.1a). The observed total width of a resonance (Γ_{obs}) is determined from its natural width (Γ_{tot}), the Doppler width (ΔE_{dop}) and the resolution width (ΔE_{res}). The observed width at half maximum may be estimated from the quadratic sum of these contributions assuming that they are approximately Gaussian in shape and independent:

$$\Gamma_{obs}^2 \simeq \Gamma_{tot}^2 + \Delta E_{res}^2 + \Delta E_{dop}^2 \tag{6.13}$$

Examples of the overall time resolution as a function of energy, and the Doppler contribution are shown in Figure 6.1b. At low energies, the Doppler broadening is the dominating effect. For higher neutron energies the contribution of the resolution effect increases. The relative contribution of the natural width to the overall observed width depends on the isotope under investigation.

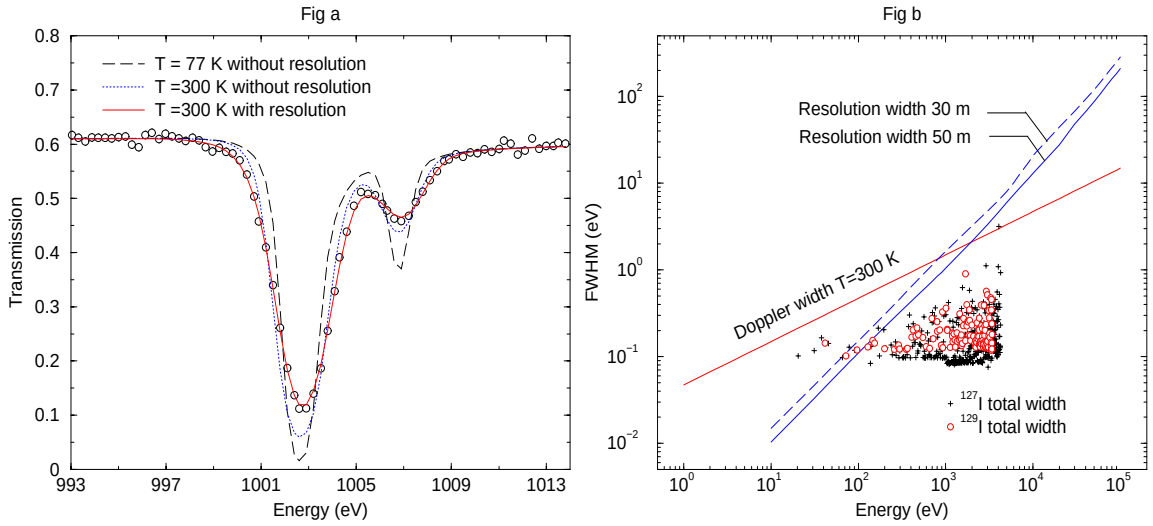

Figure 6.1: (a) Doppler and resolution broadening of the 1002.7 keV and 1006.7 kev resonances respectively of ^{129}I and ^{127}I. (b) Energy dependence of the Full Width at Half Maximum (FWHM) of the Doppler broadening (Free Gas Model), together with the resolution width of the capture (L=30 m) and transmission (L =50 m) experimental set-up.

6.2.1 Doppler effect

The shape of the absorption line is distorted by the so-called Doppler effect which broadens the natural width of the resonances and attenuates their amplitude. The theoretical cross sections must be averaged over the thermal motion of the target nuclei. Doppler-broadened cross sections (σ_D) are obtained by convoluting the unbroadened cross sections (σ) with the so-called scattering function [107]:

$$\sigma_D(E) \;=\; \int S(E', E)\; \sigma(E')\; \mathrm{d}E' \tag{6.14}$$

where E' is the energy transfered to the target nucleus, E is the initial neutron energy and $S(E', E)$ contains all information on the nuclei dynamics and neutron scattering process.

The Doppler broadening calculations are widely based on the free gas model derived from the works of Bethe and Placzek [108]. This formalism assumes that the target nuclei have a velocity distribution characteristic of a free gas at a given thermodynamic temperature (T). The use of a more realistic model derived from the Lamb's harmonic crystal model [109] is recommended when atoms are bound in a crystal lattice.

These models were widely studied because of the large effect of the temperature on reaction rates in thermal nuclear reactor [110]. Detailed description of each theoretical approach are given in References [111, 112]. The formula available in SAMMY [27]and REFIT [113] are summarised in this section.

According to the Lamb's formalism, the scattering function here below characterises the neutron capture by harmonic crystals:

$$S_{CLM}(E', E) = \frac{1}{2\pi} \int_{-\infty}^{+\infty} e^{iE't} e^{g_C(E,t)} \mathrm{d}t \tag{6.15}$$

Function $g_C(E, t)$ depends on such crystal characteristics as the phonon vibration spectrum of the target nucleus in the crystal lattice. A suitable analytic expression of $g_C(E, t)$ was obtained under the assumption that the lattice has a cubic symmetry. As Lamb suggested [109], in the case of a weakly bound crystal, we may generally account for the solid state effect with the free gas model by replacing the thermodynamic temperature (T) with an effective temperature (T_{eff}) deduced from an appropriate phonon spectrum [114]. The Doppler broadening for the free gas model may be obtained via the following scattering function:

$$S_{FGM}(E', E) = \frac{1}{\Delta\sqrt{\pi}} \sqrt{\frac{E'}{E}} \left[e^{-4\left(\frac{E-\sqrt{EE'}}{\Delta}\right)^2} - e^{-4\left(\frac{E+\sqrt{EE'}}{\Delta}\right)^2} \right] \tag{6.16}$$

in which the so-called Doppler width Δ is given by:

$$\Delta \;=\; \sqrt{\frac{4\; E\; k_B\; T_{eff}}{A}} \tag{6.17}$$

where A is the target mass and k_B is the Boltzmann's constant. The value of T_{eff} is generally deduced from the thermodynamic temperature (or sample temperature T) as follows:

$$T_{eff} \;\simeq\; \frac{3}{8}\, \theta_D\; \coth\left(\frac{3}{8}\frac{\theta_D}{T}\right) \tag{6.18}$$

This expression is a widely used approximation of T_{eff}. It is valid in the case of an effective temperature slightly higher than the sample temperature. The determination of T_{eff} depends on the Debye temperature (θ_D) introduced in the specific heat theory [115]. The Debye temperature of the crystal is interpreted as a parameter proportional to the average vibrational frequency of the crystallographic unit cell.

Figure 6.2 shows the S_{CLM} and S_{FGM} scattering functions obtained for a UO_2 sample at 77 K and 300 K. At a low temperature the free gas model is not adequate to account for the lattice vibration effect. At a room temperature, the Free Gas Model (Equation 6.16) becomes

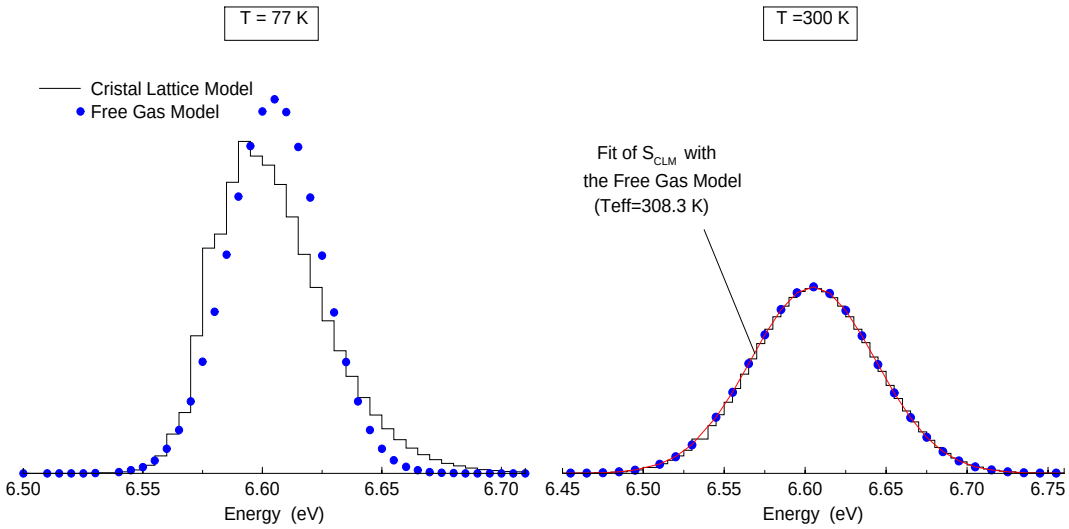

Figure 6.2: Scattering function S_{CLM} and S_{FGM} obtained with the *Dirac delta option* of SAMMY at 77 K and 300 K in the case of UO_2 sample around 6.6 eV. The effective temperature used in the Free Gas Model calculation results from the least squares fit of S_{CLM} with Equation 6.16.

a relevant alternative to describe the Doppler broadening of the neutrons resonances above few eV. The least squares fit of S_{CLM} with Equation 6.16 provides an effective temperature of 308.3 K. This value is in excellent agreement with the expected value of T_{eff}=309.5 K given by Equation 6.18 with a Debye temperature of $\theta_D = 248$ K [115]. Therefore, we may conclude that Equation 6.18 provides satisfactory T_{eff} values, without introducing significant systematic errors.

Our PbI_2 measurements are analysed with the Free Gas Model as the solid state effect above 20 eV is not significant at ~300 K. Thus, the Lamb's effective temperature (T_{eff}) connected to θ_D becomes the relevant parameter to be used in our analysis. The Debye temperature reported in the literature is often related to homonuclear diatomic molecules. Respective values of about ~ 105 K and ~ 106 K for lead and iodine are given in Reference [115]. These two information are used to estimate the Debye temperature of our PbI_2 sample. In the case of a crystalline solid solution involving polyatomic crystal cell, the Vegard's rule can be applied as follows [116]:

$$\theta_D^{PbI_2} \simeq x\,\theta_D^{I} + (1-x)\,\theta_D^{Pb} \tag{6.19}$$

where x and $(1-x)$ stand for the iodine and lead concentrations in the PbI_2. With $x = 0.55$ and $1 - x = 0.45$, Equation 6.19 gives a debye temperature ($\theta_D^{PbI_2}$) close to 105.5 K. To check the validity of this phenomenological combination rule, the results are compared in Figure 6.3 with θ_D experimental available from Reference [116]. Relatively large deviations between the calculated and the experimental values of θ_D take place over the crystals under investigation. For $\theta_D < 200$ K, we may assign an error of about 53 K on $\theta_D^{PbI_2}$. The maximum error on T_{eff} involved by this method together with the maximum variation of the sample temperature, as continuously recorded during the experiment, should be less than 4 K in transmission and 7 K in capture measurements. Figure 6.4 shows the effect of the effective temperature on the neutron width of the 469 eV resonance of ^{129}I. A systematic deviation of about 0.1 meV/K can

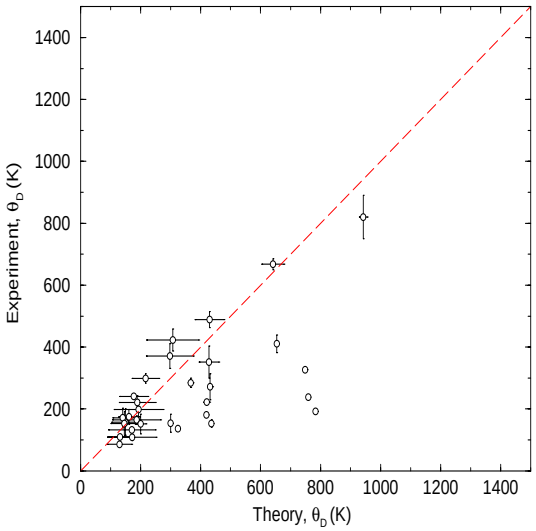

Figure 6.3: Comparison of experimental [116] and calculated (Equation 6.19) Debye temperature.

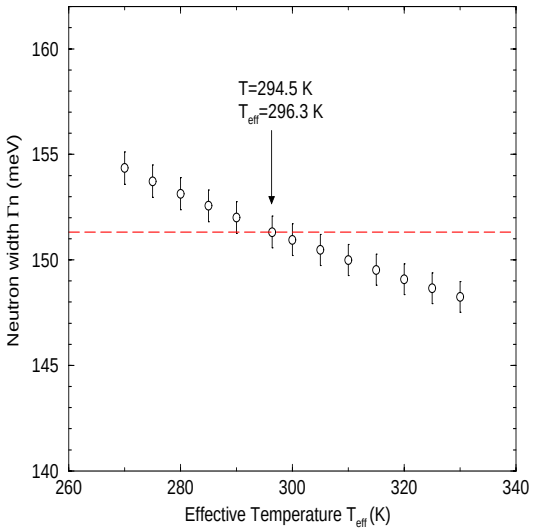

Figure 6.4: Neutron width dependence of the 469 eV resonance of ^{129}I with the effective temperature T_{eff}.

be deduced from the Γ_n behaviour. According to these preliminary remarks, the error on the resonance parameters introduced by the uncertainty related to the effective temperature can be discarded compared to the uncertainties linked to the data reduction process

6.2.2 Experimental resolution function

The experimental resolution function of the GELINA facility is fully described in Appendices B and C. The investigation was performed in three steps:

- Appendix B gives a detailed description of the analytic formula implemented by M.Moxon in REFIT. The modelisation was improved with the help of Coceva's simulations.
- Appendix C presents the implementation of the resolution function in the SAMMY code. The analytic treatment in SAMMY, namely RPI, is not adequate to described the GELINA resolution. Therefore, a new option was implemented by N.M.Larson called the User-Defined-Resolution (UDR). In the UDR option, resolution functions are introduced as point-wise distributions. The results from the RPI and UDR options are compared with those from REFIT.
- The final step is presented in this Section. It consists of optimising the parameters of the analytic treatment in REFIT.

The shape of the final resolution function results from the convolution of six main processes related to the initial electron burst ($I_p(t)$), the timing channel ($I_c(t)$), the uranium target ($I_t(t)$), the water moderator ($I_m(t)$), the angle of the flight path ($I_\theta(t)$) and the detector ($I_d(t)$):

$$R(t) = I_p(t) \star I_c(t) \star I_t(t) \star I_m(t) \star I_\theta(t) \star I_d(t) \tag{6.20}$$

In REFIT, the initial burst may be described with a trapezium function and the channel width is currently taken into account with a square function. Owing to the large discrepancies between the analytic treatment proposed in REFIT and the simulations, it is recommended to account for the time response of the detector with Monte-Carlo simulations.

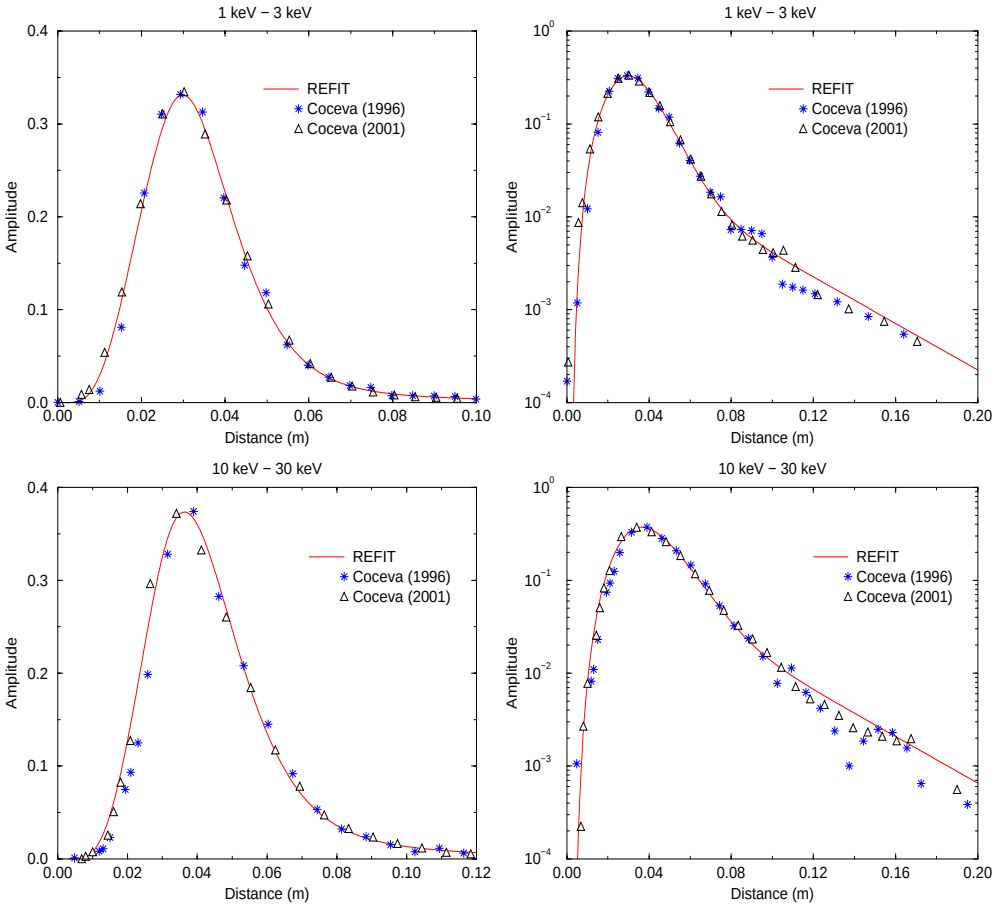

Figure 6.5: Analytic resolution functions and Coceva simulations of the target-moderator assembly ($\theta = 9^o$)

The contribution of the uranium target is reproduced with two exponential decays. The time distribution is adequately described by:

$$I_t(t) = \frac{\ln 2}{\tau_0} \mathrm{e}^{-\frac{\ln 2\, t}{\tau_0}} + \frac{\ln 2}{\tau(E)} \left(k_1 + k_2 E^{k_3}\right) \mathrm{e}^{-\frac{\ln 2\, t}{\tau(E)}} \quad \text{with} \quad \tau(E) = \lambda_\tau \frac{72.298}{\sqrt{E}} \tag{6.21}$$

The first exponential decay represents the time taken by a fast neutron to cross the uranium target, and the second exponential decay account for the neutron scattering process. The λ_τ parameter stands for an effective mean distance between collisions.

The distribution related to the moderation time is approximated by a chi-squared function with six degrees of freedom. The calculations conducted by Groenewold and Groendijk [155] give the following expression for neutron energies above few eV:

$$I_m(t) = \frac{1}{2} \left(\frac{\sqrt{E}}{72.298 \Lambda} \right)^3 t^2 e^{-\frac{\sqrt{E}}{72.298 \Lambda} t} \qquad \text{with} \qquad \Lambda(E) = \frac{\lambda_0}{\lambda(1eV)} \lambda(E) \tag{6.22}$$

in which, $\lambda(E)$ represents the theoretical neutron mean free path in the water moderator, and λ_0 stands for a free parameter.

The time distribution ($I_\theta(t)$) related to the angle θ of the flight path is approximated by the following simple formula:

$$I_\theta(t) \propto \sqrt{T_m^2 - (T_m - 2t)^2} \qquad \text{with} \qquad T_m = \frac{72.298\ D_c \tan\theta}{\sqrt{E}} \tag{6.23}$$

where D_c is the diameter of the first collimator seen by the neutrons escaping from the moderator.

The optimisation of the analytic resolution function consists of determining five parameters (τ_0, k_i (i=1,3), λ_τ). This work has been done with the help of Monte-Carlo simulations performed by Coceva in 1996 and 2001 (Figure 6.5). From a least squares fit of the distributions, we obtained the following results:

$$\begin{aligned} \tau_0 &= 2.5 \text{ ns} \\ \lambda_\tau &= 24.1 \text{ mm} \\ k_1 &= 3.738 \times 10^{-2} \\ k_2 &= 1.196 \times 10^{-3} \\ k_3 &= 4.629 \times 10^{-1} \end{aligned}$$

For the calculation, λ_0 is set to 5.83 mm, being the value recommended by M.Moxon. The results for τ_0 and λ_τ are in a satisfactory agreement with the dimensions of the 4 cm-thick uranium target. Indeed, for fast neutrons (1-2 MeV), the 2.5 ns decay time would correspond to a distance ranging from 3 cm to 5 cm. The present parametrisation gives a set of valuable prior parameters for future improvements with the help of Time-Of-Flight data.

Since the analytic treatment of the resolution function is deduced from the Coceva's simulation, the choice of using directly the point-wise Coceva distributions was done to analyse the ^{127}I and ^{129}I resolved resonance range. In the meantime, a sensitivity study has been conducted for obtaining information on the neutron width uncertainty with respect to the choice of the resolution function. Below 4 keV, an overall systematic error lower than 1.5% was found (see Section 7.4).

6.3 Multiple scattering correction

In capture measurements, the multiple scattering of a neutron inside a sample can involve large corrections. In the resolved resonance region, these corrections imply a complex analytic treatment. In practice, suitable approximations are used in order to simplify the numerical treatment of the multiple scattering theory. The approximations in the REFIT shape analysis program are based on an original derivation by Case et al. [121]. The single-scattering approximation used in the SAMMY code is based on an initial description by Perey [122], with further development by Larson [123]. The so-called double-plus-scattering approximation in SAMMY is an independent derivation and implementation based on verbal description from Moxon. In the present study, two Monte-Carlo codes, MCNP4C [124] and SAMSMC [123], have been used to check the validity of the numerical treatments implemented in REFIT and SAMMY-M6.

MCNP is a general-purpose Monte-Carlo N-Particles code that can be used for neutron transport in an arbitrary three-dimensional configuration of materials. The Monte-Carlo method rigorously treats the neutron transport in the sample. For the calculation, the neutron source is assumed to be a uniform parallel neutron beam normally incident on a finite cylinder placed at the flight path length L. The results, given in time, are converted into energy via the time/energy relation $E = (72.298\ L_n/t_n)^2$. Calculations were performed with the ENDF/B-VI (MCNP library called ENDF60) point-wise energy cross section data.

SAMSMC is based upon a code provided by Gerard de Saussure. It was modified by F.Perey and by N.M.Larson. It calculates the contribution to the cross section of zero, one or many elastic scatterings that will preceed the capture in the sample. A suitable interface was implemented to read the cross sections and the energy grid provided by SAMMY.

Comparisons of the results from the two codes (SAMMY and REFIT) with those from the Monte-Carlo simulations were performed for sample thicknesses ranging from 0.1 mm to 50 mm, and for various isotopes (^{197}Au, ^{56}Fe, ^{136}Ba, ^{127}I and natural silicon). The results are discussed to investigate the validity of the single scattering correction, the back scattering and the 90^o scattering correction, the multiple scattering correction in the case of an isolated resonance and the multiple scattering correction in the case of non-isolated resonances.

6.3.1 Definition

In order to compare the theoretical capture yield $Y(E)$ with the experiment, the self-shielding and multiple scattering corrections are included in the calculations. It is convenient to subdivide $Y(E)$ into a primary yield Y_0 and a multiple yield $(Y_1 + Y_2)$. Thus, the fraction of the incident neutrons captured in the sample could be expressed as:

$$Y(E) = Y_0(E) + Y_1(E) + Y_2(E) \tag{6.24}$$

The primary yield Y_0 is also defined as the self-shielding correction. It refers to the partial interactions which occur at the first collision. For neutrons at energy E, Y_0 is equal to the number of primary interactions per incident neutron integrated over the sample thickness n. It is expressed as:

$$Y_0(E) = \left(1 - e^{-n\sigma_t(E)}\right) \frac{\sigma_\gamma(E)}{\sigma_t(E)} \tag{6.25}$$

where σ_t and σ_γ are the total and capture cross sections.

The multiple interactions $(Y_1 + Y_2)$ involve the absorption of the neutrons scattered in the primary collision. The yield Y_1 refers to the neutron capture at the second interaction in the sample, and Y_2 represents the capture after two or more collisions. It is convenient to think about the multiple yield as a correction applied to the primary yield. With $Y_1 + Y_2 = \alpha Y_0$, Equation 6.24 becomes:

$$Y(E) = (1 + \alpha(E))\, Y_0(E) \tag{6.26}$$

The function $\alpha(E)$ is the fraction of capture following neutron scattering and $(1 + \alpha(E))$ represents the multiple scattering correction factor. It can be defined as the average absorption per atom in the sample to the average absorption per atom in an infinitely thin foil exposed to the same flux [125].

Extensive work has been performed to derive analytic expressions of $Y_1(E)$ and $Y_2(E)$ for basic sample geometries. The case of a finite cylinder, with a flat surface perpendicular to the beam, was implemented in REFIT and SAMMY. The neutron beam intensity is assumed as uniform over its area, having a diameter larger, equal to or smaller than the diameter of the sample. The analytic expressions of Y_1 and Y_2 implemented in SAMMY are given in Reference [27]. The calculation for two or more scatterings is based on algorithms similar to those used in reactor calculations. Approximations are needed both to obtain a suitable numerical treatment and to enable REFIT and SAMMY to carry out the calculations in a finite time. Three main approximations currently used are given below:

• After two scatterings, neutrons are uniformly distributed both in direction of motion and in position within the sample.

• In REFIT, the capture after an initial scattering interaction is usually carried out assuming no Doppler broadening in the energy distribution of the scattered neutrons (the full Doppler effect on the scattered neutron energy distribution takes longer time in the REFIT implementation.) In SAMMY, the full Doppler broadening is included, as the computer run-time increment is negligible.

• The time required for a neutron to transverse the sample to the capture site, on a direct path with no scatterings, may be significantly shorter than the time the neutron actually spends en route when there are scatterings. This time differential is assumed to be small compared to the timing channel width; hence it is ignored in the calculations. This may cause some discrepancy with the observed data if there are many scatterings.

6.3.2 Single scattering correction in a thin sample of Gold

The mathematical description of the single scattering correction $Y_1(E)$ can be written exactly. Consequently, it becomes interesting to investigate this correction in order to study the accuracy of the numerical procedure implemented in the shape analysis codes taking into account the following condition. In REFIT, the double-plus scattering cannot be "turned-off". Therefore, the comparison of the single scattering correction in SAMMY vs. REFIT is a comparison of SAMMY (single scattering option) to REFIT (full multiple scattering correction). In this section, the comparison is performed with the help of a very thin gold sample making the double-plus scattering effect negligible.

The sample thicknesses used to analyse the resonance range of bodies characterised by a high density and/or a high capture cross section of several kilo barns range typically from 0.1 mm to 1 mm. In the case of very thin samples, the two or more scattering corrections can be neglected in order to simplify the analysis. Equation 6.24 then becomes:

$$Y(E) \simeq Y_0(E) + Y_1(E) \tag{6.27}$$

For a round disk, with a flat surface perpendicular to the beam, the capture yield Y_1 comes down to:

$$Y_1(E) = \underbrace{Y_{1\infty f}(E) + Y_{1\infty b}(E)}_{\text{infinite size}} + \underbrace{Y_{1\ f}(E) + Y_{1\ b}(E)}_{\text{finite size}} \tag{6.28}$$

in which the subscript f and b refer to forward and backward scatterings. The subscript ∞ indicates that this term assumes that the sample extends to infinity in the dimension perpendicular to the beam. The other terms represent the corrections for finite size.

A capture experiment performed with a thin gold foil was used to investigate the quality of the single scattering correction implemented in SAMMY and REFIT (Figure 6.6). The first resonance of gold ($E = 4.9$ eV) is considered as a standard to normalise the capture yield spectra with the so-called saturated resonance method [127]. Table 6.1 summarises the normalisation factors N obtained with SAMMY and REFIT over three neutron energy regions. The results are consistent with the average value of about 0.547. The agreement between SAMMY and REFIT is better than 0.5%.

In Figure 6.6, in the enlargement of the top of the resonance, one may distinguish two structures which are explained as the contribution of the neutrons absorbed after one or more scatterings. The single scattering effect contributes at a 6% rate to the total area of the resonance, and less than 0.6% of the capture events occur after two or more scatterings. We have investigated these contributions with Monte-Carlo calculations. The results from MCNP4C and SAMSMC are given in Figure 6.7 together with the functions obtained with SAMMY and REFIT. This exercise shows that the capture yields given by REFIT and obtained with the single

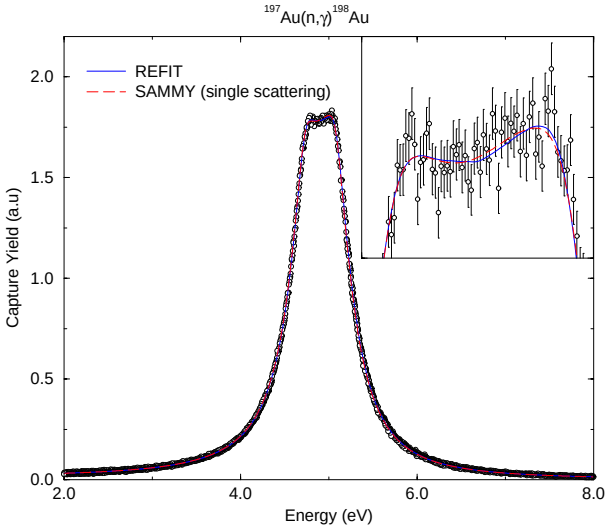

Figure 6.6: Capture yield obtained with SAMMY (single scattering option) and REFIT (full multiple scattering correction) around the lowest s-wave of the ^{197}Au(n,γ) reaction. The sample is 0.1 mm-thick ($\pm$5 μm) with a diameter of 80 mm.

Table 6.1: Normalisation of the capture yield obtained from a fit of the first resonance of gold (E=4.9 eV) over three energy regions. The quoted errors are only the statistical uncertainties given by the fitting programs.

Energy range (eV)	REFIT	SAMMY
4.6 - 5.1	0.5471 ± 0.0005	0.5469 ± 0.0005
3.5 - 6.2	0.5482 ± 0.0003	0.5467 ± 0.0003
2.0 - 9.3	0.5478 ± 0.0003	0.5462 ± 0.0003
average	0.5477	0.5466

scattering approximation of SAMMY are in good agreement in the case of a very thin sample of gold. In order to study the small discrepancies observed at the top of the resonance, the 90^o scattering correction is investigated in the next section. The large corrections involved by this effect, even in the case of thin samples, are useful to study the validity of the analytic treatment of the multiple scattering theory.

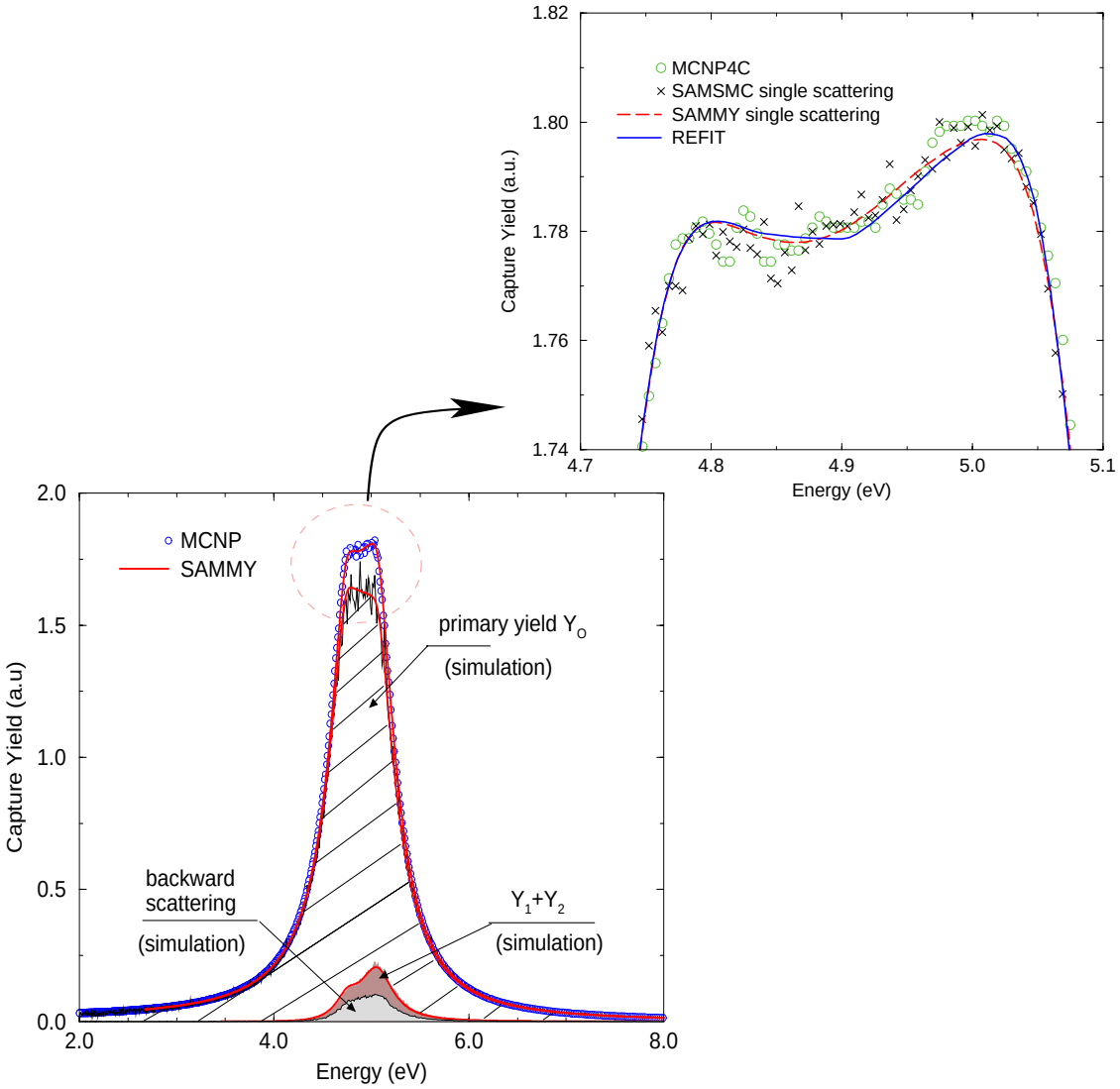

Figure 6.7: Monte-Carlo simulations of the capture yield around the 4.9 eV resonance of the ^{197}Au(n,γ) reaction together with the results given by SAMMY (single scattering option) and REFIT (full multiple scattering correction) using the same resonance parameters. In the enlargement of the top of the resonance, the fitting functions are compared with MCNP and SAMSMC results.

6.3.3 Back scattering and 90^o scattering correction

The multiple scattering process in a sample involves the so-called 90^o scattering effect. If E represents the laboratory energy of the incident neutron, E' and θ the laboratory energy and the laboratory angle of the outgoing neutron, then E' may be expressed in terms of E and θ as:

$$E' = E\left(\frac{m_n}{m+m_n}\right)^2\left[\cos\theta + \sqrt{\left(\frac{m}{m_n}\right)^2 - \sin^2\theta}\right]^2 \tag{6.29}$$

in which the mass of the target nucleus is m and $m_n = 1$ represents the neutron mass. The outgoing neutron energy for a 90° scattering is:

$$E' = E\frac{m-1}{m+1} \tag{6.30}$$

The lowest energy into which a neutron may scatter is obtained for $\theta = 180^o$:

$$E' = E\left(\frac{m-1}{m+1}\right)^2 \tag{6.31}$$

- **Thin iron sample**

Figure 6.8 shows a capture yield from a measurement performed on a thin foil of ^{56}Fe [69] together with the results obtained with REFIT and SAMMY. Monte-Carlo simulations (SAMSMC, MCNP) have been performed to study the first p-wave at 1.15 keV. The contributions of zero, one or two scatterings are shown on the left half of the figure. The area of the resonance is adequately reproduced by the primary yield Y_0. The contribution of the neutrons absorbed after two scatterings is negligible.

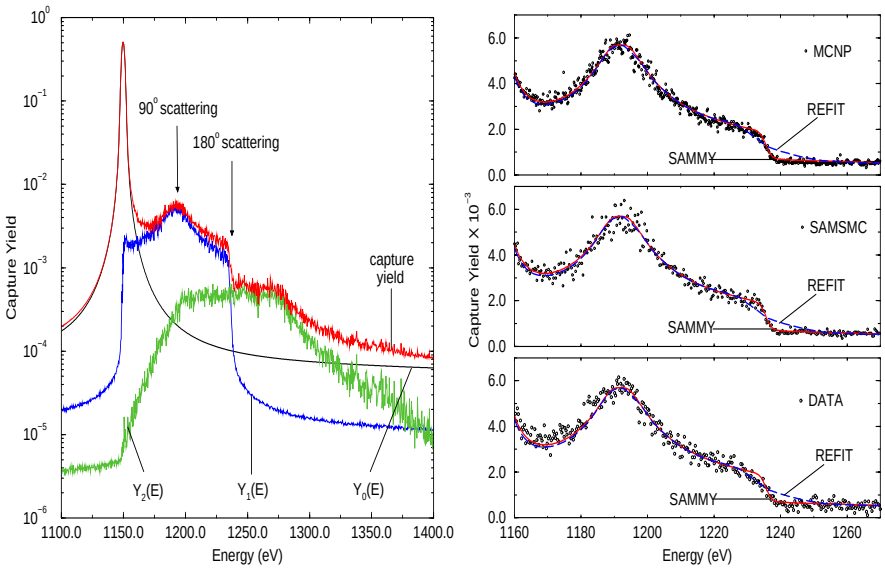

Figure 6.8: Capture yield of the ^{56}Fe(n,γ) reaction at 1.15 keV. The figure on the left hand part was obtained with SAMSMC. The thickness and the diameter of the sample is 1.3 mm and 80 mm respectively (1.0753×10^{-2} at/barns). On the right hand part, the theoretical curves from SAMMY and REFIT are compared with Monte Carlo simulations (MCNP, SAMSMC) and with experimental data [69].

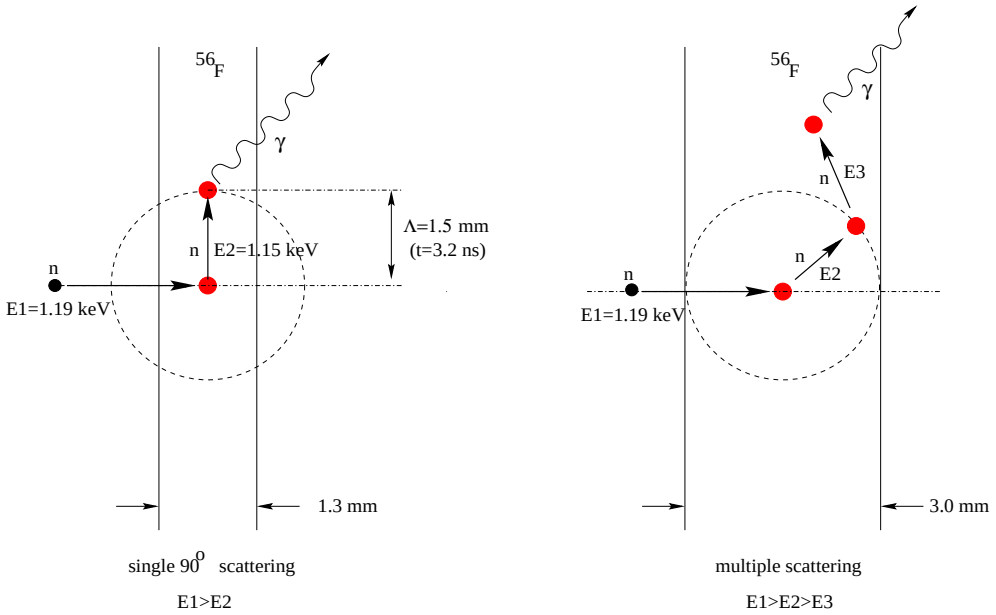

Figure 6.9: Representation of the 90^o scattering process compared to the multiple scattering process in a thin and thick iron samples. In the case of very thin samples, the single scattering contribution is reduced to the 90^o scattering effect.

In a thin sample, the single scattering contribution is mainly due to the 90^o scattering effect, otherwise after the first collision at an angle $\theta \neq 90^o$ the neutron would escape from the sample (Figure 6.9). For a diameter D and a neutron mean free path (Λ) larger than the sample thickness h, the probability for a neutron to be captured is maximal after one scattering at $\theta = 90^o$. In the case of iron, the structure around $E = 1.19$ keV is characteristic of the 90^o scattering. If an incident neutron of energy $E = 1.19$ keV is scattered at $\theta = 90^o$, the outgoing neutron of energy $E = 1.15$ keV (energy of the resonance), will be absorbed in the second collision. The time elapsed between the first and the second collision is about 3.2 ns. This time interval is too short to be discriminated by the acquisition system. The capture event is then recorded at a time corresponding to the energy of the incident neutron. This kind of capture event is accumulated in the time of flight spectrum around $E = 1.19$ keV, and it explains the additional smaller peak shown on the right half part of Figure 6.8.

The simulations performed with MCNP and SAMSMC confirm the correct analytic description of the 90^o scattering provided by SAMMY and REFIT in the case of a very thin sample. A discrepancy between the shape analysis programs exists around the edge of the back scattering effect. The numerical integration method used in REFIT to integrate Equation 6.28 over the angle θ has to be improved.

The final comparison between the experimental data and the codes (Figure 6.8) shows a slight discrepancy in the wing of the resonance (around $E = 1.17$ keV). This can be explained by the uncertainties connected to the data reduction such as the background subtraction.

• **Thin barium sample**

Figure 6.10 shows three resonances of the ^{136}Ba(n,γ) reaction. Resonances at 3.41 keV and 3.45 keV have a spacing of about $\Delta E = 40$ eV which corresponds to the energy lost by a neutron of energy $E = 3.45$ keV after a 90^o scattering. The latter involves a huge correction of about 35% in the area of the resonance at 3.45 keV. Simulations were performed for sample thicknesses ranging from 0.5 mm to 5 mm, and analysed with SAMMY and REFIT. Table 6.2 gives the resonance parameters used for the simulations.

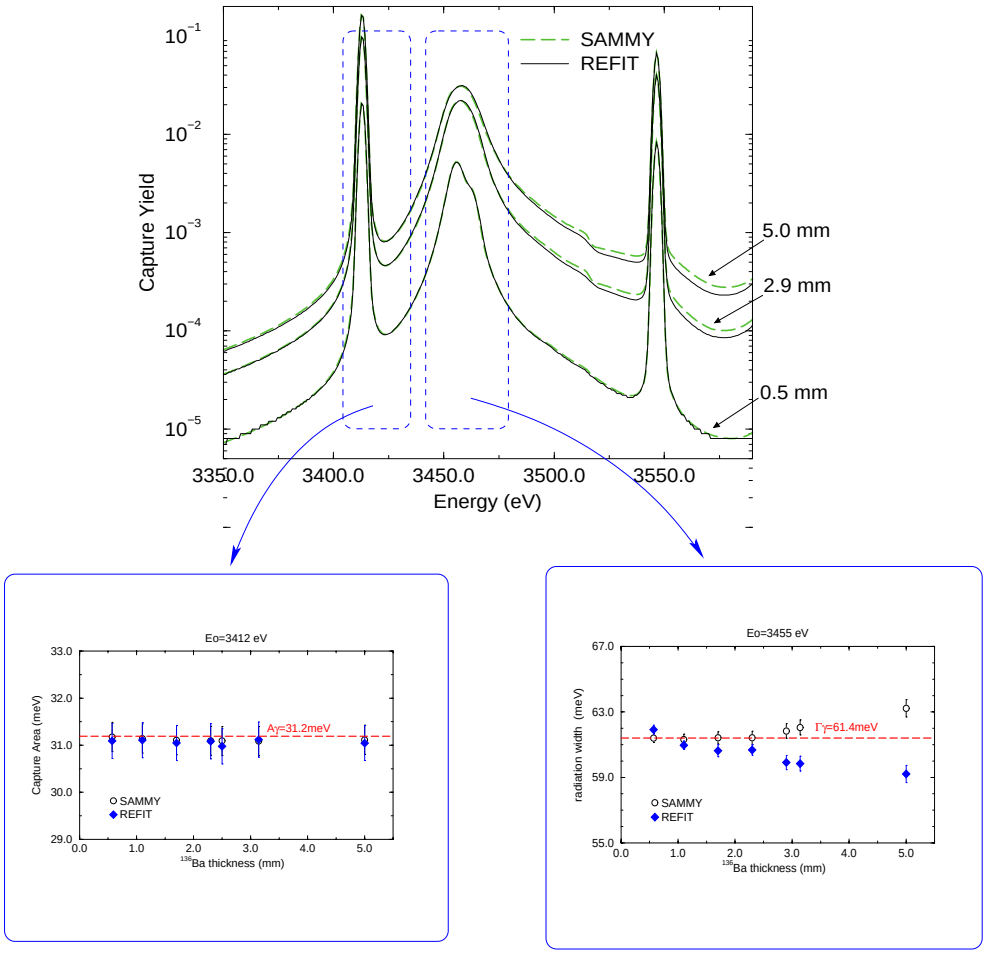

Figure 6.10: Effect of the 90° scattering correction on the radiation width of the 3.45 keV resonance and on the capture area of the 3.41 keV resonance of the ^{136}Ba(n,γ) reaction. The fit was performed on various capture yields obtained with SAMSMC (the sample diameter is 80 mm).

The capture measurements provide experimental values for the capture area $g\Gamma_n\Gamma_\gamma/\Gamma_{tot}$. In practice, if $\Gamma_\gamma << \Gamma_n$, the capture area reduces to $g\Gamma_\gamma$ making difficult a correct determination of the neutron width Γ_n. In the case of the 3.45 keV resonance of the ^{136}Ba(n,γ) reaction, the radiation width is 110 times smaller than the neutron width. Therefore, for this study we have only investigated the asymptotic form $g\Gamma_\gamma$ of the capture area. The capture area of the 3.41 keV resonance together with the radiation width of the 3.45 keV resonance obtained from the sample thicknesses under investigation are shown in Figure 6.10.

In the case of the 3.41 keV resonance, the results agree with the capture area calculated via the parameters given in Table 6.2. The multiple scattering correction can be neglected, so that the shape of the resonance is mainly due to the primary yield. For the 3.45 keV, SAMMY provides an excellent description of the single scattering effect below a sample thickness of about 3 mm. However, some problems occur when thick samples are used. The maximum discrepancies respectively reach 2.9% and 3.7% for SAMMY and REFIT. It follows that in this particular case, only samples of barium not exceeding a thickness equivalent to 2.3 mm (REFIT) and 3 mm (SAMMY) can be used without introducing significant systematic errors.

Table 6.2: Resonance parameters of the ^{136}Ba(n,γ) reaction [54].

Energy (keV)	gΓ_n (meV)	Γ_γ (meV)
3.41	74.2 $\pm$ 0.4	196.0
3.45	6762.0	61.4 $\pm$ 12.0
3.54	51.0	49.7 $\pm$ 1.2

6.3.4 Multiple scattering correction in a thick sample

The validity of the multiple scattering correction in SAMMY was tested with the Monte-Carlo code SAMSMC [123]. The simulations performed on a thick sample of silicon over a large energy range are given in Reference [128]. The correction for two or more scatterings is systematically overestimated by SAMMY. Similar calculations were performed over a smaller energy range on a 10 mm thick sample of silicon in order to study the validity of the numerical treatment of REFIT. Figure 6.11 shows the results provided by REFIT and SAMMY in comparison to SAMSMC simulations. The number of capture events which occur after two or more scatterings cannot be neglected in the wing of the resonances around 64.9 keV and 82.0 keV. In these energy ranges, REFIT and SAMMY overestimate the double-plus scattering correction by at least 10%.

• Ideal case: isolated resonance

The sensitivity to the resonance parameters was studied on an isolated resonance (Γ_γ = 100 meV and Γ_n = 10 meV) for two masses: A=50 and A=100. The capture yields were obtained by Monte-Carlo calculations for sample thicknesses h varying from 1 mm to 50 mm equivalent to 1 g/cm^2. The Y_0, Y_1 and Y_2 contributions are shown in Figure 6.12. In neutron capture measurements, the analysis of isotopes with a density of about 10 g/cm^3 involves a sample thickness lower than 1 mm. If the material to be analysed consists of a mixture of several isotopes in powder form, the sample thickness to be used typically ranges from 5 mm to 15 mm [50]. A sample thickness of about 30 mm can be used to measure the neutron capture cross sections of gaseous materials, which are characterised by a weak density [119].

The comparisons between SAMMY and REFIT are shown in Figures 6.13 and 6.14 together with SAMSMC simulations. The agreement is better when A=100. The contribution of the multiple interactions depends on the number of nuclei per unit volume defined as:

$$n = \frac{\mathcal{N}}{A}\frac{m}{S\,h} \tag{6.32}$$

For this exercise, the mass (m) and the surface (S) of the sample are constant over the sample thicknesses under investigation. Consequently, for materials with the same density ($m/S\ h$),

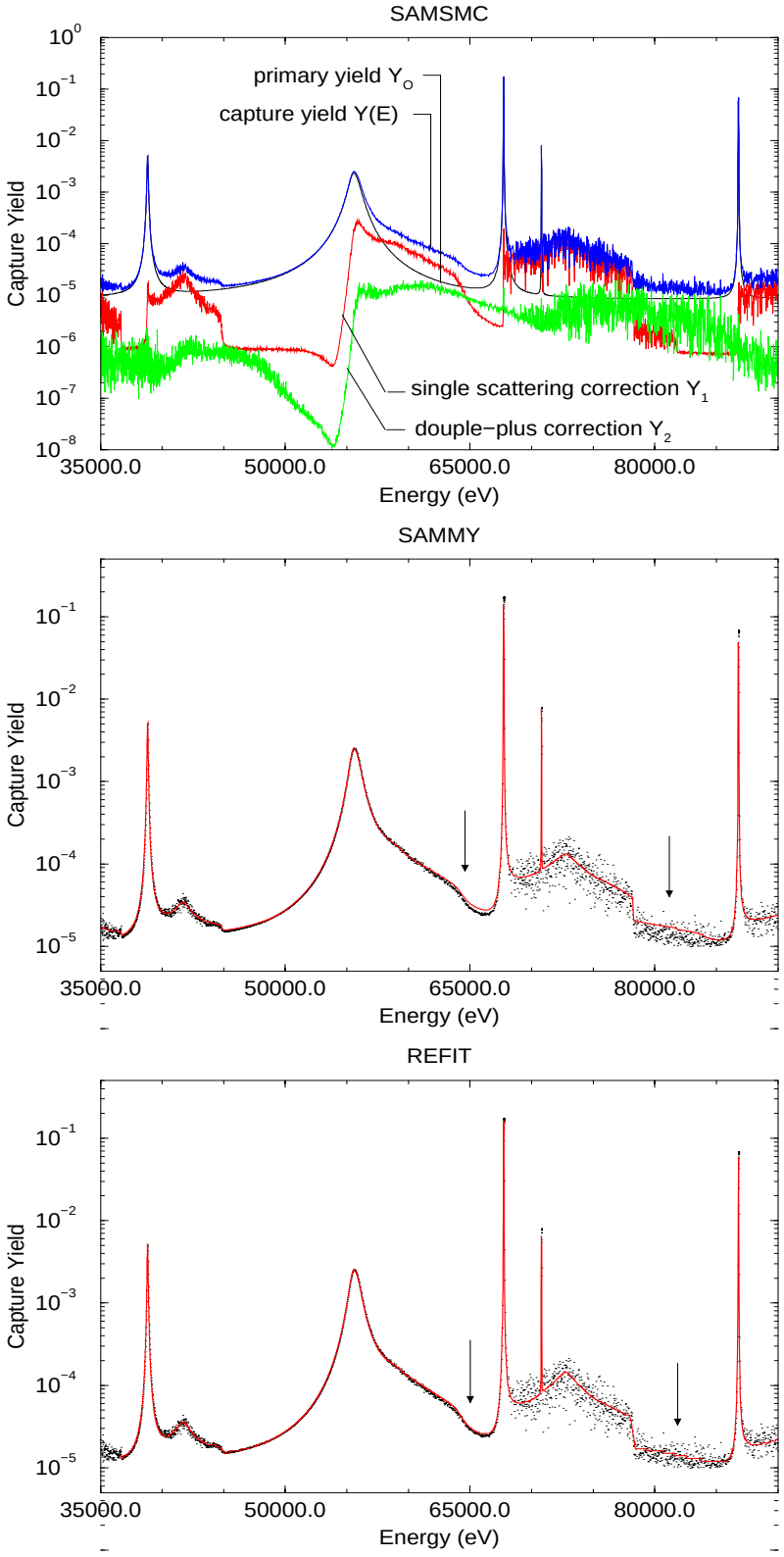

Figure 6.11: Neutron capture yields for a thick sample of silicon. The various contributions to the SAMSMC calculation are shown in the top plot. Results from SAMMY (center plot) and REFIT (bottom plot) are compared with summed SAMSMC calculations. The thickness and the diameter of the sample are 10 mm and 80 mm respectively.

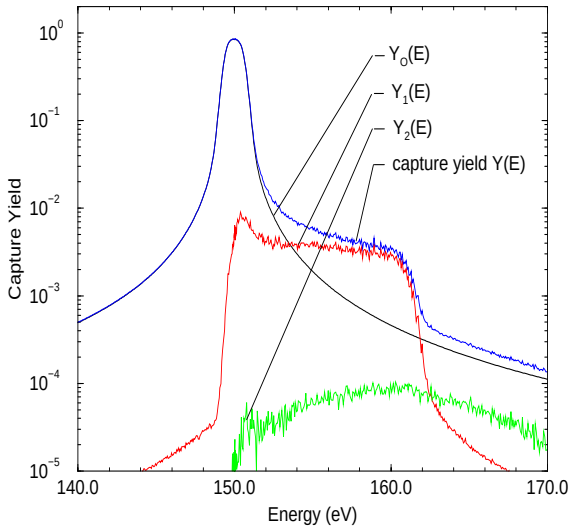

Figure 6.12: Neutron capture yield simulated with SAMSMC. The calculations were performed for an isolated dummy resonance ($\Gamma_\gamma = 100$ meV and $\Gamma_n = 10$ meV). The mass of the isotope is A=50. The sample thickness is equivalent to 1 g/cm^2, the diameter of the sample is 80 mm.

multiple interactions are reduced when heavy nuclei are used. An improvement by at least a factor of two is observed when A=100.

Below 160 eV, SAMMY agrees with the simulation. The shape of the resonance is mainly defined by the primary yield Y_0 and the capture yield Y_1. This study confirms the rigorous single scattering treatment implemented in SAMMY. The wing of the resonance above 160 eV is affected by the multiple scattering contribution. When A=50, SAMMY cannot accurately reproduce this effect above a sample thickness of about 5 mm. The results provided by REFIT show the same spurious behaviour in the vicinity of the back scattering edge together with an additional numerical artifact around 165 eV. The latter demands further investigation in order to determine its origin. Above a sample thickness of 20 mm, the numerical treatment implemented in REFIT drastically fails to describe the contribution of the multiple interactions.

The resonance parameters obtained with SAMMY and REFIT are plotted in Figure 6.15. Below a sample thickness of 10 mm, an excellent agreement, better than 1%, is obtained on each parameter. In the case in which $\Gamma_n < \Gamma_\gamma$, the extracted neutron width is in a first approximation independent from the multiple scattering effect. For a sample thickness of 50 mm, the discrepancies reach only 1% (SAMMY) and 2% (REFIT). The bias on the radiation width remains below 3%. Consequently, the full multiple scattering correction in SAMMY and REFIT becomes inadequate when the radius and the thickness of the sample have the same order of magnitude in accordance with the third approximation given in Section 6.3.1. In the case of the 50 mm-thick sample, the channel width used in the calculation is 10 times smaller than the time takes a neutron to cross the sample. The approximation which consists of assuming that the neutron captured at the time when it is incident on the front face of the sample cannot be applied.

- **Real situation: non-isolated resonances**

The multiple scattering effect has been investigated through the complex composition of our PbI_2 sample (mixture of ^{127}I, ^{129}I and lead). A simulation was performed on the thick sample ($h = 14.8$ mm) in order to know if an accurate capture area value could be achieved from the

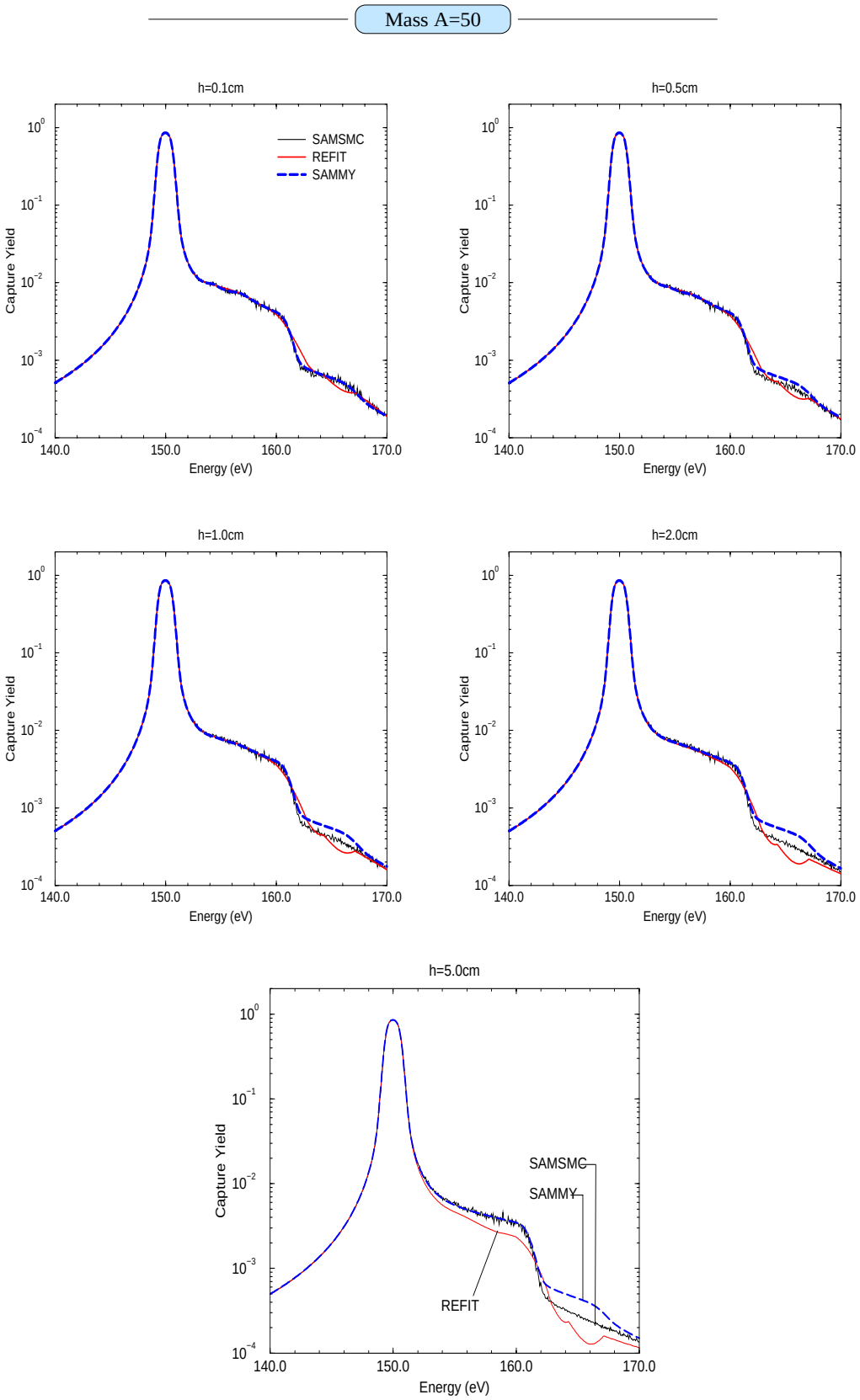

Figure 6.13: Neutron capture yields simulated with SAMSMC for several sample thicknesses h. The radius of the sample is 4 cm. The yields are compared to the results from REFIT and SAMMY in the case of an isolated resonance (Γ_γ =100 meV, Γ_n =10 meV). The mass of the target nucleus under investigation is A=50.

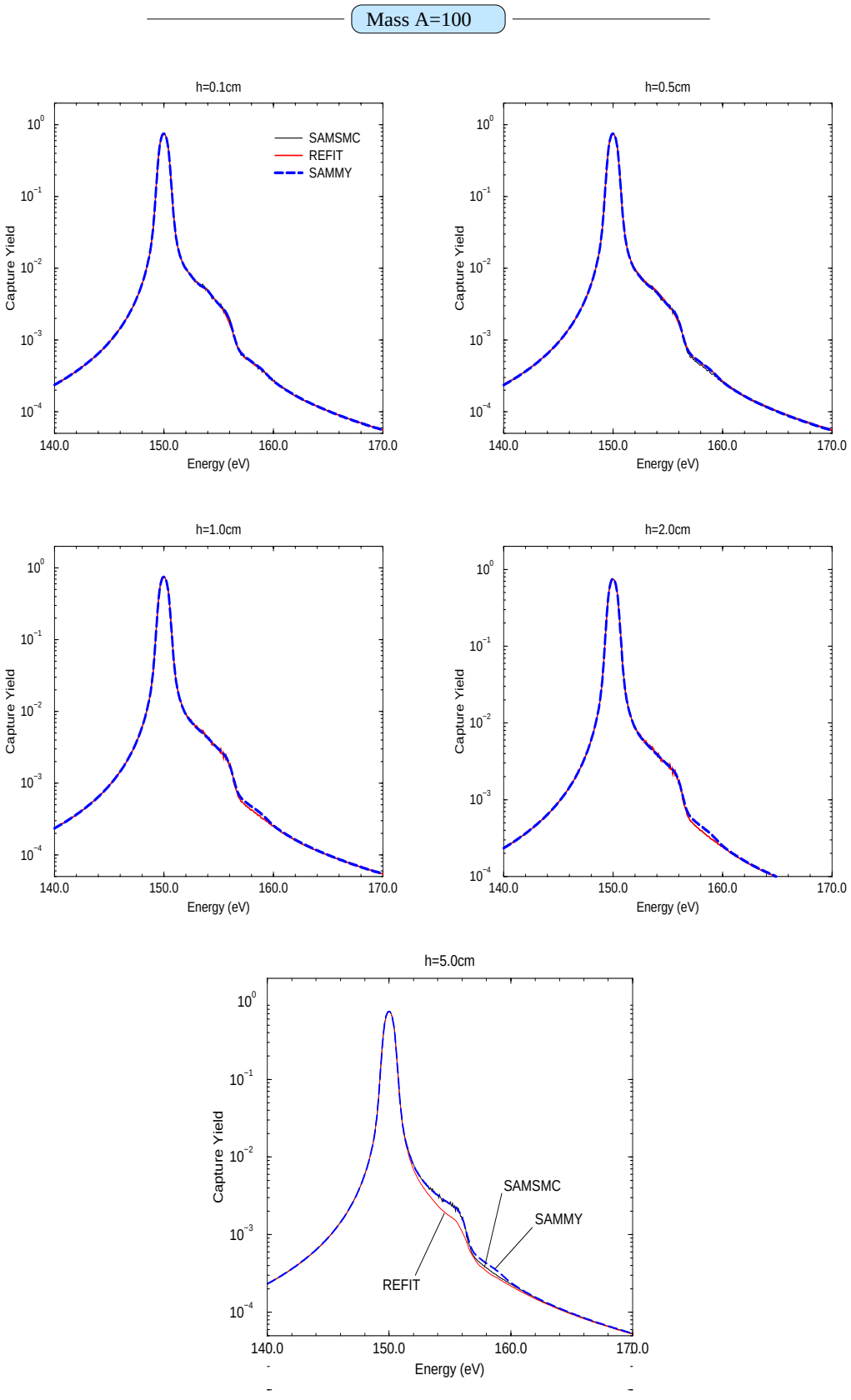

Figure 6.14: Neutron capture yields simulated with SAMSMC for several sample thicknesses h. The radius of the sample is 4 cm. The yields are compared to the results from REFIT and SAMMY in the case of an isolated resonance (Γ_γ =100 meV, Γ_n =10 meV). The mass of the target nucleus under investigation is A=100.

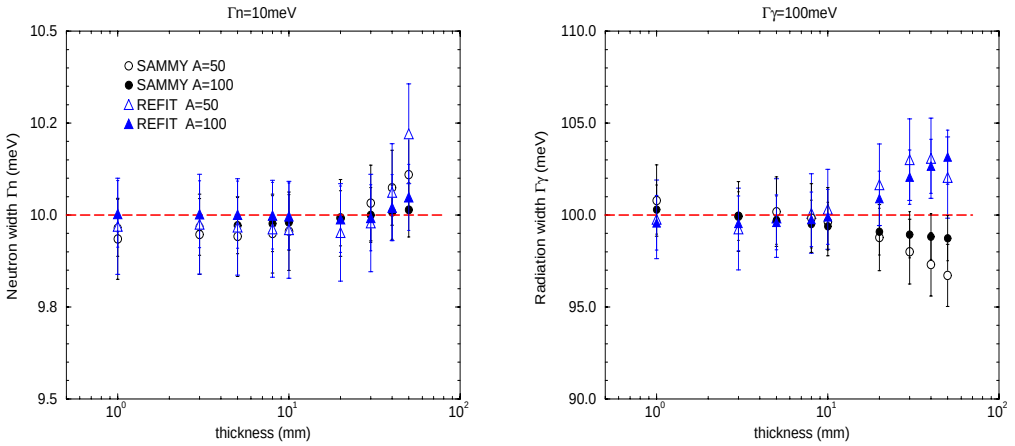

Figure 6.15: Systematic errors on the resonance parameters given by SAMMY and REFIT over several sample thicknesses. The full multiple scattering correction was used. The sample thickness in at/b is a constant.

analysis of this sample. Figure 6.16 shows the Monte-Carlo results provided by SAMSMC for the 31.2 eV, 37.6 eV and 45.4 eV resonances of ^{127}I. SAMMY and REFIT fail to give a correct description of the shape of these resonances. The discrepancies in the capture area values of the 31.2 eV and 37.6 eV resonances are not significant (Table 6.3). By contrast, SAMMY overestimates the capture area of the 45.4 eV by a factor of 1.035. Consequently, there seems to be an additional problem in the numerical computation of Y_2, which is possibly due to the mixture of several isotopes. Such an assumption requires further investigations to be confirmed.

Table 6.3: Capture area A_γ of the 31.2 eV, 37.6 eV and 45.4 eV resonances of ^{127}I given by SAMMY and REFIT. The SAMSMC calculations are based on the resonance parameters available in the JENDL3.3 data base. The quoted uncertainties are those given by the REFIT and SAMMY codes.

Energy (eV)	A_γ from JENDL3.2 (meV)	A_γ SAMMY (meV)	A_γ REFIT (meV)
31.2 eV	8.95	8.92 ± 0.14	9.03 ± 0.38
37.6 eV	14.84	14.80 ± 0.15	14.94 ± 0.23
45.4 eV	8.23	8.52 ± 0.14	8.21 ± 0.27

We conclude that the two programs give spurious results when they are used to describe very thick sample geometry. On the basis of this exercise, the question of the validity of the multiple scattering theory for thick samples is left opened. The assumptions used to derive suitable analytic expressions of Y_2 together with the numerical treatment implemented in each code fail to describe the wings of the resonances. In neutron resonance analysis, the wings of a resonance may contain valuable information such as the interference with the potential scattering, the shape of the background and/or the tail of the experimental resolution function. Owing to the previous discrepancies, such informations cannot be accurately derived from a sample thickness $h > 10$ mm.

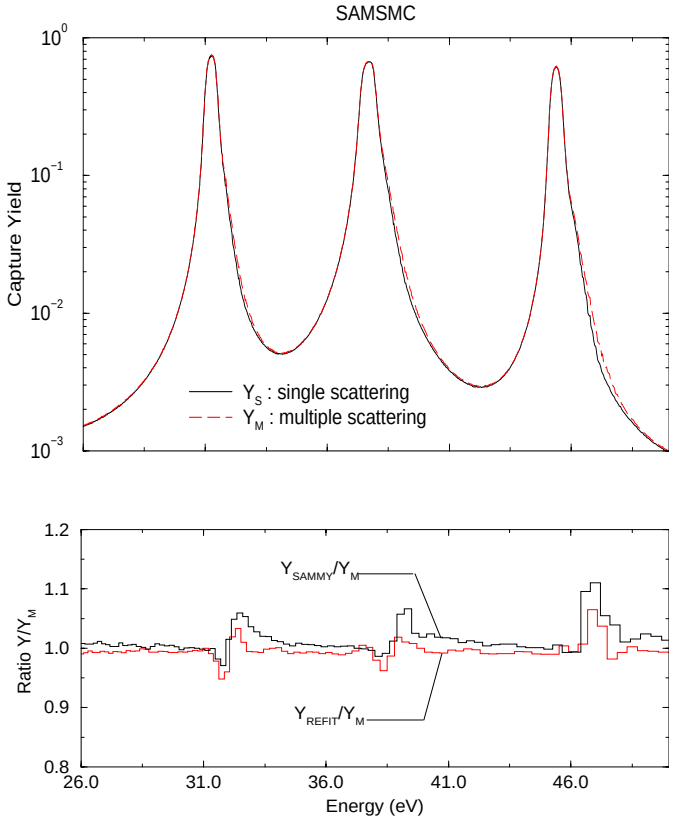

Figure 6.16: Capture yield obtained with SAMSMC. The simulation reproduces the result for the thick PbI_2 sample (h=14.8 mm). The figure shows the 31.2 eV, 37.6 eV, 45.4 eV resonances of ^{127}I.

• **Experimental conditions**

This study is mainly based on simulations, but it shows that especial care must be taken to derive accurate resonance parameters from samples with realistic thicknesses.

i) At the IRMM, such measurements are performed with a total energy detector C_6D_6 to which a weighting method is applied. In Reference [69] a sample thickness less than 1 g/cm^2 (equivalent to 1 mm of iron) is recommended in order to apply the weighting function measured by Corvi et al. [83]. Indeed, some experiments on iron using the experimental weighting function have shown a decrease with the sample thickness of the fitted neutron width. Thus, thin capture samples are recommended to avoid this experimental bias.

ii) An additional uncertainty should be taken into account, which is due to the neutron sensitivity of the C_6D_6 detectors. The prompt detection of scattered neutrons mainly coming from the sample is indistinguishable from capture events and directly contributes to the resonance areas. This effect acquires importance for structural materials when the ratio Γ_n/Γ_γ typically ranges from 10^3 to 10^4. The capture yield can be rewritten as follows [126]:

$$Y(E) = Y_0(E) + Y_1(E) + Y_2(E) + Y_S(E) \tag{6.33}$$

The yield $Y_S(E)$ is the fraction of scattered neutrons that escape from the sample, multiplied

by the efficiency for detecting a scattered neutron relative to detecting a neutron capture event in the sample. The measurements of this efficiency performed at the IRMM are described in References [54, 69]. As an uncertainty on $Y_S(E)$ better than 50% is hardly achievable, thin samples are recommended to minimise the number of the scattered neutrons in the vicinity of the detector.

Thick sample geometries should be avoided in order to reduce the systematic errors induced by the above described effects. The errors introduced by these effects can be disregarded as long as the sample thickness does not exceed a few millimeters.

6.3.5 Conclusion

On the basis of the present study, it is shown that the errors introduced by the SAMMY and REFIT resonance analysis programs are of similar magnitudes. Both programs provide spurious results compared to Monte-Carlo simulations when excessively thick samples are studied.

From the examples we have given here, an order of magnitude of the maximum acceptable sample thickness can be obtained in cases involving sample diameter of 80 mm. In the case of isolated resonances with $\Gamma_n/\Gamma_\gamma \sim 0.1$, the double-plus scattering treatments of SAMMY and REFIT may be applied on neutron capture measurements as long as the sample thickness does not exceed 10 mm. An accuracy on the capture area better than 1% is expected. For materials with a smaller mean spacing, a more accurate description of the double-plus scattering is recommended to avoid systematic errors due to the overlap of nearby resonances. The study of barium samples suggests the use of a sample thickness lower than 3 mm, equivalent to 0.3 g/cm^2. Beyond this thickness the systematic bias on the capture area may reach 3.5% depending on the code and on the scattering cross section of the material under investigation. Before turning these conclusions into generalities, further work is needed on a larger set of materials involving various sample featuring (radius, composition and density).

6.4 Conclusion

The Doppler effect, the resolution broadening and the multiple scattering are three experimental effects which may affect the accuracy of the resonance parameters. Their analytic treatments in the shape analysis codes play a crucial role in determining reliable cross section values.

The Doppler effect has been widely investigated in previous PhD thesis [70, 111]. In this work, the cross sections are Doppler broadened with the Free Gas Model. The errors connected to the effective temperature are negligible over the entire Resolved Resonance Range. By contrast, the experimental resolution function of the Geel facility implemented in REFIT and its impact on the resonance parameters was poorly documented. From the comparison with Coceva's simulation implemented in REFIT by A.Brusegan, we have improved the analytic treatment proposed by M.Moxon. Accurate transmission and capture experiments are then recommended to validate the new analytic treatment. In this work, we use the Monte-Carlo simulations provided by Coceva. The associated distributions are introduced in the SAMMY calculations with the recent UDR option. The systematic error affecting the area of isolated resonances may reach 3%. For strong overlaps, the more complex situation can be solved with the stringent determination of correlation coefficients between the resonance parameters.

The validation of the multiple scattering correction in REFIT has never been reported in a previous work. In face of the comparison with Monte-Carlo simulations, we may conclude that the analytic treatment in REFIT and SAMMY cannot deal with large corrections. In order to

avoid any systematic error exceeding 1%, we did not include in the present analysis the capture yield from the thick ^{129}I sample (h=14.8 mm). In order to analyse data from thick capture samples it is recommended to calculate the multiple scattering correction with Monte-Carlo algorithms of the SAMSMC type.

Chapter 7

The ^{127}I and ^{129}I total and capture cross sections

This chapter presents the ^{127}I(n,tot), ^{127}I(n,γ), ^{129}I(n,tot) and ^{129}I(nγ) cross sections determined within the 0.5 eV to 100 keV energy range over eighteen measurements (Tables 7.1 and 7.2). A preliminary evaluation of the total and capture cross sections is also proposed from thermal energy up to 20 MeV. Below 5 keV, the resonance parameters are the result of a simultaneous analysis involving transmission and capture measurements. Within the 5 keV to 10 keV energy range, the resonance parameters are only extracted from transmission measurements. Above 100 keV, we have normalised the partial cross sections available in the JEFF3 library with the information provided by the present results.

In the Resolved Resonance Range (RRR), we decided to take advantage of the simultaneous REFIT fitting procedure. The consistency of the results was then verified with the SAMMY code. In this way, the computation time needed to achieve this final step was noticeably decreased. The analysis of the Unresolved Resonance Range (URR) was also performed with the statistical model code FITACS of F.Froehner, incorporated into SAMMY by N.M.Larson.

In a last step, the final resolved parameters and the average cross sections were converted into ENDF-6 format making possible the calculation of integral quantities with the NJOY code [145].

Table 7.1: Experimental data available to investigate the Resolved Resonance Range.

Isotope	Energy range	Transmission	Capture
Iodine 127	0.5 eV - 11 eV	Thick sample 100 Hz (Cd+Co+Na)	
	11 eV - 500 eV	Thick sample 100 Hz (Cd+Co+Na)	Thin sample 800 Hz (Na)
		Thick sample 800 Hz (without filters)	Thin sample 800 Hz (S)
		Thick sample 800 Hz (Na)	Thick sample 800 Hz (Na+S)
		Thick sample 800 Hz (W+Mo+Co+Bi+Na+S)	
		Thin sample 800 Hz (Na)	
		LiI sample 100 Hz (Cd+Co+Na)	
	500 eV - 2500 eV	Thick sample 800 Hz (without filters)	Thin sample 800 Hz (Na)
		Thick sample 800 Hz (Na)	Thin sample 800 Hz (S)
		Thick sample 800 Hz (W+Mo+Co+Bi+Na+S)	Thick sample 800 Hz (Na+S)
	2500 eV - 3500 eV	Thick sample 800 Hz (without filters)	Thin sample 800 Hz (S)
	3500 eV - 5000 eV	Thick sample 800 Hz (without filters)	Thick sample 800 Hz (Na+S)
	5000 eV - 10 keV	Thick sample 800 Hz (without filters)	
Iodine 129	0.5 eV - 11 eV	Thick sample 800 Hz (Cd+Co+Na)	
	11 eV - 700 eV	Thin sample 100 Hz (Cd+Co+Na)	Thin sample 800 Hz (Na)
		Thick sample 100 Hz (Cd+Co+Na)	Thin sample 800 Hz (S)
		Thick sample 800 Hz (without filters)	
		Thick sample 800 Hz (Na)	
		Thick sample 800 Hz (W+Mo+Co+Bi+Na+S)	
		Thick sample 800 Hz (without filter)	
		Thick sample 800 Hz (Na+S)	
	700 eV - 1500 eV	Thick sample 100 Hz (Cd+Co+Na)	Thin sample 800 Hz (Na)
		Thick sample 800 Hz (without filters)	Thin sample 800 Hz (S)
		Thick sample 800 Hz (Na)	
		Thick sample 800 Hz (W+Mo+Co+Bi+Na+S)	
		Thick sample 800 Hz (without filter)	
		Thick sample 800 Hz (Na+S)	
	1500 eV - 2200 eV	Thick sample 800 Hz (without filters)	Thin sample 800 Hz (Na)
		Thick sample 800 Hz (Na)	Thin sample 800 Hz (S)
		Thick sample 800 Hz (W+Mo+Co+Bi+Na+S)	
		Thick sample 800 Hz (without filter)	
		Thick sample 800 Hz (Na+S)	
	2200 eV - 5000 eV	Thick sample 800 Hz (without filters)	Thin sample 800 Hz (S)
	5000 eV - 10 keV	Thick sample 800 Hz (without filters)	

Table 7.2: Experimental data available to investigate the Unresolved Resonance Range.

Isotope	Energy range	Transmission			Capture		
Iodine 127	3.5 keV - 100 keV	Thick sample	800 Hz	(without filters)	Thin sample	800 Hz	(S)
		Thick sample	800 Hz	(Na)	Thick sample	800Hz	(Na+S)
		Thick sample	800 Hz	(W+Mo+Co+Bi+Na+S)			
	100 keV - 1 MeV	Thick sample	800 Hz	(W+Mo+Co+Bi+Na+S)			
Iodine 129	3.5 keV - 100 keV	Thick sample	800 Hz	(Na)	Thin sample	800 Hz	(Na)
		Thick sample	800 Hz	(W+Mo+Co+Bi+Na+S)	Thin sample	800 Hz	(S)
		Thick sample	800 Hz	(W+Mo+Co+Bi+Na+S)			

7.1 Resolved Resonance Range (RRR)

The ^{127}I and ^{129}I resonance parameters fitted in this work are given in Appendix D. The respective identification of 719 and 400 resonances improve significantly the knowledge of the iodine Resolved Resonance Range (Table 7.3). For this analysis, the thermal capture (σ_γ^{th}) and total (σ_t^{th}) cross sections are essential ingredients in the determination of the contribution of the external levels and of the potential scattering. Careful state-of-the-art measurements of the natural iodine thermal capture cross section was performed by Molnar et al. at the guided cold neutron beam of the research reactor of the Budapest Neutron Center (BNC). The value reported in this work is a not yet published preliminary result. For ^{129}I, measurements are planned at BNC before the end of the year.

Table 7.3: Upper energy limit of the Resolved Resonance Range and number of resonances.

	Iodine 127		Iodine 129	
BROND2.2			2175.0 eV	66
ENDFB-VI	1037.0 eV	93	153.0 eV	5
JEFF3	2027.0 eV	188	3004.0 eV	126
JENDL3.3	4259.0 eV	374	3004.0 eV	127
This work	10035.0 eV	719	10022.0 eV	400

7.1.1 ^{127}I resonance parameters

Below 100 eV, the resonance parameters are determined from the simultaneous analysis of all available data. The ^{129}I capture and transmission measurements are also included in the calculation together with those of natural iodine. Beyond 5 keV, the resonance parameters are deduced only from the transmission measurements.

• External levels and distant level parameters

The thermal cross section is the resulting cross section of the tails of all resonances including negative resonances corresponding to levels below the neutron binding energy. Various ad-hoc approaches exist to describe their contributions. A convenient approximation consists in using fictious broad negative resonances [28].

The resonance parameters as well as the effective potential scattering length (R') are determined together from the simultaneous analysis of our capture and transmission data including the recent ^{127}I thermal capture cross section from Molnar et al. [59]. The given value of (6.0±0.1) barns is in excellent agreement with the weighted average value determined from all available thermal capture cross sections reported in the literature (Table 7.4). Starting with the prior parameters recommended in JENDL3.3 and with a channel radius $a_c = 6.801$ fm, we obtain the following posterior estimates:

$$E_-(J^\pi = 2^+) = -55.64 \pm 0.14 \text{ eV}, \quad \Gamma_\gamma = 103.9 \pm 0.9 \text{ meV}, \quad \Gamma_n = 196.5 \pm 1.5 \text{ meV}$$

$$E_-(J^\pi = 3^+) = -47.84 \pm 0.10 \text{ eV}, \quad \Gamma_\gamma = 103.8 \pm 0.8 \text{ meV}, \quad \Gamma_n = 108.5 \pm 0.8 \text{ meV}$$

$$R' = 5.47 \pm 0.09 \text{ fm}$$

The accuracy quoted for the resonance parameters comes from the SAMMY code. The uncertainty budget in the determination of R' is given in Table 7.5. The new ^{127}I total and capture cross sections below 100 eV are shown in Figure 7.1 together with the cross sections recommended in ENDF/B-VI, JEFF3 and JENDL3.3.

Table 7.4: ^{127}I thermal capture cross section.

Author		Year	σ_γ^{th} (barns)
Seren et al.	Phys. Rev., 72,p888	1947	6.65±1.3
Pomerance	Phys. Rev., 83,p641	1951	6.3±0.32
Tattersall et al.	J. Nucl. Energy, Part A, Reactor Sci, 12, p32	1960	6.6±0.3
Meadows et al.	Nucl. Sci. Eng., 9, p132	1961	6.22±0.15
Jozefowicz	Nucleonics, 8, p437	1963	5.84±0.2
Ryves	J. Nucl. Phys. Energy., 24, p35	1970	6.12±0.12
Friedmann et al.	Radiochimica Acta, 33, p182	1983	4.7±0.2
Katoh et al.	J. Nucl. Sci. and Tech., 36, p223	1999	6.4±0.29
Molnar et al.	Private Communication	2003	6.0±0.1
mean value			6.01±0.06

Table 7.5: Uncertainty budget in the determination of (R'). The procedure to derive the uncertainties connected to the normalisation factor and the sample composition are fully described by V.Gressier in Reference [70]. The uncertainty due to the background comes from the study conducted in Appendix A.

Description	Uncertainty
Statistical uncertainty	0.030 fm
Normalisation factor (transmission measurement)	0.018 fm
Smooth background vs. structured background	0.042 fm
^{127}I sample thickness uncertainty (Thick PbI_2 sample)	0.045 fm
Thickness uncertainty (Dummy of lead)	0.058 fm
Total	0.092 fm

- **Spin and parity**

Spin and parity information are important to account for level-level interference of nearby resonances. A first parity assignment is usually based on the inspection of the transmission data. Most s-wave resonances are recognizable in that they are made quite assymetric by the interference between resonant and potential scattering, while p-wave resonances tend to be narrower and symmetric [23]. For the ^{127}I nucleus, the parity of the resonance states cannot be determined from the shape of the resonances. The interference between the potential and the resonant scattering is indeed too small to derive any information. For that reason, below 400 eV, the parity is assigned on the basis of parity violation studies in ^{127}I p-wave neutron resonances [129, 130, 131]. Starting from these information, we use the ESTIMA code to distinguish resonances with $(l = 0)$ and $(l = 1)$. The selection is made possible according to a Bayesian criterium (P_B) below which the s- and p-waves probabilities become indistinctive. The P_B value is an arbitrary threshold

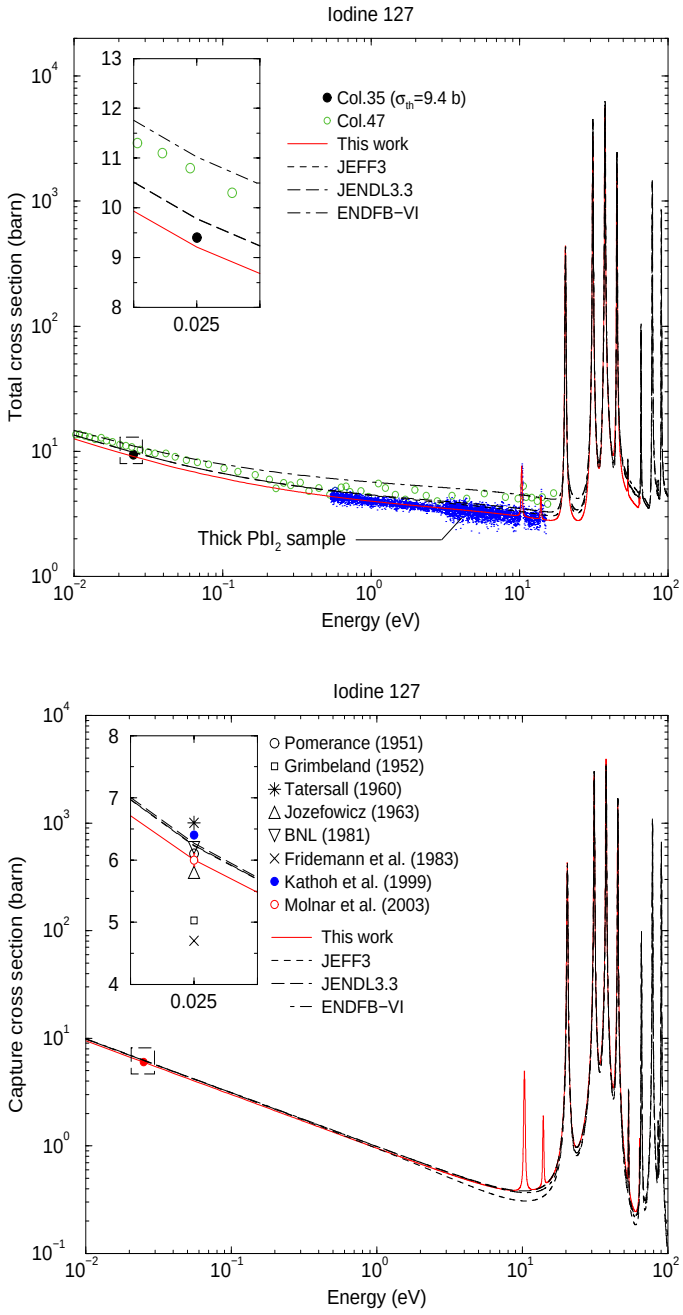

Figure 7.1: ^{127}I total and capture cross sections below 100 eV (References are available in the EXFOR data base).

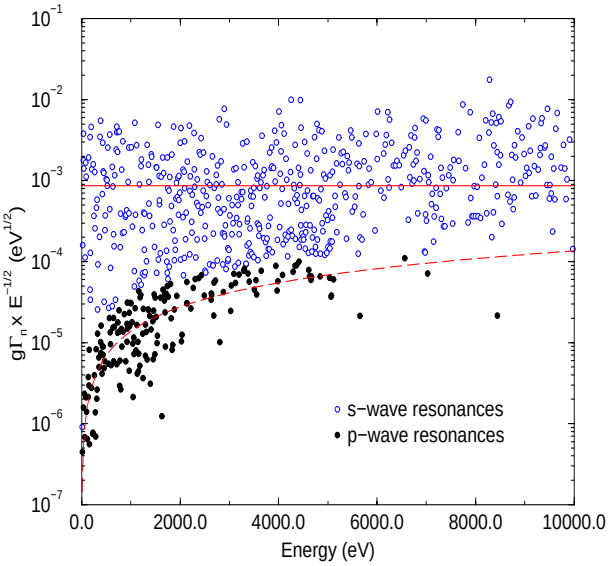

Figure 7.2: ^{127}I neutron widths in terms of $g\Gamma_n/\sqrt{E}$ obtained in this work. The results are divided in s- and p-wave resonances together with their average values up to 10 keV.

probability chosen by the user to accurately described the experimental s-wave reduced neutron widths distribution with the Porther-Thomas formula (Expression 2.53). In Figure 7.2, the ^{127}I neutron widths are expressed in terms of $g\Gamma_n/\sqrt{E}$ as a function of the resonance energy. The results are divided in s- and p-wave resonances.

The spin information for some s-waves is deduced from the level-level interference of nearby resonances. An example of the correct spin assignment for the 31.2 eV, 37.6 eV and 45.3 eV resonances is shown in Figure 7.3. The behaviour of the residual obtained with the J^π values recommended in the JENDL3.3 neutron library suggests a wrong spin assignment. The reduced chi-squared per degree of freedom is improved by replacing the configuration (2^+, 2^+, 2^+) with (3^+, 3^+, 2^+).

• Average resonance parameters from the RRR

The prior average parameters for analysing the URR are deduced from the s-wave resonances sample suggested by ESTIMA. The parameters that can be extracted are the distant level parameter (R_0^∞), the mean radiation width ($< \Gamma_{\gamma,0} >$), the level spacing (D_0) and the strength function (S_0). From the following relationship between the channel radius, the distant level parameter and the effective potential scattering length deduced together with the external levels [56]:

$$R' \;=\; a_c\,(1 \;-\; R_0^\infty) \tag{7.1}$$

we obtain:

$$R_0^\infty \;=\; 0.19 \;\pm\; 0.01$$

The radiation width is determined for 155 resonances by shape fitting up to 4.5 keV (Figure 7.4a). The weighted average value and the standard deviation of the fitted Γ_γ values are:

$$< \Gamma_{\gamma,0} > = \;\; 100.0 \;\; \text{meV} \qquad \sigma_{<\Gamma_\gamma,>} \;=\; 22.6 \;\; \text{meV}$$

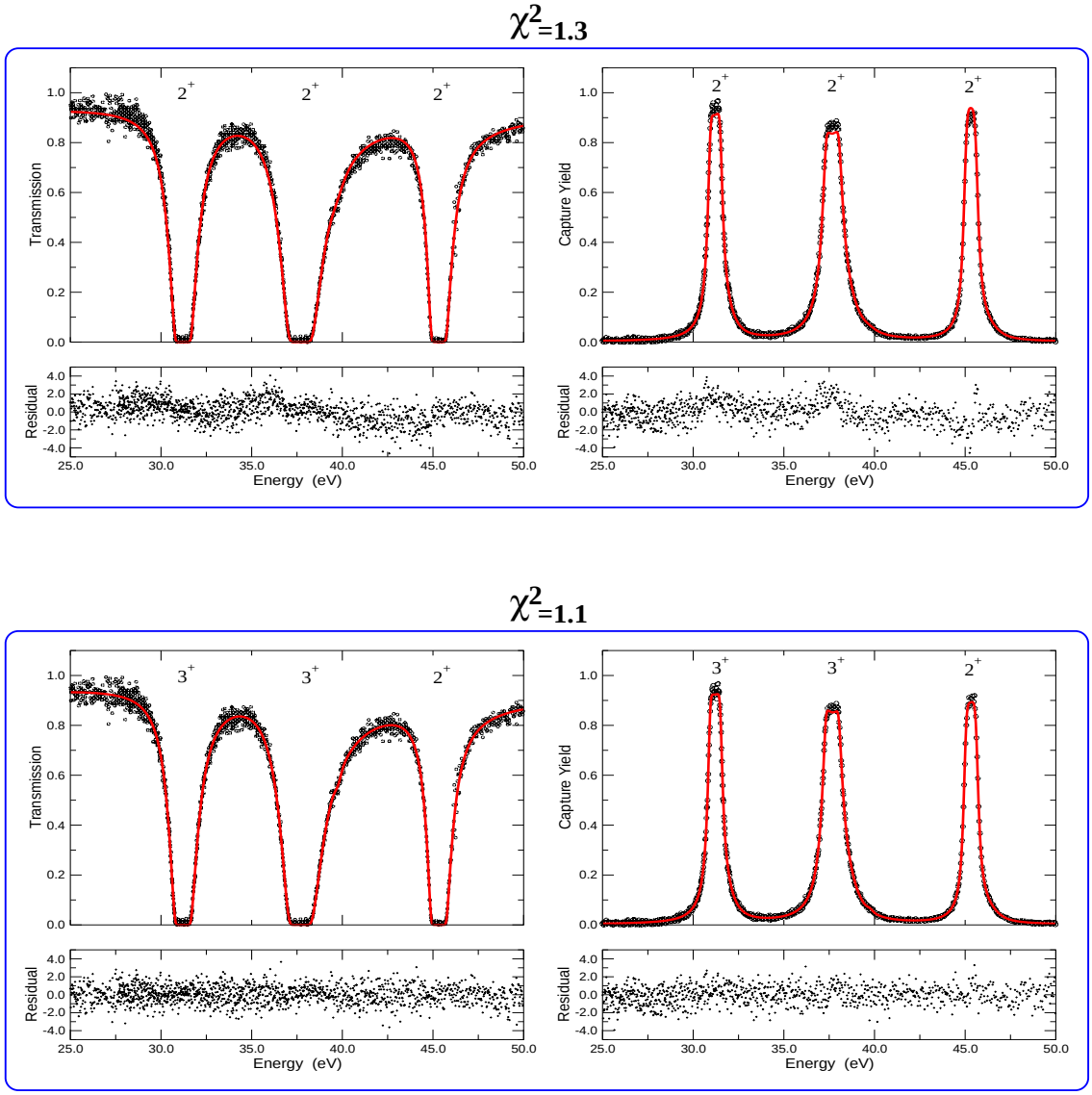

Figure 7.3: The effect of spin assignment and level-level interference for the 31.2 eV, 37.6 eV and 45.3 eV ^{127}I resonances. In the upper curves, the spin assignments of JENDL3.3 are used; in the bottom curves, the chi-squared values are improved by changing the spin assignments. Also shown in the plots are the residuals, defined as the difference between the theory and the measurement, divided by the uncertainty (see Equation 6.12). Note that the residuals for the upper curves show structure unseen in the residuals for the corrected spin assignments.

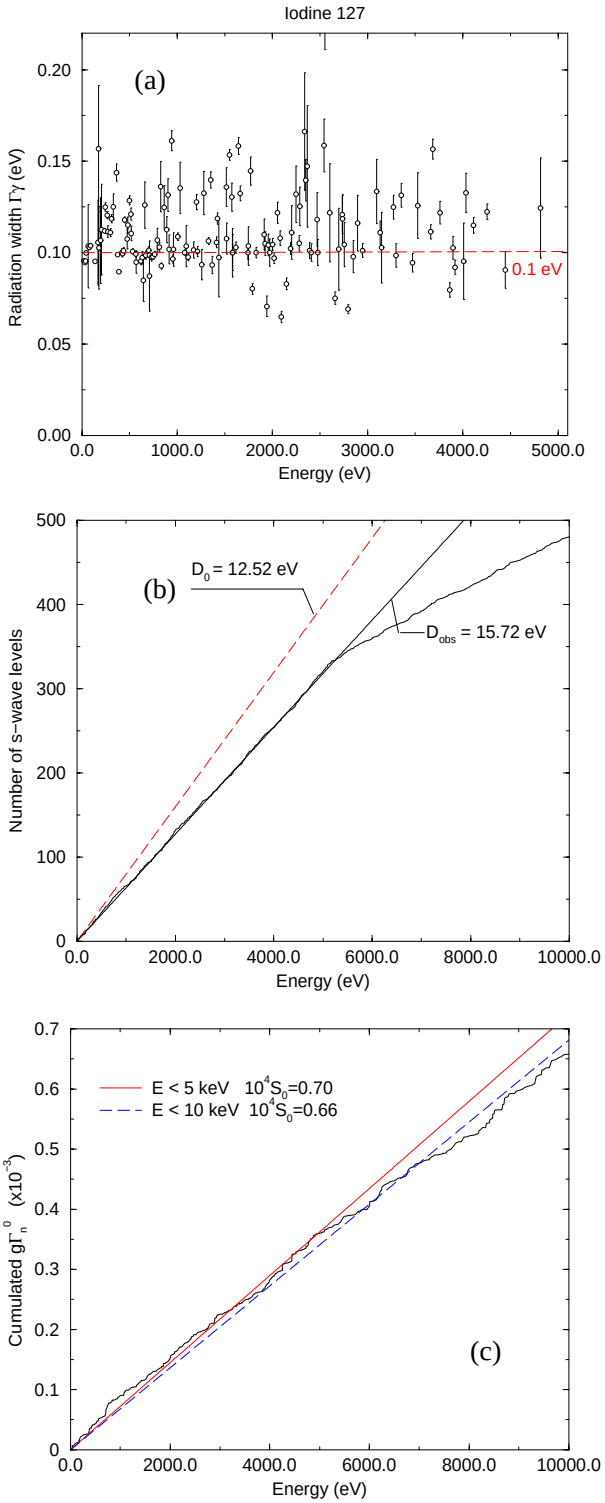

Figure 7.4: ^{127}I average parameters: (a) average radiation width $< \Gamma_{\gamma,0} >$; (b) cumulative number of s-wave resonances as a function of neutron energy (the slope of the curves yields the observed level density); (c) staircase plot of the s-wave reduced neutron widths versus neutron energy (the slope of the curves yields the s-wave strength function).

The most straightforward method to obtain (D_0) from a set of resonances consists in determining the level density (ρ_0) from the slope of the cumulative number of levels as a function of the neutron energy (Figure 7.4b). In the same way, the cumulative sum of the reduced neutron widths is related to S_0 (Figure 7.4c). However, the slopes of the level spacing distribution indicate that many weak levels are not identified, which results in an incomplete information. A more reliable method was implemented in ESTIMA to account for the missing levels [39]. The estimation procedure in this code uses methods based on the Porter-Thomas integral distribution. The number of resonances $N(x_0)$ with the same orbital momentum, having a value $x \equiv \frac{g\Gamma_n^l}{<g\Gamma_n^l>}$ larger than a threshold x_0, is given by integrating the Porter-Thomas distribution ($P(x)$):

$$N(x_0) = N \int_{x_0}^{x} P(x)\, \mathrm{d}x \;=\; N\left(1 - \mathrm{erf}\sqrt{\frac{x}{2}}\right) \tag{7.2}$$

in which N is the number of resonances estimated with ESTIMA. A large number of small resonances is missed beyond 5 keV. In this context, two parallel studies must be compared. The first one covers the overall energy range ($E < 10$ keV), and the second one is restricted to energies below 5 keV. In Figure 7.5, the number of assigned s-wave resonances is shown in two cumulative plots together with the theoretical Porter-Thomas integral distributions. The resulting (D_0) and (S_0) values are given in Table 7.6. The uncertainties include the fitting and sampling errors as explained in the ESTIMA user's manual. The results directly extracted from the cumulative sum of the reduced neutron widths (Figure 7.4c) are compatible with those from ESTIMA. The neutron strength function is not noticeably affected by the missing weak levels. The prior adopted values are then:

$$D_0 \;=\; 12.52 \;\pm\; 0.3 \text{ eV} \qquad\qquad S_0 \;=\; (0.72 \;\pm 0.06) \times 10^{-4}$$

The p-, d-, and f-wave mean level spacings are then calculated using the Gilbert and Cameron level density formula (Expression 2.44). The only free parameter is the fermion gas level density parameter (a). From the D_0 value, we obtain:

$$a \;=\; 17.416 \;\pm\; 0.041 \text{ MeV}^{-1}$$

Using this value, the D_1, D_2 and D_3 mean level spacings are:

$$D_1 \;=\; 6.48 \;\pm\; 0.15 \text{ eV}$$
$$D_2 \;=\; 4.57 \;\pm\; 0.11 \text{ eV}$$
$$D_3 \;=\; 3.62 \;\pm\; 0.09 \text{ eV}$$

Table 7.6: Mean level spacing and s-wave strength function deduced from the RRR.

	Energy Range	Mean level spacing (eV)	Strength function ($\times 10^{-4}$)
Cumulative plot	E < 10.0 keV		0.66
Cumulative plot	E < 5.0 keV	15.72	0.70
ESTIMA	E < 10.0 keV		0.66 ± 0.04
ESTIMA	E < 5.0 keV	12.52±0.3	0.72 ± 0.06

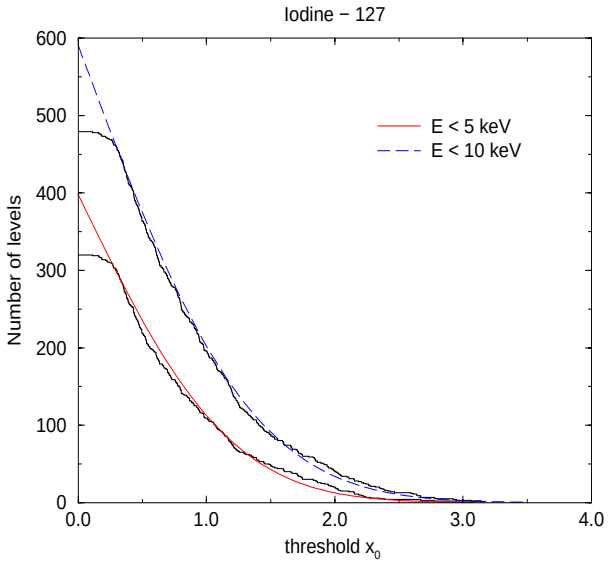

Figure 7.5: Cumulative number of s-wave resonances versus x_0 (Equation 7.2). The smooth curves are the Porter-Thomas integral distributions calculated with ESTIMA.

• Results and discussion

The ^{127}I resonance parameters available in the neutron data bases are mainly taken from three earlier TOF measurements. In 1965, the total cross section was investigated by Garg et al. up to 500 keV at a 200 m flight path of the Columbia University Synchro-Cyclotron, using three transmission samples of solid elemental iodine (9.3×10^{-2}, 2.0×10^{-2}, and 3.5×10^{-3} at/b) [132]. Some ten years later, in 1976, a series of capture, self-indication and transmission measurements were carried out at a 60 m flight path of the GELINA facility by Rhor et al., using three PbI_2 samples (1.236×10^{-2}, 2.485×10^{-3}, and 7.438×10^{-3} at/b), within the 20 eV to 5.0 keV energy range [133]. Finally, in 1983, Macklin determined the capture cross section at the ORELA facility from 2.5 keV to 500 keV, using a PbI_2 sample having dimensions of $20\times52\times1.6$ mm and weighing 11.91 g [16]. In ENDF/B-VI and JEFF3, the evaluation was done on the basis of the Brookhaven compilation [56], which contains the results obtained by Garg and Rhor. The JENDL3.3 data base includes those from Macklin.

We have compared our results with the reduced neutron widths ($g\Gamma_n^0$) from Garg et al., with the ($g\Gamma_n$) values from Rhor et al., and with the capture areas (A_γ) given by Macklin. The ratios of these quantities as a function of the neutron energy are shown in Figures 7.6, 7.7 and 7.8. The results from Garg et al. are affected by a systematic error of about 13%, possibly due to the use of unstable elemental iodine sample. The peak of the distribution obtain with the results from Macklin is centered around 0.95. The larger part of this bias can be easily explained with the thickness and normalisation uncertainties. Indeed, an overall accuracy better than 4% cannot be achieved from the analysis of a single capture measurement performed with a very thin sample in powder form. The best agreement is obtained with the results from measurements performed more than twenty years ago at the IRMM. Below 1 keV, the discrepancy is about 2% in average.

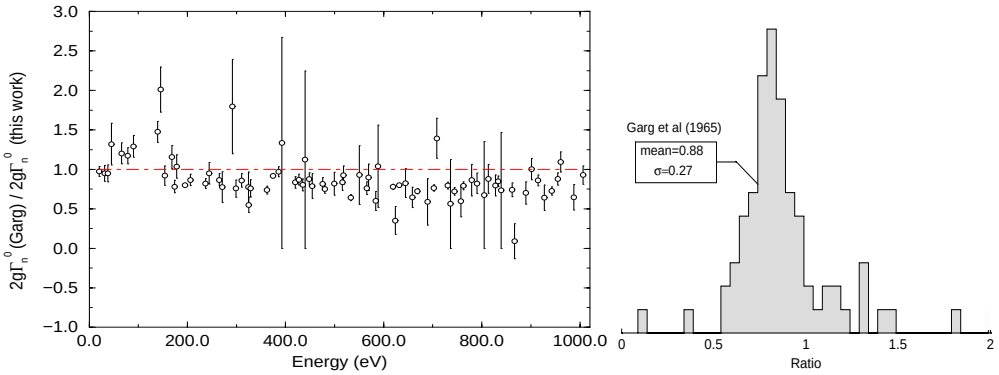

Figure 7.6: Comparison between the s-wave reduced neutron widths from Garg et al. [132] and our results.

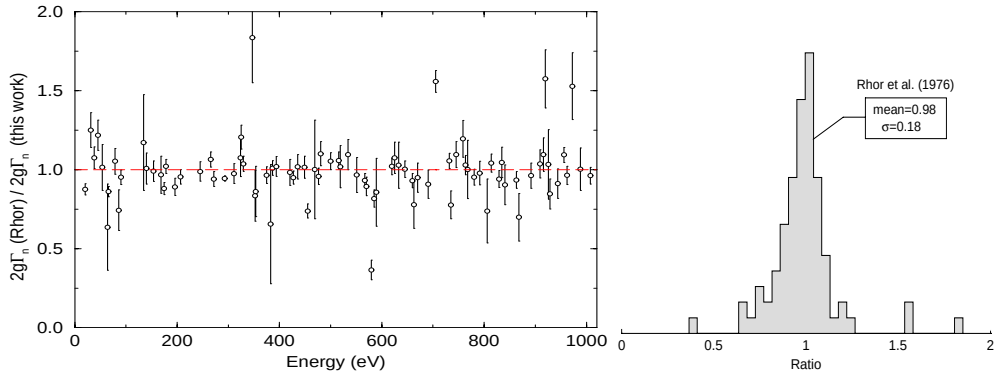

Figure 7.7: Comparison between the s-wave neutron widths from Rohr et al. [133] and our results.

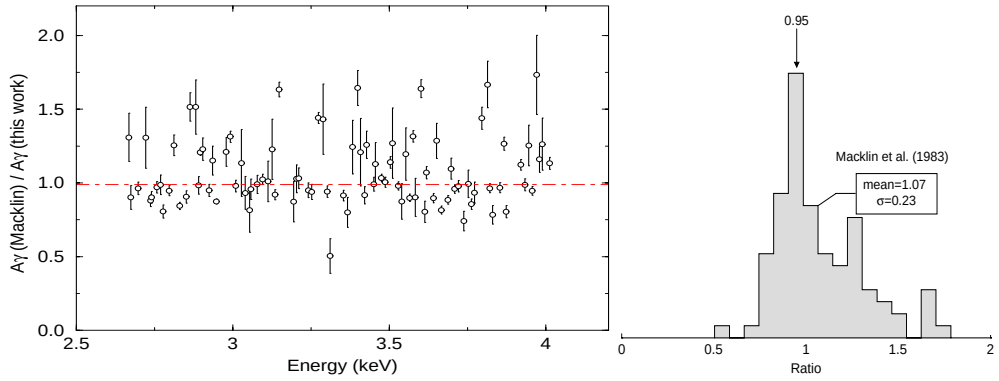

Figure 7.8: Comparison between the capture areas from Macklin [16] and our results.

7.1.2 ^{129}I resonance parameters

The resonance parameters given in this work are preliminary values, since a new elemental sample composition and thermal capture cross section will be provided by Molnar et al. at the end of the year [59].

The first fourteen resonances are extracted from a simultaneous analysis involving nine TOF spectra (Table 7.1). The simultaneous transmission and capture analyses is completed up to 5 keV. Beyond 5 keV, the neutron widths are only deduced from a single transmission measurement. Examples of data and theoretical curves are shown in Figures 7.9 and 7.10.

• External levels and distant level parameters

Five earlier works report ^{129}I thermal capture cross sections (Table 7.7). Among them, Roy et al., Friedmann et al. and Nakamura et al. used the activation technique with a near-core reactor based thermal spectrum. Whereas, Block et al. and Pattenden have measured the total cross section at the ORNL fast chopper Time-Of-Flight neutron spectrometer. They deduced the capture cross section by subtracting the scattering cross section.

Table 7.7: ^{129}I thermal capture cross section.

Author		Year	σ_γ^{th} (barns)
Roy et al.	Can. J. Chem., 36, p1424	1958	26.7 ± 2.0
Block et al.	Nucl. Sci. Eng., 8, p112	1960	31.0 ± 4.0
Pattenden	Nucl. Sci. Eng., 17, p371	1963	28.0 ± 2.0
Friedmann et al.	Radiochimica Acta, 33, p182	1983	33.9 ± 1.9
Nakamura et al.	Nucl. Sci. Tech., 33, p283	1996	30.3 ± 1.2
mean value			30.0 ± 0.8

The three measurements based on the activation technique yield discrepant values. The result provided by Roy et al. is questionable because the existence of the isomeric ^{130m}I (9.2 min) has been established latter in 1966 [134]. The radiative capture of neutrons is then complicated by the possibility of the activation of the metastable state and the ground state of ^{130}I. Nakamura et al. pointed out that the analysis carried out by Roy et al. did not take into account the full contribution from the isomeric state.

The in-beam technique used by Block and Pattenden is insensitive to the isomer. From the information reported by Pattenden, we find a total cross section of about 34.8 barns, which agree with the value of (35±4) barns reported by Block. The latter deduced a ^{129}I capture cross section of 31 barns by assuming a ^{127}I scattering cross section of 4 barns [135]. By contrast, the capture cross section of (28±2) barns was deduced by Pattenden from a least squares fit of the data within the [0.01 eV-0.7 eV] energy range with the following equation:

$$\sigma_t(E) \;=\; \frac{a}{\sqrt{E}} \;+\; b \tag{7.3}$$

in which (a) describes the $1/v$ capture cross section and (b) stands for an energy independent scattering cross section. A SAMMY calculation with the total cross section from Block and Pattenden together with our transmission measurement carried out at 100 Hz repetition rate, gives a capture cross section of about 28.6 barns. This result confirms the Pattenden capture cross section.

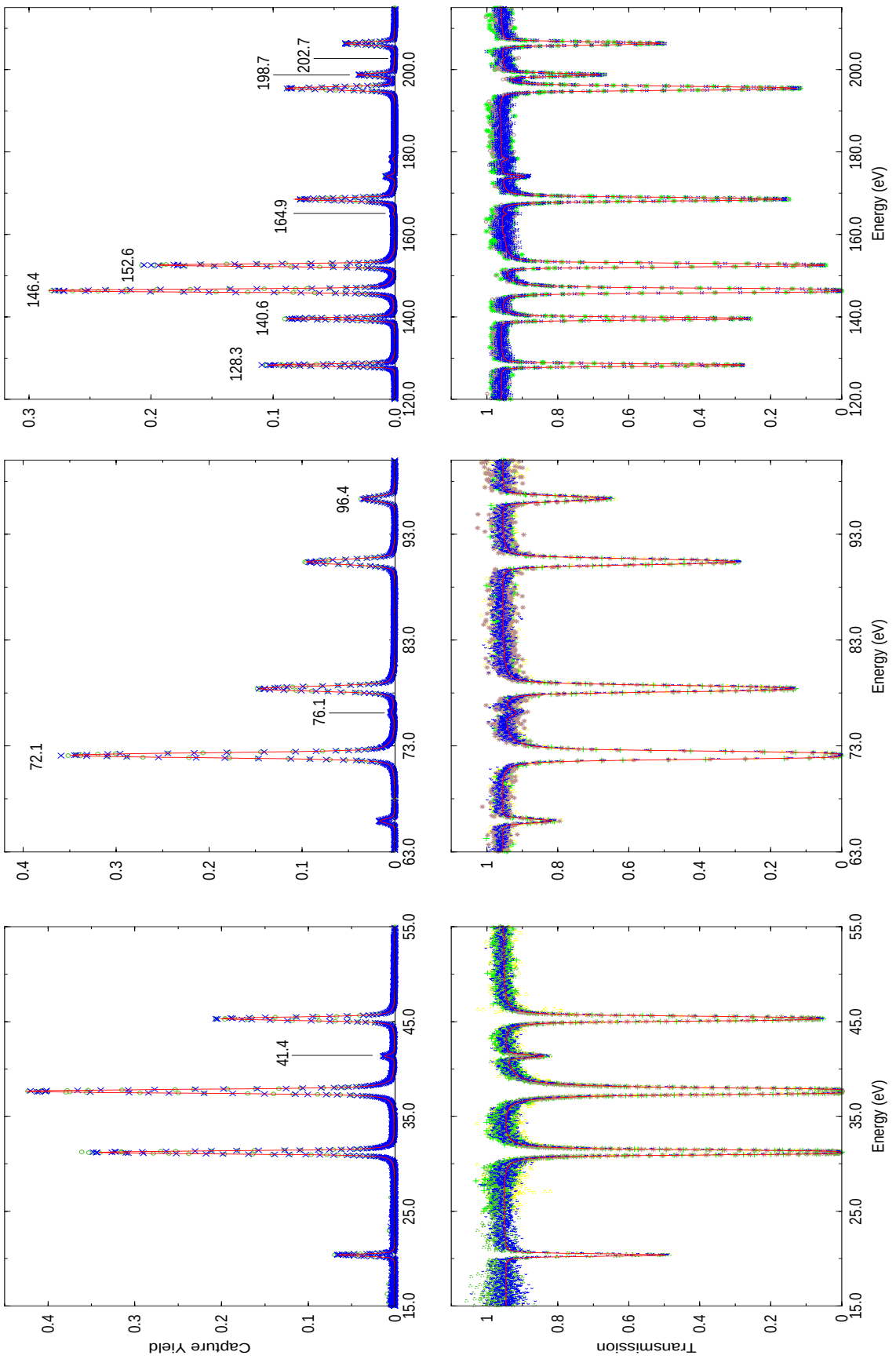

Figure 7.9: Examples of resonance peaks in the thick transmission samples and in the thin capture samples together with their adjusted theoretical curves (solid line). The energy of the ^{129}I resonances are indicated.

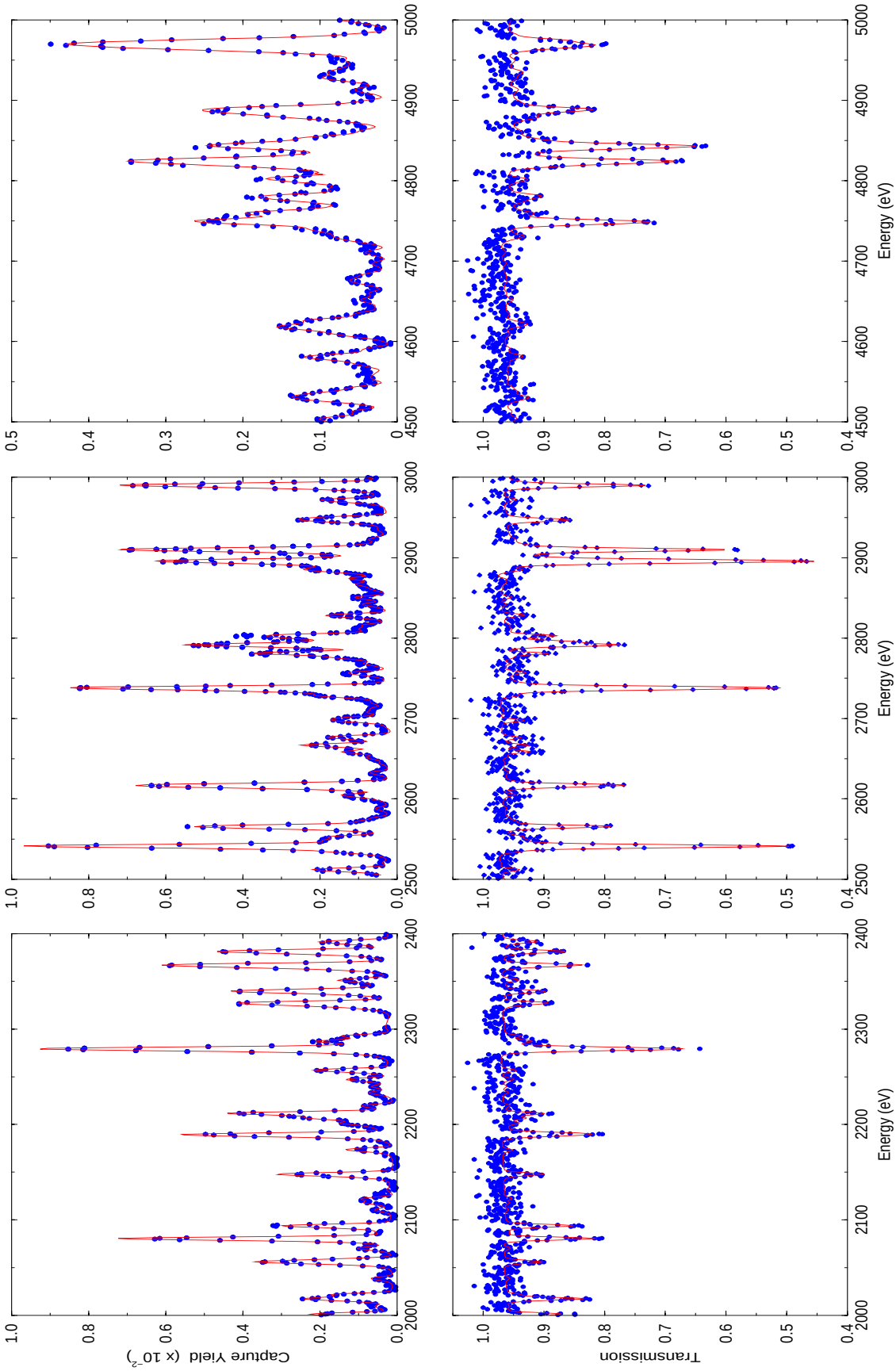

Figure 7.10: Examples of capture and transmission data obtained respectively with the thin and thick radioactive PbI_2 samples over three energy ranges. The solid line is the result of the least-squares fit.

Table 7.8: Uncertainty budget in the determination of (R'). The analytic determination of the uncertainties are explained in Reference [70].

Description	Uncertainty
Statistical uncertainty	0.020 fm
Normalisation factor (transmission measurement)	0.057 fm
^{129}I sample thickness uncertainty (thick PbI_2 sample)	0.071 fm
Natural iodine contribution	0.058 fm
Oxygen contribution	1.457 fm
Hydrogen contribution	0.307 fm
Sulfur contribution	0.036 fm
Sodium contribution	0.046 fm
Nitrogen contribution	0.684 fm
Natural lead contribution	0.335 fm
Total	1.67 fm

On the basis of these remarks, the relevant ^{129}I thermal values that can be used in this work are those reported by Pattenden, Friedmann and Nakamura. There are not many possibilities to improve the trend brought by these three existing thermal capture cross sections without the future result from Molnar et al. Therefore, in accordance with the good agreement between the Japanese work and the weighted average value, we decided to adopt the value of (30.3±1.2) barns.

With the prior input parameters recommended in the JEFF3 library, the posterior parameters obtained with SAMMY are:

$$E_-(J^\pi = 4^+) = -10.76 \pm 0.07 \text{ eV}, \quad \Gamma_\gamma = 109.3 \pm 4.0 \text{ meV}, \quad \Gamma_n = 44.68 \pm 0.86 \text{ meV}$$

$$R' \ = \ 5.9 \ \pm \ 1.67 \text{ fm}$$

The accuracy of the resonance parameters are those given by SAMMY. The uncertainty budget in the determination of R' is given in Table 7.8. Detailed procedure to determine the R' accuracy is given by V.Gressier in Reference [70]. Without improved oxygen, hydrogen and nitrogen mass fraction, we cannot achieve a better estimate of the effective potential scattering length. With this modest change of the external parameters, a satisfactory agreement is obtained between the calculated and experimental values as shown in Figure 7.11.

- **Spin and parity**

For the ^{129}I nucleus, the interference between the potential and resonant scattering is too small to derive any parity or spin information. Without any experimental evidence, we assign the orbital momentum of the resonances on the basis of the suggestion provided by the Bayesian approach implemented in the ESTIMA code [39]. The result is shown in Figure 7.12.

Similarly, the spin of the ^{129}I resonances is unknown. Therefore, we use the SPGSIG option of the CALENDF code for spin assignment applications [36]. The suggestion is based on the repulsion law proposed by Wigner (Equation 2.49) in association with the Gilbert and Cameron formula (Equation 2.44).

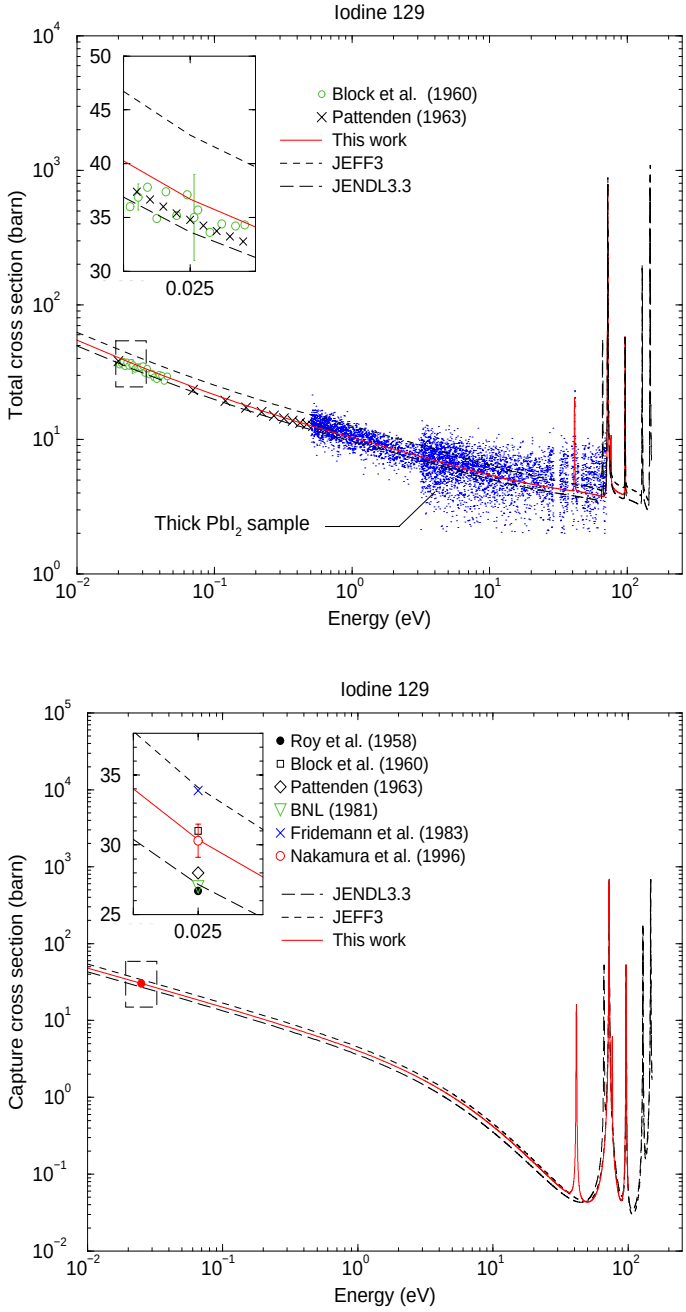

Figure 7.11: ^{129}I total and capture cross sections below 100 eV compared with the JEFF3 and JENDL3.3 data bases together with experimental thermal capture cross sections reported in the literature.

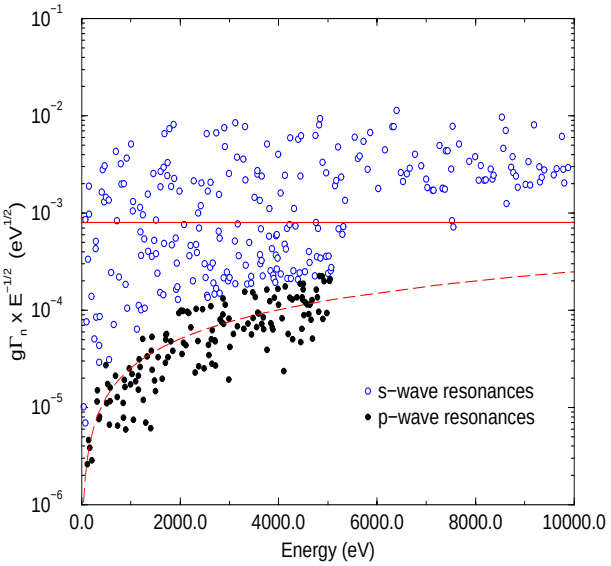

Figure 7.12: ^{129}I neutron widths in terms of $g\Gamma_n/\sqrt{E}$ up to 10 keV. The results are divided in s- and p-wave resonances together with their average value.

• Average resonance parameters from the RRR

A careful determination of the prior ^{129}I average parameters has never been performed since the resonance parameters available in the ENDF files were only deduced from the capture areas reported by Macklin [16]. In the JEFF3 data base, all resonances were assumed to be s-wave resonances. For each resonance, a neutron width value was generated from the measured capture area, assuming a radiative capture width of 90 meV. Therefore, in the Unresolved Resonance Range, the earlier theoretical calculations were mostly based on nuclear systematics. In this work, the prior average parameters are deduced from the confident s-wave resonances sample provided by ESTIMA.

The distant level parameter is deduced from the effective potential scattering length determined together with the negative resonance. From the R' value of 5.9 fm and a channel width equal to 6.837 fm, we obtain:

$$R_0^{\infty} \simeq 0.137$$

Owing to the poor thickness accuracy associated to the structureless hydrogen and nitrogen isotopes, the above mentioned value is questionable.

The radiation widths obtained from the simultaneous capture and transmission analysis are shown in Figure 7.13 as a function of the resonance energy. The mean radiation width and the associated standard deviation given below are obtained from 55 Γ_γ values.

$$< \Gamma_{\gamma,0} > = 106.0 \text{ meV} \qquad \sigma_{<\Gamma_{\gamma,0}>} = 15.2 \text{ meV}$$

The mean level spacing, the strength function and the number of missing levels are determined simultaneously with the ESTIMA code. The Porter-Thomas integral distribution method (Equation 7.2) is applied within the 40 eV to 5 keV energy range. The theoretical Porter-Thomas integral distribution is shown on the right hand of Figure 7.13 together with the experimental distribution. The number of missing levels reaches 38 resonances and the s-wave average resonance parameters given by ESTIMA are:

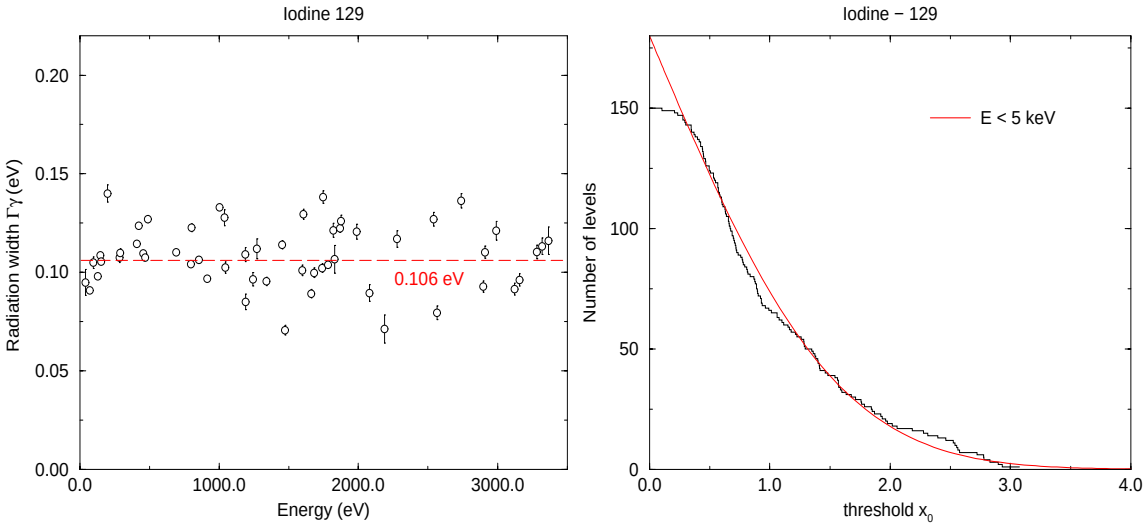

Figure 7.13: ^{129}I average radiation width and cumulative number of s-wave resonances versus x_0 (Equation 7.2). The smooth curves are the Porter-Thomas integral distributions calculated with ESTIMA.

$$D_0 = 27.3 \pm 0.9 \text{ eV} \qquad S_0 = (0.54 \pm 0.07) \times 10^{-4}$$

The p-wave mean level spacing is then deduced from the Gilbert and Cameron formula (Expression 2.44). From the D_0 value we obtain a fermion gas level density parameter close to:

$$a = 16.56 \pm 0.06 \text{ MeV}^{-1}$$

Using this value, the p-wave mean level spacing is:

$$D_1 = 14.1 \pm 0.53 \text{ eV}$$

• Results and discussion

Very little experimental works have been done on neutron cross sections of ^{129}I. The first five s-wave resonances were reported in 1963 by Pattenden [13]. The $g\Gamma_n$ values were derived from transmission studies carried out at the ORNL chopper assuming a mean radiation width of 100 meV. Some twenty years later, neutron capture by ^{129}I was reported by Macklin [16]. The capture measurements were carried out at the Oak Ridge Electron Linear Accelerator up to 500 keV with a PbI_2 sample having dimension of $26 \times 52 \times 2$ mm and weighing 18.76 g. The ^{129}I content of 1.3×10^{-3} at/barn was determined by comparison of the sample radioactivity with an Amersham standard. The thickness accuracy reported in the Macklin's article is about 3%. The recommended resonance parameters in the ENDF/B-VI neutron data base come from the Pattenden's results. Those available in the JEFF3, JENDL3.3 and BROND2.2 neutron libraries were generated from the capture area given by Macklin.

In figure 7.14, we compare the capture areas reported by Macklin below 2.3 keV with the present results. The mean discrepancy between the two data sets is about 3.6%. This systematic uncertainty agrees with the ^{129}I mass fraction accuracy close to 3% quoted for the present data and reported by Macklin. For the first broad s-wave resonance at 72.1 keV, the discrepancy reaches 10%. We cannot explain this bias with the thickness accuracy alone. As any meaningful

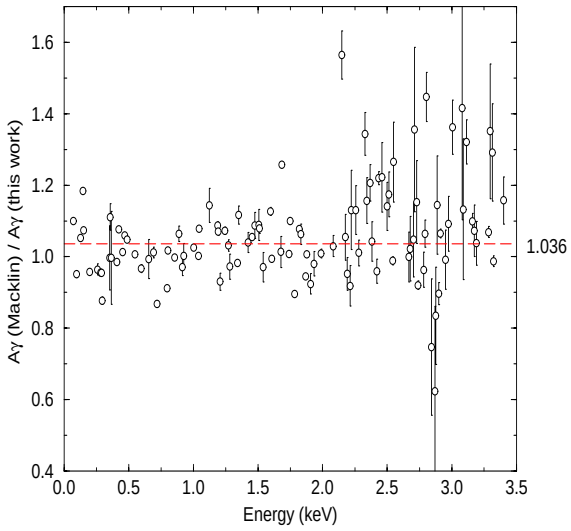

Figure 7.14: Comparison between the ^{129}I capture areas given by Macklin [16] and the present values.

systematic trend from level to level can be distinguished in Figure 7.14, the larger part of this discrepancies probably come from the data processing and the resonance peak parametrisation.

Macklin has fitted the neutron capture peaks of ^{129}I by least squares adjustment of Single Level Breit-Wigner parameters, assuming throughout an average s-wave spin factor $g \simeq 0.5$. Moreover, above 2 keV, the capture areas were analysed using a sample data from which ^{127}I capture cross section had been subtracted. Results obtained from this technique are often questionable, because of the resonance overlaps, the effect of the resolution function and the use of prior multiple scattering corrections. The SAMMY and REFIT codes include such experimental corrections in the fitting procedure. That may explain the larger spread around the mean value observed in Figure 7.14 above 2 keV.

The present set of ^{129}I resonance parameters is then the first to be extracted over a wide energy range with modern shape analysis techniques.

7.2 Unresolved Resonance Range (URR)

We used the generalised Hauser-Feshbach formalism implemented in the FITACS option of SAMMY to analyse the iodine URR (see Chapter 2). Although resonance structures are still visible above 10 keV, resonances are very much overlapping. In the present analysis, the energy region above 10 keV is considered to be the Unresolved Resonance Range (Figure 7.15). The energetically allowed reactions are the radiative capture, the elastic and inelastic scattering. The first ^{127}I and ^{129}I inelastic channels open respectively at 57.6 keV ($7/2^+$) and 27.8 keV ($5/2^+$).

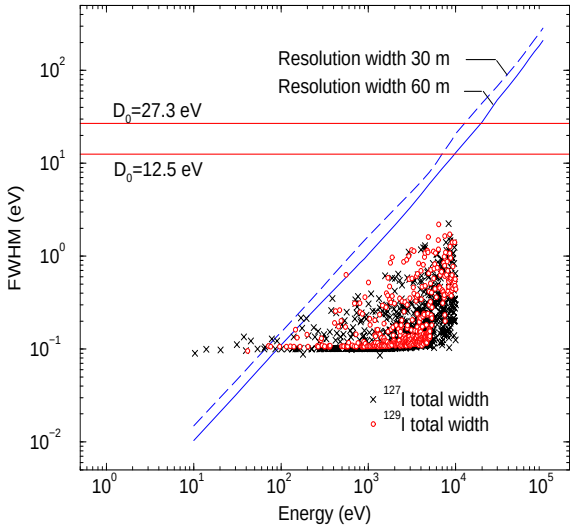

Figure 7.15: The experimental resolution of the facility and the level density of the body under investigation are the main criteria which define the upper energy limit of the Resolved Resonance Range. The ^{127}I and ^{129}I mean level spacing are respectively 12.5 eV and 27.3 eV.

In order to deduce a set of average resonance parameters (S_l, D_l, R_l^{∞} and $< \Gamma_{\gamma,l} >$) from experimental capture and transmission data, one has to account for the fluctuations of the cross section and the multiple scattering effects [136]. For this purpose we used the Monte-Carlo code SESH [137, 138].

7.2.1 Data corrections

The familiar exponential relationship $T = e^{-n\sigma_t}$ between the transmission (T), the sample thickness (n) and the Doppler broadened total cross section (σ_t) is applicable only if the cross section is smooth and does not vary noticeably within the width of the resolution function. Generally, these variations cannot be neglected. The relationship between the average transmission and the average total cross section becomes [23]:

$$\begin{aligned} < T > &= < e^{-n(\sigma_t - <\sigma_t>)} > \mathrm{e}^{-n<\sigma_t>} \\ &= e^{-n<\sigma_t>} \left(1 + \frac{n^2}{2} var(\sigma_t) + \frac{n^4}{24} var^2(\sigma_t) + \cdots\right) \end{aligned} \tag{7.4}$$

in which the variance, $var(\sigma_t) =< (\sigma_t - < \sigma_t >)^2 >$, and higher moments of the total cross section distribution indicate how pronounced the resonant structures are. Similarly, the direct capture yield divided by the sample thickness cannot be equated to the capture cross section,

except in the limit of very thin samples. For practical sample thicknesses, the capture yield is always affected by the self-shielding and the multiple scattering [23]:

$$< Y >=< \left(1 - e^{-n\sigma_t}\right) \frac{n\sigma_\gamma}{n\sigma_t} + Y_1 + Y_2 + \cdots > \tag{7.5}$$

where Y_k is the probability that detected capture occurs after k scatterings in the sample.

Dresner was the first to solve the self-shielding and multiple scattering problems for neutron capture data [125]. He proposed an analytic solution for a target disk with a radius much larger than its thickness and a cylindrical neutron beam perpendicular to its surface. Macklin [139] gave a relatively simple analytic expressions approximating the Dresner's results. A similar approach was implemented in REFIT by Moxon to describe the resolution function of the Li-glass detector used in transmission (see Appendix B). Dresner's and Macklin's results depend on a number of assumptions that are generally justified for thin samples. In order to avoid these limits, one must resort to Monte-Carlo sampling of resonance ladders. Such a simulation can be performed by using the MCNP or the SESH code. Using MCNP, one has to be careful since the sampling of the cross section is based on point-wise data. On the contrary, the SESH code was especially written for the calculation of sample thickness corrections to resonance-averaged transmission and capture data. The program simulates multiple collision events and calculates the self-shielding correction for a cylindrical sample. For each neutron energy, it generates a resonance environment by sampling resonance spacing and partial widths from the familiar level statistics. The Doppler broadened total, capture and scattering cross sections are then computed from the sampled resonance parameters in SLBW approximation.

The self-shielding and multiple scattering corrections from MCNP, SESH and the Dresner's formula were compared in Reference [140] over ^{232}Th capture data from 4.0 keV up to 40 keV. Within this energy range, the self shielding correction reaches 0.03. The discrepancies between the SESH code and the Dresner's results is about 0.005 in average. The results from MCNP are systematically overestimated by at least 0.001.

We used the SESH code to correct our capture and transmission data. The final results consists in two correction factors C_T and C_Y. The total and capture cross sections are then deduced from the transmission and capture yield as follows:

$$< \sigma_t >\equiv -\frac{1}{n}\left(\ln(< T >) - \ln(C_T)\right) \tag{7.6}$$

$$< \sigma_\gamma >\equiv \frac{1}{n}\frac{< Y >}{C_Y} \tag{7.7}$$

7.2.2 The ^{127}I average cross sections

The average cross sections are obtained from a simultaneous FITACS fit over three transmission data and two capture data. Pointwise cross sections and FITACS results are shown in Figure 7.16. The experimental total cross sections come from the thick transmission sample data taken without any black filters in the neutron beam, with the Na filter alone, and with all the black filters. Due to the sulphur filter which was kept permanently in the neutron beam and natural lead resonances, averaged pointwise capture data in the vicinity of 30 keV have been left out of this analysis. The arrow indicates the first inelastic level at 57.6 keV. The solid lines represent the capture and total cross sections given by FITACS.

The ^{127}I average resonance parameters and their correlation coefficients are listed in Table 7.9. They have been obtained with the help of the prior s-wave parameters extracted from the Resolved Resonance Range analysis. In FITACS, the s-wave mean level spacing is a fixed input parameter. $D_{l=1,2,\ldots}$ are then calculated with the Gilbert and Cameron formula. It should be

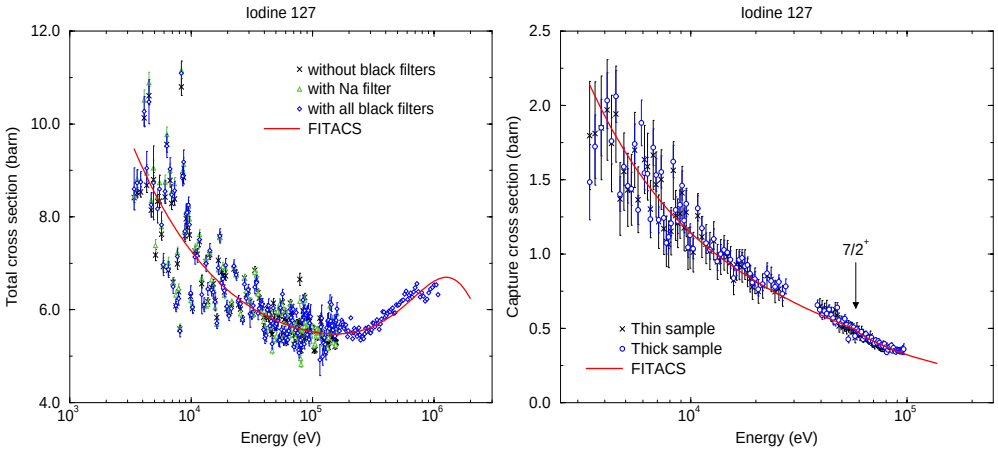

Figure 7.16: Experimental ^{127}I total and capture cross sections together with the FITACS results.

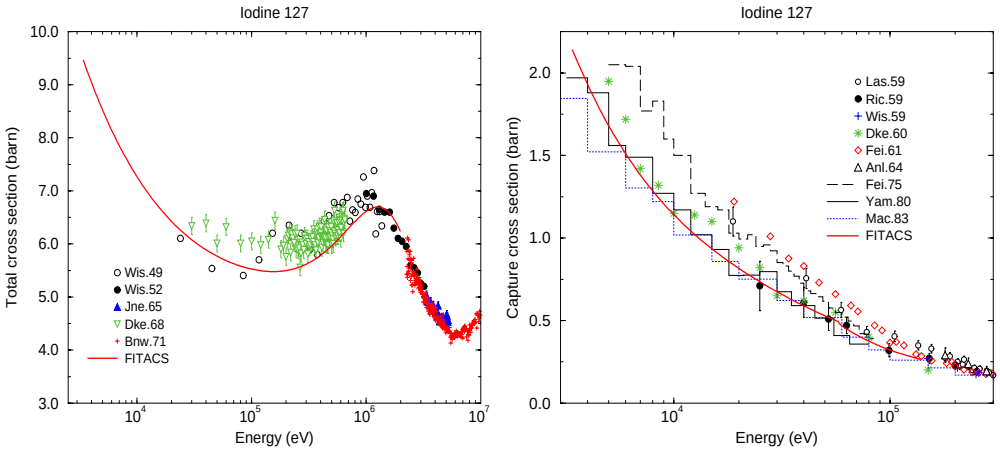

Figure 7.17: Comparison of the present work with the experimental cross sections available in the EXFOR data base.

also mentioned that the d- and f-wave parameters are probably affected by somewhat crude approximations. In FITACS, $< \Gamma_{\gamma,0} >$ and $< \Gamma_{\gamma,1} >$ are free parameters, while for higher partial waves they are defined as follows:

$$< \Gamma_{\gamma,2} > = < \Gamma_{\gamma,0} >$$
$$< \Gamma_{\gamma,3} > = < \Gamma_{\gamma,1} >$$

Consequently, accurate determination of the average parameters uncertainties is not straightforward and the correlation coefficients given herein are questionable. In Section 7.4, we give global systematic errors on the cross sections rather than on the average parameters.

In Table 7.10, the ^{127}I average parameters are compared with the values reported in the literature. The s-wave parameters from FITACS are consistent with those deduced from the RRR. The values of the p- and d-wave parameters agree with the trend deduced from other works and from optical model calculations. Estimates of (S_1) and (S_2) are readily obtained from the plots presented in Reference [56].

Our FITACS results are compared in Figure 7.17 with experimental cross sections available in the EXFOR data base. A wide number of experimental capture cross sections are available

Table 7.9: ^{127}I average resonance parameters and their correlation coefficients. The quoted errors are the statistical uncertainties given by SAMMY. The mean radiation widths are in meV. $<\Gamma_{\gamma,2}>$ and $<\Gamma_{\gamma,3}>$ are fixed parameters.

Parameters				correlation coefficients									
$10^4 S_0$	0.779	±	0.009	1.000									
R_0^∞	0.1954	±	0.0001	0.066	1.000								
$<\Gamma_{\gamma_0}>$	112.4	±	0.1	-0.017	-0.041	1.000							
$10^4 S_1$	1.532	±	0.002	-0.228	0.419	-0.023	1.000						
R_1^∞	-0.1293	±	0.0096	-0.041	-0.043	-0.096	0.016	1.000					
$<\Gamma_{\gamma_1}>$	103.2	±	0.1	-0.026	-0.065	-0.123	-0.031	-0.160	1.000				
$10^4 S_2$	1.832	±	0.014	0.098	-0.045	-0.075	-0.624	0.561	-0.129	1.000			
R_2^∞	0.2819	±	0.0025	-0.039	0.010	0.024	0.383	-0.017	0.042	-0.502	1.000		
$<\Gamma_{\gamma_2}>$	112.4												
$10^4 S_3$	1.628	±	0.071	-0.033	0.011	0.019	0.284	-0.032	0.033	-0.405	-0.170	1.000	
R_3^∞	-0.2216	±	0.0119	-0.007	0.002	0.002	0.054	-0.009	0.004	-0.053	-0.035	-0.038	1.000
$<\Gamma_{\gamma_3}>$	103.2												

covering a large energy range. Our results are in excellent agreement with the capture cross section measured by Yamamuro et al. from 3.2 to 80 keV [144]. The measurement were carried out at the 46 MeV linac accelerator of the Kyoto University Research Reactor Institute using the time-of-flight method. The discrepancy reaches 0.7% in average. After Macklin's article [16], no new experimental results have been published. The latter is systematically 3.8% lower than the present cross section. This discrepancy remains consistent with the systematic trend observed over the Resolved Resonance Range (Figure 7.14).

For the total cross section, TOF measurements covering the energy range from 4 keV to 25 keV have never been reported in the literature. The average resonance parameters recommended in the neutron data bases were often deduced from the partial cross sections or adjusted to smoothly join experimental data above 100 keV with the Resolved Resonance Range. This work is then the first to cover a wide energy range from 0.5 eV to 1 MeV. However, around 100 keV, the comparison between our FITACS curve and the experimental data available in the EXFOR library exhibits some discrepancies. They cannot be explained with the main sources of error which are discussed in Section 7.4. Before the final evaluation, the trend of the present ^{127}I total cross section should be confirmed with the help of optical model calculations.

Table 7.10: ^{127}I average resonance parameters extracted from the resolved and the unresolved resonance range compared with other works, optical model calculations and recommended values. Within the 0.5 eV and 5 keV energy range, the D_0 and S_0 parameters are those obtained with the ESTIMA code. The mean radiation width and the distant level parameter come from the resonance analysis. The Unresolved Resonance Range parameters are those provided by FITACS, given the D_0 value as a fixed parameter. The level density for higher partial waves are calculated with the Gilbert and Cameron formula. The mean level spacings are in eV and the mean radiation widths are in meV.

Resolved Resonance Range

Parameters		Pattenden [13] $E < 170$ eV (1963)	Seth et al. [141] 3 eV-650 eV (1964)	Garg et al. [132] 150 eV-4 keV (1965)	Rhor et al. [133] 20 eV-2 keV (1976)	Macklin [16] 2 keV-4 keV (1983)	This work 0.5 eV-5 keV
s-wave	D_0	38.0 ± 12.0		13.5 ± 0.8	13.3 ± 1.0	9.7 ± 0.8	12.52 ± 0.3
	$10^4 S_0$	0.7 ± 0.3	0.55 ± 0.20	0.62 ± 0.09	0.90 ± 0.09		0.72 ± 0.06
	R_0^∞						0.19 ± 0.01
	$< \Gamma_\gamma >$	100.0		110.0	80.0 ± 8.0	136.0 ± 8.0	100.0 ± 22.6

Unresolved Resonance Range

Parameters		Gibbons et al. [142] 7 keV-170 keV (1960)	Camarda [143] 1 keV-600 keV (1973)	Mughabghab [56] (1981)	JENDL3.3 ~ 70 keV	JEFF3 2 keV-60 keV	This work* 3.5 keV-1 MeV
s-wave	D_0	13.4		9.7 ± 0.8		11.3	12.52
	$10^4 S_0$	0.84		0.8 ± 0.1	0.76	0.87	0.779 ± 0.009
	R_0^∞		0.145 ± 0.03	0.162 ± 0.03	0.176		0.1954 ± 0.0001
	$< \Gamma_\gamma >$	107.0		90.0 ± 10.0	117.5	98.6	112.4 ± 0.1
p-wave	D_1						6.48
	$10^4 S_1$	3.0 ± 1.5	1.55 ± 0.5	$\sim 2.0^\dagger$	1.58	2.2	1.532 ± 0.002
	R_1^∞		0.25 ± 0.1				-0.1293 ± 0.0096
	$< \Gamma_\gamma >$			50-100			103.2 ± 0.1
d-wave	D_2						4.57
	$10^4 S_2$			$\sim 1.5^\dagger$	0.99		1.832 ± 0.014
	R_2^∞						0.2819 ± 0.0025
	$< \Gamma_\gamma >$						112.4
f-wave	D_3						3.62
	$10^4 S_3$						1.628 ± 0.071
	R_3^∞						-0.2216 ± 0.0119
	$< \Gamma_\gamma >$						103.2

† From optical model calculations

* The quoted errors are the statistical uncertainties given by FITACS

7.2.3 The ^{129}I average cross sections

Three transmission spectra and two capture yields are used to determine the average cross sections from 3.5 keV to 100 keV (Table 7.2). Owing to the lead, oxygen, and sulfur resonances, the transmission data above 100 keV cannot be used and are left out of the analysis. In Figure 7.18 the fitted average cross sections are shown, together with the average pointwise data. The arrows indicates the energies of the first inelastic levels. The s- and p-wave average parameters extracted simultaneously from the total and capture cross sections with the FITACS option of SAMMY are given in Table 7.11. They are compared with the European, Japanese and Russian evaluations in Table 7.12. In the JEFF3, JENDL3.3 and BROND2.2 data bases, the average cross sections were calculated from the statistical description of the capture cross section measured by Macklin up to 500 keV [16].

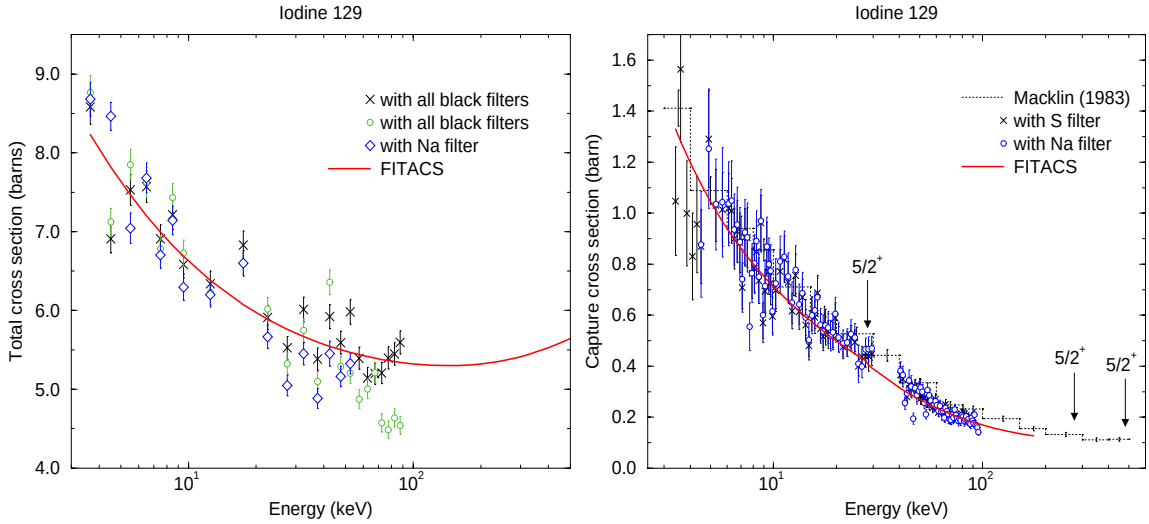

Figure 7.18: Experimental ^{129}I total and capture cross sections together with the FITACS results. The capture cross section is compared with the results obtained by Macklin in 1983 [16].

The estimated values of S_0 and $< \Gamma_{\gamma 0} >$ in the URR agree with those extracted from the RRR. Similarly, the s-wave parameters recommended in JEFF3 are in a satisfactory agreement with the present work. Below 10 keV, the average discrepancy between the capture cross section provided by Macklin and our results remains below 10%. It reaches 18% between 10 keV and 100 keV. These discrepancies result from the combination of several sources of errors. In the URR, the resonance self-shielding and multiple scattering correction applied to our data are dominated by scattering. From the SESH calculation the later ranges from 6% to 7.7%. Macklin reports in his article a correction ranging from 4.3% to 7%. Owing to the complex composition of the samples under investigation, the accuracy of these large corrections are questionable. The additional uncertainty introduced by subtracting the ^{127}I capture cross section is also able to explain the larger part of the above mentioned discrepancies. The main sources of errors affecting the determination of the resolved resonance parameters and the cross sections are discussed in Section 7.4.

7.3 Systematic average parameters

In this section a special care is given to the trend of the average resonance parameters with respect to the mass number of the compound nucleus. Required parameters for statistical model

Table 7.11: ^{129}I average resonance parameters and their correlation coefficients. The quoted errors are the statistical uncertainties provided by SAMMY. The mean radiation widths are expressed in meV.

Parameters		correlation coefficients					
$10^4 S_0$	0.584 ± 0.004	1.000					
R_0^∞	0.1662 ± 0.0017	0.387	1.000				
$< \Gamma_{\gamma_0} >$	108.3 ± 0.9	-0.011	-0.214	1.000			
$10^4 S_1$	1.41 ± 0.13	-0.187	0.415	-0.413	1.000		
R_1^∞	-0.1084 ± 0.0104	-0.004	-0.010	-0.010	-0.011	1.000	
$< \Gamma_{\gamma_1} >$	114.2 ± 1.4	0.028	-0.122	-0.081	-0.268	-0.031	1.000

Table 7.12: ^{129}I average resonance parameters deduced from the s-wave resonances sample suggested by ESTIMA and those obtained with the FITACS option of SAMMY. For the Unresolved Resonance Range analysis, D_0 is kept fixed, and D_1 is calculated with the Gilbert and Cameron formula. The mean level spacings are in eV and the mean radiation widths are in meV.

Parameters		JEFF3 $>$ 25 keV	JENDL3.3 $\sim$70 keV	BROND2.2 2 keV-500 keV	This work $<$5 keV	This work* 3.5 keV-100 keV
s-wave	D_0	23.1		25.0	27.3±0.9	27.3
	$10^4 S_0$	0.52	0.532	0.8	0.54±0.07	0.584±0.004
	R_0^∞		0.212	0.174	$\sim$0.137	0.1662±0.0017
	$< \Gamma_\gamma >$	104.5	160.0		106.0±15.0	108.3±0.9
p-wave	D_1					14.1
	$10^4 S_1$	2.08	1.332	2.0		1.41±0.13
	R_1^∞					-0.1084±0.0104
	$< \Gamma_\gamma >$					114.2±1.4
d-wave	D_2					
	$10^4 S_2$		0.887	0.8		
	R_2^∞					
	$< \Gamma_\gamma >$					

* The quoted errors are the statistical uncertainties given by SAMMY

calculations are the neutron strength functions, the average radiative widths and the mean level spacings. The systematic trend of these parameters as a function of (A+1) is a key ingredient to describe properties of the nuclei and neutron induced nuclear reactions. Recommended input parameters for theoretical calculations are compiled in the Reference Input Parameter Library (RIPL).

For any applications of the statistical theory, reliable level densities are required. In the FITACS code, they are calculated with the help of the Gilbert and Cameron model (Equation 2.44), for which the fermion gas level density parameter (a) play a crucial role. The variation of the latter with mass number is shown in Figure 7.19. The data available in the RIPL-2 library is compared with those recommended in the JENDL3 library together with the parameters calculated by A.S.Iljinov et al.[1] and A.Mengoni et al.[2]. For the mass number $A = 128$ and $A = 130$,

[1] A.S.Iljinov et al., Nucl. Phys., A543 (1992) 517.
[2] A.Mengoni, Y.Nakajima, J. Nucl. Sci. Tech., 31 (1994) 151.

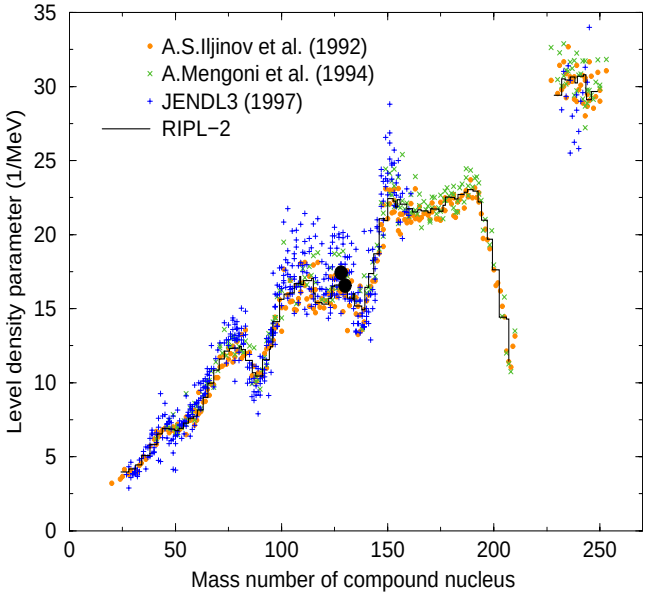

Figure 7.19: Variation of the level density parameter (a) for the Fermi gas model with compound nucleus mass number. The values extracted from the ^{127}I and ^{129}I resonance analysis (circle) are compared with the recommended data available in the RIPL-2 and JENDL3 libraries, together with those calculated by Iljiniv et al. and Mengoni et al.

the mean values are:

$$a_{A=128} \simeq 16.79 \text{ MeV}^{-1}$$

$$a_{A=130} \simeq 16.54 \text{ MeV}^{-1}$$

The iodine level density parameters obtained from the ^{127}I and ^{129}I resonance analyses are respectively equal to (17.42±0.04) MeV^{-1} and (16.56±0.06) MeV^{-1}. The latter is in excellent agreement with the systematic trend calculated around A=130, while the comparison with the $a_{A=128}$ mean value suggests a slight 3.7% overestimation of our natural iodine result.

The Figure 7.20 compares the ^{127}I and ^{129}I average resonance parameters obtained in this work with those available in the RIPL-2 library. We deduce our D_0 value from the s-wave sample suggested by the ESTIMA code. The Gilbert and Cameron formula is then applied to calculate the D_1 parameter with the help of the fermion gas level density parameter. The s- and p-wave neutron strength functions and average radiation widths are those given by FITACS. The S_0, S_1, $< \Gamma_{\gamma,0} >$ and $< \Gamma_{\gamma,1} >$ parameters are in excellent agreement with the systematic trend suggested by the RIPL data. By contrast, the D_0 behaviour exhibits ambiguous results. Around the 128 and 130 mass numbers, our s-wave mean level spacings seem to be underestimated. For the D_1 data, the situation is not straightforward because of the lack of experimental information.

The present results confirm the difficulty in determining confident s-wave mean level spacing from the Resolved Resonance Range analysis. Owing to the experimental resolution and to the limited sensitivity of the capture and transmission measurements, the information on the resonance parameters is incomplete. The strength function and the resonance spacing cannot be directly deduced from available resonances sample without careful estimate of missing resonances. Therefore, the final experimental D_0 value depends on the number of identified resonances, on the analytic model applied to distinguish s- and p-wave resonances and on the method which account for missing levels. In this work, we use the Bayesian approach implemented in

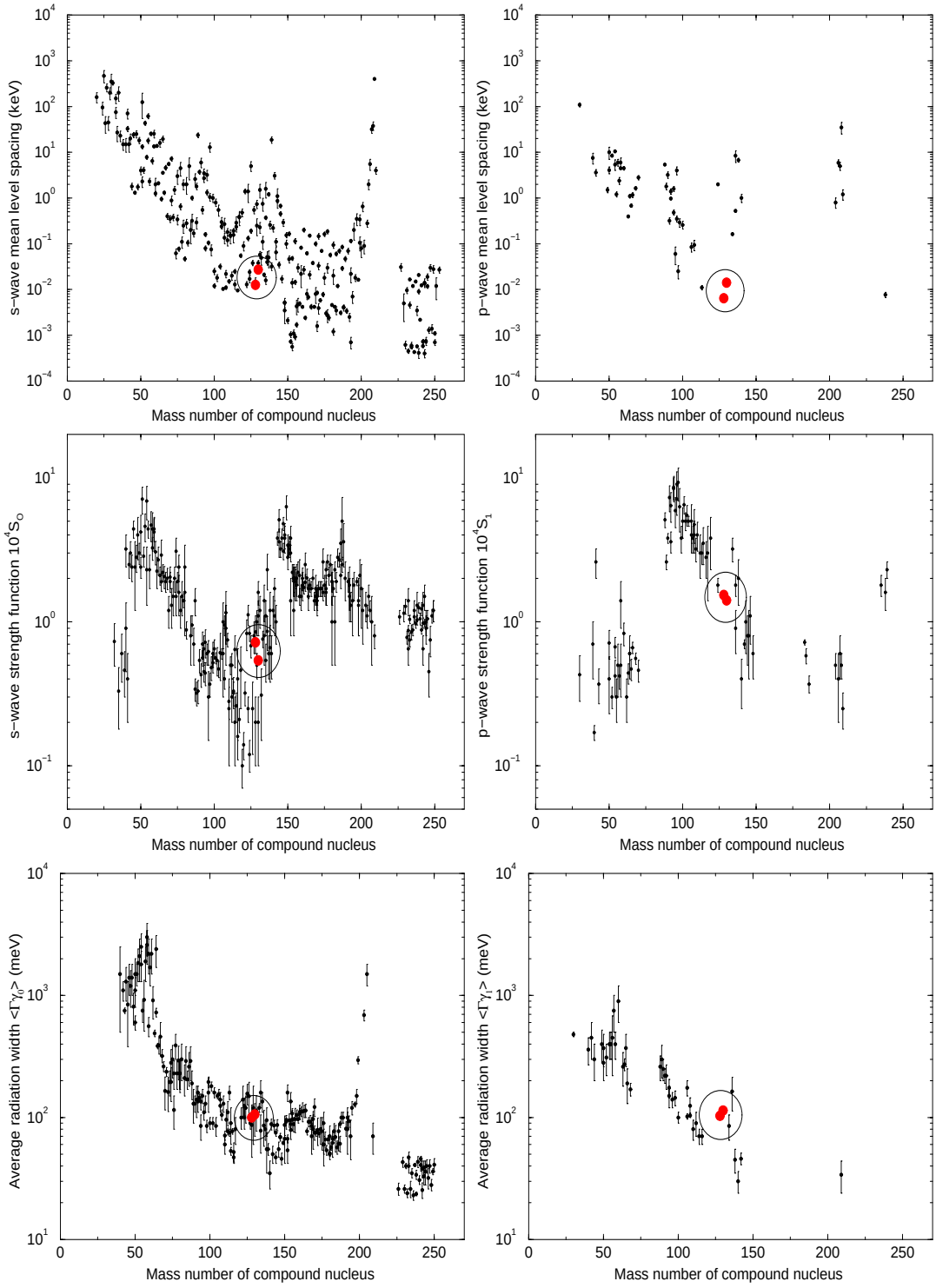

Figure 7.20: Systematic trend of the mean level spacing, of the neutron strength function and of the average radiation width with respect to the compound nucleus mass number. The s- and p-wave resonance parameters are shown separately. The ^{127}I and ^{129}I average resonance parameters obtained in this work (circle) are compared with those available in the RIPL-2 library. The D_0 value comes from the s-wave sample suggested by the ESTIMA code. The Gilbert and Cameron formula is applied to calculate the D_1 parameter with the help of the fermion gas level density parameter. The s- and p-wave neutron strength functions and average radiation widths are those given by FITACS.

the ESTIMA code in association with the properties of the Porter-Thomas distribution. Owing to the above mentioned corrections, the comparison of experimental mean level spacings with values reported in the literature is not straightforward.

7.4 Discussion of uncertainties

The production of an Evaluated Nuclear Data File (ENDF format) is shown in Figure 7.21 together with the uncertainty propagation procedure. In this format, the resonance parameters (RRR+URR) are stored in *File 2*. Their respective correlation coefficient can be stored in *File 32*. This scheme illustrates the "standard" route to be applied for analysing RRR and URR using the AGS, SAMMY and SESH codes as explained in the previous sections.

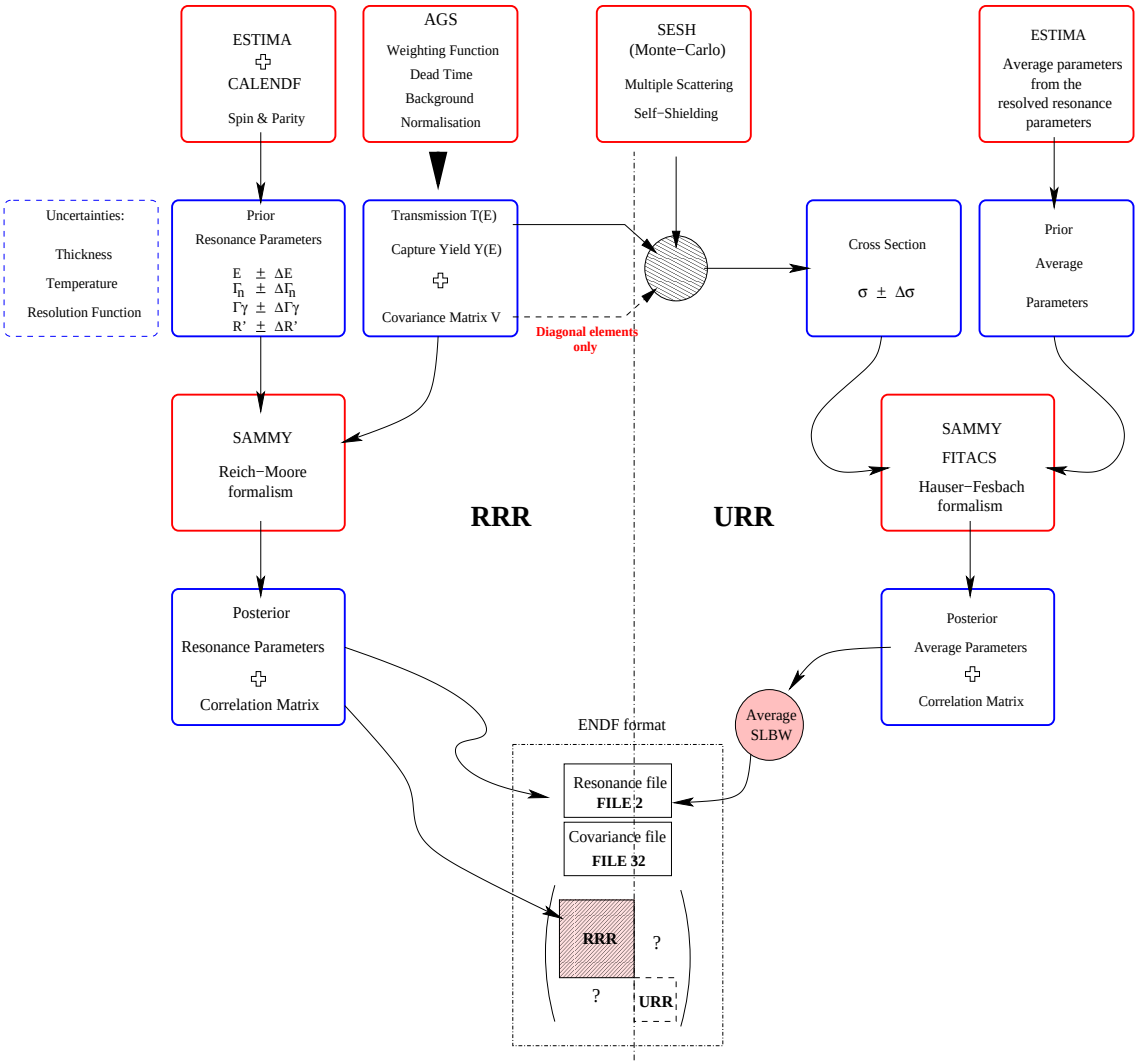

Figure 7.21: Production of an Evaluated Nuclear Data File (ENDF format) with the uncertainty propagation.

The AGS code is an efficient tool for the treatment of uncertainty information. It produces capture yields and transmission spectra along with their associated covariance matrices (Chap-

Table 7.13: Uncertainty budget in the determination of the resonance parameters. The relative neutron widths accuracies are deduced from the thick transmission samples. The results connected to the experimental resolution function is an average value obtained over the entire Resolved Resonance Range. The 2.4% accuracy involved by the description of the time dependent background is an estimate deduced from the model described in Appendix A. For practical purposes, we assume the result for the natural iodine as the same for ^{129}I. For isolated resonances, the neutron width and the sample thickness accuracies are linearly dependent as suggested by the Equation 2.35. The sample characteristics are given in Chapter 3.

Iodine 127

Statistical uncertainties	From the REFIT code
Systematic uncertainties $\Delta\Gamma_n/\Gamma_n$:	
• Sample thickness	1.6%
• Description of the resolution function	1.5%
• Smooth background vs. structured background	2.4%
• Temperature - Doppler width	$< 1\%$
Total	3.25%
Standard deviation of the fitted Γ_γ values	22.6 meV

Iodine 129

Statistical uncertainties	From the REFIT code
Systematic uncertainties $\Delta\Gamma_n/\Gamma_n$:	
• Sample thickness	2.4%
• Description of the resolution function	1.2%
• Smooth background vs. structured background	$\sim 2.4\%$
• Temperature - Doppler width	$< 1\%$
Total	3.6%
Standard deviation of the fitted Γ_γ values	15.2 meV

ter 5). Such problems as handling the data from the huge experimental matrices, rounding errors (numerical precision) and excessive consumption of computer time have recently been solved by implementing SAMMY with the capability to read the AGS output format [27]. Therefore, we are now able to analyse the Resolved Resonance Range including the full experimental covariance matrix. However, uncertainty information on the final resonance parameters are still incomplete. Up to now, there is no obvious way to include in the calculation uncertainties on fixed data related parameters (resolution function, sample thickness, effective temperature). It is clearly needed to calculate the partial derivatives with respect to these parameters without changing their value.

The procedure for analysing the Unresolved Resonance Range is also incomplete. We cannot obtain with the AGS code the full experimental covariance matrix associated to the average capture or total cross sections. For uncertainty propagation purposes, it is necessary to modify an existing AGS command - namely *agscnds* - in order to average transmission or capture yield over

Table 7.14: Uncertainty budget in the determination of the average cross section. The systematic error involved by the time dependent background is described in Appendix A. We assume its magnitude similar for both iodine isotopes. The uncertainties connected to the sample composition and the normalisation factor are readily obtained from the definition of the transmission and capture yield, and from the equations given in Section 7.2.1.

Iodine 127

Description	$\Delta\sigma_\gamma/\sigma_\gamma$	$\Delta\sigma_t/\sigma_t$
Statistical uncertainties:	From the SAMMY code	
Self-shielding and multiple scattering corrections	From the SESH code	
Systematic uncertainties		
• ^{127}I sample thickness	1.8%	1.6%
• Normalisation	3.1%	$< 3.8\%$
• Smooth background vs. structured background	1.7%	0.9%
Total	3.9%	$< 4.2\%$

Iodine 129

Description	$\Delta\sigma_\gamma/\sigma_\gamma$	$\Delta\sigma_t/\sigma_t$
Statistical uncertainties	From the SAMMY code	
Self-shielding and multiple scattering corrections	From the SESH code	
Systematic uncertainties:		
• ^{129}I sample thickness	2.4%	2.4%
• Normalisation	3.3%	$< 13\%$
• Smooth background vs. structured background	$\sim 1.7\%$	$\sim 0.9\%$
• Sample composition	2.6%	$\sim 15\%$
Total	5.1%	$< 20\%$

an energy grid supplied by the user. Nevertheless, rigorous uncertainty propagation fails because ENDF format supports only one representation for the unresolved resonance parameters, namely Average SLBW. SAMMY allows the conversion of the Hauser-Feshbach parameters into ENDF format, but no solution exists to convert the associated correlation matrix. The final task is the determination of the correlation coefficients between the resolved and unresolved parameters. No straightforward solutions to overcome these difficulties exist. The only way to derive correlation coefficients and reliable uncertainties, consists in deducing sensitivity coefficients via a sensitivity study. An illustration of this method applied on ^{232}Np over a wide number of data related parameters is reported in Reference [82].

For the resolved resonance parameters, the sources of systematic errors are mainly the sample thickness, the incomplete description of the resolution function and the time dependent background (Table 7.13). We neglect the uncertainty connected to the Doppler width in accordance with the effective temperature accuracy (± 4 K). From the combination of the above mentioned effects, we may affect respectively on the ^{127}I and ^{129}I neutron width values, an average systematic error of about 3.25% and 3.6%. Similarly, the global systematic error on the average cross section was deduced from the accuracy of the sample composition, of the background and of the normalisation (Table 7.14). The latter induced on the ^{127}I and ^{129}I average total cross sections an error of about 0.21 barns and 0.85 barns. The final errors are always lower than 5%, except for the ^{129}I(n,tot) cross section. A better accuracy cannot be achieved without improved knowledge

of the sample composition. The accuracy associated to the self-shielding and multiple scattering corrections provided by the SESH code is not well known. Some additional investigations are needed to obtain a realistic uncertainty on these corrections. The latter have been left out of the uncertainty propagation.

7.5 Multi-group cross section calculation

We use the NJOY code[3] to verify the right transcription of our results into ENDF-6 format. The total, capture and elastic point-wise cross sections are shown in Figure 7.22. In order to compare the present cross sections with those from other evaluated data files (JEFF3, JENDL3.3, ENDF/B-VI and BROND2), a NJOY calculation of the unshielded multi-group cross sections at 293.6 K was performed. For practical purposes, we choose the 33 broad-group structure as used in the European reactor calculation scheme JEF/ECCO/ERANOS. Results for the ^{127}I and ^{129}I total and capture cross sections are shown in Figure 7.23. The average capture cross sections and the uncertainties are given in Tables 7.15 and 7.16. The resonance parameters beyond 5 keV are not included in the multigroup calculations.

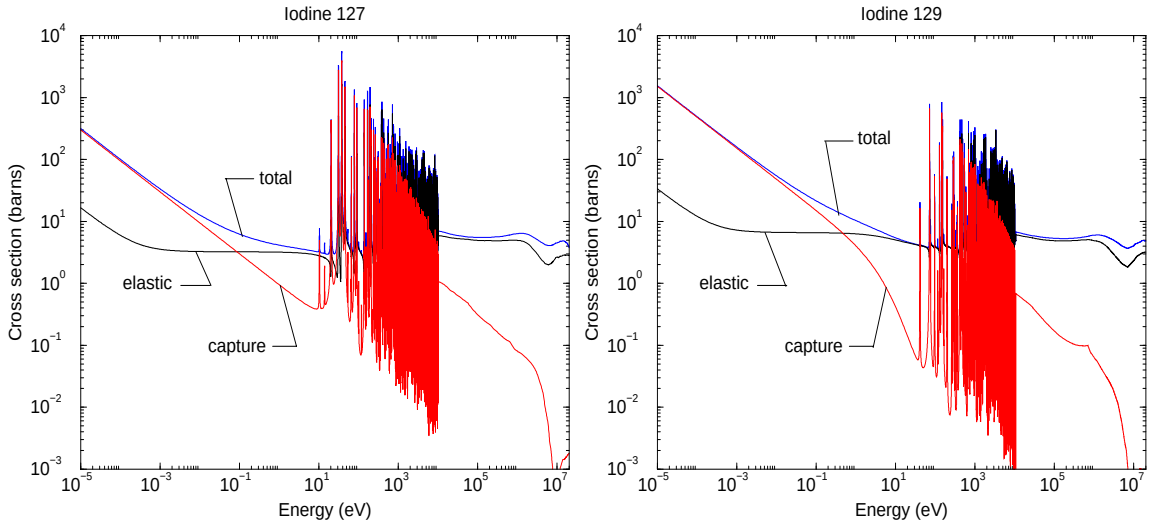

Figure 7.22: ^{127}I and ^{129}I point-wise cross sections calculated at 293.6 K with NJOY

- **^{127}I capture cross section:**

Table 7.15 presents the ^{127}I multigroup capture cross sections obtained in this work and compares them to those of the ENDF/B-VI, JEFF3 and JENDL3.3 neutron libraries. The global uncertainty in a given energy group results from the quadratic sum of each source of error listed in Tables 7.13 and 7.14.

The (*Data base/This work*) ratios highlight the large discrepancies between the present work and the capture cross section predicted by the ENDF/B-VI library. The trends of the JEFF3 and JENDL3.3 values exhibit an overestimation of the contribution of the negative resonances and of the average capture cross section. By contrast, our work suggests an increase of the resolved resonance range contribution by at least 5% in average. The comparison of the different results obtained over the 16^{th} energy group has to be weighted by the significant uncertainty quoted on the present capture cross section. Within the 3.3 keV to 5.5 keV energy range, the statistical uncertainty is no longer negligible as compared to the systematic error. In addition, the resonances are very much overlapping, and the adjustment of the resonance parameters with the SAMMY or REFIT codes becomes rather "formidable". The uncertainty on the resonance

[3]The NJOY nuclear data processing system is a comprehensive computer code package for producing pointwise, multigroup cross sections and related quantities from any evaluated nuclear data file in ENDF format [145].

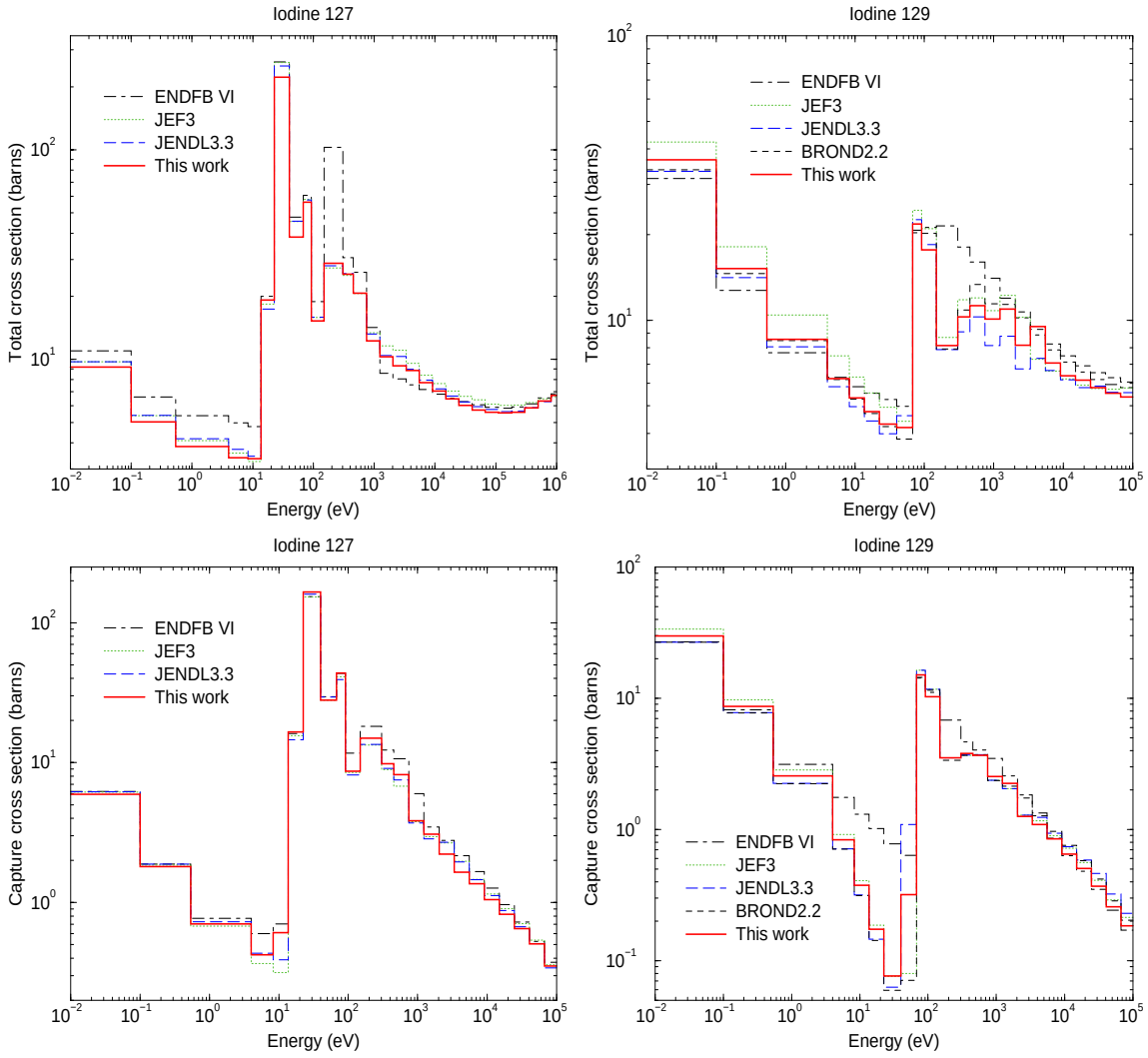

Figure 7.23: ^{127}I and ^{129}I unshielded multi-group cross sections obtained in this work, and compared with the JEFF3, JENDL3.3, ENDF/B-VI and BROND2.2 neutron libraries.

energies as well as the effect of the resolution function may involve large discrepancies on the final $g\Gamma_n$ values.

- **^{129}I capture cross section:**

The ^{129}I multigroup capture cross section values, the accuracies on the present results and the comparison with the JEFF3, JENDL3.3 and BROND2.2 libraries are given in Table 7.16. The global error in a given energy group is the quadratic sum of each source of uncertainties presented in Section 7.4.

We can easily distinguished the three energy ranges corresponding to the $1/v$ behaviour (groups 1 to 6), to the RRR (groups 7 to 16) and to the URR (groups 17 to 23). Owing to the large discrepancies between the experimental thermal capture cross sections, an accurate determination of the $1/v$ contribution over the first energy groups cannot be achieved. The results over the Resolved Resonance Range are in a satisfactory agreement with the three main data bases, excepted for the 7^{th} energy group. The large discrepancy is due to the new s-wave

resonances at 41.37 eV. The comparisons between our results and the JEFF3, JENDL3.3 and BROND2.2 evaluations suggest an average decrease of the ^{129}I capture cross section in the RRR of respectively 1.5%, 2.3% and 4.8%. By contrast, the discrepancies beyond 5 keV range from 5.8% to 27.2%. Without additional measurements, no evident solutions exist to solve these ambiguous results. A series of activation measurements performed within the 67 keV to 100 keV energy range are recommended to check the observed trend on the present average capture cross section.

7.6 Capture resonance integral

In the thermal reactor business, the quantities of interest are the thermal cross sections and the resonance integrals. The latter helps determining the probability that a neutron will be absorbed before reaching thermal energies. The capture resonance integral at infinite dilution in a $1/E$ spectrum is expressed by the following relationship:

$$I_0 = \int_{E_{Cd}}^{\infty} \frac{\sigma_\gamma(E)}{E} \mathrm{d}E \tag{7.8}$$

where $E_{Cd} = 0.5$ eV is the effective cadmium cut-off energy. The I_0 values calculated with NJOY are given in Table 7.17 together with the values reported in the literature and those recommended in evaluated nuclear data files. For comparison, the resonance integral to thermal cross section ratios (I_0/σ_γ^{th}) are also listed in the same table. This ratio can be calculated from the I_0 and σ_γ^{th} data, or directly measured in reactor facility with the Cd-ratio measurement method [146, 147].

7.6.1 Simple analytic expressions

Accurate capture resonance integrals are currently obtained from the numerical integration of the $\sigma_\gamma(E)/E$ ratio as used in NJOY. However, I_0 can be alternatively roughly estimated from explicit expressions calculated within the SLBW approximation. In this Section, we define the capture resonance integral as a function of the thermal capture cross section, of the resolved and unresolved resonance parameters. Therefore, it is convenient to subdivide the resonance integral into a sum over the contributions from the $1/v$ shape, the resolved and the unresolved resonances:

$$I_0 \;=\; I_0(1/v) \;+\; I_0(RRR) \;+\; I_0(URR) \tag{7.9}$$

The $I_0(1/v)$ contribution can be readily obtained by integrating from 0.5 eV the tail of the negative resonance used to reproduce the thermal capture cross section (σ_γ^{th}). The very simple expression proposed in Reference [56] has been corrected assuming negligible the total width of the fictious resonance compared to its resonance energy ($E_r < 0$). The $I_0(1/v)$ contribution can be estimated as follows:

$$I_0(1/v) \simeq 2\sigma_\gamma^{th}\sqrt{\frac{E_{th}}{E_{Cd}}} + \frac{3\pi}{2}\sigma_\gamma^{th} E_r \sqrt{E_{th}}(E_{Cd} - E_r)^{-3/2} \tag{7.10}$$

in which $E_{th} = 0.0253$ eV stands for the thermal energy.

If the Resolved Resonance Range is described by a sum of Single-Level Breit-Wigner formula, the $I_0(RRR)$ contribution can be approximated by the following expression [56]:

$$I_0(RRR) \simeq \frac{\pi}{2} 2.608 \times 10^6 \left(\frac{A+1}{A}\right)^2 \sum_i \frac{A_{\gamma,i}}{E_j^2} \tag{7.11}$$

Table 7.15: ^{127}I multigroup capture cross section obtained in this work at 293.6 K. The quoted uncertainties come from the information listed in Tables 7.13 and 7.14. Errors from each source are added quadratically. The recommended cross sections from ENDF/B-VI, JEFF3 and JENDL3.3 are compared with the present evaluation from 0.1 eV to 110 keV.

Energy group	(eV)		σ_γ	$\Delta\sigma_\gamma/\sigma_\gamma$	Data base / This work		
			(barn)	(%)	ENDF/B-VI	JEFF3	JENDL3.3
1	0.100	0.540	1.807± 0.054	3.0%	1.043	1.026	1.039
2	0.540	4.000	0.703± 0.022	3.1%	1.097	0.964	1.036
3	4.000	8.315	0.423± 0.014	3.2%	1.417	0.866	1.025
4	8.315	13.710	0.610± 0.013	2.2%	1.154	0.516	0.639
5	13.710	22.603	16.549± 0.528	3.2%	0.978	0.942	0.881
6	22.603	40.169	166.300± 3.830	2.3%	0.925	0.919	0.962
7	40.169	67.904	27.986± 0.741	2.6%	1.056	0.999	1.053
8	67.904	91.661	43.639± 1.337	3.1%	0.998	0.943	0.899
9	91.661	148.63	8.663± 0.213	2.5%	1.347	0.983	0.941
10	148.63	304.32	14.941± 0.672	4.5%	1.216	0.896	0.903
11	304.32	454.00	9.836± 0.241	2.4%	1.253	0.907	0.923
12	454.00	748.52	8.224± 0.320	3.9%	1.296	0.827	0.914
13	748.52	1234.1	3.848± 0.120	3.1%	1.561	0.983	0.964
14	1234.1	2034.7	3.074± 0.183	6.0%	1.126	0.963	0.929
15	2034.7	3354.6	2.220± 0.199	9.0%	1.250	1.203	1.212
16	3354.6	5530.8	1.647± 0.240	14.6%	1.312	1.193	1.183
17	5530.8	9118.8	1.364± 0.050	3.7%	1.216	1.071	1.066
18	9118.8	15034.0	1.050± 0.039	3.8%	1.208	1.094	1.065
19	15034.0	24788.0	0.825± 0.035	4.3%	1.170	1.098	1.061
20	24788.0	40868.0	0.651± 0.029	4.6%	1.112	1.082	1.032
21	40868.0	67379.0	0.506± 0.023	4.5%	1.042	1.062	1.004
22	67379.0	111090.0	0.352± 0.013	3.8%	1.064	1.017	0.969
23	111090.0	183160.0	0.252± 0.009	3.8%	1.079	1.011	0.942

Table 7.16: ^{129}I multigroup capture cross section obtained in this work at 293.6 K. The quoted uncertainties result from the quadratic sum of each source of errors given in Tables 7.13 and 7.14. The recommended cross sections from JEFF3, JENDL3.3 and BROND2.2 are compared with the present evaluation from 0.1 eV to 110 keV.

Energy group (eV)			σ_γ (barn)	$\Delta\sigma_\gamma/\sigma_\gamma$ (%)	Data base / This work		
					JEFF3	JENDL3.3	BROND2.2
1	0.100	0.540	8.695± 1.075	12.4%	1.123	0.893	0.890
2	0.540	4.000	2.558± 0.294	11.5%	1.114	0.878	0.875
3	4.000	8.315	0.834± 0.083	10.0%	1.098	0.855	0.849
4	8.315	13.710	0.376± 0.034	8.9%	1.086	0.842	0.834
5	13.710	22.603	0.174± 0.014	8.0%	1.075	0.839	0.824
6	22.603	40.169	0.076± 0.005	7.1%	0.996	0.823	0.780
7	40.169	67.904	0.319± 0.013	4.1%	0.251	3.412	0.222
8	67.904	91.661	15.070± 0.443	2.9%	1.089	1.088	0.958
9	91.661	148.630	10.289± 0.278	2.7%	1.139	1.138	1.123
10	148.630	304.320	3.522± 0.113	3.2%	1.000	1.001	0.956
11	304.320	454.000	3.805± 0.111	2.9%	0.966	0.970	0.967
12	454.000	748.520	3.675± 0.242	6.6%	1.007	1.013	1.010
13	748.520	1234.100	2.539± 0.077	3.1%	0.936	0.936	0.928
14	1234.100	2034.700	2.250± 0.088	3.9%	0.913	0.913	0.949
15	2034.700	3354.600	1.260± 0.107	8.5%	1.022	1.022	1.381
16	3354.600	5530.800	1.093± 0.150	13.8%	1.064	1.131	1.165
17	5530.800	9118.800	0.849± 0.045	5.2%	1.058	1.106	1.143
18	9118.800	15034.000	0.651± 0.033	5.1%	1.109	1.138	1.160
19	15034.000	24788.000	0.504± 0.026	5.1%	1.113	1.160	1.150
20	24788.000	40868.000	0.370± 0.019	5.2%	1.109	1.251	1.132
21	40868.000	67379.000	0.258± 0.013	5.2%	1.127	1.248	1.109
22	67379.000	111090.000	0.184± 0.009	4.9%	1.163	1.245	1.107
23	111090.000	183160.000	0.139± 0.009	6.4%	1.175	1.272	1.125

where E_j is the resonance energy and $A_{\gamma,j}$ represents the capture area of the resonance j.

The contribution of the Unresolved Resonance Range to the capture resonance integral has been treated by Dresner [148]. From the integration of the pure Hauser-Feshbach formula (Equation 2.62), he found an explicit form for a given J^π sequence. For the sake of convenience in carrying out simple expressions, we can rewrite the Dresner results for a given parity. With the help of somewhat crude assumptions, the s-wave contribution to the resonance integral above some cut-off energy E^* can be expressed as follows:

$$I_0(URR) \simeq a_{cor}^{l=0}\, 2\pi^2 \lambda\!\!\!^{-*2} \frac{<\Gamma_{\gamma 0}>}{D_0} \frac{B_0 - \ln(1+B_0)}{B_0^2} \qquad \text{(for s-waves)} \tag{7.12}$$

in which B_0 is defined as:

$$B_0 = \frac{1}{2} \frac{<\Gamma_{\gamma 0}>}{S_0 D_0 \sqrt{E^*}} \tag{7.13}$$

As a further refinement, the contribution of p-wave resonances above E^* must be included in the calculation. Then we obtain from the Dresner expression:

$$\begin{aligned} I_0(URR) \simeq\ & a_{cor}^{l=1}\, 2\pi^2 \lambda\!\!\!^{-*2} \tfrac{<\Gamma_{\gamma 1}>}{D_1} \left[\tfrac{1}{B_1^{2/3}\sqrt{3}} \left(\tfrac{\pi}{2} + \arctan\left(\tfrac{B_1^{1/3}-2}{B_1^{1/3}\sqrt{3}} \right) \right) \right. \\ & \left. - \tfrac{1}{6B_1^{2/3}} \ln\left(\tfrac{(B_1^{1/3}+1)^2}{B_1^{2/3}-B_1^{1/3}+1} \right) \right] \qquad \text{(for p-waves)} \end{aligned} \tag{7.14}$$

The B_1 function may be expressed as follows:

$$B_1 = \frac{1}{12} \frac{<\Gamma_{\gamma 1}>}{D_1 S_1 \rho^2 \sqrt{E^*}} \tag{7.15}$$

where $\rho = k^* a_c$ stands for a function of the channel radius a_c and of the wave number k. The starred quantities in the above equations are evaluated at E^*. The (a_{cor}) parameter is a correction given by Dresner to account for the statistical fluctuations in the reduced neutron width. In this work, they have been calculated with the Mathematica code from the generalised Hauser-Feshbach formula given in Section 2.4.

Somewhat more sophisticated analytic treatment can be used to calculate I_0 from a set of resolved and unresolved resonance parameters. In the simpler cases as above, direct estimation of I_0 can be easily obtained together with relevant information on its accuracy. The latter may be deduced by using the conventional error propagation laws. Since the $I_0(1/v)$, $I_0(RRR)$ and $I_0(URR)$ contributions are not independent, the associated errors do not obey root-mean-square sum rule. They should be simply added arithmetically.

7.6.2 The ^{127}I resonance integral

The ^{127}I resonance integral resulting from this work is 153.7 ± 4.8 barns. The contributions to the resonance integral of the $1/v$ shape, of the resolved and unresolved resonances are:

$$\begin{aligned} I_0(1/v) &\simeq 2.07 \pm 0.03 \text{ barns} \\ I_0(RRR) &\simeq 148.68 \pm 4.66 \text{ barns} \\ I_0(URR) &\simeq 2.93 \pm 0.11 \text{ barns} \end{aligned}$$

Applying the Equations 7.10, 7.11, 7.12 and 7.14, we find respectively 2.07 barns, 148.66 barns and 3.13 barns. The latter contribution is calculated with $a_{cor}^{l=0} = 0.69$ and $a_{cor}^{l=1} = 0.75$ for $E^* > 5$ keV.

Table 7.17: Summary of the ^{127}I and ^{129}I capture resonance integral (I_0).

Iodine 127

Author		Year	I_0 (barns)	I_0/σ_γ^{th}
Klimentov et al.	Soviet At. Energy, 3, p1387	1957	106 ± 13	
Tattersall et al.	J. Nucl. Energy, Reactor Sci. 12, p32	1960	183 ± 30	
Pattenden	Nucl. Sci. and Eng., 17, p371	1963	140 ± 20	
Ricabarra et al.	Can. J. Phys., 46, p2474	1968	156 ± 6	27.8 ± 0.5
Van der Linden et al.	J. radioanal. Chem. , 20, p695	1974	147 ± 10	23.7 ± 0.9
Moen et al.	J. Radioanal. Chem., 54, p377	1979		25.1 ± 0.7
Friedmann et al.	Radiochimica Acta, 33, p182	1983	109 ± 5	23.2 ± 1.4
Katoh et al.	J. Nucl. Sci. and Tech., 36, p223	1999	162 ± 8	25.3 ± 1.7
Moen et al.†		1979		24.6
BNL†		1981	147±6	23.7±1.2
JEFF3†			144.3	23.3
ENDFB-VI†			157.5	25.3
JENDL-3.3†			148.2	23.9
This work			153.7 ± 4.8	25.6 ± 0.9

Iodine 129

Author		Year	I_0 (barns)	I_0/σ_γ^{th}
Roy et al.	Can. J. Chem., 36, p1424	1958	36.0 ± 4.0	1.34 ± 0.18
Pattenden	Nucl. Sci. Eng., 17, p371	1963	22 ± 7	0.78 ± 0.25
Macklin*	Nucl. Sci. Eng., 85, p350	1983	34.2 ± 1.9	
Friedmann et al.	Radiochimica Acta, 33, p183	1983	30.6 ± 1.6	0.90 ± 0.07
Nakamura et al.	Nucl. Sci. Tech., 33, p283	1996	33.8 ± 1.4	1.11 ± 0.06
BNL†		1981	36 ± 4	1.32 ± 0.18
JEFF3†			30.28	0.89
ENDFB-VI†			35.56	1.31
JENDL3.3†			28.98	1.07
BROND2†			28.35	1.05
This work			28.83±1.71	0.95±0.07

† recommended value * from the resonance analysis

The present result is about 3.7% higher than the JENDL3.3 recommended value, and 5.4% lower than the resonance integral measured by Katoh et al.[149]. Owing to the respective accuracies of these results, both values are consistent with this work. The resonance integral to thermal cross section ratio may give more consistent information on I_0. The weighted mean value of I_0/σ_γ^{th} calculated from the values reported in the literature is 26.10 ± 0.35. Using the thermal capture cross section from Molnar et al. (see Table 7.4), we may deduce a resonance integral of 156.6 ± 3.5 barns. The agreement with the present capture resonance integral is then clearly improved.

7.6.3 The ^{129}I resonance integral

The ^{129}I resonance integral calculated with the NJOY code is 28.83±1.71 barns with the following contributions:

$$
\begin{array}{rcrcl}
I_0(1/v) & \simeq & 7.97 & \pm & 0.92 \text{ barns} \\
I_0(RRR) & \simeq & 19.07 & \pm & 0.68 \text{ barns} \\
I_0(URR) & \simeq & 1.79 & \pm & 0.11 \text{ barns}
\end{array}
$$

The respective calculated values are equal to 7.12 barns, 19.07 barns and 1.83 barns. For the URR, we use the same energy cut-off definition as for ^{127}I to distinguish the s- and p-wave contributions. The correction factors provided by Mathematica are $a_{cor}^{l=0} = 0.70$ and $a_{cor}^{l=1} = 0.72$. We obtain analogously to the natural iodine a satisfactory agreement between the numeric and analytic methods.

The comparison of the present result with the resonance integrals reported by Friedmann et al. [14] and by Nakamura et al. [15] exhibits an ambiguous trend. Although we use in our resonance analysis the thermal capture cross section reported by the Japanese team, the I_0/σ_γ^{th} ratios suggest our result is in a better agreement with the work of Friedmann et al. The discrepancy with the latter is significantly reduced by using their thermal capture cross section of 33.9 barns rather than 30.3 barns (Table 7.7). The present I_0 value will become ~ 30.3 barns. At the moment, the situation cannot be improved without the thermal capture cross section from Molnar et al. available in few months.

The present analysis improved noticeably the accuracy of the iodine capture cross section in the Resolved Resonance Range and to a lesser extend in the unresolved range. Accurate integral measurements are still required to validate these results.

Chapter 8

Conclusion

During this work, the ^{127}I(n,γ), ^{127}I(n,tot), ^{129}I(n,γ) and ^{129}I(n,tot) cross sections have been measured and analysed within the 0.5 eV to 100 keV energy range. Results from the Resolved and Unresolved Resonance Range were converted into ENDF-6 format. The NJOY code was used to process preliminary MCNP and ERANOS libraries.

Iodine neutron cross sections have been extensively studied over eighteen high-resolution TOF capture and transmission measurements. We have used four PbI_2 samples containing natural and radioactive iodine, four natural lead iodine samples and a 1 mm-thick LiI liquid sample for high homogeneous sample applications. The Resolved Resonance Range has been analysed up to 10 keV. Below 5 keV, the resonance parameters have been extracted from a simultaneous REFIT adjustment of the capture and transmission data. Above this energy, neutron width values and resonance energies were obtained from one single transmission measurement. We have then cross-checked the consistency of the resonance parameters with the SAMMY code. The average total and capture cross sections were analysed within the 3.5 keV to 100 keV energy range.

For ^{127}I, 719 resonances have been identified and described in terms of Reich-Moore parameters. From the shape fit of 155 resonances, we found an average radiation width of 100 meV, with a standard deviation of 22.6 meV. This average value was then kept fixed for all other resonances. The statistical treatment of the s-wave resonances with the ESTIMA code provided a mean level spacing of (12.5 ± 0.3) eV. Using this given input parameter in FITACS, the s-, p-, d- and f-wave strength functions were extracted from the average capture and total cross sections. The results were $S_0 = (0.78 \pm 0.01) \times 10^{-4}$, $S_1 = (1.53 \pm 0.01) \times 10^{-4}$, $S_2 = (1.83 \pm 0.01) \times 10^{-4}$ and $S_3 = (1.63 \pm 0.07) \times 10^{-4}$. The quoted uncertainties are only statistical errors provided by the FITACS option of SAMMY.

From the ^{129}I capture and transmission data, 400 resonances have been analysed. The average radiation width has been deduced from 55 resonances for which both Γ_γ and Γ_n have been determined. We found a mean value of 106 meV, and a standard deviation of 15.2 meV. The mean level spacing of (27.3 ± 0.9) eV has been obtained from the s-wave resonances sample suggested by ESTIMA. The s- and p-wave strength functions deduced from the statistical treatment of the average cross sections were $S_0 = (0.58 \pm 0.01) \times 10^{-4}$ and $S_1 = (1.41 \pm 0.13) \times 10^{-4}$.

The comparison of the results shows a fairly good agreement between the average resonance parameters obtained from the Reich-Moore analysis of the RRR and those determined in the URR with the generalised Hauser-Feshbach model. Similarly, the present results agree with the systematic trend of the average parameters with respect to the mass number of the compound nucleus. Owing to the lack of relevant experimental p-wave mean level spacings in the Reference Input Parameter Library (RIPL) around the mass number A=130, a statistical analysis of the p-wave resonances sample provided by ESTIMA is highly recommended.

These new ^{127}I and ^{129}I evaluated data were then converted into ENDF-6 format. The capture resonance integrals calculated with NJOY were $I_0^{127} = (153.7 \pm 4.8)$ and $I_0^{129} = (28.83 \pm 1.71)$ barns. These results are consistent with the JEFF3 and JENDL3.3 recommendations. The I_0^{127} accuracy depends strongly on the Resolved Resonance Range treatment. Indeed, about 96.7% of the capture resonance integral is given by the resolved resonances. By contrast, for I_0^{129}, the thermal capture cross section, the Resolved Resonance Range and the Unresolved Resonance Range contribute respectively at a 27.6%, 66.1% and 6.3% rate. Each contribution is no longer negligible faced in determining accurate cross section. In view of these considerations, special care will be given to the future ^{129}I thermal capture cross section measured by Molnar et al. at the cold neutron guide of the Budapest research reactor.

In the meantime, the accuracy of these newly measured capture and total cross sections have been estimated with the help of systematic studies performed over four major experimental effects. We have evaluated (1) the impact of the weighting function applied on the capture γ-rays spectra, (2) the systematic bias introduced by the time dependence of the background, (3) the effect of the experimental resolution of the GELINA facility on the resonance parameters and (4) the validity of the multiple scattering algorithm implemented in the REFIT and SAMMY codes.

The weighting function is used to get a capture detection efficiency independent of the mode of decay. The efficiency depends only on the excitation energy E^* of the compound nucleus. This condition is achieved by appropriately weighting the pulse amplitude response of the C_6D_6 detectors. For iodine, we have demonstrated the marginal contribution of the weighting function on the global systematic uncertainty. That suggested to have from level to level a nearly constant hardness of the γ-rays spectra emitted by the compound nucleus after neutron capture in the sample. The ^{127}I and ^{129}I capture areas were then assumed to be independent of the shape of the weighting function.

Previous TOF analyses performed at the IRMM have shown that the time dependence of the background is not well known. In this work, a time dependent algorithm was applied to define the background as a function of the incident neutron flux as hypothesised by M.Moxon and A.Lepretre. This approach makes possible to handle structured contributions, which would correspond to detection at a later time of incident neutrons scattered out of the incident neutron beam. Studies conducted over several TOF data suggested that the experimental area, the detector and its surroundings could be the main sources of such a structured background. Including this assumption in our sensitivity studies, we derived systematic errors involved by the choice of the analytic background function. We concluded as negligible the effect of the structures on the iodine capture areas. By contrast, it could induce a systematic error as large as 2.4% on the Γ_n values extracted from the transmission measurements as well as on the average capture and total cross sections. Nevertheless, deeper investigations are needed to confirm the present conclusions. As it is known, the neutron induced background in TOF measurements and the tail of the experimental resolution function of the facility imply similar experimental biases. However, their respective contributions are hardly distinguishable without high resolution measurements with high signal to background ratio.

In this work, the time resolution of GELINA has been widely investigated for its implementation in the SAMMY code. The analytic treatment available in REFIT has been improved with the help of Monte-Carlo simulations performed by C.Coceva. In the light of these results, an alternative solution has been proposed which consists in introducing point-wise distributions in the SAMMY code via the UDR option. The systematic uncertainty on the neutron widths involved by the poor knowledge of the tail of the resolution function remains below 1.5% in

average, but has a detrimental effect on the resonance parameters in the case of strong overlaps. That cannot be solved without experimental validation of the resolution function. The latter is in progress at the IRMM by using the ^{56}Fe(n,γ) reaction.

In the final step of this sensitivity study, we have compared the multiple scattering corrections calculated by the REFIT and SAMMY codes. Results from Monte-Carlo simulations (MCNP and SAMSMC) have shown that the two codes provide spurious results when thick samples are studied. It follows that the double-plus scattering correction can be applied on our PbI_2 data as long as the sample thickness does not exceed 10 mm. In order to avoid any systematic error exceeding 1%, we should not include in the analysis the capture yields related to the thick radioactive sample ($h = 14.8$ mm). Within this condition, the SAMMY and REFIT codes give similar results. However, agreement between the two codes is subject to linearity restriction. In the case of data with modest accuracy or strong resonance overlap, local discrepancies higher than 5% are expected.

Independent additional errors have to be introduced in the uncertainty propagation. We should add contributions of the normalisation, of the sample composition and of the sample temperature. The impact of the Doppler effect has been left out of this analysis since it was widely investigated by V.Gressier with ^{237}Np transmission measurements. In accordance with the good accuracy of the measured sample temperature, we have neglected the uncertainty connected to the Doppler effect. In view of these considerations, the global systematic error on the ^{127}I capture cross section is lower than 4%, and it remains within 3.5% and 5% for the ^{129}I(n,γ) reaction. The present accuracy improves significantly the knowledge of the iodine cross sections for transmutation studies.

Owing to the lack of ^{129}I experimental data above 100 keV, new microscopic measurements are recommended. They are required to improve the description of the total and partial cross sections with the help of optical model calculations. Recent calculations performed with the EMPIRE code of the ^{127}I(n,2n), ^{127}I(n,p), ^{127}I(n,α) and ^{129}I(n,2n) reactions on the basis of experimental data measured at the 7 MeV Geel Van de Graaff accelerator should be introduced in the final evaluated data file. The validation of the natural iodine evaluation is in progress with the help of integral measurements carried out at the High Flux Reactor at Petten in the frame of the EFTTRA collaboration. Cell or core calculations using the ERANOS code are also in preparation for a preliminary validation of the ^{129}I evaluation.

Appendices

Appendix A

Neutron and γ-rays induced background in Time Of Flight experiments

In recent years, an increased interest from the n-TOF collaboration has arisen for reliable determination of background induced by neutron and γ-ray in time-of-flight (TOF) experiments [150]. Several physical processes may explain the behaviour of the background and its complex time dependence. According to studies based on transmission measurements, performed ten years ago at the Geel LInear Accelerator GELINA of the Institute for Reference Materials and Measurements (IRMM), the origin of the background is not well understood and may not be well defined with simple functions as used in most of the TOF measurements. Time dependence and a possible origin of the background in capture and transmission measurements are proposed over the study of three detection systems (^{10}B ionisation chamber, C_6D_6 liquid scintillator and Li-glass detector).

A.1 Introduction

Capture measurements give the number of capture events ($N_c(t)$) per incident neutron called the capture yield ($Y(t)$). The experimental capture yield is expressed as a function of $N_c(t)$ and of the incident neutron flux $\phi(t)$:

$$Y(t) \;=\; N_Y \,\frac{N_c(t)}{\phi(t)} \propto \frac{N_\gamma^w(t) - B_\gamma(t)}{\varepsilon_c(t)\phi(t)} \tag{A.1}$$

in which N_Y stands for the normalisation factor, $\varepsilon_c(t)$ is the capture γ-ray detector efficiency, $N_\gamma^w(t)$ represents the weighted count rate and $B_\gamma(t)$ is the background. The simultaneous measurement of the neutron flux with the number of capture events is achieved by using a boron ionisation chamber and a pair of C_6D_6 liquid scintillators. The observed count rate $N_F(t)$ delivered by the ionisation chamber is defined as the product of the incident neutron flux with the detector efficiency $\varepsilon(E)$. Introducing the background contribution ($B_F(t)$), $N_F(t)$ is expressed as follows:

$$N_F(t) \;=\; \varepsilon(t)\;\phi(t) \;+\; B_F(t) \tag{A.2}$$

Transmission measurements consist of a sequence of *in* (sample in the beam) and *out* (sample out of the neutron beam) sample changer positions. The experimental transmission is given by:

$$T(t) \;=\; N_T \frac{N_{in}(t) - B_{in}(t)}{N_{out}(t) - B_{out}(t)} \tag{A.3}$$

where N_T stands for the normalisation factor, $B_{in}(t)$ and $B_{out}(t)$ represent the background contributions. The measurements are performed with a Li-glass detector placed in the neutron beam line.

The background is one of the main sources of uncertainty in TOF measurements. The shape of the background is defined as a sum of a constant term and a time dependent function:

$$B(t) = \alpha + \beta(t) \tag{A.4}$$

Constant background may be due to detector environment and cosmic radiations. An additional contribution may be taken into account when a radioactive sample is used. The time dependent background is induced by the accelerator pulses. A fraction of the background is produced by neutrons scattered in the target hall of the GELINA facility, in the tube guide and in the vicinity of the detector.

The time dependence of the background is currently determined using the black resonance technique. This method consists of placing a resonance filter in the neutron beam, that is thick enough so that at least one of the resonances has "zero" transmission ($10^{-4} < T(E) < 10^{-3}$) over several timing channels at the position of the peak. The disadvantage of this technique is that the exact shape of the background between black resonances well-spaced over the entire energy range is unknown. An estimate of the background in capture γ-rays spectrum can be obtained by replacing the sample with a body with similar scattering properties and with negligible capture yield. The influence of the sample makes "sample-out" background determination often questionable. The background may reflect the resonance structure of the scattering cross section of the sample.

Two independent analytic approaches were proposed by M.Moxon [98] and A.Lepretre [82] in order to estimate reliable time dependent background between the black resonances. In addition, a fraction of the time dependent background induced by γ-rays has been measured in transmission experiments by A.Brusegan [151].

A.2 "Structured" background

The existence of structures in the time dependent background was deduced from results of two natural silver transmission experiments and from background behaviour in a capture γ-rays spectrum of a thin PbI_2 sample. Measurements were carried out at 30 m flight distance in two different experimental areas.

A.2.1 Transmission experiment

The contribution of the time dependent background ($\beta(t)$) was studied over two transmission measurements of natural silver ($n = 2.9 \times 10^{-4}$ at/b). A first measurement ($M1$) was carried out with an appropriate electronic set-up. A second experiment ($M2$) was performed in the same experimental conditions with an electronic set-up modified to increase the background contribution. Figure A.1a shows the transmission of the first s-wave resonance of the ^{109}Ag(n,tot) reaction. The transmissions (T_{M1}) and (T_{M2}) were obtained without background correction. T_{M1} is in a reasonable agreement with the theoretical curve (T_0) given by SAMMY with the JEFF3 resonance parameters. The discrepancy between the capture area $A_\gamma = \Gamma_n\Gamma_\gamma/(\Gamma_n + \Gamma_\gamma)$

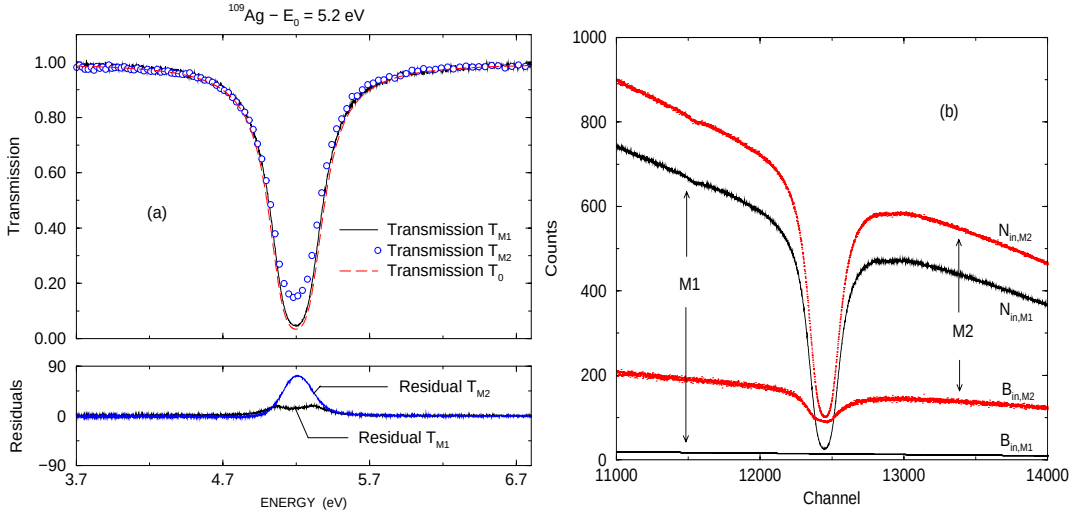

Figure A.1: (a) Transmissions (T_{M1}) and (T_{M2}) obtained from two natural silver transmission experiments. No background subtraction was applied in the data reduction procedure. The $M1$ experiment was carried out with an adequate electronic set-up. It was modified for $M2$ to increase the background to signal ratio. The theoretical curve (T_o) was calculated with SAMMY by using the resonance parameters recommended in the JEFF3 neutron data base. (b) Count rates N_{in} and time dependent backgrounds B_{in}. The background for $M2$ is deduced from the $M1$ experiment in order to obtained a satisfactory agreement between the two transmission T_{M1} and T_{M2}.

calculated with the JEFF3 parameters and the parameters extracted from the T_{M1} remains within 2.4%. The discrepancy is larger than 20% with results from T_{M2}. Therefore, we may deduce from T_{M1} a suitable time dependent background for the transmission T_{M2}. The better agreement between the two transmission measurements is obtained with backgrounds shown in Figure A.1b. The spurious behaviour in the vicinity of the resonance demonstrates the necessity to account for *structures* in the time dependent background.

A.2.2 Capture experiment

Similar conclusions can be deduced from the ^{127}I capture γ-rays spectrum shown in Figure A.2. The capture measurement was carried out with two permanent black filters (S and Na). In the resolved energy range, the shape of the background is obtained from the resonance analysis (Section 5.4). Below 10 keV, the background is easily fitted by the sum of two exponential decaying functions. Such time dependent background is adequate to describe the bottom of the sulfur resonance at 102 keV. However, results around the 2.8 keV resonance of Na overestimate the expected background given by the bottom of the black resonance. Consequently, additional structured background corrections have to be taken into account in the data reduction procedure.

A.3 Analytic model

An analytic model was developed by M.Moxon in a fitting program called BACFIT to account for structures in the background of ^{238}U transmission measurements [98]. Similar treatment was developed by A.Lepretre to improve background corrections in ^{237}Np capture measurements [82]. The origin of the time dependent background given by the two studies is different. According to

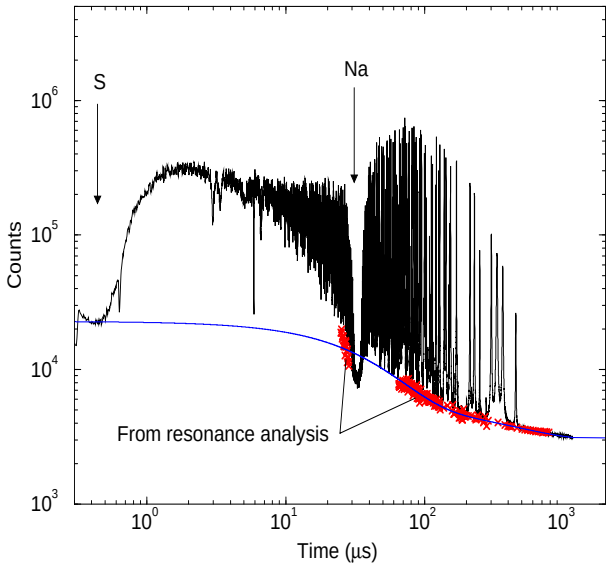

Figure A.2: ^{127}I capture γ-rays spectrum and smooth time dependent background deduced from the resonance analysis below 10 keV.

the ^{238}U transmission measurements, the detection at a later time of incident neutrons scattered by the detector and the surrounding materials, is probably the best source of the structured background. From the ^{237}Np capture experiments, the background may be induced by neutrons scattered in the target hall, the collimators and the tube guide. Analytic expressions used for modeling the background depend on its expected origin. In the model implemented in BACFIT, some equations take into account the neutron flux passing between the detector, the flux transmitted by the detector and the flux scattered by the detector. A more general treatment is used in this work. It is based on the modelisation proposed in Reference [82], which assumed a fraction of the background as a function of the measured quantities (incident neutron flux, capture γ-rays).

A.3.1 Definition of the time dependent background $B(t)$

Several contributions were deduced from the analysis of capture and transmission TOF spectra. The background may be defined as a sum of three main components:

$$B(t) = \alpha + B_0(t) + \mathcal{F}\left(\phi(t)\right) \tag{A.5}$$

$$B_0(t) = a\, \mathrm{e}^{-\frac{\ln 2}{\tau_1} t} + b\, \mathrm{e}^{-\frac{\ln 2}{\tau_2} t} \qquad \text{and} \qquad \mathcal{F}\left(\phi(t)\right) = B_\gamma(t) + B_n(t) \tag{A.6}$$

where $\phi(t)$ stands for the incident neutron flux. The possible origin of each contribution is shown in Figure A.3. The origin of $B_0(t)$ is well understood. The neutron source as well as the complex history of the neutron production in the target hall explains this component. The behaviour of $B_0(t)$ is characterised by two exponential decaying functions with half-life τ_1 and τ_2 depending slightly on the experimental area. $B_\gamma(t)$ and $B_n(t)$ are assumed to be functions of the incident neutron flux. The background $B_\gamma(t)$ is probably induced by γ-rays produced in the experimental area after capture of neutrons in the vicinity of the detector. An experimental procedure was developed by A.Brusegan to measure such contributions in a Li-glass detector. Results, shown in Section A.3.4, indicate the existence of a structured background.

The background $B_n(t)$ results from the detection of neutrons scattered out of the neutron beam and returning later to the detector.

The contribution $B_n(t)$ in a capture γ-rays spectrum may has a slightly different meaning. It is probably connected to the neutron sensitivity of the C_6D_6 detector. Secondary neutrons produced in reactions like (n,n), (n,n'), (n,2n) and captured in the detector create signals which are indistinguishable from the sample capture event, and contribute directly to the resonance area. The neutron sensitivity is defined as the ratio between the detection efficiency of scattered neutrons ε_n and that of the capture ε_γ. The shape analysis program REFIT [26] accounts for such prompt background through an additional capture yield ($Y_S(E)$). The correct form of the theoretical capture yield should be:

$$Y(E) = \frac{\mu(E)\sigma_\gamma(E)}{\sigma_t(E)}\left(1 - e^{-n\sigma_t(E)}\right) + Y_S(E) \tag{A.7}$$

$$Y_S(E) = \frac{\varepsilon_n}{\varepsilon_\gamma}\frac{\sigma_s(E)}{\sigma_t(E)}\left(1 - e^{-n\sigma_t(E)}\right) \tag{A.8}$$

where σ_s, σ_γ and σ_t are the scattering, capture and total cross section. $\mu(E)$ is the multiple scattering correction and n is the sample thickness in atoms per barn. Combining Equations A.1 and A.7, $B_n(E)$ may be expressed as:

$$B_n(E) \;\propto\; Y_S(E)\;\phi(E) \tag{A.9}$$

The neutron sensitivity ($\varepsilon_n/\varepsilon_\gamma$) of the C_6D_6 detectors ranges from 10^{-3} to 10^{-4}; this effect acquires importance for structural materials where $\Gamma_n/\Gamma_\gamma > 10^3$.

The sum $B_\gamma(t)+B_n(t)$ is currently taken into account by using simple functions of time. According to the time dependence of the neutron flux, a power function (bt^c) should be a reasonable approximation. A more realistic description is based on results taken from References [98, 82]. For a neutron flux measurement (boron chamber or Li-glass detector), it is assumed that a fraction ($F(t)$) of incident neutrons are scattered out of the beam and return later to the detector with an exponential decaying intensity of half-life $\tau(t)$:

$$\mathcal{F}_{Flux}\left(\phi(t)\right) = \int_0^t \varepsilon(t_o)\phi(t_o)F(t_o)\mathrm{e}^{-\frac{\ln 2}{\tau(t_o)}(t-t_o)}\mathrm{d}t_o \tag{A.10}$$

A similar expression may describe the capture γ-rays background. However, effect of the sample has to be included using the relationship from Equation A.9. The correct analytic form of ($\mathcal{F}$) should be:

$$\mathcal{F}_\gamma\left(\phi(t)\right) = \int_0^t \varepsilon_o(t_o)Y(t_o)\phi(t_o)F(t_o)\mathrm{e}^{-\frac{\ln 2}{\tau(t_o)}(t-t_o)}\mathrm{d}t_o \tag{A.11}$$

The half-life decay may be defined as a function of the mean distance l_o traveled by the scattered neutron and detected at energy E_o (or time t_o), and at the flight path length L:

$$\tau(t_o) = \frac{72.298\; l_o}{\sqrt{E_o}} = \frac{l_o\; t_o}{L} \tag{A.12}$$

According to this definition, l_o is assumed to be independent of the neutron energy over a large energy range. The energy behaviour of the exponential decay of the background may be compared to the exponential tail of the resolution function. Similar neutron scattering processes are involved. It has been demonstrated that the meaningful parameter describing the resolution

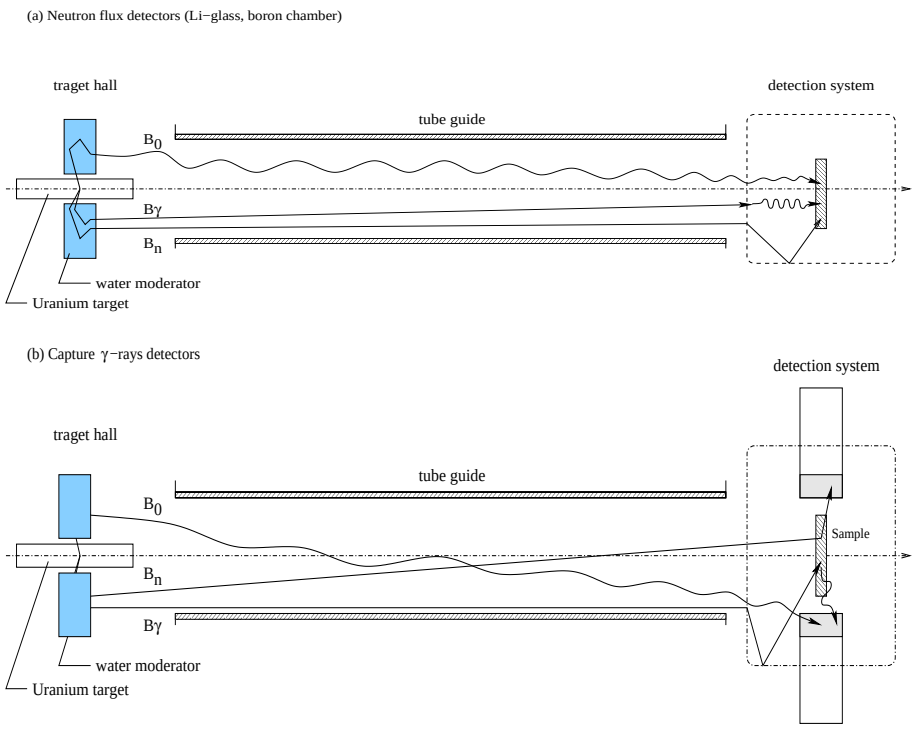

Figure A.3: Expected origin of the main background components ($B_0(t)$, $B_\gamma(t)$ and $B_n(t)$).

tail is a parameter which is equivalent to the mean distance (l_o) instead of the half-life decay (τ) [152].

Several assumptions are needed to propose a suitable analytic expression for $F(t_o)$. Since the exact origin of the background is not well known, the fraction of neutrons scattered out of the beam is assumed to be proportional to the exponential decaying intensity of the returning neutrons. A crude estimate of the time dependence of $F(t_o)$ may be given by:

$$F(t_o) \;=\; \kappa\,\frac{\ln 2}{\tau(t_o)} \qquad (\kappa = \mathrm{cst}) \tag{A.13}$$

The iterative form of the structured background is then defined as:

$$B(t) \;=\; \alpha \;+\; B_0(t) \;+\; \kappa\,\frac{\ln 2\;L}{l_o}\int_0^t \frac{(N(t_o)-B(t_o))}{t_o}\;\mathrm{e}^{-\frac{\ln 2\;L}{l_o}\frac{(t-t_o)}{t_o}}\,\mathrm{d}t_o \tag{A.14}$$

where $N(t_o)$ may be the capture γ-rays spectrum (N_γ^w), the flux spectrum (N_F), or the *in* and *out* spectra (N_{in}, N_{out}) depending of the detection system under investigation.

A.3.2 Determination of α

Figure A.4 shows the neutron flux spectrum given by a ^{10}B ionisation chamber. The constant background α was measured without the neutron beam (flight path 15 closed). The bottom of the Na, Bi, Co, Mo and W black resonances are well described by α . According to the

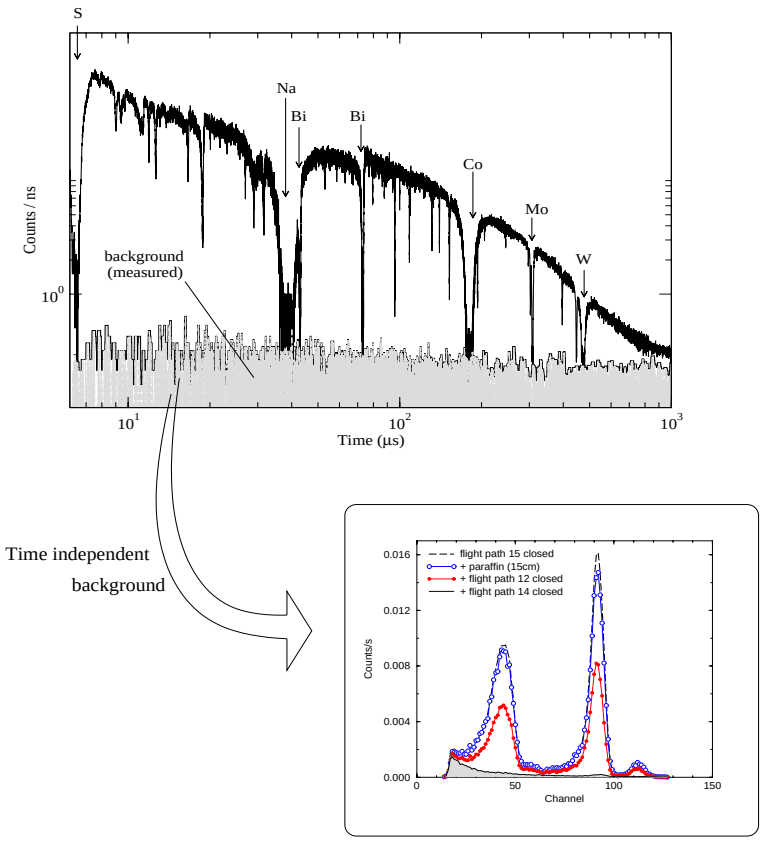

Figure A.4: Neutron flux spectrum and time independent background (α) together with the ^{10}B ionisation chamber pulse height signal.

information provided by the anode pulse height signal of the detector, about 90% of α (equivalent to 1 neutron/s) is due to neutrons scattered out of the neighbouring flight path (flight path 12 and 14). The remaining is due to electronic background, and cosmic radiations. Neutrons due to cosmic rays are mainly produced by muons into the lead shielding placed in the front of the ionisation chamber. The number of neutrons may be estimated from the number of muons intercepted by the lead shielding times the number of neutrons produced by capture of muons in the lead ($N_{n/\mu} = 1.8$ neutrons per muons):

$$N_n = N_{n/\mu} \times I_o \int \int S \cos^2\theta \sin\phi \, \mathrm{d}\phi \, \mathrm{d}\theta \tag{A.15}$$

where S is the surface of the lead shielding, and I_0 is the flux of muons per unit surface and per unit solid angle (I_0 =80 muons.m^{-2}.s^{-1}.st^{-1}). A count rate of about 1 neutron/min can be deduced from Equation A.15 taken into account the acceptance of the detector.

A.3.3 Determination of $B_0(t)$

The behaviour of $B_o(t)$ was deduced from two capture measurements carried out at 14.4 m and 60 m flight distance (Figure A.5). Above 20 μs the background is perfectly fitted using two exponential decaying functions of half-life $\tau_1 = 22.0 \pm 1.0$ μs and $\tau_2 = 282.0 \pm 50.0$ μs. Such background is inherent in TOF measurement. Time of flight data from measurement on a 60 mm thick polyethylene filter taken in 1993 at the GELINA facility (100 Hz repetition rate) were easily fitted below 200 eV with a similar smooth function by M.Moxon ($\tau_1 = 27.34$ μs,

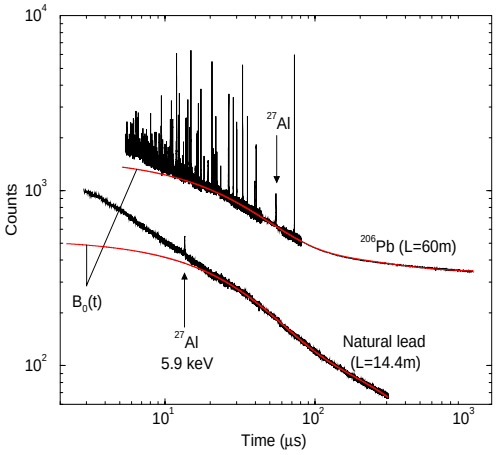

Figure A.5: Capture γ-rays spectra obtained with a thin natural lead sample and a 1.1 mm thick ^{206}Pb sample.

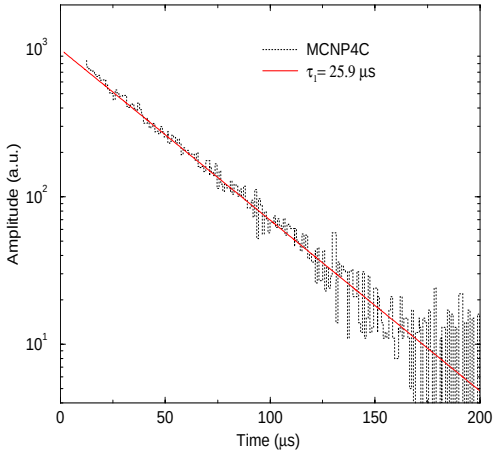

Figure A.6: Typical slowing down time of fission neutrons in the water moderator of the GELINA facility.

$\tau_2 = 205.9$ μs) [98]. More recently, "sample-out" measurements carried out at the n-TOF facility show a similar time dependent background. Below 100 keV, two exponential decays have been found with $\tau_1 = 160$ μs and $\tau_2 = 1800$ μs [150].

At the GELINA facility, one explanation of the double exponential could be the consequence of a photon flux coming from the target hall. MCNP Monte-Carlo simulation was performed to study the lifetime of fission neutrons in the water moderator of the GELINA neutron source. It can be divided into two parts:

- the slowing down time, which is the mean time required for fission neutrons to slow to thermal energies.
- the diffusion time, which is the average time that thermal neutrons will diffuse before absorption.

The uranium target emits high energy neutrons that are slowed in the water moderator by elastic scattering. At thermal levels, the neutrons diffuse through the moderator until they undergo thermal capture. The slowing down process and the capture is dominated by hydrogen. MCNP simulation is shown in Figure A.6. The neutron lifetime from the simulation is about 26 μs which is in excellent agreement with τ_1. Origin of the larger half-life τ_2 is not clearly identified. It may correspond to the neutron lifetime in the bunker concrete wall.

The background in the higher energy range of the TOF spectra shown in Figure A.5 cannot be fitted using two exponential decaying components. Additional contribution $B_\gamma(t) + B_n(t)$ has to be included.

A.3.4 Determination of $B_\gamma(t)$

An experimental method was applied in transmission measurements to deduce structured background induced by γ-rays. The anode pulse height signal provided by the photomultiplier is shown in Figure A.7. The full energy peak of the (n,α) reaction is the neutron response of the Li-glass detector. In order to measure the incident neutron flux and its background, hardware windows select events falling in Z0, Z1, Z2, Z3 and Z4. γ-rays background in the (n,α) reaction

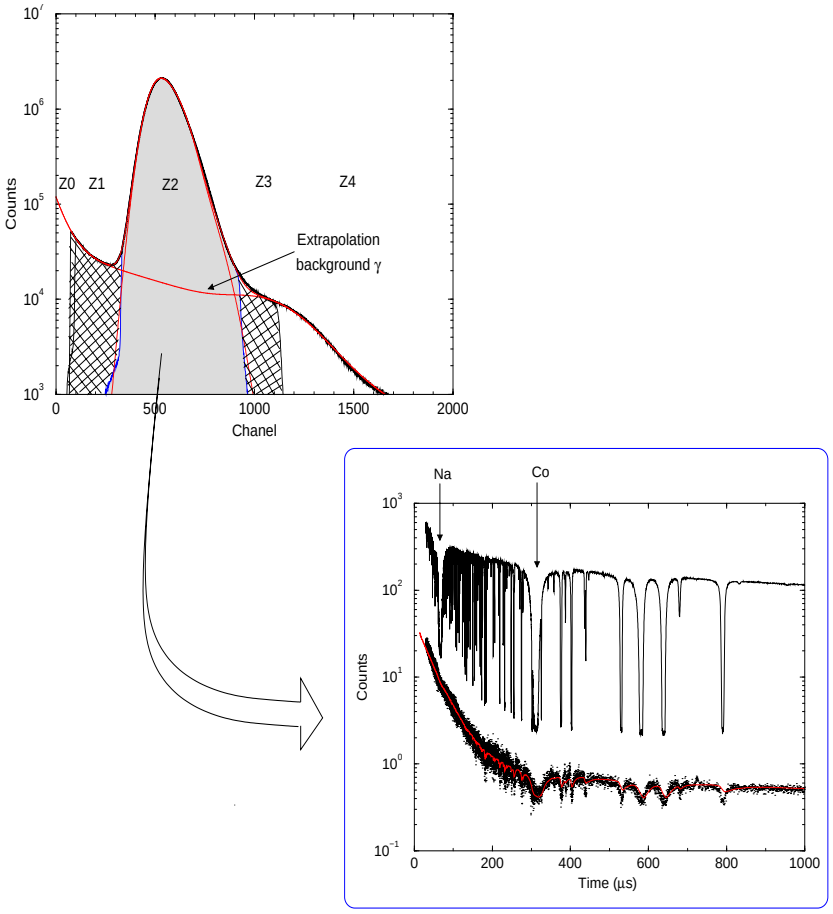

Figure A.7: Anode signal pulse height of the Li-glass detector and neutron flux $N_{in}(t)$ transmitted by a thick PbI_2 sample containing natural iodine. Time dependent background $B_\gamma(t)$ was deduced from TOF spectra corresponding to event falling in the hardware windows (Z1) and (Z3). The curve results from a least squares fit of $B_\gamma(t)$ with Equation A.6.

peak (Z2) is extrapolated from events (Z1) and (Z3). Final time of flight spectra B_γ resulting from the analytic combination of these events is shown in Figure A.7. A least square fit with expression A.14 provides a value of l_o close to 8 cm. Photons are probably produced by capture of neutrons in the aluminum sphere surrounding the Li-glass detector.

A.3.5 Determination of $B_n(t)$

The $B_n(t)$ component can be deduced from the neutron flux spectrum provided by the ^{10}B ionisation chamber. The background is mainly induced by neutrons. The γ-rays contribution can be neglected. Equation A.5 becomes:

$$B(t) = \alpha + B_n(t) \tag{A.16}$$

The background is a small fraction of about 10% of the incident neutron flux. At 2.8 keV, the contribution of the background is on the order of 1.8% and reaches 28% around 10 eV. The neutron flux detector was optimised to reduce the perturbation of the neutron flux. This intrinsic feature explains the small contribution of the background. Over the entire energy range of interest [10 eV-100 keV], $B(t_o)$ can be neglected in Equation A.14. Reliable time dependent

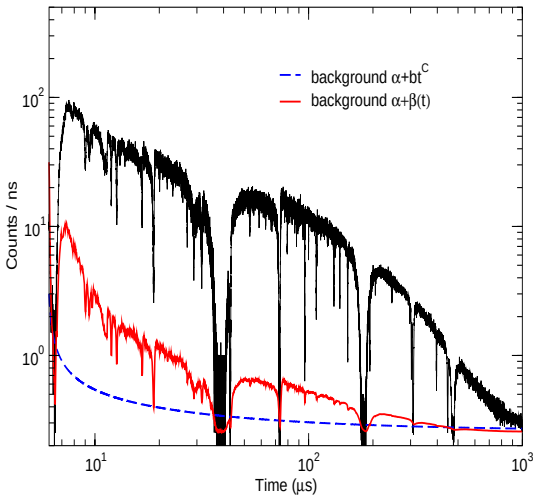

Figure A.8: Neutron flux spectrum and time dependent background $B_n(t)$.

background is achieved without an iterative step. Results of the least square fit of the data are shown in Figure A.8 together with the background obtained with a simple function of time. In the time range above 30 μs, the discrepancy is not significant because of the large statistical uncertainty. At higher energy (below 10μs), the behaviour between 30 keV and 80 keV is no longer negligible. We found a l_o value close to 11 cm. Therefore, the larger part of the background seems to be produced in the vicinity of the ^{10}B ionisation chamber.

A.3.6 Final background $B(t)$

The full time dependent background was investigated over a large number of capture and transmission measurements carried out in different experimental areas. TOF spectra and backgrounds are shown in Figure A.9. The bottom of the black resonances was fitted with Equation A.5 to obtain relevant information on parameters α, κ, l_o, a, b, τ_1 and τ_2.

The parameter l_o deduced from transmission measurements carried out at 30 m and 50 m flight distance is about (8.0 ± 4.0) cm. Values for the ^{10}B ionisation chamber and the C_6D_6 detector are respectively on the order of (11.0 ± 2.0) cm and (40.0 ± 10.0) cm. The best source of the structured background is probably the detector and its surrounding. The accuracy of l_o depends on the knowledge of $B_o(t)$. Decay parameters τ_1 and τ_2 are found to be nearly independent of the experimental area and of the accelerator conditions. Estimate of τ_1 and τ_2 are respectively equal to (22.0 ± 7.0) μs and (277.0 ± 52.0) μs. Only α, κ, a_1 and a_2 depend on the experimental situation.

A.4 Nuclear parameters sensitivity

A.4.1 Transmission measurement

Two transmissions $T(E)$ and $T'(E)$ were obtained and analysed with REFIT. The neutron widths (Γ_n) extracted from the transmission built with the smooth background ($B(t) = \alpha + bt^c$)

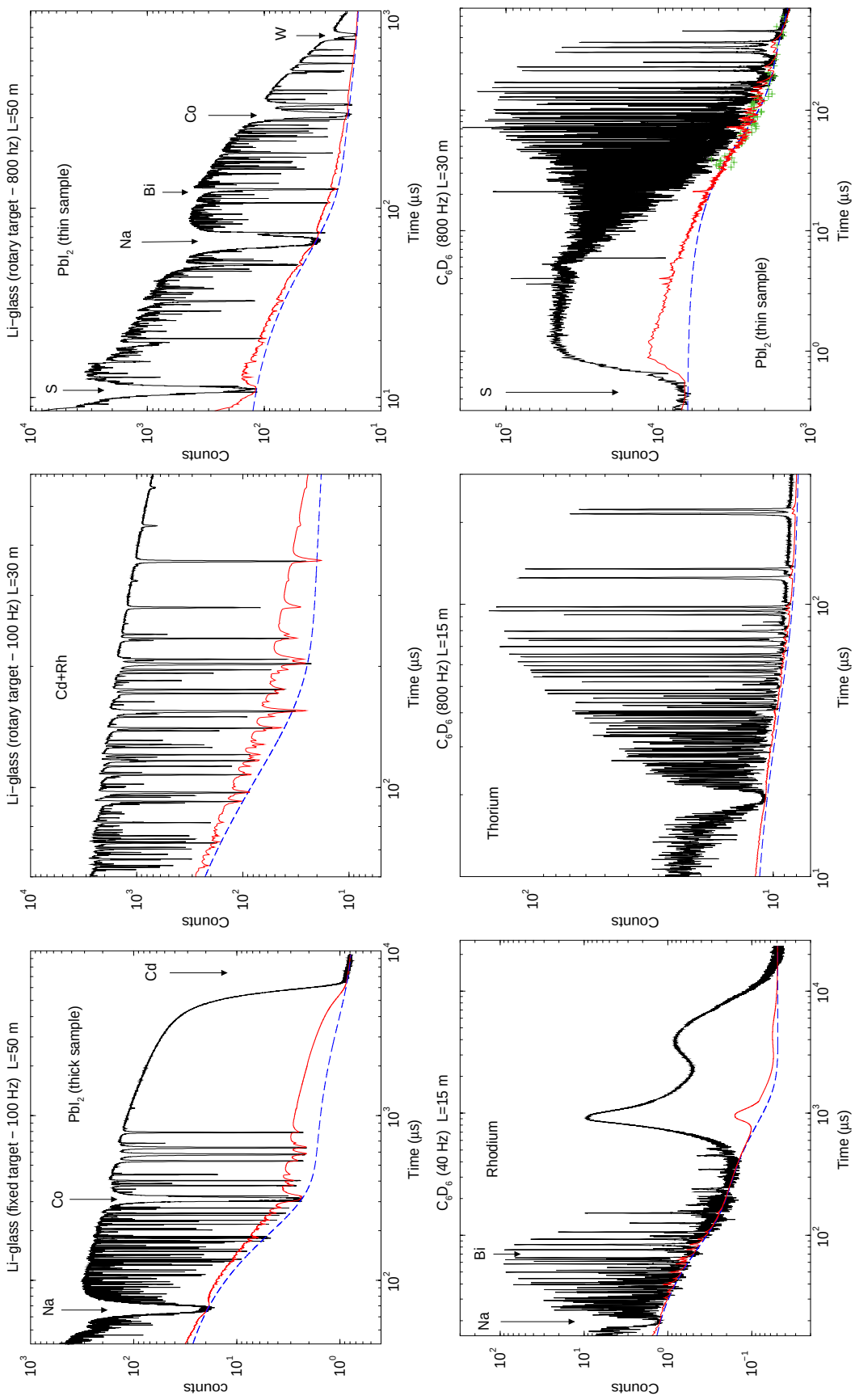

Figure A.9: Neutron flux and capture γ-rays spectra together with the structured background. The dashed line is the $B_0(t)$ component. TOF measurements were carried out on several flight paths at different distance (L) from the neutron source. For the first transmission, neutrons were produced with a *fixed* uranium target. Water moderators were the same for all the measurements. Cadmium and boron antioverlap filters were used at 40/100 Hz and 800 Hz repetition rate respectively.

are compared with the neutron widths (Γ'_n) extracted from the transmission built with the structured background.

Results are shown in Figure A.10. The mean value of the distribution of the Γ'_n/Γ_n ratio is about 1.024. The structured background cannot be neglected without introducing a significant systematic error on the neutron width values. Over the unresolved energy range, the discrepancies between $T(E)$ and $T'(E)$ involve errors lower than 1% on the total cross section. Improvements in the determination of $B(t)$ are then needed to confirm the systematic bias observed over the Resolved Resonance Region.

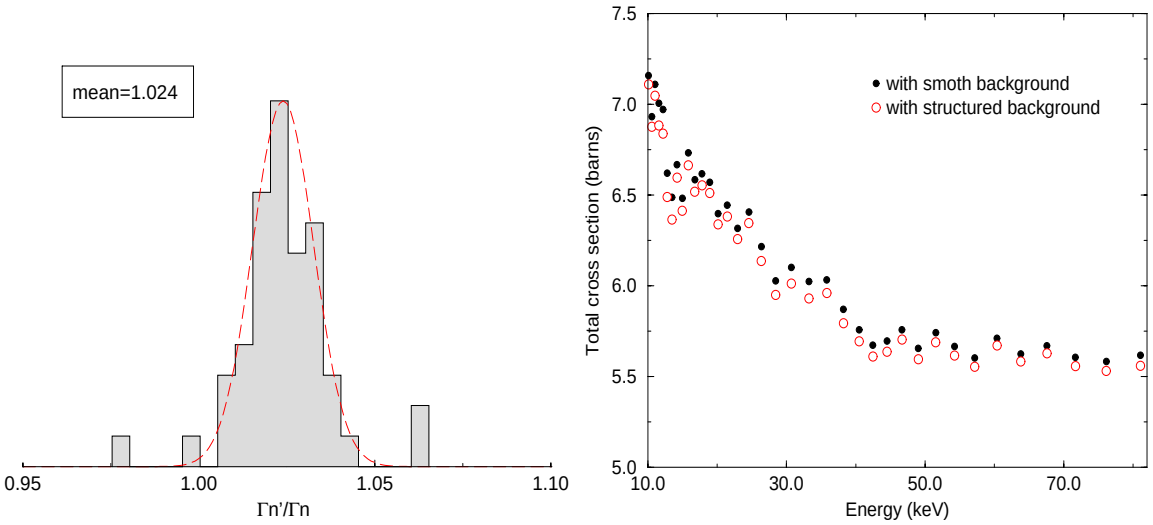

Figure A.10: Neutron widths Γ_n and Γ'_n are related to values extracted from a ^{127}I transmission measurement, obtained respectively with a smooth background ($B(t) = \alpha + bt^c$) and a structured background.The resonance analysis was performed with the program REFIT up to 1 keV.

A.4.2 Capture measurement

Similarly, two ^{127}I capture yields obtained with and without structured backgrounds were analysed with REFIT. Results obtained around 30 eV and within the 5 keV to 85 keV energy range are shown in Figure A.11. On the left half of the figure, the similar behaviour of the two residuals suggests negligible the discrepancy on the capture area $A_\gamma = \Gamma_\gamma\Gamma_n/(\Gamma_\gamma + \Gamma_n)$ extracted from the capture yields obtained with a smooth background and calculated with a structured background. This result agrees with the negligible contribution of B_n resulting of the low neutron sensitivity of the C_6D_6 detectors. By contrast, in the Unresolved Resonance Range, the capture yield seems to be overestimated by at least 1.7% in average when smooth background is used. We may affect a similar systematic error on the average capture cross section.

A.5 Conclusion

The time dependent background investigated over several TOF measurements seems to be well understood. Conclusions are consistent with those given in Reference [98] . The larger part of the γ-rays background is produced by the neutron source of the GELINA facility. Additional

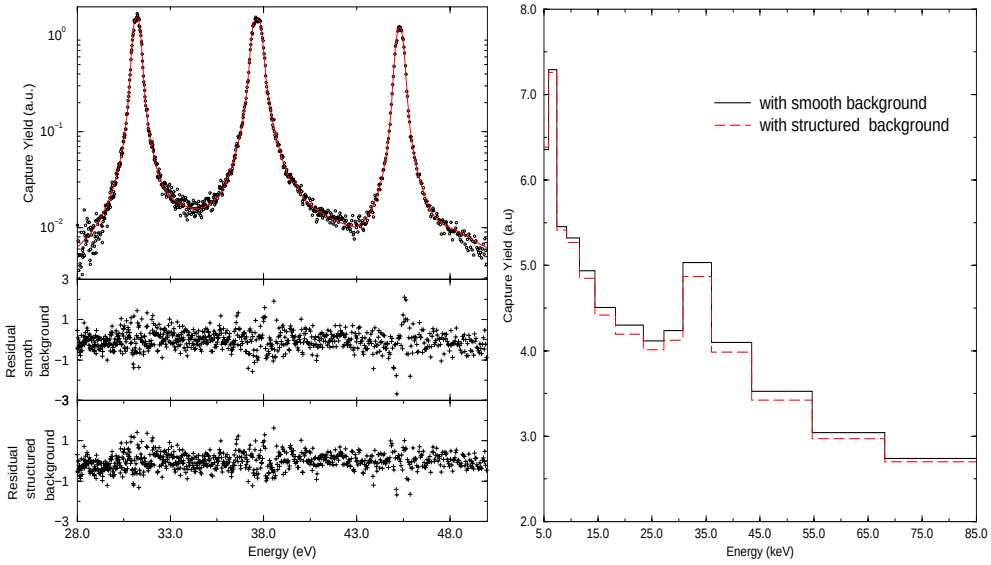

Figure A.11: Effect of the background over the resolved and unresolved energy range in capture measurement. The capture yield $Y_m(E)$ was obtained from a thin PbI_2 sample containing natural iodine. In the resonance range, the theoretical curve $Y_{th}(E)$ is calculated with REFIT. Around 30 eV, the comparison between the two capture yields obtained with smooth and structured backgrounds is achieved via their residual defined as $R(E) = (Y_m(E) - Y_{th}(E))/\sigma_m(E)$ (σ_m is the data uncertainty).

components could be neutrons scattered in the vicinity of the detection system. The analytic model to account for structured background is derived from Reference [82]. The proposed formula cannot deal with large corrections but it may be seen as a valuable tool for accessing reliable information on the background origins.

We may expect a negligible effect of the structured background in the resolved resonance range of the capture measurements as well as in the unresolved energy range of the transmission measurements. On the contrary, a correction of about 2% on the average capture cross section and on the neutron widths extracted from a transmission measurement seems to be reasonable in accordance with the limit of validity of the model used in this work.

In order to derive accurate corrections involved by the unknown background behaviour, similar investigations should be performed with the program BACFIT in association with a modified version of REFIT developed by M.Moxon. This newly version directly allows a simultaneously adjustment of the background, of the experimental resolution and of the nuclear parameters on the count rate spectra.

Appendix B

Experimental resolution function of the GELINA facility

A detailed study of the resolution function of the linear accelerator GELINA was performed in order to analyse with the code SAMMY the measurements carried out at Geel. This work is based on the development in SAMMY of the resolution function of the Geel facility. An accurate description of this resolution function is needed to extract the resonance parameters from differential measurements. The time distribution of the neutrons escaping from the water moderator of the rotating uranium target assembly, the time response of the neutron detector, the electron burst contribution and the channel width define the resolution function of GELINA. The purpose of this appendix is to describe the analytic treatment available in REFIT currently in use at Geel. In REFIT, the resolution function is described by some analytic expressions based on the neutron physics properties of the spectrometer. The description includes free parameters, which have been determined by M.Moxon from various TOF measurements. The limitation of this treatment and possible improvements are discussed together with Monte-Carlo simulations recently implemented in REFIT

B.1 Introduction

The determination of meaningful nuclear resonance parameters from neutron time of flight data requires an accurate description of the energy resolution of the facility as a function of neutron energy. The time of flight of a neutron has a distribution in time (or equivalently in distance) called the resolution function. Several numerical treatments are available in the shape analysis program SAMMY [27] that are not suitable to describe the resolution function of GELINA. The implementation of such a resolution function in SAMMY requires a better understanding of the analytic treatment available in the program REFIT [26], developed by M.Moxon and currently in use at the IRMM. The purpose of this appendix is to describe the REFIT implementation of the GELINA experimental resolution function, its limitations, and possible improvements.

The 140 MeV electron accelerator GELINA produces short bursts of neutrons originating from (γ,n) and (γ,f) reactions in a rotating uranium target, cooled by Hg [65]. The fast neutrons produced in the uranium target are moderated in the water contained in beryllium cans located above and below the target. The resolution function can be split into various components, reflecting the neutron transport from the target to the detection system. The relative

contributions of these components depend on the experimental conditions and on the neutron energy. The resonance shape analysis code REFIT includes such a description of the resolution function especially designed for the GEEL facility. The free parameters involved can be related to physically observable and measurable quantities like the electron pulse width, the neutron cross-sections, and the dimensions of the target, the moderator and the detector [153]. However, a reliable quantification of the parameters is a quite elaborated task. It involves accurate measurements of isolated resonances, and a comparison of the resolution function obtained from analytic expressions and from Monte-Carlo simulations. Recently the REFIT code has been upgraded by A.Brusegan to be able to handle the resolution functions obtained by Monte-Carlo simulations.

The observed total width of a resonance Γ_{obs} resulting from capture or transmission TOF-measurements, is determined from the natural width Γ_{tot}, the additional Doppler width (ΔE_{dop}) and the resolution broadening width (ΔE_{res}). The observed width at half maximum may be estimated from the quadratic sum of these contributions assuming they are approximately Gaussian in shape and independent:

$$\Gamma_{obs}^2 = \Gamma_{tot}^2 + \Delta E_{res}^2 + \Delta E_{dop}^2 \tag{B.1}$$

An example of the overall time resolution as a function of energy, together with the different contributions, is shown in Figure B.1a. The free gas model is used to describe the Doppler broadening. The data result from transmission measurements of ^{84}Kr, ^{99}Tc, and ^{237}Np with a sample temperature close to 300 K. The measurements were performed at a 50 m distance from the target. The angle of the flight path with respect to the normal of the moderator is 9°. The Doppler broadening is the dominating effect at low energies. For higher neutron energies the contribution of the Doppler broadening can be neglected and the resolution effect becomes more important. The relative contribution of the natural width to the overall observed width depends on the isotope under investigation.

As mentioned above, the resolution broadening is the result of various contributions. In Figure B.1b, six main processes are taken into account. The channel width and the initial burst of neutrons can be expressed in term of time of flight uncertainty ΔT. The target, the moderator, the angle of the flight path and the detector (in the case of transmission measurements) introduce an uncertainty ΔL on the flight path length L. Equation B.2 gives the relationship between the energy uncertainty and the time and distance uncertainties in the case of components Gaussian in shape.

$$\frac{\Delta E}{E} = \frac{2}{L}\sqrt{\frac{E}{t^2(1eV)}\Delta T^2 + \Delta L^2} \tag{B.2}$$

with

$$\Delta T^2 = \Delta T_{CW}^2 + \Delta T_{burst}^2 \qquad \Delta L^2 = \Delta L_{mod}^2 + \Delta L_{det}^2 \tag{B.3}$$

where $t(1eV)$ is the time a 1 eV neutron takes to cover 1 meter, equal to 72.298 μs/m.

SAMMY and REFIT account for the contribution of the channel width and of the initial burst of neutrons in a similar way. The channel width is described by a square function. The burst of neutron is assumed to be Gaussian in shape in SAMMY, and a trapezium function is used in REFIT. Here, we only discuss the processes affecting the flight path length L. In the first section, we investigate the spread on the flight path length due to the multiple scattering of fast neutrons in the target-moderator assembly together with the contribution of the flight

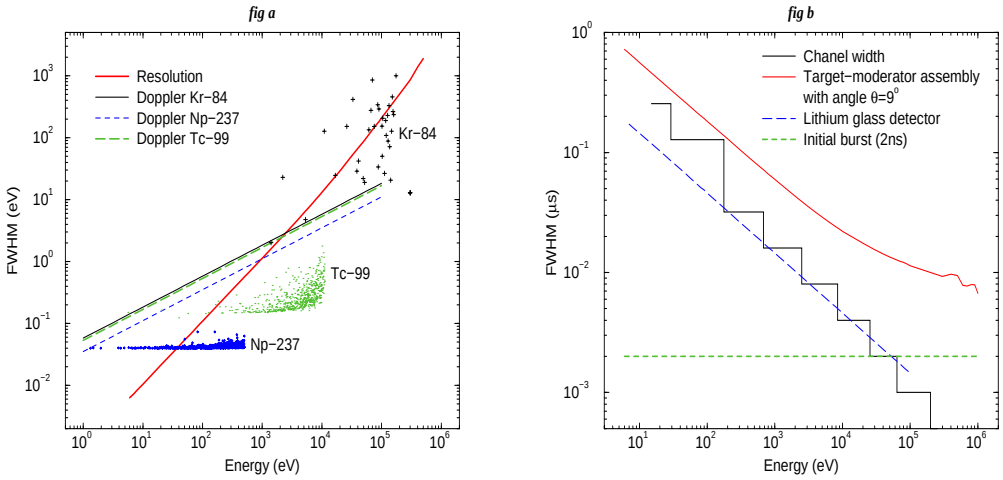

Figure B.1: (a) Energy dependence of the full width at half maximum of the Doppler broadening and experimental resolution of the Geel facility (flight path 4, L=50 m) compared to the natural width of krypton, neptunium and technetium. (b) Main contributions of the resolution.

path angle. The analytic description of the response function of a Li-glass detector used in transmission measurement is given in the second section. In the third section, the improvements performed in the analytic formula available in REFIT are compared with simulations from Coceva [117] recently implemented in REFIT-IRMM [154].

B.2 Neutron source description in REFIT

B.2.1 Uranium rotary target effect

The time distribution $I(t)$ due to neutron interactions in the source material (Figure B.2) is described through a phenomenological treatment split in two parts.

$$I(t) = \underbrace{I_p(t) \star D_1(t)}_{normalised} + k(E)[\underbrace{I_p(t - d(E)) \star D_2(t - d(E))}_{normalised}] \tag{B.4}$$

$$D_1(t) = \frac{\ln 2}{\tau_0} e^{-\frac{\ln 2 t}{\tau_0}} \tag{B.5}$$

$$D_2(t) = \frac{\ln 2}{a_1\tau_1 + a_2\tau_2} \left(a_1 e^{-\frac{\ln 2 t}{\tau_1}} + a_2 e^{-\frac{\ln 2 t}{\tau_2}} \right) \tag{B.6}$$

The first term of Equation B.4 represents the time taken by a neutron to cross the source convoluted with the initial burst of fast neutrons. The second term represents the effect of the surrounding materials reproduced in REFIT by a second pulse with a long tail of small amplitude which last up to 1.5 μs. $k(E)$ and $d(E)$ are respectively the amplitude and the delay of this second pulse expressed as a function of energy.

$$k(E) = k_1 + k_2 E^{k_3} \text{ and } d(E) = d_1 + d_2 E^{d_3} \tag{B.7}$$

The half life τ_0 of the target decay is assumed to be proportional to the time taken by a fast neutron to cover a mean free path in the volume where the neutrons are produced. It is set to 3.5 ns. The other parameters have been fitted by M.Moxon to reproduce the resonances of ^{60}Ni in the energy range of 2.25 keV. For a delay $d(E)$ equal to zero and a secondary pulse amplitude $k(E) = 0.1$, he found:

$$\begin{array}{llll} \tau_1 &= 29.48 \text{ ns} & a_1 &= 1.0 \text{ ns}^{-1} \\ \tau_2 &= 99.30 \text{ ns} & a_2 &= 0.0814 \text{ ns}^{-1} \end{array}$$

M.Moxon confirmed the shorter decay by fitting to some higher energy resonances, while the larger decay of 99.3 ns was not seen clearly. The determination of the latter was rather difficult because of the presence of the nearby resonances together with the multiple scattering effects. Further work would be required to improve the fits.

Owing to such analytic description, the resolution distribution is assumed to be independent of the neutron energy. Equation B.4 then becomes:

$$I(t) = I_p(t) \star I_t(t) \text{ with } I_t(t) = D_1(t) + k_1 D_2(t) \tag{B.8}$$

The maximum time value of the distribution $I_t(t)$ chosen by Moxon is $T_m = 15\tau_2$. Figure B.2b illustrates the source materials decay.

B.2.2 Moderator time distribution

- **Analytic description**

The target-moderator assembly of the GELINA facility is shown in Figure B.3a. The time distribution of a neutron escaping from the water moderator with an energy E is given by the following equations:

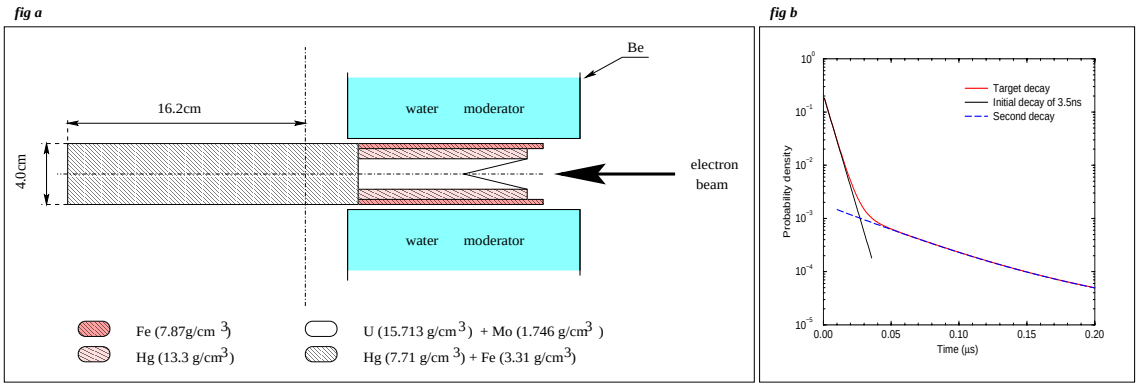

Figure B.2: (a) Schematic of the rotary target from [117]. The given composition assumes that the various materials are homogeneous mixtures. (b) Expected exponential decay of the fast neutron source obtained with Equation B.8 without initial pulse I_p.

$$I(t) = \begin{cases} \frac{1}{2}\left(\frac{\sqrt{E}}{t(1eV)\Lambda}\right)^3 t^2 e^{-\frac{\sqrt{E}}{t(1eV)\Lambda}t} & \text{if } E \geq 2.0eV \\ \frac{1}{2}(1-R)\left(\frac{\sqrt{E}}{t(1eV)\Lambda}\right)^3 t^2 e^{-\frac{\sqrt{E}}{t(1eV)\Lambda}t} + \Phi(t) & \text{if } E < 2.0eV \end{cases} \tag{B.9}$$

with

$$\Phi(t) = R\frac{\alpha^3\beta}{(\alpha-\beta)^3}\left[e^{-\beta t} - e^{-\alpha t}\left(1 + (\alpha-\beta)t + \frac{1}{2}(\alpha-\beta)^2 t^2\right)\right] \tag{B.10}$$

$$\frac{1}{\alpha} = \frac{t(1eV)}{\sqrt{E}}\Lambda(E)\left(a_1 + a_2^2 E^{a_3}\right) \tag{B.11}$$

$$\frac{1}{\beta} = b_1 + b_2 E^{b_3} \tag{B.12}$$

$$R = e^{-\frac{E}{c_1 + c_2 E^{c_3}}} \tag{B.13}$$

The time distribution of the moderation process is approximated by a χ^2-function with six degrees of freedom. The time distribution due to the storage in the moderator of slow neutrons is expressed by the function $\Phi(t)$ [113]. The function $1/\alpha$ is the time associated to the neutron mean free path (Λ) multiplied by a correction factor due to the thermal storage. $1/\beta$ is the decay half-life of thermal neutrons in the moderator and R represents the ratio of the area of the storage to the slowing down distribution. This value is simply expressed by a Boltzmann function. Examples of distributions expressed in terms of equivalent distance are shown in Figure B.3b.

Assuming an infinite hydrogeneous medium without absorption and a constant mean free path (Λ), Groenewold and Groendijk [155] first calculated the delay-time distribution of moderated neutrons from a point source. Integrating over all space and assuming the initial neutron energy to be much greater than the final neutron energy, they calculated a chi-square function with 6 degrees of freedom. A similar result was obtained by Michaudon [156], and finally Coceva et al. have successfully fitted a function of this form from Monte-Carlo simulations of the pulse neutron source of the Oak Ridge Electron Linear Accelerator (ORELA) in the energy range [3 eV

Table B.1: Parameters used in REFIT to describe the moderator seen by a sample from an angle of 9^o with respect to the normal of the moderator. Detailed explanation on the choice of Dp=12.15 cm is given in section B.2.3.

Free parameters to describe the moderator	variable	value
Thickness of moderator	ω	3.6 cm
Hydrogen thickness	n_H	0.2409 at/b
Projection of the first collimator	Dp	12.15 cm

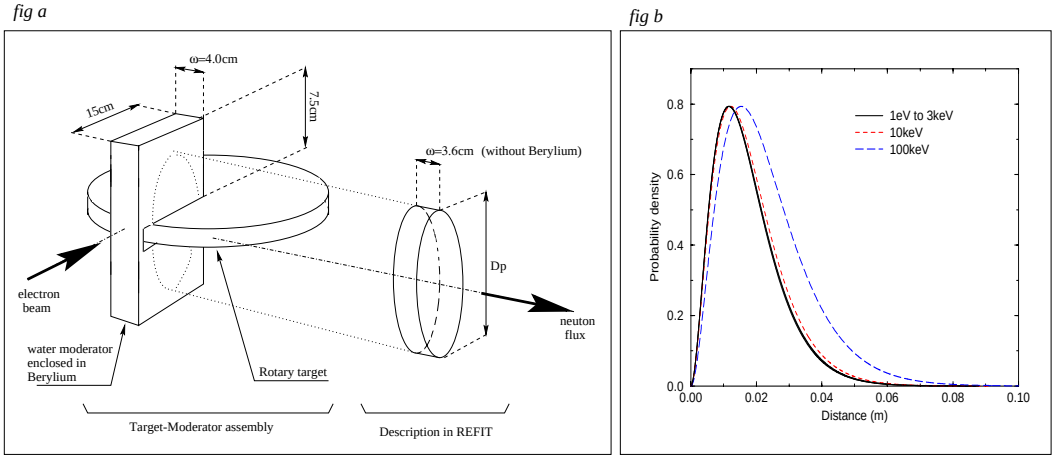

Figure B.3: (a) Geometry of the target-moderator assembly of GELINA and the associated description used by Moxon to calculate the time spread due to the water moderator. The beryllium thickness (0.2 cm) is omitted in the calculation. In REFIT, the moderator is represented by a cylinder of thickness 3.6 cm with a diameter defined by the projection of the first collimator on the moderator surface. (b) Neutron pulses shape due to the moderation process (Equation B.9).

- 3 MeV] [157]. The water moderator of ORELA can be schematically represented by a disc of thickness $\omega = 3.18$ cm and diameter $Dp = 14.6$ cm. In REFIT, the water moderator of GELINA is described in a similar way (Figure B.3), Dp being the projection of the first collimator on the moderator surface (see Table B.1).

The function $\Phi(t)$ is based on the work of Ikeda and Carpenter [158]. For the polyethylene moderator ($\omega = 4.9$ cm) of the Intense Pulsed Neutron Source (IPNS) at Argonne National Laboratory (University of Chicago), Ikeda and Carpenter have shown that the neutron pulse shapes in the region E <2 eV are very different from those in the high-energy region. Their measurement shows a long tail characteristic of a storage time in the moderator. Slow neutrons are generated by an initial source expressed by a χ^2-function and a fraction of them (in ratio R to the total) is stored in the moderator and decays with a time constant $1/\beta$.

Several modifications of the formula applied in REFIT were made to obtain the expressions proposed in Reference [158]. Some additional works were performed to find the free parameters a_i (i=1,2,3) given in Table B.2. Ikeda and Carpenter give the neutron wavelength dependence of $1/\alpha$. The expression can be written as a function of E:

$$\frac{1}{\alpha} = \frac{t(1eV)}{\sqrt{E}} \left(10^4 + \frac{2.9921}{E}\right)^{-1/2} \text{ in } \mu s \tag{B.14}$$

In REFIT, the expression B.11 uses the energy dependence of the mean free path Λ. To approach as much as possible the treatment proposed by Ikeda and Carpenter, we determined the coefficients a_i by a least squares data fit obtained from Equation B.14 with the function B.11. The agreement of the parameters (Table B.2) with Monte-Carlo simulations is discussed in section B.4.3.

Table B.2: Parameters found by Ikeda and Carpenter to account for the storage of low energy neutrons in a polyethylene moderator [158].

parameter	i=1	i=2	i=3
a_i	1.7	3.54 meV$^{-1/2}$	-1
b_i	27 $\pm$ 3 μs	0	0
c_i	190 meV	0	0

• **Mean free path Λ**

The neutron mean free path in the water moderator calculated in REFIT is given by Equation B.15. A linear dependency between the expected mean free path $\Lambda(E)$ and the theoretical value $\lambda(E)$ is assumed:

$$\Lambda(E) = \Omega\lambda(E) \qquad \Omega = \frac{\lambda^o(1eV)}{\lambda(1eV)} \tag{B.15}$$

with

$$\lambda(E) = \frac{\omega}{n_H \sigma_H} \left(1 - \Sigma \frac{e^{-\Sigma}}{1 - e^{-\Sigma}}\right) [1 - \mathcal{P}(\Sigma)] \tag{B.16}$$

$$\Sigma = n_H \left(\sigma_H + \frac{1}{2}\sigma_O\right) \tag{B.17}$$

The correction factor Ω represents the fraction of the mean free path at 1 eV and λ^o is a free parameter. The latter makes possible the handling of some effects involved in the modification of the standard deviation of the distribution (beryllium thickness contribution, radiolysis of the water by neutron and γ ray irradiation from the target, unknown temperature of the moderator higher than its surroundings).

The theoretical mean free path $\lambda(E)$ is mainly due to neutron interactions with hydrogen. The contribution of the oxygen and the slab geometry are introduced as a correction factor.

The hydrogen and oxygen total cross sections are calculated by interpolation of data tabulated in REFIT. Below 10 keV, σ_O is set to 3.83 b. In Figure B.4, we compare the values used by REFIT with the data available in the JENDL-3.2 Japanese data base. The hydrogen cross section is accurately reproduced whereas the interpolation of the oxygen cross section in the resonance range needs some improvements.

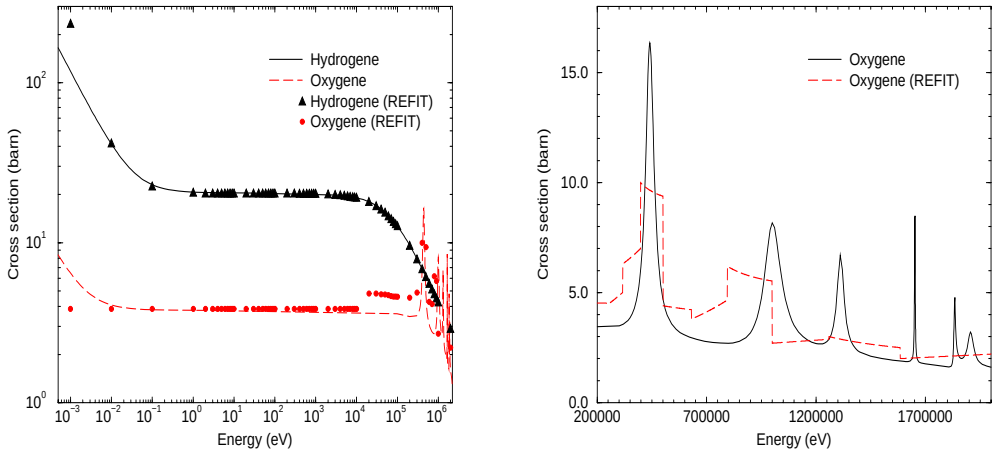

Figure B.4: Hydrogen and Oxygen total cross sections tabulated in REFIT (BNL325 - 1981) compared to the most recent data available in the Japanese data base (JENDL3.2 - 1993).

The term $\mathcal{P}(\Sigma)$ in Equation B.16 is the average escape probability. In the process of slowing down, neutrons collide with nuclei and may be absorbed in the slab moderator. A neutron at a point r has a probability $P_o(r)$ of escaping from the moderator. If neutrons are scattered within the body with isotropic distribution $q_o(r)$, the average escape probability may be expressed as follows:

$$\mathcal{P} = \frac{\int_V q_o(r) P_o(r) \mathrm{d}r}{\int_V q_o(r) \mathrm{d}r} \tag{B.18}$$

The average probability $1 - \mathcal{P}$ that the neutron will be absorbed is often referred as the collision probability. Extensive works were performed to extend the theoretical expression of $\mathcal{P}$ for various slab geometry. If it assumed that the scattered neutrons are distributed uniformly throughout the sample, then the neutron escape probability from an infinite slab can be derived from expressions given in Reference [121]:

$$P_3(\Sigma) = \frac{\omega^2}{\Sigma} \int_\omega^\infty \left(1 - e^{-\frac{\Sigma}{\omega}u}\right) \frac{\mathrm{d}u}{u^3} = \frac{1}{\Sigma}\left[\frac{1}{2} - E_3(\Sigma)\right] \tag{B.19}$$

In REFIT, the correction for finite size is carried out using the relationship:

$$\mathcal{P}(\Sigma) = \frac{P_2(\Sigma)}{P_1(\Sigma)} P_3(\Sigma) \tag{B.20}$$

with

$$P_1(\Sigma) = \frac{1}{1 + S_1(\Sigma)} \qquad P_2(\Sigma) = \frac{1}{1 + S_2(\Sigma)} \tag{B.21}$$

The escape probabilities P_1 and P_2 are derived from the Wigner approximation used in reactor calculations for cylindrical fuel assemblies embedded in a concentric cylindrical moderator [159]. These probabilities depend on form factors S_1 and S_2 calculated as follow:

$$S_1 = \frac{2\Sigma}{1 - \mathcal{C}} \qquad \text{and} \qquad S_2 = \frac{S_1}{1 + \frac{D_p}{2\omega}} \tag{B.22}$$

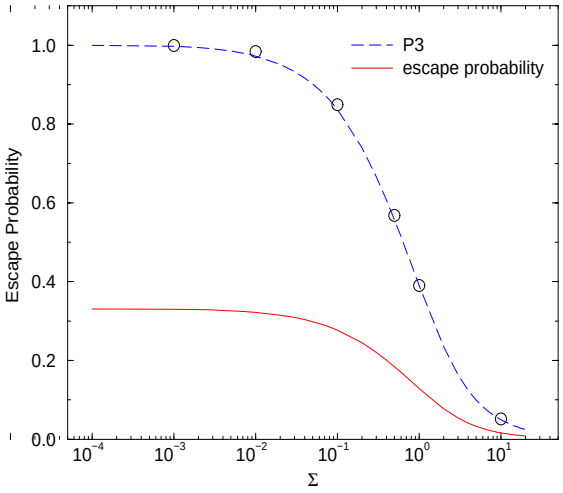

Figure B.5: Neutron escape probability from the GELINA moderator defined as a function of $\Sigma = n_H(\sigma_H + 0.5\sigma_O)$. The solid curve is the escape probability corrected for finite slab size (Equation B.20). P_3 is the escape probability from an infinite slab derived from expressions given in Reference [121]. The circles are calculated with Equation B.19 and the dashed line comes from Equation B.24.

The so-called Dancoff factor $\mathcal{C}$ account for the flux reduction in the medium and depends on the penetrability factor tabulated in Reference [159]. In REFIT, $\mathcal{C}$ is defined as :

$$\mathcal{C} = -a_1 \left(1 - e^{-2a_2\Sigma}\right) e^{-2a_3\Sigma} + a_4 e^{-2a_5\Sigma} + (1 - a_4) e^{-2a_6\Sigma} \tag{B.23}$$

Numerical values for the a_i's are provided in Table B.3. In REFIT, the escape probability P_3 is determined by interpolating data obtained for sample thickness correction in slab geometry. The data are tabulated inside the code. For the 3.6 cm-thick water moderator of GELINA, the dependence of P_3 as a function of Σ is well reproduced with the following expression (Figure B.5):

$$P_3(\Sigma) = \left(1 + \frac{2\Sigma}{1 + a_1\left(1 - e^{-2a_2\Sigma}\right) e^{-2a_3\Sigma} - a_4 e^{-2a_5\Sigma}}\right)^{-1} \tag{B.24}$$

Table B.3: Fitted parameters given by Moxon to reproduce the Dancoff factor $\mathcal{C}$ (Equation B.23).

Parameter of fit	value
a_1	0.3812 ± 0.0026
a_2	1.4898 ± 0.0463
a_3	0.1263 ± 0.0012
a_4	0.2207 ± 0.0216
a_5	4.8363 ± 0.8210
a_6	75.045 ± 18.110

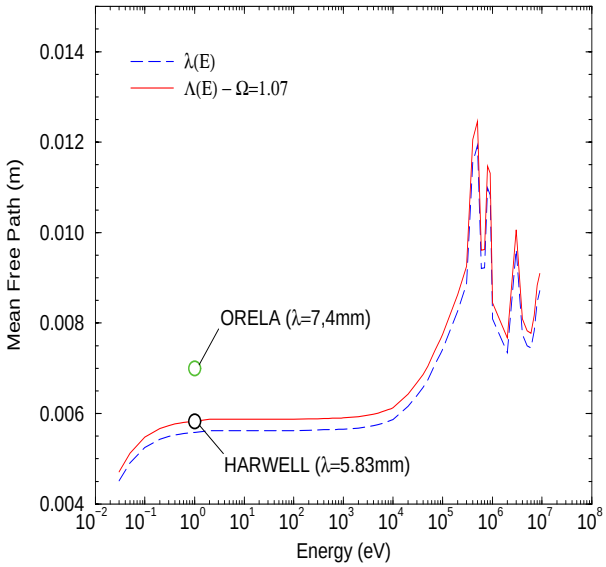

Figure B.6: Neutron mean free path in the GELINA moderator calculated in REFIT (Equation B.15) compared to the value of the water moderator of ORELA [157] and to the polyethylene moderator of Harwell [26].

The energy dependence of the average mean free path ($\lambda(E)$) obtained with Equation B.16 is shown in Figure B.6 together with the value at 1 eV of the water moderator of ORELA (ω =3.18 cm, D_p =14.6cm) and of the 2.5 cm-thick polyethylene moderator of the old Harwell 45 MeV linac. The theoretical expressions proposed by M.Moxon underestimate the expected neutron mean free path. In Reference [26], it is then recommended to increase $\lambda(E)$ by a factor $\Omega = 1.07$ by using the value $\lambda^o = 5.83$ mm corresponding to the moderator of the Harwell linac.

As a first approximation and below 10 keV, the treatment implemented in REFIT gives a satisfactory estimate of the neutron mean free path. The latter can be improved with an accurate determination of λ^o.

B.2.3 Angle of the flight path

A time spread in the resolution function is also introduced by the angle θ between the flight path and the normal of the moderator. To describe this effect, the neutrons escaping from the moderator are assumed to be a parallel beam with a radius R_c. The radius R_c is defined by the diameter D_c of the first collimator.

Referring to the geometry shown in Figure B.7a, the distance d(z) is given by the expression:

$$d(z) = (\frac{D_c}{2} - z)\tan\theta \tag{B.25}$$

The maximum spread in flight distance D_m is obtained for $z = -D_c/2$:

$$D_m = D_c \tan\theta = D_p \sin\theta \tag{B.26}$$

in which D_p stands for the projection of the first collimator on the moderator. If L is the distance between the surface of the moderator and the surface of the detector, the true flight distance used by REFIT must be $L - \frac{D_m}{2}$.

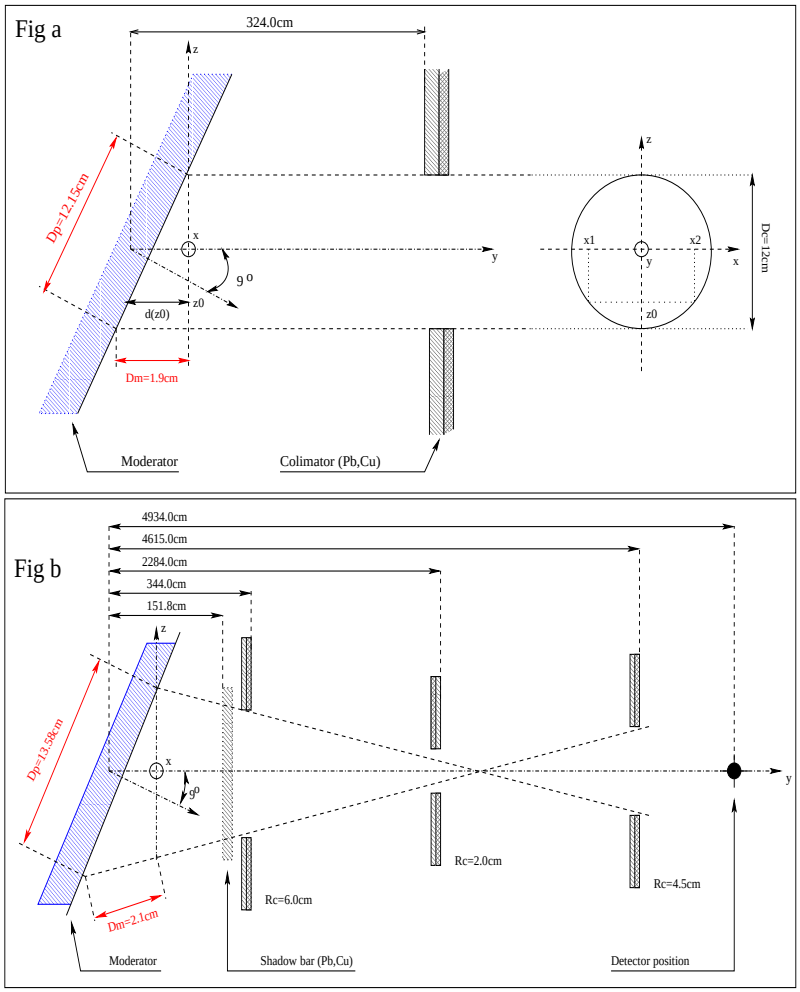

Figure B.7: Scheme describing the geometry at an angle of $\theta = 9^o$. (a) REFIT: projection of the diameter of the first collimator on the moderator. (b) Scheme of the actual collimators used for the simulation.

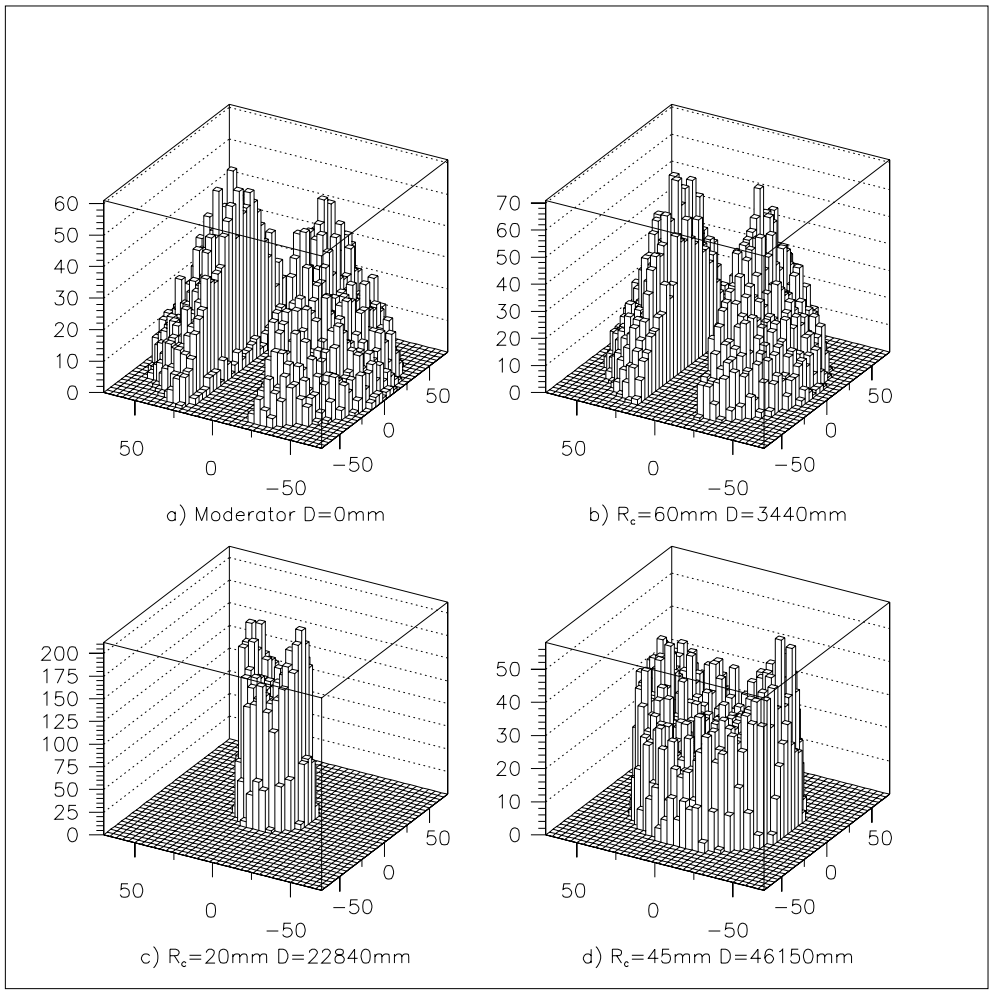

Figure B.8: Two-dimensional beam profile obtained by simulation. R_c is the radius of the collimator and D the distance from the center of the uranium target.

The probability distribution $I(z)$ of z is given by:

$$I(z) = \int_{x_1}^{x_2} dx = 2\sqrt{R_c^2 - z^2} \tag{B.27}$$

with the following integration limits:

$$x_1 = -\sqrt{R_c^2 - z^2} \qquad x_2 = -x_1$$

The resolution function in equivalent distance is obtained by folding together Equations B.25 and B.27:

$$I(d) = \frac{1}{\tan\theta}\sqrt{D_m^2 - (D_m - 2d)^2} \tag{B.28}$$

The time distribution I(t) from a slab moderator viewed by the neutrons through a circular collimator is derived from Equation B.28. The shape is assumed to be a half circle of radius $T_m/2$ centered at $t = T_m/2$ (with $T_m = 72.298 D_m/\sqrt{E}$ the maximum time spread for the outgoing neutron at energy E).

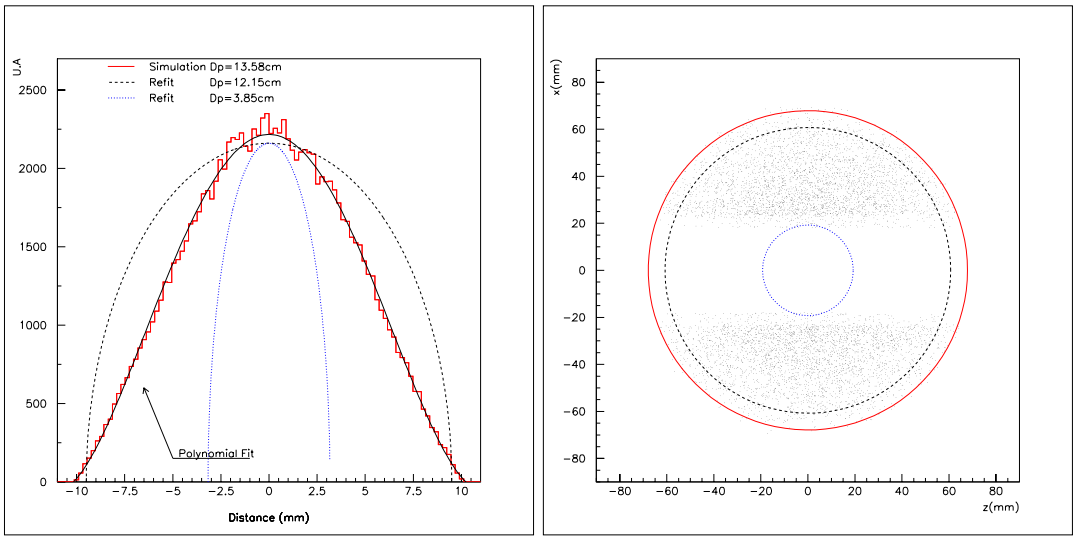

Figure B.9: The figure on the left shows a comparison of resolution functions in equivalent distance due to an angle $\theta = 9^o$. The value $D_p = 12.15$ cm is assumed for a measurement with a shadow bar and the value $D_p = 3.95$ cm must be used to study fast neutrons. The Figure on the right represents the projection of the collimator on the moderator surface for each case. The dots are the neutrons escaping from the moderator that can reach the detector.

$$I(t) \propto \sqrt{T_m^2 - (T_m - 2t)^2} \tag{B.29}$$

To verify this approximation, a Monte-Carlo simulation was performed, taking the real geometry into account (Figure B.7b). The simulation reproduces the movement in a straight line of the neutrons through the collimators of the flight path. The first collimator ($R_c = 6.0$ cm) is located at the beginning of the pipe, the second one ($R_c = 2.0$ cm) and the third one ($R_c = 4.5$ cm) are used respectively to focus the neutron beam on the sample and on the lithium glass detector. A shadow bar, composed of lead and copper, is introduced to eliminate the fast neutrons leaving the rotary target. The two-dimensional beam profiles obtained by simulation are shown in Figure B.8. Figure B.9 compares the resolution distributions obtained from equation B.28 for two diameter values with the result from the simulation. The latter gives quite similar results for the maximum distance D_m and the projection of the circular collimator D_p (Table B.4). However, the standard deviation resulting from the REFIT calculations is overestimated.

Table B.4: Comparison of the result obtained from REFIT with the simulation of the actual collimation ($D_c = 12$ cm, $\theta = 9^o$).

	Distance D_m	Projection of the First Collimator D_p	Standard deviation
Moxon	1.9 cm	12.15 cm	4.75 mm
simulation	2.1 cm	13.58 cm	4.10 mm

B.3 Lithium glass detector description in REFIT

B.3.1 Response of the lithium detector

At Geel, a lithium glass detector NE912 is used for neutron transmission experiments. The slab detector is a silicate glass containing lithium activated by cerium enriched in ^{6}Li (7.7%). It can be described as a disk of thickness $\omega = 6.35$ mm in the direction of the neutron beam with a radius of R=8 cm. Table B.5 gives the composition of the silicate glass.

Table B.5: The slab detector is composed of SiO_2 (74.7%), Ce_2O_3 (4.6%) and Li_2O (20.7%)

element	mass fraction	thickness (g/cm^2)	thickness n_i (at/b)
^{28}Si	34.86 %	0.5312	$1.1420.10^{-2}$
^{140}Ce	3.93 %	0.0598	$2.5733.10^{-4}$
^{6}Li	7.73 %	0.1178	$1.1819.10^{-2}$
^{7}Li	1.24 %	0.0189	$1.6252.10^{-2}$
^{16}O	52.24 %	0.7961	$2.9954.10^{-2}$

The response of such a detector can be split into two parts, the initial interaction Ip(x), and the component due to the multiple interaction Im(x). An example of the response of the detector is shown in Figure B.10. Such resolution function in equivalent distance x is defined as follows:

$$Ip(x) = \frac{n_r\sigma_r}{n_s\sigma_s + n_r\sigma_r}\left(1 - e^{-(n_s\sigma_s+n_r\sigma_r)}\right)\frac{e^{-(n_s\sigma_s+n_r\sigma_r)\frac{x}{\omega}}}{\int_0^\omega e^{-(n_s\sigma_s+n_r\sigma_r)\frac{x}{\omega}}dx} \qquad 0 < x < \omega \tag{B.30}$$

$$Im(x) = \begin{cases} B_1 Y_m \dfrac{e^{-\frac{x}{\Lambda}} - e^{-\frac{n_s\sigma_s+n_r\sigma_r}{\omega}x}}{\int_0^\omega \left(e^{-\frac{x}{\Lambda}} - e^{-\frac{n_s\sigma_s+n_r\sigma_r}{\omega}x}\right)dx + \int_\omega^{Dm}\left(e^{-\frac{\omega}{\Lambda}} - e^{-(n_s\sigma_s+n_r\sigma_r)}\right)e^{-\frac{x-\omega}{\Lambda}}dx} & 0 < x < \omega \\ B_1 Y_m \dfrac{\left(e^{-\frac{\omega}{\Lambda}} - e^{-(n_s\sigma_s+n_r\sigma_r)}\right)e^{-\frac{x-\omega}{\Lambda}}}{\int_0^\omega \left(e^{-\frac{x}{\Lambda}} - e^{-\frac{n_s\sigma_s+n_r\sigma_r}{\omega}x}\right)dx + \int_\omega^{Dm}\left(e^{-\frac{\omega}{\Lambda}} - e^{-n_s\sigma_s-n_r\sigma_r}\right)e^{-\frac{x-\omega}{\Lambda}}dx} & x > \omega \end{cases} \tag{B.31}$$

.

where Y_m represents the total number of capture events per incident neutron. In REFIT, the D_m parameter is defined as follows:

$$D_m \;=\; 10\,\Lambda$$

in which Λ stands for the mean free path of a scattered neutron in the material of the detector which is corrected for its finite size.

$$\Lambda = 2B_2\frac{\omega}{n_s\sigma_s + n_r\sigma_r}\ln\left(\frac{1}{1 - \frac{1}{2}\left(1 - e^{-2\frac{n_s\sigma_s+n_r\sigma_r}{1+\omega/R}}\right)}\right) \tag{B.32}$$

The thicknesses for the scattered and absorbed incident neutrons are respectively n_s and n_r. They are defined as:

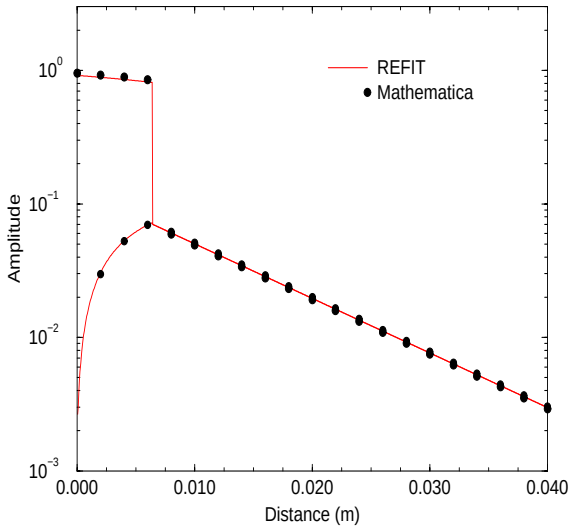

Figure B.10: Resolution function of the lithium glass detector versus the equivalent distance for a neutron energy of $E_n = 700$ eV. The result from REFIT is compared with Mathematica calculations based on Equation B.30 and B.31.

$$n_s = \sum_i n_i = 5.5075.10^{-2} \text{ at/b} \qquad n_r = n_{^6Li} = 1.1819.10^{-2} \text{ at/b} \tag{B.33}$$

In REFIT, the scattering cross section (σ_s) is assumed to be constant and the capture cross section (σ_r) follows a $1/v$ dependence. The macroscopic total cross section is given by:

$$\Sigma_{tot}(E) \;=\; n_s\sigma_s \;+\; n_r\sigma_r(E)$$

with:

$$\sigma_s = \frac{\sum_i n_{s,i}\sigma_{s,i}}{n_s} = 2.67 \text{ b} \qquad \sigma_r(E) = \frac{149.5}{\sqrt{E}} \tag{B.34}$$

The parameters available in REFIT are given in Tables B.5 and B.6. The contribution of ^{140}Ce to the scattering cross section is less than 0.5% which makes it possible to omit the resonances up to 25 keV. However, due to the silicon resonances (Figure B.11), the above choices limit the validity of the resolution function to the energy region below 30 keV.

Table B.6: Scattering cross section used in REFIT [56]

element	Scattering cross sections $\sigma_{s,i}$ (b)
^{28}Si	2.043 ± 0.002
^{140}Ce	2.83 ± 0.11
^{6}Li	0.75 ± 0.02
^{7}Li	0.97 ± 0.04
^{16}O	3.761 ± 0.006

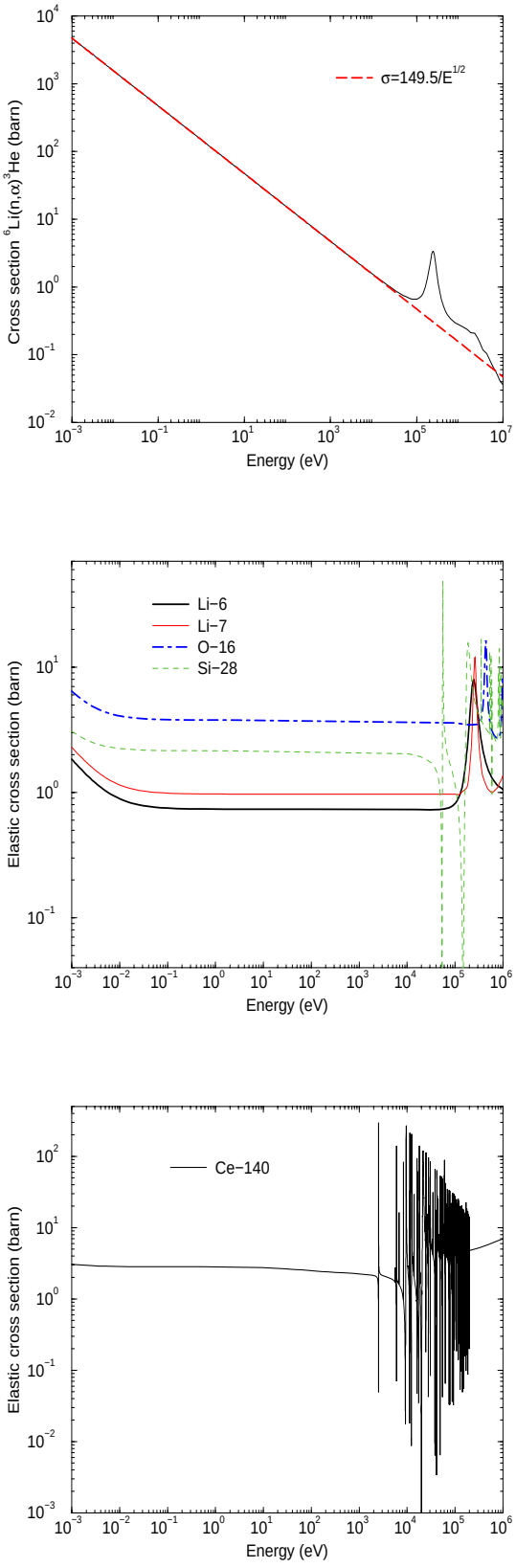

Figure B.11: Li, O and Si cross sections from the European data base JEF-2.2.

B.3.2 Multiple scattering theory

The free parameters B_1 and B_2 (Equations B.31 and B.32) take into account the scattering in the detector and the effect of the surrounding materials. For detectors having the glass in the neutron beam and the photomultiplier outside, the values of B_1 and B_2 are close to unity (the neutrons are scattered only by the lithium glass). When the lithium glass is located in an air gap, the contribution of the air to the multiple scattering can be accounted for by increasing the two constants up to a value larger than unity. The effects of the surroundings are not so well represented with this approach and need some additional work. For future improvements, two possible contributions should be distinguished: one from the transmitted flux and a second from the flux scattered by the detector. The time dependence of these components is possibly an exponential delay due to the distance the neutrons have to travel out and return to the detector.

The effect of single and multiple neutron scattering collisions can be large even for thin samples. Some experiments with a lithium glass detector [160] have shown a long tail of small amplitude persisting for several microseconds. In Equation B.31, Y_m is an algorithm which approximately reproduces the effect of the multiple interactions from a parallel neutron beam at normal incidence on a disk in which only elastic scattering and capture can occur. Finally, the *total number of captures per incident neutron* Y_m is a sum over the collision n defined as:

$$\begin{aligned} Y_m &= \left(1 - e^{-(n_s\sigma_s + n_r\sigma_r)}\right) \frac{n_s\sigma_s}{n_s\sigma_s + n_r\sigma_r}(1 - T2_1)\frac{n_r\sigma_{r,1}}{n_s\sigma_{s,1} + n_r\sigma_{r,1}} \\ &+ \left(1 - e^{-(n_s\sigma_s + n_r\sigma_r)}\right) \frac{n_s\sigma_s}{n_s\sigma_s + n_r\sigma_r} \sum_{i=2}^{n}(1 - T2_i)\frac{n_r\sigma_{r,i}}{n_s\sigma_{s,i} + n_r\sigma_{r,i}} \prod_{j=1}^{i-1}(1 - T2_j)\frac{n_s\sigma_{s,j}}{n_s\sigma_{s,j} + n_r\sigma_{r,j}} \end{aligned} \tag{B.35}$$

To take the average energy lost by multiple scattering into account, the quantities $\sigma_{s,i}$ and $\sigma_{r,i}$ are introduced in the calculation. They represent the transfer energy cross section averaged over the energy loss. In the REFIT code, σ_s is assumed constant ($\sigma_{s,i} = \sigma_s$) and $\sigma_{r,i}$ is defined as follows:

$$\sigma_{r,i} = \int_{kE}^{E} \frac{\sigma_r(x)}{T_m} dx \tag{B.36}$$

with

$$T_m = (1 - k)E \qquad k = \left(\frac{A - 1}{A + 1}\right)^2 \tag{B.37}$$

where k is the kinematic factor and A=18.34 represents the average mass in uma of the lithium detector. In Equation B.35, $T2_i$ may be defined as follows:

$$T2_i = \langle \mathrm{e}^{-\frac{n_s\sigma_s + n_r\sigma_{r,i}}{\omega} x_i} \rangle \tag{B.38}$$

where x_i stands for the geometric path length in the disk for a neutron after the i^{th} scattering. For a relatively thin disk (~0.1 mean free path) and for constant scattering and capture cross sections over several neutron collisions, it has been shown that [142]:

$$T2 = T2_1 = T2_2 = ... = T2_i \tag{B.39}$$

Introducing these approximations in the calculation of Y_m, Equation B.35 becomes:

$$Y_m = \left(1 - e^{-(n_s\sigma_s + n_r\sigma_r)}\right) \frac{n_r\sigma_r}{n_s\sigma_s + n_r\sigma_r} \frac{X}{1-X} \tag{B.40}$$

with

$$X = (1 - T2)\frac{n_s\sigma_s}{n_s\sigma_s + n_r\sigma_r} \tag{B.41}$$

where X represents the average path length correction factor derived for a thin disk [142]). The $T2$ correction has been determined explicitly for cylindrical geometry [139, 142]. The results for a disk of radius R and thickness ω are given below:

$$T2 = \begin{cases} 0 & \text{if } T2 < 0 \\ \frac{1+e^{-(n_s\sigma_s+n_r\sigma_r)}}{2(1-e^{-(n_s\sigma_s+n_r\sigma_r))}}(\chi - X_1 + X_2) & \text{if } 0 < T2 < 1 \\ 1 & \text{if } T2 > 1 \end{cases} \tag{B.42}$$

$$\chi = 1 - e^{-(n_s\sigma_s+n_r\sigma_r)}\left[1 - \frac{1}{2}(n_s\sigma_s + n_r\sigma_r)\frac{\omega}{R}\right] - e^{\frac{R}{\omega}(n_s\sigma_s+n_r\sigma_r)} + e^{-(n_s\sigma_s+n_r\sigma_r)\left(1-\frac{R}{\omega}\right)^{1/2}} \tag{B.43}$$

The series X_1 and X_2 implemented in REFIT have been modified following the indications reported in Reference [142]. Their mean values are approximated by the following expressions:

$$X_1 = -\frac{1}{2}(n_s\sigma_s + n_r\sigma_r)^2\left[\ln(n_s\sigma_s + n_r\sigma_r) + 0.0772\right] + \sum_{n=1}^{6}\frac{(-1)^{n-1}(n_s\sigma_s + n_r\sigma_r)^{n+2}}{n!n(n+2)} \tag{B.44}$$

$$\begin{aligned} X_2 &= \frac{(n_s\sigma_s + n_r\sigma_r)^2}{2} \\ &\times \left[-0.5772 - \ln\left(\frac{n_s\sigma_s + n_r\sigma_r}{2}\sqrt{1 + \left(\frac{R}{\omega}\right)^2}\right) + \sum_{n=1}^{8}(-1)^{n-1}\frac{\left(\frac{n_s\sigma_s+n_r\sigma_r}{2}\sqrt{1+\left(\frac{R}{\omega}\right)^2}\right)^n}{n!n}\right] \end{aligned} \tag{B.45}$$

Figure B.12 represents the $T2$ parameter as a function of the neutron energy. The correction is negligible below ~ 5 eV and increases rapidly to reach 70% above 1 keV.

B.4 Coceva simulation of the resolution function

Coceva has simulated the resolution function of the time of flight facility GELINA for several neutron energies [117, 161]. Two separate calculations were performed to describe the neutron source (target-moderator assembly with the contribution of the angle of the flight path) and the lithium glass detector used in transmission measurements.

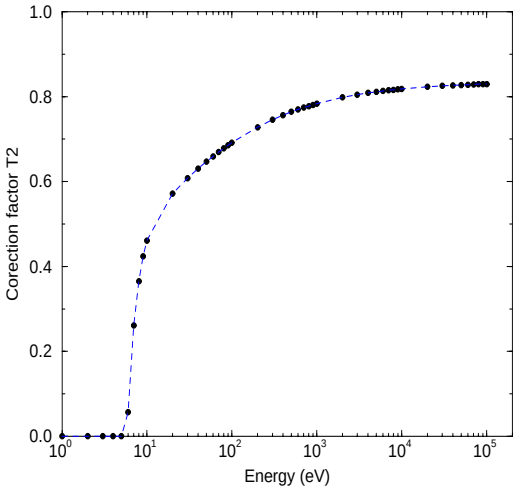

Figure B.12: Variation of T2 versus energy. Calculation made with REFIT from Equation B.42.

B.4.1 Coceva simulation of the target-moderator assembly

The delay time distributions of neutrons emitted from the GELINA water moderator and Hg cooled uranium rotary target assembly were calculated by Coceva using time dependent three-dimensional Monte-Carlo techniques. The energy of the neutron source is sampled from a spectrum resulting from photo-neutron and photo-fission processes such as in Reference [161]. Neutrons escaping from the uranium target are eliminated by a shadow bar. The calculated distributions (Figure B.13) take into account the effect of the target-moderator assembly and the contribution of the flight path angle. The solid angle under which the neutron source views the detector is assumed to be 1% of a sphere to get a high efficiency in the Monte-Carlo calculation (whereas the real aperture is close to 10^{-3}% of a sphere).

Below 10 keV, the FWHM of the distributions calculated in REFIT agree with the simulation. Within this energy range, the neutron mean free path Λ in the moderator is nearly independent from the neutron energy. By contrast, above 100 keV, Figure B.13 shows an increasing discrepancy between the simulations and the results from REFIT.

The agreement between the analytic formula and the simulations is significantly improved by changing the parametrisation of the target decay. In REFIT, its phenomenological description accounts for the multiple scattering of fast neutrons in the uranium rotary target and the effects of the surroundings (section B.2.1). There are three exponential decay modes having respectively a half life of 3.5 ns, 29.48 ns and 99.3 ns. The 3.5 ns one is always assumed to be independent of neutron energy and due to neutrons crossing the source. From capture measurements, Moxon found necessary to add two more decays which are also independent of neutron energy. The 29.48 ns decay was determined around 2.25 keV from some fits of resonances in ^{60}Ni. In the meantime, the presence of the longer one was not confirmed.

To improve the analytic description of the resolution, a new parametrisation of the tail of the resolution distribution was investigated on the basis of the preliminary observation performed by V.Gressier on ^{237}Np transmission experiments [70]. Fits of resonances below 30 eV were slightly improved by the inclusion of a new exponential decay of about 850 ns. At low energy, it becomes difficult to confirm such a decay because the effect is almost lost in the moderation function and the background statistics. However, the existence of this decay is confirmed by

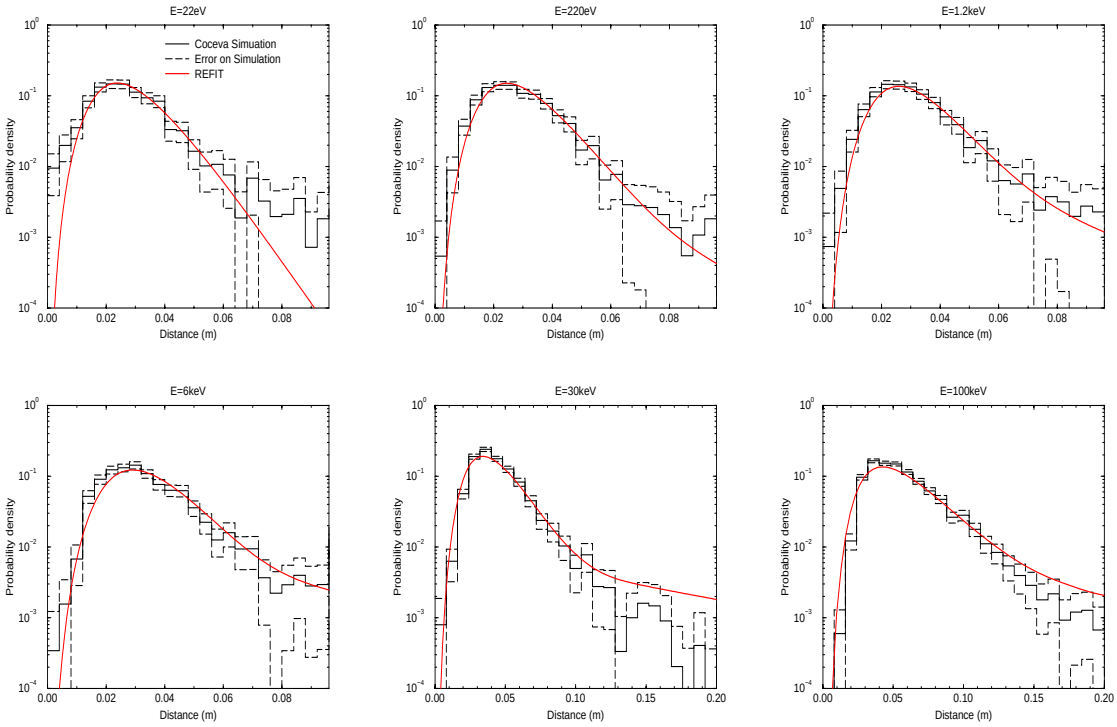

Figure B.13: Target-moderator assembly distributions corresponding to flight path 4 ($\theta = 9^o$).

the work of Ikeda and Carpenter [158]. At low energy, they recommended to add a long tail corresponding to the storage of thermal neutrons in the moderator (see Section B.2.2).

The discrepancy between the various half-life decays of 29.48 ns, 99.3 ns and 850 ns suggests a neutron energy dependence. Figure B.14 shows the neutron energy dependence of the main decay mode required to describe the tail of the Coceva distributions below 20 keV. In a first approximation the energy dependence of this half-life could be expressed as follows:

$$\tau(E) = \lambda_\tau \frac{t(1eV)}{\sqrt{E}} \tag{B.46}$$

If we assume that the decays are due to neutrons transport effect in the vicinity of the target-moderator assembly, the time a neutron takes to cover the mean distance between two collisions corresponds to the half-life of the decay mode. If one assumes that the neutrons do not loose any energy, at 2.25 keV the decays of 29.48 ns and 99.3 ns are equivalent to a distance λ_τ equal to 19.3 mm and 65.15 mm respectively. At 10 eV, the decay time would then correspond to 442 ns and 1500 ns, within the range of the 850 ns found for the neptunium data. The shorter mean distance of 19.3 mm is confirmed by the simulations (Figure B.14), whereas the existence and the origin of the longer one demand further investigations. Owing to this study, the two decays (29.48 ns and 99.3 ns) should be replaced by the mean distance between collisions.

B.4.2 Simulation of the response of the lithium glass detector

Examples of lithium glass resolution functions are given in Figure B.15. The distributions from REFIT at various neutron energies are compared with two simulations. A *new simulation* was performed using the same assumptions as the analytic treatment implemented in REFIT

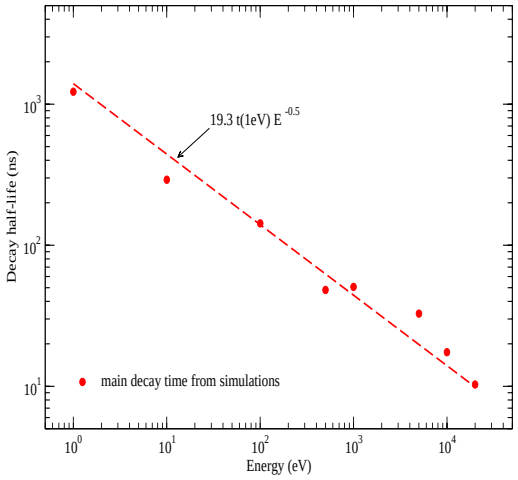

Figure B.14: Energy dependence of the main decay mode used to reproduce the tail of the Coceva distribution below 20 keV.

(the neutrons interact with a thin disk of homogeneous matter and a constant scattering cross section is assumed). Above 32 eV, the description of the tail of the resolution provided by this new simulation is in a satisfactory agreement with the REFIT treatment. Whereas the Coceva simulations exhibits significant discrepancies which suggest a wrong parametrisation of the analytic treatment.

Figure B.16 represents the contribution of the tail to the total area of the resolution function. We only consider the area of the tail given by the following expression:

$$\frac{A_{tail}}{A_{tot}} = \frac{\int_{\omega}^{D_m} I_m(x)dx}{\int_0^{\omega} I_p(x)dx + \int_0^{D_m} I_m(x)dx} \tag{B.47}$$

using Equations B.30 and B.31, the above expression becomes:

$$\frac{A_{tail}}{A_{tot}} = \Lambda Y_m B_1 \frac{e^{-\frac{\omega}{\Lambda}} - e^{-(n_s\sigma_s+n_r\sigma_r)}}{\left[Y_m B_1 + \frac{n_r\sigma_r}{n_s\sigma_s+n_r\sigma_r}\left(1-e^{-(n_s\sigma_s+n_r\sigma_r)}\right)\right]\left(\Lambda - \frac{\omega}{n_s\sigma_s+n_r\sigma_r}\right)\left(1-e^{-(n_s\sigma_s+n_r\sigma_r)}\right)} \tag{B.48}$$

In Figure B.16, the first ratio A_{tail}/A_{tot} results from an old parameterization of X_1 and X_2 in REFIT. A better agreement with the *new simulation* is obtained by using the expressions B.44 and B.45.

At low energy, the multiple scattering correction in the detector is overestimated compared with the simulations. The discontinuity of the function $T2$ (Equation B.42) explains the structure around 5 eV. A better agreement with the simulation is expected above 1 keV due to the limit of validity of $T2$ given by Gibbons et al. [142]. Their expression is valid to better than 1%

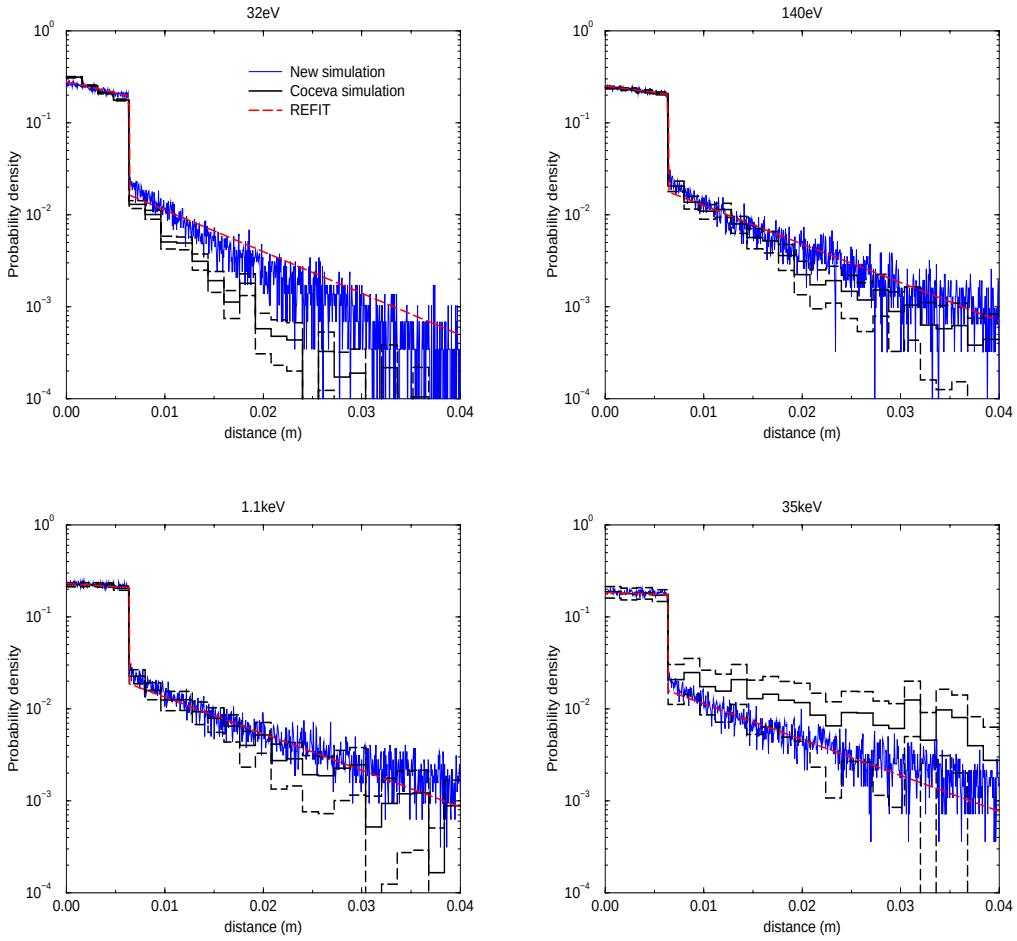

Figure B.15: Resolution function of the Li-glass detector in equivalent distance given by REFIT and Monte-Carlo simulations. The "new" simulation results from Monte-Carlo calculations carried out under the same basic assumptions as used in the analytic REFIT approach.

for $n_s\sigma_s + n_r\sigma_r \leq 0.2$ and $R \geq 2\omega$. However, at higher energy, the analytic expression cannot reproduce accurately the time response of the detector because of the silicon resonances.

B.4.3 Simulation of the full resolution function

A.Brusegan has implemented the Coceva distributions in a newest version of REFIT [154]. Figure B.17 gives the Full Width at Half Maximum (FWHM) and the standard deviation obtained from:

- the analytic treatment of REFIT (old REFIT)
- the same analytic treatment with further improvement (new REFIT) as discussed in the previous sections.
- the Monte-Carlo simulations performed by C.Coceva.

The FWHM (in μs) of the distributions represented in Figure B.17 are in good agreement.

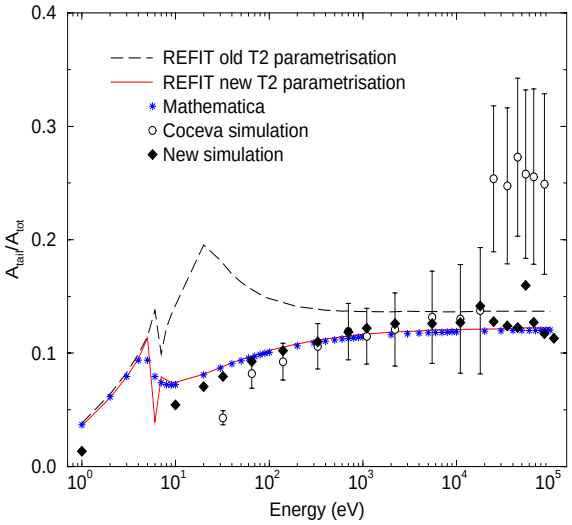

Figure B.16: Comparisons of the tails calculated by REFIT with those obtained by simulations. The parameterization of $T2$ proposed in Equations B.42 to B.45 shows a better agreement with the simulation than the old expression available in REFIT. The calculation performed with Mathematica is based on Equation B.48.

The maximum discrepancy reaches 9%. Below 100 keV, the FWHM is approximately described by a constant plus a term inversely proportional to the square root of the neutron energy. The broken line is obtained with the following expression:

$$FWHM = 5.6238.10^{-3} + \frac{1.8646}{\sqrt{E}} \qquad (\text{in } \mu s) \tag{B.49}$$

The second term is mainly due to the moderation process. A similar result was obtained by Michaudon [156]. Below 10 keV, he found a width $\Delta t = 1.8/\sqrt{E}$ in the case of a 3 cm thick water moderator.

The standard deviation (σ) of the distribution shown in Figure B.17 is defined as:

$$\sigma^2 = \int_0^{+\infty} (t - t_m)^2 R(t) \mathrm{d}t \tag{B.50}$$

where t_m is the mean time of the distribution and $R(t)$ is the normalised amplitude of the resolution function. The large discrepancies observed on the standard deviation are significantly decreased by using the target decay defined in Equation B.46.

Figure B.18 gives some examples of distributions obtained from each treatment (old REFIT, new REFIT and Coceva simulations). The structures seen in Coceva's curves are due to poor statistics and do not have a significant effect on the results. The new analytic treatment of REFIT includes the energy dependence appearing in Equation B.46. The parameters to be used in REFIT are given in Table B.7. The value of these parameters should be optimised with a new analysis of suitable capture , transmission or fission measurements. However, the description of the complicated interactions and the need of high signal to background ratios may strongly hinder the determination of the parameters of the analytic function from the shape of resonances. Without additional improvement of the analytic treatment available in REFIT with experimental data, Coceva simulation seems to be a good compromise for the description of the tail of the resolution function.

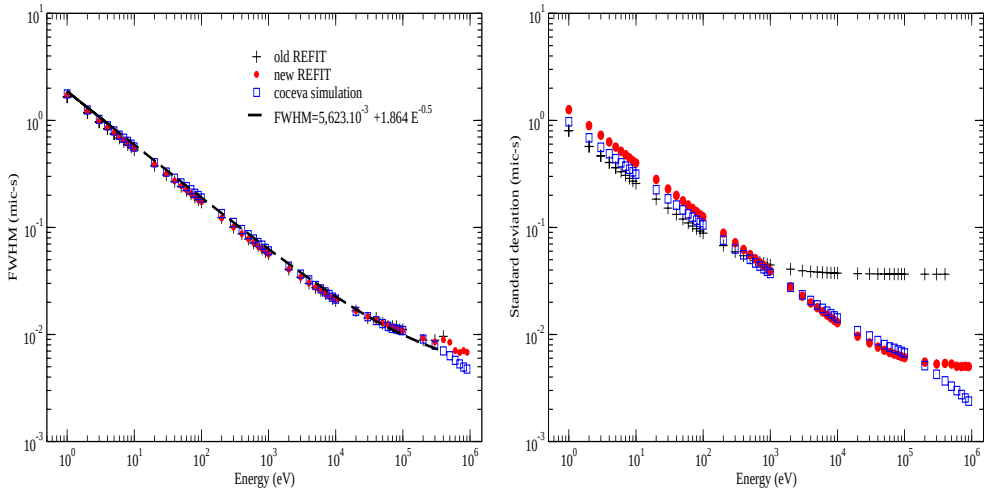

Figure B.17: FWHM and standard deviation of the resolution function given by REFIT in μs. The broken line is the result of Equation B.49.

B.5 Conclusion

The resolution function of the GELINA facility may be modeled with suitable analytic expressions based on the theoretical descriptions of the neutron interaction with the target-moderator assembly and the surrounding materials. These formulas contain some parameters that may be fitted to the shape of well-known resonances observed in capture and transmission measurements. Their optimisation is not straightforward and several measurements are required. A complementary approach to the determination of the resolution function is given by Monte-Carlo simulations.

The resolution function implemented in REFIT by M.Moxon to describe both the water moderator and the lithium glass detector is based on neutron multiple scattering theory. Further assumptions are used which limit the validity of Moxon's analytic functions. For the moderator, the beryllium thickness is omitted and the modeling is not adequate beyond 100 keV with respect to the contribution of oxygen resonances. The best description is expected in the energy range [2 eV - 10 keV] because of the negligible effect of the oxygen and the constant energy dependence of the hydrogen scattering cross section. In this energy range, the value of the mean free path of the neutron can be normalised with a free parameter λ^o at a value close to 5.83 mm. For the detector, the description of the multiple scattering needs improvement below 10 eV (overestimation of the multiple scattering effect) and above 25 keV (silicon resonances are not taken into account). The best agreement with simulation is obtained around 1 keV which is confirmed by the expected limit of the analytic expression developed in Reference [142].

The Coceva simulations of the experimental resolution give a FWHM close to the analytic treatment of REFIT. A maximal discrepancy of 9% is obtained below 100 keV. The standard deviations of the distributions include more information. The strong discrepancy between the two resolution descriptions is due to the phenomenological long tail of small amplitude, used to reproduce the target decay and the surrounding effect in the target hall. Vincent Gressier [70] proposed an increase in the amplitude of the tail of the resolution distribution around 20 eV in order to improve the fit of ^{237}Np resonances. This work is confirmed by the exponential decay given by the simulations and the work of Ikeda and Carpenter [158]. The Coceva simulation

shows that an energy dependent target decay should be implemented in REFIT to improve the analytic description of this tail.

The need for improved accuracy on resonance parameters demands an optimal description of the resolution function. Due to the limited validity of the analytic treatment in REFIT, the Coceva calculations may be seen as a valuable tool on a large energy scale [154]. Recently, the SAMMY code has been upgraded to access the same capabilities of REFIT by using Monte-Carlo calculations. This option in SAMMY is called the User-Defined-Resolution (UDR).

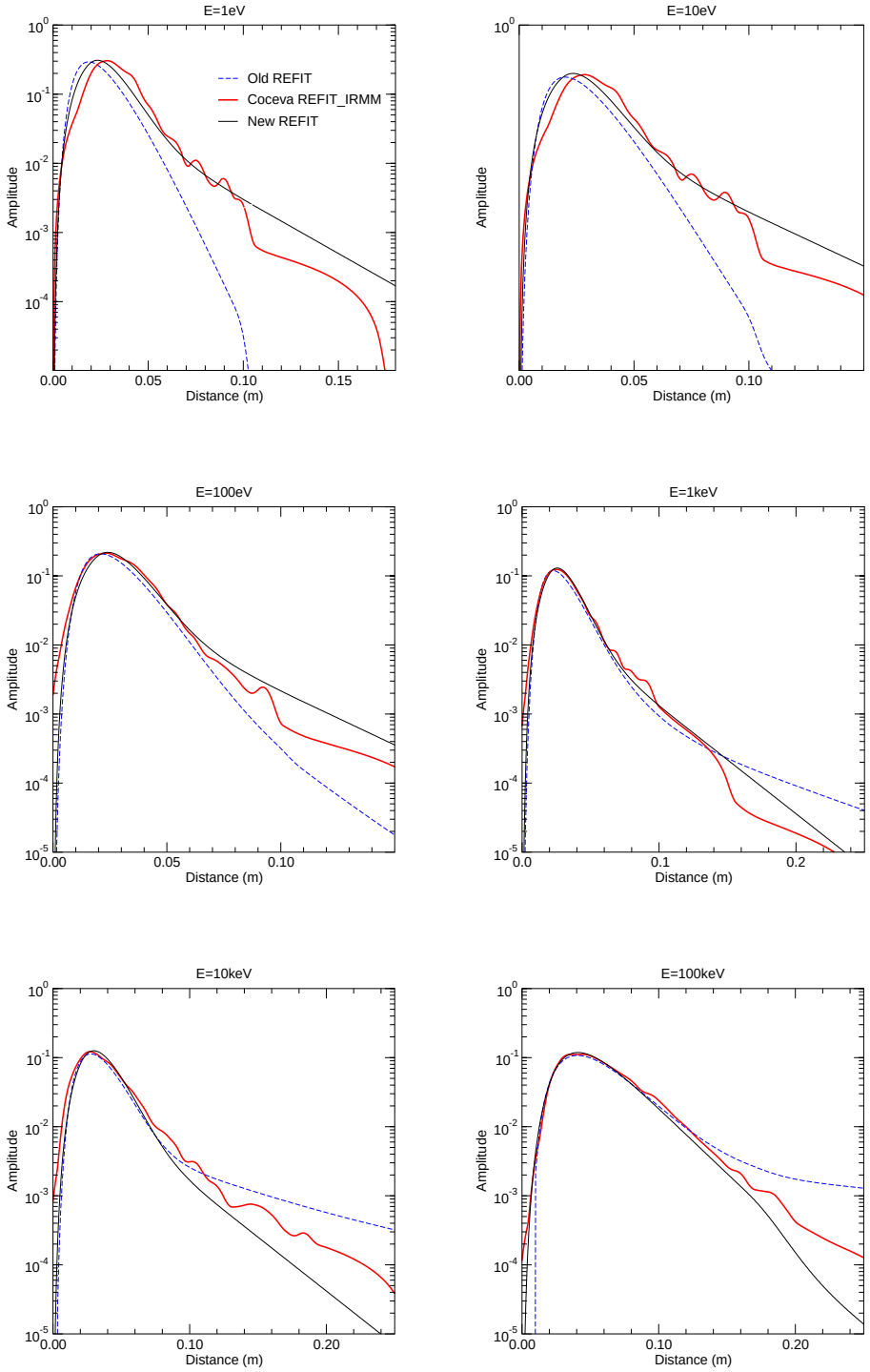

Figure B.18: Full resolution function (flight path 4, $\theta = 9^o$, L=50m) calculated with REFIT without the contribution of the initial burst and the timing channel. REFIT-IRMM is the new version of the code developed at the IRMM including the Coceva simulations.

Table B.7: Parameters of the resolution function for transmission measurement (flight path 4, $\theta = 9^o$).

description	parameter name in REFIT	value for transmission
moderator thickness	AS(3)	3.6 cm
hydrogen thickness	AS(4)	0.2409 at/b
target decay time	BR(1)	$\leq$ 3.5 ns
mean width of the burst	BR(2)	1.5 - 12 ns
ratio of top to bottom	BR(3)	0.7
diameter of the collimator projected on to the moderator	BR(4)	8.1 - 12.15 cm
effective mean free path of a neutron in the moderator	BR(5)	$\geq$ 5.83 mm
angle of the flight path to the normal of the target	BR(6)	0.1571 rad
detector length in neutron beam	BR(13)	6.35 mm
detector diameter	BR(14)	16.0 cm
thickness for scattering	BR(15)	5.5075^{-2} at/b
thickness for reaction	BR(16)	1.1189^{-2} at/b
scattering cross section	BR(17) ,BR(18), BR(19)	2.67 b
reaction cross section	BR(20), BR(21), BR(22)	149.5 $E^{-1/2}$
multiplying factor for mean free path	BR(23)	$\geq$ 1.0
multiplying factor for scattering correction	BR(24)	$\geq$ 1.0
amplitude of secondary pulse relative to the primary pulse	BR(25)	0.1418
amplitude of the exponential component in tail	BR(34)	1.0
mean distance between collision	BR(35)	$\simeq$19.3 mm
multiplying factor for mean free path due to thermal storage	BR(37), BR(38), BR(39)	1.7+3.54 E^{-1}
decay half life of thermal neutrons in the moderator	BR(40), BR(41), BR(42)	27 μs
ratio of the area of the storage to the slowing down distribution	BR(43), BR(44), BR(45)	190 meV

Appendix C

Resolution function of the GEEL facility GELINA in SAMMY-M6

The experimental resolution is one of the major corrections affecting time of flight experiments. An accurate description of the resolution function of the facility is needed for reliable estimates on nuclear parameters. Several processes contribute to the resolution and are assumed to be non correlated to obtain the total shape of the resolution as a function of the neutron energy. The description of the resolution function may be given by Monte-Carlo calculations or formulated with analytic expressions based on the theoretical descriptions of the neutron interaction with the target-moderator assembly (and detector in transmission measurements).

The purpose of this appendix is the description of the experimental resolution function of the GELINA facility in the shape analysis program SAMMY. The RPI and UDR options in SAMMY are compared with the treatments available in the REFIT code.

C.1 Formalisms available in REFIT-IRMM and SAMMY-M6

C.1.1 Analytic formula and Monte-Carlo distributions in REFIT-IRMM

Analytic descriptions [26] and Monte-Carlo simulations of Coceva [117] are available in REFIT. The analytic resolution function results of the numerical convolution of six main components largely described in Appendix B. The distributions we used to describe the timing channel, the electron burst, the uranium target, the water moderator, the angle of the flight path and the detector (Li-glass NE212) are shown in figure C.1. The comparison of the analytic resolution function with Coceva distributions has shown a poor knowledge of the tail. The discrepancy was mainly due to a wrong parametrisation of the multiple scattering of fast neutrons in the uranium target and of the effects of the surrounding materials (Appendix B). Analytic description of the tail was improved by the addition of an exponential function with a neutron energy dependent decay. The half-life (τ) of the target decay could be expressed as:

$$\tau(E) = \lambda_\tau \frac{72.298}{\sqrt{E_n}} \tag{C.1}$$

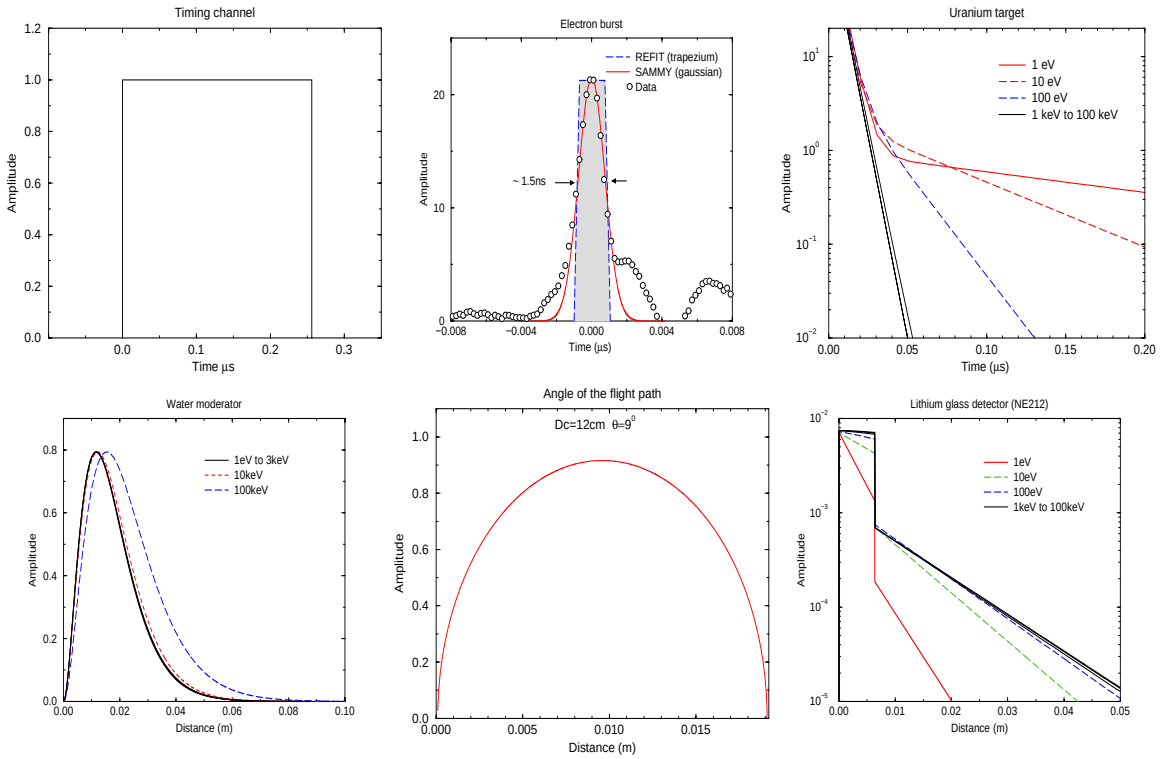

Figure C.1: Main analytic distributions used in REFIT to reproduce the experimental resolution function of the GELINA facility. The channel width , the initial burst of neutrons and the target contributions can be expressed in term of time of flight uncertainty, while the moderator, the angle of the flight path and the detector contributions introduce an uncertainty on the flight path length L.

The λ_τ parameter is assumed to be the mean distance between two collisions. Consequently, it is necessary to distinguish three options available in REFIT, which are:

i) the original analytic description previously proposed by M.Moxon (old)

ii) the new analytic version, that is to say the old description with further analytic improvements (new)

iii) the Coceva distributions implemented in REFIT by A.Brusegan (coc).

The new analytic treatment is based on the information provided by the Coceva simulations. Consequently, the description of the experimental resolution of the Geel facility GELINA in SAMMY-M6 is only discussed in the case of the old REFIT formalism (old), and the Coceva simulations (coc).

C.1.2 RPI function in SAMMY

In SAMMY, several analytic formulae were implemented to describe various experimental resolution functions [27]. The treatment designed to describe the experimental situation for the linac at the Rensselaer Polytechnic Institute of New York (RPI) [118] should be the best realistic function available to reproduce the old resolution function of GELINA. The RPI function results from the analytic convolution of three components $R_i(t)$ $(i = 1, 2, 3)$:

$$R(t) \;=\; R_1(t) \star R_2(t) \star R_3(t) \tag{C.2}$$

The channel width is taken into account with a square function ($R_1(t)$). A Gaussian shape is assumed to reproduce the electron burst contribution ($R_2(t)$). The target-moderator assembly, the angle of the flight path and the detector (in transmission measurements) should be taken into account with a chi-squared function with 6 degrees of freedom plus two exponential terms ($R_3(t)$). Five additional exponential terms were added in order to obtain a better description of the old resolution function of REFIT at all energies. The $R_3(t)$ function is defined as follows:

$$R_3(t) = \begin{cases} A_0 \left\{ \frac{(t+\tau)^2}{2\Lambda^3} e^{-\frac{t+\tau}{\Lambda}} + \sum_{i=1}^{5} B_{2i-1}\, e^{-B_{2i}(t+t_o)} \right. & \\ \qquad \left. + A_1 \left[A_2 e^{-A_3(t+t_o)} + A_4 e^{-A_5(t+t_o)} \right] \right\} & \text{if } t \geq T_o \\ A_0 \left\{ \frac{(t+\tau)^2}{2\Lambda^3} e^{-\frac{t+\tau}{\Lambda}} + \sum_{i=1}^{5} B_{2i-1}\, e^{-B_{2i}(t+t_o)} \right\} & \text{if } \tau \leq t < T_o \\ 0 & \text{if } t < \tau \end{cases} \tag{C.3}$$

with

$$T_o = \frac{\ln(-A_4/A_2)}{A_5 - A_3} - t_o \tag{C.4}$$

The value of A_0 is chosen to give an overall normalisation of unity. Parameters Λ, τ and A_1 are functions of energy:

$$\begin{aligned} \Lambda(E) &= \Lambda_0 + \Lambda_1 \ln(E) + \Lambda_2 [\ln(E)]^2 + \Lambda_3 E^{\Lambda_4} && \text{(in ns)} \\ \tau(E) &= \tau_1 e^{-\tau_2 E} + \tau_3 e^{-\tau_4 E} + \tau_5 + \tau_6 E^{\tau_7} && \text{(in ns)} \\ A_1(E) &= a_1 e^{-a_2 E} + a_3 e^{-a_4 E} + a_5 + a_6 E^{a_7} && \text{(in ns}^{-1}\text{)} \end{aligned} \tag{C.5}$$

An example of the $R_3(t)$ component built with the program SAMRPT [27] is shown in Figure C.2. Some conditions limit the flexibility of the RPI formalism. The value of τ is chosen equal to 0 because the flight path length in REFIT is defined as the distance from the emitting face of the moderator to the incident face of the sample (or detector). Parameters A_4 and A_2 have opposite signs and the positive value of T_o gives the following condition:

$$t_o < \frac{\ln(-A_4/A_2)}{A_5 - A_3} \tag{C.6}$$

Exponential decay amplitudes A_3, A_5 and B_{2i} are independent from the neutron energy. Therefore, only the old analytic description proposed in REFIT can be partially reproduced with the RPI function. The parameters given in Table C.1 were determined by a least squares fit of the resolution function of flight path 15 (capture experiment at 0^o) and flight path 4 (transmission experiment at 9^o). Three energy ranges can be distinguished. Below 50 eV neutron energy, only a chi-squared function is used. Above 50 eV and 1 keV two exponential terms are successively added. It is not possible to obtain a complete and coherent description of the old resolution function of REFIT with the RPI formalism over the whole energy range under investigation [1 eV-100 keV]. The RPI distributions from 1 eV to 100 keV are shown in Figure C.3 together with the old analytic treatment of REFIT and the Coceva simulations. The old REFIT distributions for the capture experiment are reasonably reproduced with the RPI treatment. At 1 eV the agreement of the Full Width at Half Maximum (FWHM) of the distributions is better than 1%. The discrepancy reaches 7% at 10 keV. In the transmission

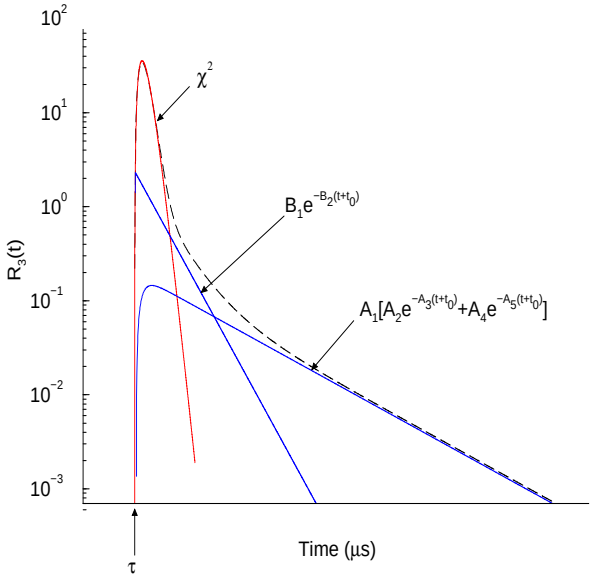

Figure C.2: RPI resolution function built with SAMRPT [27] without burst and channel width components.

case, the RPI formalism cannot accurately reproduce the experimental situation. The effect of the flight path angle cannot be taken into account. At 1 eV, the FWHM is underestimated by a factor 1.15.

C.1.3 UDR formalism in SAMMY

Owing to the difficulties in obtaining a simple and accurate analytic expression capable of describing the full resolution function of GELINA at various flight path angles, the User-Defined-Resolution (UDR) was recently implemented in SAMMY. It is based on the treatment used by REFIT to build the resolution function from the Coceva distributions. The input consists of point-wise distributions in time $R_i(t)$. The full resolution is the numerical convolution of the individual distributions:

$$R(t) \;=\; R_1(t) \;\star\; R_2(t) \;\star \cdots \star\; R_n(t) \tag{C.7}$$

In REFIT, the resolution function is built at the mean value of the energy range under investigation, while in SAMMY a distribution is built for each data point. To avoid any problem of computation time, it is recommended to introduce in SAMMY a single data file containing the full resolution function (electron burst + channel width + other components in time of the resolution). This treatment becomes a good alternative to a complex analytic treatment when the resolution function is well known. In the following study, the UDR function contains the Coceva distributions.

C.1.4 Neutron energy definition

The neutron energy E_n depends on the experimental resolution of the facility and has to be defined carefully. The well known time/energy relationship is:

$$E_n = \left(72.298\frac{L_n}{T_n}\right)^2 \tag{C.8}$$

Table C.1: RPI parameters for the modelisation of the capture and transmission experimental resolutions. The values were obtained by a least square fit of the old resolution function of REFIT (target decay without neutron energy dependence).

Parameter name	values for $E < 50$ eV		values for 50 eV$< E <$1 keV		values for $E > 1$ keV	
	Capture	Transmission	Capture	Transmission	Capture	Transmission
τ	0	0	0	0	0	0
Λ_0	1.66	1.68	1.66	1.68	1.66	1.68
Λ_1	0	0	0	0	0	0
Λ_2	0	0	0	0	0	0
Λ_3	415.77	472.81	415.77	472.81	415.77	472.81
Λ_4	-0.492	-0.475	-0.492	-0.475	-0.492	-0.475
a_1	0	0	0	0.2805	0	0.2805
a_2	0	0	0	0.0496	0	0.0496
a_3	0	0	0	0	0	0
a_4	0	0	0	0	0	0
a_5	0	0	3.9×10^{-3}	4.1×10^{-3}	$3.9 \times 10{-}3$	4.1×10^{-3}
a_6	0	0	0.7729	0.2711	0.7729	0.2711
a_7	0	0	-1.0541	-0.7992	-1.0541	-0.7992
A_2	0	0	-0.0646	-0.0646	-0.0646	-0.0646
A_3	0	0	0.0936	0.0936	0.0936	0.0936
A_4	0	0	0.0540	0.0540	0.0540	0.0540
A_5	0	0	6.9×10^{-3}	6.9×10^{-3}	6.9×10^{-3}	6.9×10^{-3}
t_o	0	0	-1.5	-1.5	-1.5	-1.5
B_1	0	0	0	0	2.725×10^{-3}	2.725×10^{-3}
B_2	0	0	0	0	0.023	0.023

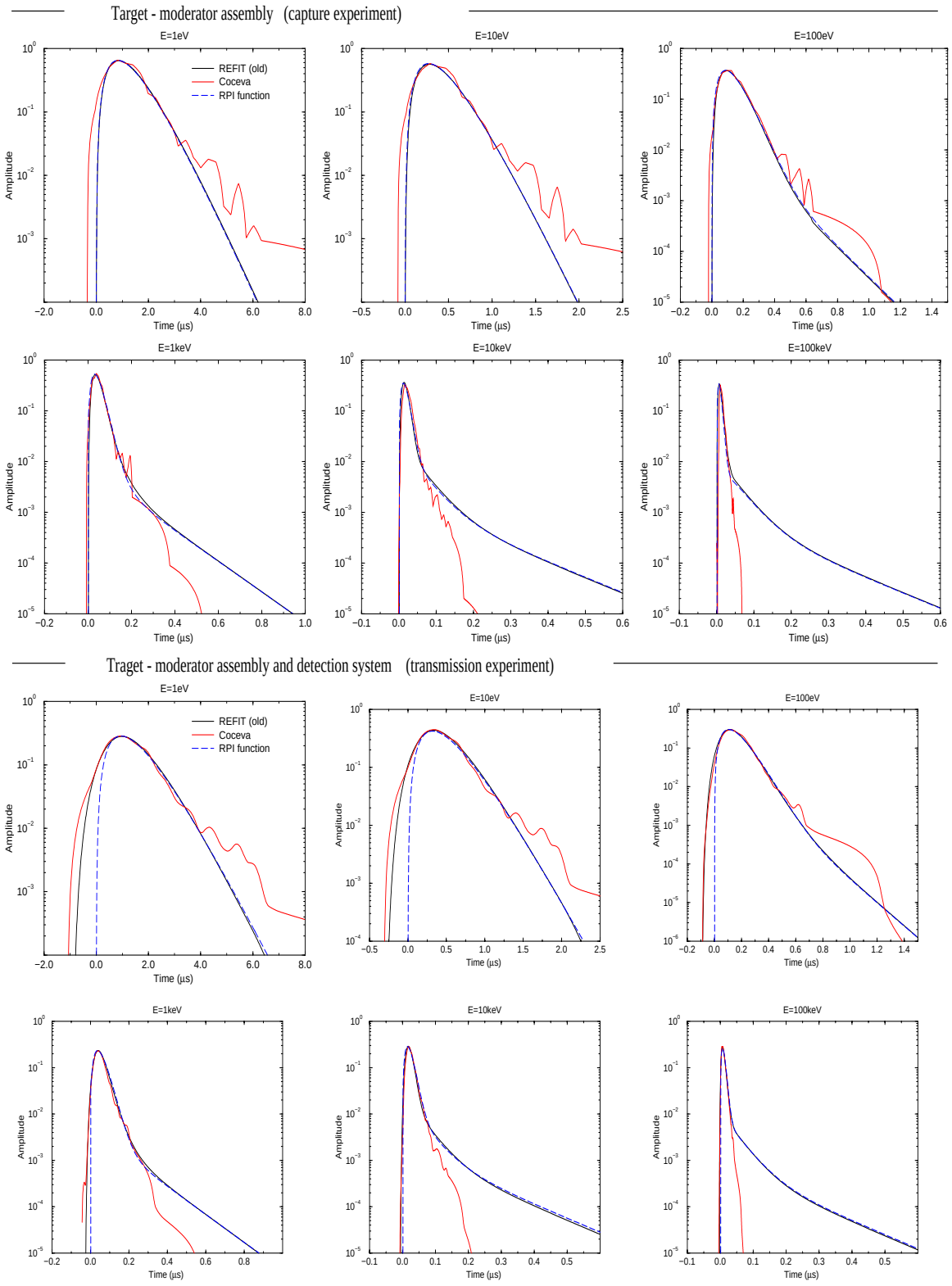

Figure C.3: Resolution functions given by REFIT (old analytic description and Coceva simulations) and distributions calculated with the RPI formalism for two experimental areas of the GELINA facility. The structures seen in the Coceva distributions are due to poor statistics. The solid line for the analytic description is almost entirely obscured by the dashed curve. The capture and the transmission experimental areas are respectively placed at 0^o and 9^o to the moderator surface.

The resolution function has an effect on the flight path length and on the initial delay due to the finite rise time of the components of the resolution. In REFIT, the measured flight path length L is defined as the distance between the emitting surface of the neutron source and the incident face of the sample (or detector in transmission measurement). The mean distance ΔL_{res} traveled by a neutron in both the moderator and detector have to be added to get the correct effective flight distance L_n:

$$L_n = L + \Delta L_{res} \tag{C.9}$$

Similar considerations have to be taken into account to define the flight time T_n. In REFIT, the measured time T is the time from the end of the electron pulse to the start of the channel n (Figure C.4). T_n is then defined as follows:

$$T_n = T + \Delta + \frac{1}{2}\Delta t_p + \frac{1}{2}\Delta t_n \qquad \text{with} \qquad T = \sum_{i=1}^{n-1} \Delta t_i \tag{C.10}$$

where Δt_i is the width of channel i and T is the time grid used to build the data file in REFIT format. The initial delay Δ is calculated via the so-called γ-flash position to obtain the exact flight time of the interacting neutron.

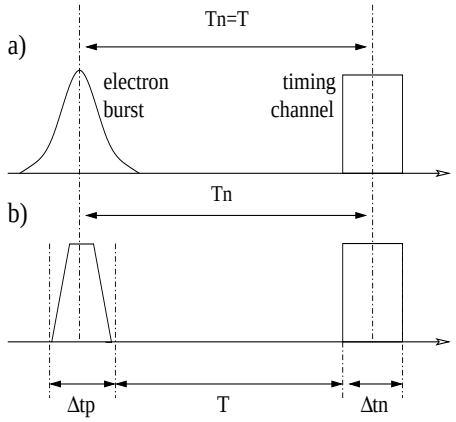

Figure C.4: Time components in SAMMY (a) and REFIT (b) according to the electron burst and the channel width definition.

In SAMMY, the data files are given in energy. Consequently, such corrections have to be performed by an external program. In order to analyse the TOF experiments carried out at the GELINA facility, the use of the REFIT code is a suitable way to generate a reliable data file for SAMMY. Parameters L_n and E_n become the input value for SAMMY and the origin of the full resolution function has to be the centroid of the distribution. For this purpose, it is necessary when using the RPI function to explicitly indicate *SHIFT RPI RESOLUTION FUNCTION TO CENTER*.

C.2 SAMMY-M6 vs. REFIT-IRMM

Before comparing the results from REFIT and SAMMY, a comparison of the results obtained with the REFIT treatments are given below. The original model of REFIT based on analytic

formula has been widely used before implementing the results of Coceva simulations. The old analytic function is characterised by a long tail of small amplitude. A systematic study of the uncertainties connected to the resolution function of the GELINA facility was performed on various transmission data (^{84}Kr,^{237}Np, ^{99}Tc and natural xenon). The transmission experiments were carried out on the same experimental area of our PbI_2 measurements.

C.2.1 Resonance parameter sensitivity

The observed transmission results from the convolution of $T = e^{-n\sigma_T}$ with the resolution function R:

$$T_R(E) = \int_0^{+\infty} R(E, E')\, T(E')\, \mathrm{d}E' \tag{C.11}$$

Owing to the finite numerical calculation, the integration limits become:

$$T_R(E) = \int_{E-\delta E}^{E} R(E, E')\, T(E')\, \mathrm{d}E' \tag{C.12}$$

where δE is the maximum energy spread of the resolution function at energy E. A preliminary estimate of the resolution effect on the transmission T_R is given in Figure C.5. The quantities T_{old} and T_{coc} are transmissions built with each resolution function. For this exercise, ^{99}Tc and ^{84}Kr transmission spectra were obtained with REFIT. These results are in good agreement for resonances with a peak transmission $T > 0.4$. The results in the case of nearly black resonances are more scattered. After a least square fit of the resonance parameters, the discrepancies for resonances with a peak transmission less than 0.1 are always significant. The T_{coc}/T_{old} ratio can be expressed as:

$$\begin{aligned} \frac{T_{coc}}{T_{old}} \;\approx\; 1 \;+\; & \frac{1}{T}\int_{E-\delta E_{coc}}^{E} R_{coc}(E, E')T(E')\mathrm{d}E' \\ - \; & \frac{1}{T}\int_{E-\delta E_{old}}^{E} R_{old}(E, E')T(E')\mathrm{d}E' \end{aligned} \tag{C.13}$$

At 1 keV, the long tail of the analytic resolution function reaches $\delta E_{old} = 53$ eV and the Coceva distribution couples the shape of the resonance as far as $\delta E_{coc} = 15$ eV. According to the condition $\delta E_{old} > \delta E_{coc}$, valid above 200 eV, Equation C.13 becomes:

$$\frac{T_{coc}}{T_{old}} \;\approx\; 1 \;+\; \frac{\phi_{\Delta E_{res}}(E) - \phi_{tail}(E)}{T} \tag{C.14}$$

in which

$$\phi_{\Delta E_{res}}(E) = \int_{E-\delta E_{coc}}^{E} \left(R_{coc}(E, E') - R_{old}(E, E')\right) T(E')\mathrm{d}E' \tag{C.15}$$

$$\phi_{tail}(E) = \int_{E-\delta E_{old}}^{E-\delta E_{coc}} R_{old}(E, E')T(E')\mathrm{d}E' \tag{C.16}$$

The function $(\phi_{\Delta E_{res}} - \phi_{tail})$ depends on the neutron energy. It can be seen as an average factor which expresses the contribution of the tail compared to the width ΔE_{res} of the resolution. The minimum value of this function is about -0.007 (Figure C.5). The negative value is well explained by the increasing skewness with the neutron energy of the old distributions, which involves significant effect of the tail ($\phi_{tail} > \phi_{\Delta E_{res}}$). The criteria based on the resolution width alone and used to estimate the sensitivity to the resolution function lie below the real effect of the resolution broadening.

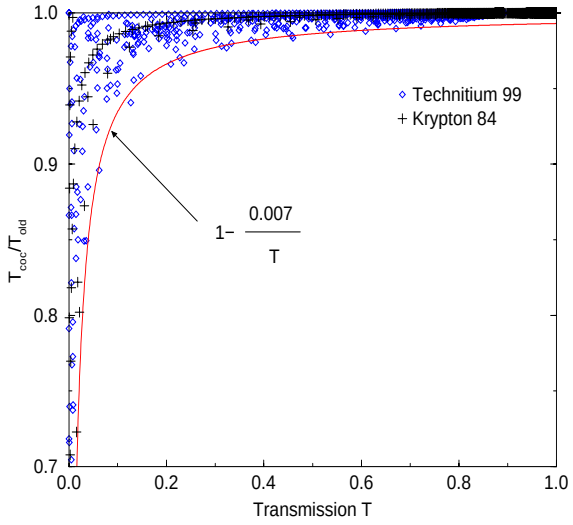

Figure C.5: Ratios of transmission obtained with the old resolution function and the Coceva simulations in the case of ^{99}Tc and ^{84}Kr experiments [71, 119].

The sensitivity of the resonance parameters was investigated below 1.5 keV in the case of ^{99}Tc, ^{237}Np and of natural xenon transmission data [70, 71, 72]. For this purpose, the total widths ($\Gamma_{tot} = \Gamma_\gamma + \Gamma_n$) and the neutron widths Γ_n are adjusted simultaneously. The assessment of the total width is valid only when the resolution contribution represents a small fraction of Γ_{tot}. Nevertheless, in the context of this study, such a determination gives useful information. Figure C.6 shows the total width sensitivity together with the contribution of the doppler width (ΔE_{dop}) and the resolution width (ΔE_{res}). Below 200 eV, the total width obtained with the two formalisms are in good agreement. When the total width becomes smaller than the resolution width, the results from the old REFIT treatment lie below those using Coceva distributions. The spread reaches 20% around 1 keV. According to Equation 6.13, the observed width for the two resolution treatments is given by:

$$\Gamma^2_{obs} \approx \begin{cases} \Delta E^2_{dop} + \Delta E^2_{res,old} + \Gamma^2_{tot,old} \\ \\ \Delta E^2_{dop} + \Delta E^2_{res,coc} + \Gamma^2_{tot,coc} \end{cases} \tag{C.17}$$

As a result, the observed width becomes independent from the resolution when $\Gamma_{tot} >> \Delta E_{res}$, and inversely when $\Gamma_{tot} << \Delta E_{res}$. In the case of intermediate situations, a crude estimate of the absolute error $\Delta\Gamma_{tot}$ is obtained by folding together the above equations:

$$\Delta\Gamma_{tot} \propto \Delta E_{res,old} - \Delta E_{res,coc} \tag{C.18}$$

In the case of the isotopes under investigation, the neutron width is smaller than the radiation width. Equation C.18 becomes:

$$\Delta\Gamma_{\gamma} \propto \Delta E_{res,old} - \Delta E_{res,coc} \tag{C.19}$$

The above equation involves an increasing dependence of Γ_γ with the uncertainties connected to the resolution width. According to the theory, the radiation width should be a nearly constant value because of the numerous decay possibilities in the face of the scattering process [22]. The behaviour observed in Figure C.6 is then an artifact of the resolution. It illustrates the well

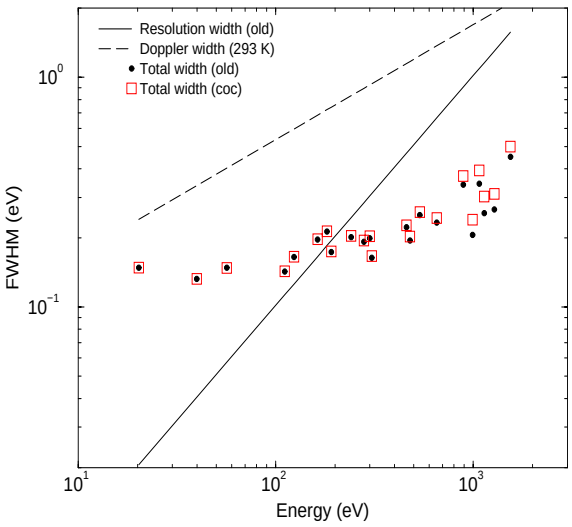

Figure C.6: Total width Γ_{tot} for some ^{99}Tc resonances below 1.5 keV obtained with the old analytic resolution function and the Coceva simulation together with the doppler width ΔE_{dop} and the resolution width ΔE_{res}.

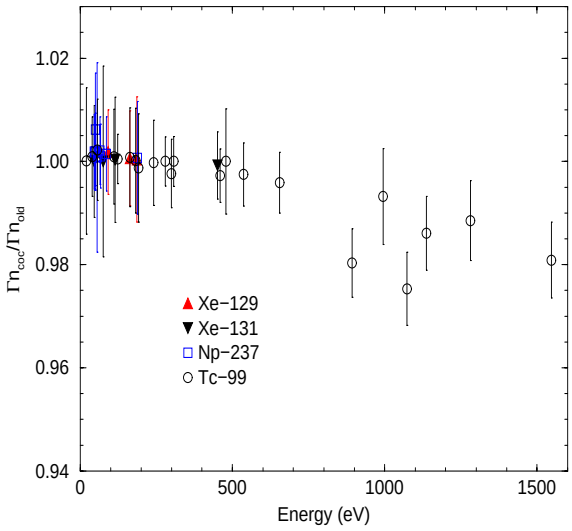

Figure C.7: Ratio of the neutron widths obtained with the Coceva simulation and the old analytic resolution function for ^{99}Tc, ^{237}Np and natural xenon [70, 71, 72]. The radiation widths are free parameters.

known condition for transmission measurement, into which an accurate total width cannot be achieved when $\Gamma_{tot} < \Delta E_{res}$.

From the results shown in Figure C.7, systematic errors on the neutron width are smaller than those on the radiation width. Below 1.5 keV, the maximum discrepancy reaches 2% for isolated resonances. This result suggests a poor dependence of Γ_n with the resolution when $\Gamma_\gamma > \Gamma_n$.

In order to investigate the Γ_n sensitivity, a study was carried out on ^{84}Kr transmission data within the energy range [1 keV-100 keV]. Figure C.8 shows the ^{84}Kr neutron widths ratios obtained with the old analytic resolution of REFIT and the Coceva simulations. The weighted average value is close to unity. The mean behaviour can be interpreted with the area formalism [22]. The area-function in transmission measurements is defined as the integral above the transmission dip between the transmission curve and unity:

$$\begin{aligned} A &= \int_0^{+\infty} (1 - T_R(E))\, \mathrm{d}E \\ &= \int_0^{+\infty} \int_0^{+\infty} R(E', E)\, (1 - T(E'))\, \mathrm{d}E' \mathrm{d}E \end{aligned} \tag{C.20}$$

If $\Gamma_{tot}/2E_r << 1$, the lower limits can be replaced by $-\infty$ and the order of integration interchanged [31]. Equation C.20 becomes:

$$A = \int_0^{+\infty} (1 - T(E')) \underbrace{\int_{-\infty}^{+\infty} R(E', E)\, \mathrm{d}E}_{=1}\, \mathrm{d}E' \tag{C.21}$$

The resolution function is a probability density normalised to unity; the area function becomes independent from the experimental resolution. The asymptotic form of Equation C.21 for a thin sample can be evaluated analytically using the single level Breit-Wigner formula (Section 2.2.4):

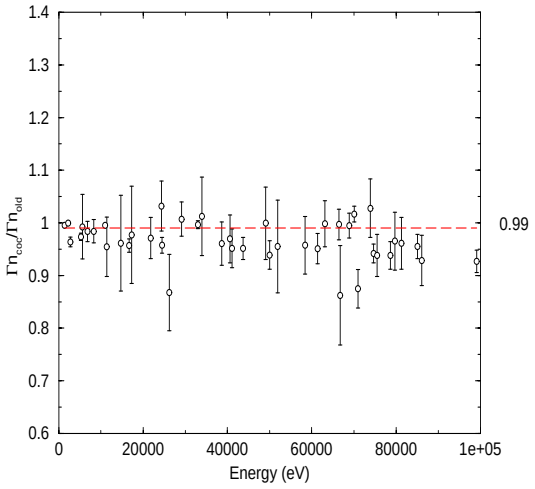

Figure C.8: Ratio of some ^{84}Kr neutron widths obtained with the old analytic resolution of REFIT and the Coceva simulations. The radiation widths are the values given by the capture measurement [119].

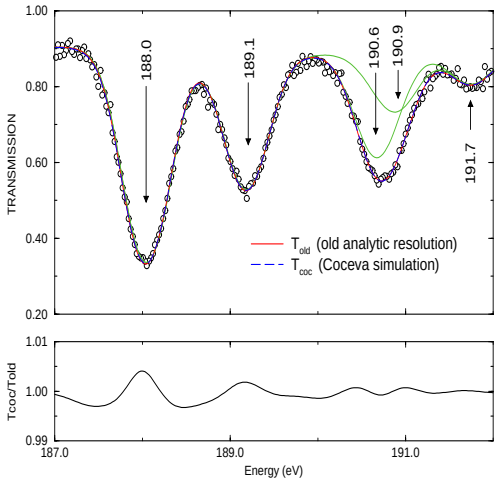

Figure C.9: Comparison of fitting functions obtained with the old analytic resolution function and the Coceva distributions in the case of ^{237}Np transmission measurement. The dashed curve for the Coceva treatment is almost entirely obscured by the solid line.

$$A = 2n\pi^2\lambda^2 g_J \Gamma_n \tag{C.22}$$

From this expression, the neutron width can be assumed in a first approximation independent from the experimental resolution. These assumptions are useful to explain the mean behaviour of the $\Gamma_{n,coc}/\Gamma_{n,old}$ ratios. However, the spread around the mean value (Figure C.8) has to be taken into account to derive accurate resonance parameters. According to Equations C.15 and C.16, $\phi_{\Delta E_{res}}$ and ϕ_{tail} can be replaced in Equation C.14 by their $\phi'_{\Delta E_{res}}$ and ϕ'_{tail} values obtained after adjustment of the neutron width. The neutron widths ratio may be expressed as follows:

$$\frac{\Gamma_{n,coc}}{\Gamma_{n,old}} \approx 1 - \frac{1}{A}\int_{-\infty}^{+\infty} \left(\phi'_{\Delta E_{res}}(E') - \phi'_{tail}(E')\right) \mathrm{d}E' \tag{C.23}$$

From the area formalism, the result of the integration should be close to zero, but realistic situations involve important fluctuations. The relative contribution of the tail compared to the resolution width affects the neutron width. Each of them features complex effects depending on the peak transmission value and on the overlap of the resonances.

An accurate estimate of the neutron width depends on the spacing between the resonances. Figure C.9 shows ^{237}Np transmission data. At 190.6 eV and 190.9 eV the fitting functions are in good agreement. However discrepancies of 5.2% and 10.1% are respectively obtained on the neutron width (Table C.2). There is a strong correlation between the Γ_n values ($C \approx -1$). The tail of the resolution function couples the shape of the resonances and affects the information contained in the wings of the nearby resonances. The respective large uncertainties of about 20% and 40% provided by the REFIT code, are consistent with this indetermination. The sum of the area of the two resonances remains constant using both resolution treatments. This sum and its uncertainty can be expressed as follows:

$$A = \sum_{i=1}^{2} g_i \frac{\Gamma_{\gamma_i}\Gamma_{n_i}}{\Gamma_{\gamma_i}+\Gamma_{n_i}} \approx \sum_{i=1}^{2} g_i \Gamma_{n_i} \tag{C.24}$$

$$\Delta A \approx \sqrt{\sum_{i=1}^{2}(g_i \Delta\Gamma_{n_i})^2 + 2\,C \prod_{i=1}^{2} g_i \Gamma_{n_i}} \tag{C.25}$$

From the neutron width values given in Table C.2, we obtain an area value close to 2.87(2) meV. The usual approximation ($C = 0$) implies a ΔA uncertainty of about 0.64, while the correlation $C = -1$ imply a value of 0.002. Consequently, reliable uncertainties on cross sections or integral quantities cannot be achieved without a careful determination of the sensitivity of the resonance parameters with respect to the experimental resolution of the facility.

Table C.2: resonance energy and neutron width for five resonances of the ^{237}Np obtained with the old analytic resolution function and the Coceva distributions (the given values are preliminary results). The radiation width is set to 40 meV. The quoted errors and the correlation coefficients are provided by the REFIT code.

old analytic resolution function

E_n	188.0	±	0.002	eV	100									
Γ_n	13.97	±	0.008	meV	0	100								
E_n	189.1	±	0.003	eV	4	2	100							
Γ_n	7.29	±	0.071	meV	-1	-2	2	100						
E_n	190.6	±	0.029	eV	-6	0	-6	-5	100					
Γ_n	3.44	±	0.774	meV	-6	0	-6	-5	97	100				
E_n	190.9	±	0.055	eV	-6	0	-6	-5	93	98	100			
Γ_n	2.62	±	1.087	meV	6	0	6	5	-98	-99	-97	100		
E_n	191.7	±	0.016	eV	-1	0	-1	-1	23	27	31	-26	100	
Γ_n	1.00	±	0.045	meV	0	0	0	0	-12	-14	-17	14	-5	100

Coceva simulations

E_n	188.0	±	0.002	eV	100									
Γ_n	14.04	±	0.008	meV	1	100								
E_n	189.1	±	0.003	eV	5	3	100							
Γ_n	7.32	±	0.072	meV	-2	-4	2	100						
E_n	190.6	±	0.027	eV	-5	-1	-6	-9	100					
Γ_n	3.62	±	0.778	meV	-4	-2	-6	-10	97	100				
E_n	190.9	±	0.060	eV	-4	-2	-6	-10	93	98	100			
Γ_n	2.38	±	1.089	meV	4	2	6	10	-98	-99	-97	100		
E_n	191.7	±	0.016	eV	-1	0	-2	-1	24	27	32	-26	100	
Γ_n	1.01	±	0.045	meV	0	-1	4	0	-13	-16	-19	15	-7	100

C.2.2 Results and discussions

The results from the RPI and UDR formalisms are compared with those from REFIT. The RPI results have to be compared with the old analytic treatment of REFIT (old) and the UDR results are compared with those from the Coceva simulations (coc).

Figure C.10 shows the ratios of the neutron widths obtained with SAMMY and REFIT from the analysis of ^{127}I transmission experiments. Below 1 keV, the RPI option agrees with the old analytic one because of the small effect of the resolution function. The average systematic error is better than 0.9%. Local discrepancies close to 5% are due to a statistical effect connected to the analysis of small resonances. In this low energy range, the RPI function can be used without introducing systematic errors on the neutron width larger than the statistical uncertainty. However, according to the sensitivity study (see section C.2.1), significant discrepancies are expected at higher energy when $\Gamma_{tot} << \Delta E_{res}$. The right hand part of Figure C.10 shows results obtained with the UDR function and the Coceva simulations. Below 3 keV, we obtain an agreement of about 0.7% in average from the comparison of the neutron widths. The discrepancies higher than 5% are connected to small resonances with a neutron width value lower than 5 meV.

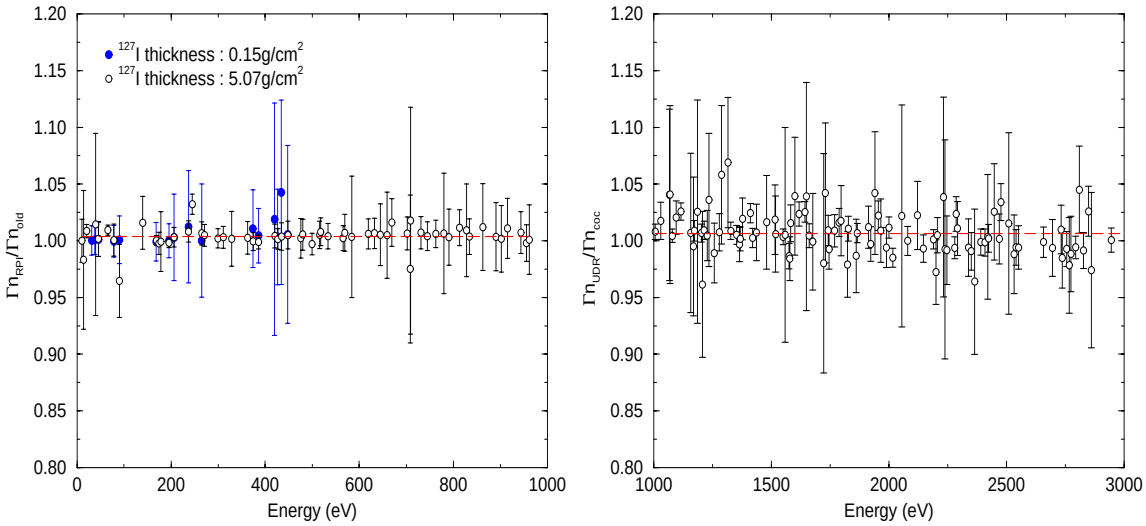

Figure C.10: Ratio of the neutron widths obtained with SAMMY and REFIT from the analysis of ^{127}I transmission measurements. The chart on the left, shows the results obtained with the RPI formalism and the old analytic treatment of REFIT below 1 keV. The chart on the right, shows results obtained with the UDR formalism and the Coceva simulation within the energy range [1 keV-3 keV].

The higher energy range is investigated with the results obtained from natural lead transmission data. Figure C.11 shows an example of transmission obtained with SAMMY and REFIT within the energy range [35 keV-50 keV]. The total width of the broad s-wave at 41 keV is ten times larger than the resolution width. The accuracy of its neutron width is not affected by the experimental resolution. The agreement between SAMMY and REFIT is about 1%. For the three other main resonances, the maximum discrepancy on Γ_n reaches 7% in the case of the RPI formalism before implementing five additional exponential terms in Equation C.3. The results are slightly improved by adding a second exponential term with a half-life decay of 30 ns: the maximum discrepancy reaches 5%. In the case of the UDR function (compared to Coceva simulations), the neutron width values are in better agreement. The maximum discrepancy remains below 3%, with a mean value of 0.6%

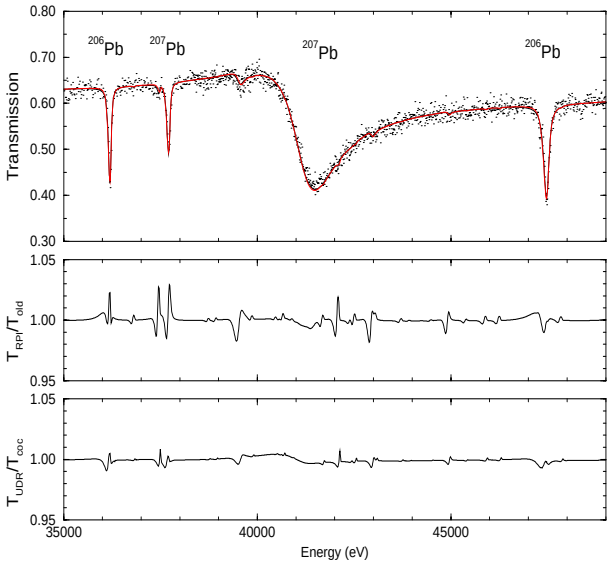

Figure C.11: Natural lead transmission reconstructed with SAMMY and REFIT. The transmission obtained with the RPI formalism is compared to the old analytic treatment of REFIT, and the transmission obtained with the UDR treatment is compared to the Coceva simulation.

C.3 Conclusion

The resolution function involves a complex behaviour of the resonance parameters when the total width of the resonance is smaller than the resolution width. Accurate description of the tail of the resolution is recommended in order to avoid any additional systematic errors larger than the statistical uncertainties. A Comparison between the results obtained with the old analytic treatment of REFIT and those from the Coceva simulations shows that the analytic formula and its parameterisation should be improved in REFIT. Accurate transmission and capture measurements with high signal to background ratio are recommended in order to validate the new analytic treatment of REFIT.

The study of the RPI function together with the old analytic treatment of REFIT shows the difficulty to obtain accurate and coherent resolution distributions with a single function even with the recent addition of five exponential terms. The UDR option is a suitable alternative to use Monte-Carlo results available to the GELINA facility. The results from the UDR option of SAMMY agree with those from REFIT. According to the cases studied in this work, the maximum systematic error is about 3%, and an average discrepancy better than 1% is expected.

Before implementing SAMMY with a reliable analytic treatment to describe the experimental situation of the Geel facility, a special care should be given to the solutions chosen to describe the experimental resolution of the n-TOF facility. Indeed, the components of the resolution are similar to those of the GELINA facility [120]. This future option could be based on the analytic convolution of several functions in time.

Appendix D

^{127}I and ^{129}I resonance parameters

Table D.1: ^{127}I resonance parameters obtained in this work. The quoted errors for the radiation widths are the statistical uncertainties given by the REFIT code. Those for the neutron widths include also the systematic errors as defined in Table 7.13. The errors for the resonance energies take into account the channel widths as well as the flight path length, the moderation distance and the time delay uncertainties.

Energy (eV)			J^π	Radiation width Γ_γ (meV)			Neutron width $g\Gamma_n$ (meV)		
-55.64	±	0.14	2^+	103.9	±	0.9	81.875	±	0.625
-47.84	±	0.10	3^+	103.8	±	0.8	63.292	±	0.467
10.35	±	0.01	1^-	90.0	±	5.9	0.003	±	0.001
13.95	±	0.01	2^-	99.2	±	21.2	0.002	±	0.001
20.38	±	0.01	2^+	95.7	±	0.6	0.719	±	0.024
31.21	±	0.01	3^+	94.7	±	0.3	9.998	±	0.290
37.65	±	0.02	3^+	95.5	±	0.4	23.250	±	0.698
39.74	±	0.02	3^-	96.3	±	9.6	0.003	±	0.001
45.31	±	0.02	2^+	99.8	±	0.3	9.438	±	0.302
53.74	±	0.02	4^-	100.0			0.017	±	0.001
64.05	±	0.03	1^-	100.0			0.005	±	0.001
65.92	±	0.03	2^+	103.5	±	10.4	0.911	±	0.027
78.42	±	0.04	3^+	102.8	±	0.5	14.717	±	0.574
85.76	±	0.04	3^-	100.0			0.019	±	0.001
90.40	±	0.08	3^+	103.8	±	0.4	10.663	±	0.373
101.10	±	0.10	4^-	100.0			0.014	±	0.001
118.27	±	0.11	2^-	100.0			0.007	±	0.001
134.10	±	0.13	3^-	100.0			0.024	±	0.002
136.83	±	0.13	1^-	100.0			0.044	±	0.002
139.59	±	0.13	3^+	95.3	±	0.8	22.819	±	0.685
145.68	±	0.14	4^-	100.0			0.036	±	0.002
153.76	±	0.14	2^-	100.0			0.101	±	0.004
159.40	±	0.15	3^-	100.0			0.007	±	0.001
167.77	±	0.16	3^+	100.0			0.585	±	0.021
168.56	±	0.16	2^+	105.5	±	0.5	44.920	±	1.437
174.09	±	0.16	2^+	156.9	±	3.9	1.686	±	0.059
178.30	±	0.17	3^+	102.6	±	4.7	0.450	±	0.015
195.46	±	0.18	3^+	106.6	±	0.5	64.513	±	1.935
201.10	±	0.15	4^-	100.0			0.039	±	0.002
206.34	±	0.15	2^+	112.6	±	0.8	19.906	±	0.916
223.62	±	0.17	2^-	100.0			0.011	±	0.001
227.12	±	0.17	3^-	100.0			0.012	±	0.001
237.31	±	0.18	2^+	111.9	±	1.5	24.419	±	0.903
244.84	±	0.18	3^+	124.9	±	2.4	5.764	±	0.248
256.68	±	0.19	4^-	100.0			0.063	±	0.003
265.23	±	0.20	3^+	120.4	±	1.9	20.660	±	0.930
271.30	±	0.20	3^+	111.5	±	3.2	4.252	±	0.179
274.48	±	0.20	3^-	100.0			0.023	±	0.009
282.60	±	0.21	2^-	100.0			0.004	±	0.002
292.41	±	0.22	1^-	100.0			0.102	±	0.004
299.57	±	0.22	2^+	111.0	±	2.2	8.005	±	0.280

Energy (eV)	J$^\pi$	Radiation width Γ_γ (meV)	Neutron width $g\Gamma_n$ (meV)
306.44 ± 0.26	4$^-$	100.0	0.035 ± 0.003
310.85 ± 0.26	2$^+$	118.6 ± 2.3	10.247 ± 0.400
314.55 ± 0.27	3$^-$	100.0	0.047 ± 0.004
324.16 ± 0.28	2$^+$	100.0	0.233 ± 0.010
325.39 ± 0.28	2$^+$	100.0	0.460 ± 0.017
329.00 ± 0.28	3$^+$	125.0 ± 7.1	1.673 ± 0.054
346.35 ± 0.29	4$^-$	100.0	0.122 ± 0.006
351.96 ± 0.30	2$^-$	100.0	0.093 ± 0.006
353.40 ± 0.30	1$^-$	100.0	0.094 ± 0.005
362.53 ± 0.31	2$^+$	143.8 ± 4.7	3.868 ± 0.128
374.74 ± 0.32	2$^+$	98.9 ± 1.0	67.339 ± 2.020
382.13 ± 0.32	3$^-$	100.0	0.198 ± 0.011
386.17 ± 0.33	2$^+$	89.6 ± 0.8	108.425 ± 3.578
392.09 ± 0.33	4$^-$	100.0	0.148 ± 0.012
393.18 ± 0.33	2$^-$	100.0	0.321 ± 0.016
413.01 ± 0.39	1$^-$	100.0	0.084 ± 0.009
420.28 ± 0.40	3$^+$	100.0	13.976 ± 0.629
421.85 ± 0.40	3$^-$	100.0	0.186 ± 0.016
426.93 ± 0.40	2$^+$	99.4 ± 0.7	60.547 ± 1.816
431.40 ± 0.41	4$^-$	100.0	0.148 ± 0.010
434.95 ± 0.41	3$^+$	100.9 ± 2.0	27.234 ± 1.334
440.06 ± 0.41	2$^-$	100.0	0.187 ± 0.010
448.27 ± 0.42	2$^+$	117.9 ± 1.5	26.581 ± 1.143
454.78 ± 0.43	3$^+$	100.0	0.677 ± 0.023
458.30 ± 0.43	1$^-$	100.0	0.104 ± 0.017
468.42 ± 0.44	3$^-$	100.0	0.128 ± 0.013
475.81 ± 0.45	2$^+$	107.5 ± 5.5	5.350 ± 0.203
480.09 ± 0.45	2$^+$	115.1 ± 4.4	8.176 ± 0.270
499.39 ± 0.47	2$^+$	128.6 ± 2.4	23.244 ± 0.790
515.35 ± 0.53	2$^+$	121.1 ± 3.3	23.131 ± 0.810
518.16 ± 0.53	3$^+$	110.5 ± 4.0	19.628 ± 0.746
533.34 ± 0.55	3$^+$	100.6 ± 1.4	59.322 ± 2.136
545.97 ± 0.56	4$^-$	100.0	0.128 ± 0.013
550.50 ± 0.57	2$^+$	100.0	0.632 ± 0.023
563.07 ± 0.58	3$^-$	100.0	0.478 ± 0.028
565.92 ± 0.58	3$^+$	99.2 ± 1.8	87.437 ± 2.711
569.14 ± 0.59	2$^+$	94.7 ± 6.0	10.626 ± 0.383
578.71 ± 0.60	2$^-$	100.0	0.321 ± 0.016
584.28 ± 0.60	2$^+$	100.0	2.012 ± 0.066
588.72 ± 0.61	4$^-$	100.0	0.233 ± 0.012
596.58 ± 0.61	1$^-$	100.0	0.128 ± 0.013
619.22 ± 0.69	3$^+$	95.5 ± 2.1	36.707 ± 1.321
624.30 ± 0.69	3$^-$	100.0	0.707 ± 0.028
632.55 ± 0.70	3$^+$	97.3 ± 3.4	21.401 ± 0.792
635.75 ± 0.71	4$^-$	100.0	0.386 ± 0.024

Energy (eV)			J^π	Radiation width Γ_γ (meV)			Neutron width $g\Gamma_n$ (meV)		
643.63	±	0.71	2^-	100.0			0.514	±	0.115
644.73	±	0.72	2^+	84.9	±	11.6	5.534	±	0.216
646.99	±	0.72	1^-	100.0			0.150	±	0.016
658.85	±	0.73	3^+	126.0	±	9.4	3.971	±	0.131
662.36	±	0.74	3^-	100.0			0.405	±	0.019
669.30	±	0.74	2^+	98.6	±	2.3	30.011	±	1.110
690.11	±	0.77	3^+	100.0			0.892	±	0.033
702.09	±	0.84	3^+	101.3	±	2.0	64.046	±	2.049
708.41	±	0.84	2^+	87.2	±	5.1	104.954	±	8.501
708.71	±	0.84	3^+	98.5	±	4.2	123.342	±	7.401
714.03	±	0.85	4^-	100.0			0.145	±	0.034
726.75	±	0.86	2^-	100.0			0.358	±	0.024
730.92	±	0.87	2^+	97.4	±	1.9	61.130	±	2.017
734.47	±	0.87	3^-	100.0			0.482	±	0.027
744.49	±	0.89	3^+	97.7	±	1.5	109.544	±	3.505
757.92	±	0.90	4^-	100.0			0.690	±	0.034
762.49	±	0.91	2^+	99.0	±	1.6	111.759	±	3.688
767.08	±	0.91	1^-	100.0			0.379	±	0.026
772.14	±	0.92	2^-	100.0			0.082	±	0.015
777.30	±	0.92	3^-	100.0			0.168	±	0.021
779.76	±	0.93	3^+	100.0			4.199	±	0.147
790.64	±	0.94	3^+	106.8	±	6.5	10.925	±	0.371
796.74	±	0.95	4^-	100.0			0.075	±	0.008
805.45	±	0.43	1^-	100.0			0.420	±	0.021
813.40	±	0.44	2^+	103.1	±	2.3	38.870	±	1.360
818.13	±	0.44	2^-	100.0			0.255	±	0.018
828.16	±	0.45	3^+	136.1	±	6.4	6.504	±	0.247
834.06	±	0.45	3^+	92.7	±	1.7	88.428	±	2.918
840.01	±	0.45	4^-	100.0			0.395	±	0.026
862.47	±	0.47	3^+	124.7	±	11.8	6.737	±	0.236
867.44	±	0.47	3^-	100.0			0.665	±	0.029
890.56	±	0.48	2^+	112.5	±	7.1	10.651	±	0.341
898.05	±	0.48	4^-	100.0			0.176	±	0.025
901.69	±	0.50	2^+	131.5	±	8.9	11.230	±	0.371
915.18	±	0.50	3^+	101.8	±	7.9	13.002	±	0.416
918.21	±	0.51	3^-	100.0			0.517	±	0.037
920.02	±	0.51	2^-	100.0			0.310	±	0.033
925.27	±	0.51	1^-	100.0			0.454	±	0.027
927.99	±	0.51	4^-	100.0			0.951	±	0.041
943.26	±	0.52	3^+	161.2	±	5.5	29.597	±	0.977
955.23	±	0.53	3^+	96.6	±	2.2	79.095	±	2.610
961.30	±	0.53	3^+	101.7	±	9.1	12.191	±	0.402
966.48	±	0.53	4^-	100.0			0.725	±	0.037

Energy (eV)			J$^{\pi}$	Radiation width Γ_γ (meV)			Neutron width $g\Gamma_n$ (meV)		
969.68	±	0.53	3$^-$	100.0			0.140	±	0.026
972.14	±	0.53	2$^-$	100.0			0.355	±	0.022
987.44	±	0.54	1$^-$	100.0			0.972	±	0.039
1003.80	±	0.56	4$^-$	100.0			0.967	±	0.083
1006.79	±	0.56	2$^+$	108.7	±	2.1	82.090	±	2.873
1020.40	±	0.57	3$^-$	100.0			0.570	±	0.034
1030.24	±	0.58	3$^+$	135.4	±	13.9	8.645	±	0.285
1036.60	±	0.58	2$^-$	100.0			0.314	±	0.021
1045.40	±	0.59	4$^-$	100.0			0.069	±	0.014
1054.30	±	0.59	1$^-$	100.0			0.376	±	0.021
1060.60	±	0.59	3$^-$	100.0			0.236	±	0.018
1066.90	±	0.60	3$^+$	100.0			1.616	±	0.073
1069.66	±	0.60	2$^+$	100.0			2.490	±	0.097
1079.29	±	0.60	3$^+$	100.0			170.557	±	5.458
1089.50	±	0.61	4$^-$	100.0			0.881	±	0.048
1095.39	±	0.61	3$^+$	103.5	±	11.3	12.512	±	0.438
1104.30	±	0.62	3$^-$	100.0			0.266	±	0.024
1116.32	±	0.63	3$^+$	97.6	±	2.0	91.928	±	3.677
1120.50	±	0.63	2$^-$	100.0			0.555	±	0.041
1125.80	±	0.63	1$^-$	100.0			0.139	±	0.021
1137.20	±	0.64	4$^-$	100.0			0.347	±	0.024
1150.10	±	0.64	3$^-$	100.0			0.149	±	0.017
1155.30	±	0.65	2$^-$	100.0			0.249	±	0.037
1157.70	±	0.65	1$^-$	100.0			1.470	±	0.068
1169.38	±	0.65	2$^+$	100.0			1.983	±	0.099
1173.06	±	0.66	3$^+$	101.4	±	4.5	30.752	±	1.046
1183.34	±	0.66	4$^-$	100.0			0.178	±	0.034
1186.10	±	0.66	3$^-$	100.0			1.251	±	0.061
1197.50	±	0.67	2$^-$	100.0			1.343	±	0.066
1202.95	±	0.67	2$^+$	127.7	±	4.2	52.463	±	1.836
1207.46	±	0.68	3$^+$	100.0			1.799	±	0.083
1214.43	±	0.68	3$^+$	100.6	±	2.7	63.580	±	2.352
1228.20	±	0.69	3$^+$	100.0			8.544	±	0.282
1234.70	±	0.69	2$^+$	100.0			2.498	±	0.097
1241.30	±	0.70	4$^-$	100.0			0.456	±	0.031
1245.00	±	0.70	3$^-$	100.0			0.129	±	0.022
1250.00	±	0.70	2$^-$	100.0			0.920	±	0.045
1257.41	±	0.70	3$^+$	93.4	±	8.3	14.262	±	0.499
1268.61	±	0.71	3$^+$	100.0			2.420	±	1.396
1269.29	±	0.71	3$^+$	100.0			4.989	±	1.527
1278.60	±	0.72	3$^+$	132.5	±	11.8	13.988	±	0.476
1288.12	±	0.72	3$^+$	100.0			2.673	±	0.102
1292.80	±	0.72	4$^-$	100.0			0.248	±	0.027

Energy (eV)			J$^{\pi}$	Radiation width Γ_{γ} (meV)			Neutron width $g\Gamma_n$ (meV)		
1296.60	±	0.73	3$^-$	100.0			0.604	±	0.036
1312.80	±	0.74	2$^-$	100.0			0.491	±	0.061
1315.61	±	0.74	3$^+$	100.0			3.674	±	0.147
1328.17	±	0.74	2$^+$	106.4	±	1.9	101.091	±	4.145
1332.64	±	0.75	4$^-$	100.0			0.225	±	0.025
1347.00	±	0.75	3$^-$	100.0			0.937	±	0.065
1353.15	±	0.76	2$^+$	139.8	±	4.5	57.505	±	2.300
1357.70	±	0.76	1$^-$	100.0			0.936	±	0.063
1364.91	±	0.76	2$^+$	100.0			19.271	±	0.713
1368.12	±	0.77	3$^+$	93.2	±	4.8	35.535	±	3.731
1377.97	±	0.77	3$^+$	100.0			13.603	±	0.449
1382.60	±	0.77	4$^-$	100.0			0.794	±	0.056
1397.90	±	0.78	3$^-$	100.0			0.116	±	0.028
1406.20	±	0.79	2$^-$	100.0			0.545	±	0.066
1411.76	±	0.79	3$^+$	105.6	±	3.0	79.679	±	2.868
1421.01	±	0.80	2$^+$	118.7	±	3.1	74.631	±	2.687
1437.00	±	0.80	2$^+$	97.3	±	9.7	10.418	±	0.354
1442.10	±	0.81	4$^-$	100.0			0.700	±	0.046
1458.10	±	0.82	3$^-$	100.0			0.239	±	0.054
1460.90	±	0.82	2$^-$	100.0			0.948	±	0.064
1474.10	±	0.83	1$^-$	100.0			1.081	±	0.111
1476.25	±	0.83	4$^-$	100.0			0.771	±	0.130
1480.07	±	0.83	2$^+$	100.0			5.864	±	0.223
1485.30	±	0.83	3$^-$	100.0			0.276	±	0.023
1492.10	±	0.84	2$^-$	100.0			1.393	±	0.063
1511.70	±	0.85	1$^-$	100.0			0.808	±	0.107
1516.55	±	0.85	2$^+$	135.8	±	10.6	57.171	±	2.630
1518.45	±	0.85	2$^+$	107.7	±	8.4	56.671	±	2.607
1522.86	±	0.85	2$^+$	100.0			2.841	±	0.139
1529.90	±	0.86	4$^-$	100.0			0.387	±	0.045
1536.90	±	0.86	3$^-$	100.0			0.477	±	0.051
1550.21	±	0.87	2$^+$	153.4	±	2.9	192.140	±	6.533
1558.97	±	0.87	2$^+$	100.0			4.189	±	0.172
1575.23	±	0.88	2$^+$	130.4	±	7.7	45.212	±	1.402
1579.01	±	0.88	2$^+$	100.0			20.289	±	0.690
1582.71	±	0.89	2$^+$	100.0			22.777	±	0.797
1600.84	±	0.90	3$^+$	100.0			5.090	±	0.188
1607.40	±	0.90	4$^-$	100.0			1.435	±	0.072
1618.08	±	0.91	2$^+$	102.8	±	3.1	45.129	±	1.760
1625.30	±	0.91	3$^-$	100.0			0.496	±	0.040
1643.79	±	0.92	3$^+$	158.3	±	4.6	78.512	±	2.983
1648.90	±	0.92	4$^-$	100.0			1.840	±	0.099
1661.76	±	0.93	2$^+$	132.4	±	4.1	50.421	±	1.714

Energy (eV)			J^π	Radiation width Γ_γ (meV)			Neutron width $g\Gamma_n$ (meV)		
1676.60	±	0.94	3^+	100.0			11.589	±	0.394
1683.60	±	0.94	2^-	100.0			1.363	±	0.090
1687.20	±	0.94	4^-	100.0			1.633	±	0.100
1695.80	±	0.95	3^-	100.0			0.977	±	0.059
1702.40	±	0.95	1^-	100.0			0.370	±	0.027
1714.70	±	0.96	2^-	100.0			1.656	±	0.078
1724.10	±	0.97	3^+	100.0			5.666	±	0.221
1729.64	±	0.97	2^+	100.0			4.140	±	0.174
1740.20	±	0.97	4^-	100.0			2.075	±	0.149
1742.75	±	0.98	2^+	100.0			80.619	±	2.580
1744.04	±	0.98	3^+	100.0			3.049	±	1.528
1745.84	±	0.98	3^+	103.6	±	10.6	33.556	±	1.174
1751.90	±	0.98	3^-	100.0			2.554	±	0.156
1756.50	±	0.98	1^-	100.0			1.549	±	0.077
1769.80	±	0.99	2^+	144.6	±	7.7	31.786	±	1.144
1779.42	±	1.00	2^+	100.0			3.671	±	0.191
1789.17	±	1.00	3^+	80.2	±	3.0	46.862	±	1.640
1797.20	±	1.01	2^+	100.0			13.336	±	0.493
1804.00	±	1.01	4^-	100.0			2.240	±	0.112
1819.00	±	1.02	2^-	100.0			0.854	±	0.089
1823.90	±	1.02	2^+	100.0			20.663	±	0.827
1827.61	±	1.02	2^+	100.0			89.812	±	2.784
1838.60	±	1.03	3^-	100.0			0.350	±	0.053
1847.40	±	1.03	4^-	100.0			0.403	±	0.055
1860.96	±	1.04	2^+	100.0			10.588	±	0.413
1865.65	±	1.04	2^+	100.0			200.266	±	6.409
1881.10	±	1.05	2^-	100.0			1.108	±	0.120
1884.52	±	1.06	3^+	100.0			4.534	±	0.268
1895.72	±	1.06	3^+	100.0			7.869	±	0.370
1900.04	±	1.06	2^+	100.0			6.129	±	0.313
1913.14	±	1.07	2^+	109.9	±	8.5	26.073	±	0.939
1923.62	±	1.08	3^+	104.9	±	6.5	41.163	±	1.441
1929.60	±	1.08	3^-	100.0			1.661	±	0.110
1940.82	±	1.09	3^+	70.6	±	5.6	27.783	±	0.972
1955.21	±	1.09	3^+	104.2	±	5.9	47.976	±	1.679
1966.06	±	1.10	2^+	100.0			16.767	±	0.637
1972.23	±	1.10	2^+	100.0			25.618	±	7.762
1973.10	±	1.10	3^+	100.0			50.647	±	1.671
1989.51	±	1.11	3^+	100.0			31.544	±	1.072
2000.70	±	1.30	2^+	104.4	±	3.3	131.052	±	5.242
2008.90	±	1.31	4^-	100.0			4.762	±	0.257
2016.70	±	1.31	2^+	97.0	±	3.0	199.974	±	5.999
2026.90	±	1.32	3^-	100.0			0.467	±	0.054

Energy (eV)			J^π	Radiation width Γ_γ (meV)			Neutron width $g\Gamma_n$ (meV)		
2039.70	±	1.33	2^-	100.0			0.567	±	0.078
2054.94	±	1.34	3^+	121.8	±	5.8	62.204	±	2.115
2055.63	±	1.34	4^-	100.0			16.042	±	4.829
2068.90	±	1.34	3^-	100.0			3.094	±	0.183
2080.66	±	1.35	2^+	107.9	±	4.0	58.880	±	2.061
2086.33	±	1.36	2^+	100.0			5.090	±	0.290
2092.97	±	1.36	3^+	64.8	±	3.1	140.050	±	5.042
2094.00	±	1.36	4^-	100.0			36.915	±	6.165
2109.99	±	1.37	2^+	100.0			8.642	±	0.432
2121.70	±	1.38	3^+	100.0			18.513	±	0.704
2131.00	±	1.39	2^-	100.0			2.587	±	0.194
2135.40	±	1.39	4^-	100.0			1.411	±	0.162
2141.70	±	1.39	3^-	100.0			1.415	±	0.207
2147.01	±	1.40	3^+	83.0	±	3.2	79.212	±	2.772
2189.87	±	1.42	2^+	102.3	±	3.3	223.648	±	6.933
2196.02	±	1.43	2^+	100.0			5.794	±	3.251
2200.70	±	1.43	2^+	111.0	±	14.7	34.940	±	1.258
2206.00	±	1.43	2^-	95.8	±	9.9	52.954	±	1.747
2214.90	±	1.44	4^-	100.0			1.245	±	0.129
2232.70	±	1.45	2^+	100.0			14.627	±	0.834
2239.21	±	1.46	3^+	100.0			10.769	±	0.506
2246.67	±	1.46	3^+	132.0	±	15.4	31.522	±	1.135
2262.50	±	1.47	3^-	100.0			2.263	±	0.249
2280.08	±	1.48	2^+	105.1	±	4.3	185.215	±	5.742
2286.50	±	1.49	3^+	125.3	±	10.5	65.662	±	2.167
2292.00	±	1.49	4^-	100.0			40.340	±	1.412
2306.90	±	1.50	2^-	100.0			2.912	±	0.303
2321.48	±	1.51	3^+	100.0			5.403	±	0.562
2338.01	±	1.52	3^+	166.2	±	32.1	25.759	±	0.979
2344.24	±	1.52	3^+	100.0			9.071	±	0.535
2350.79	±	1.53	2^+	139.6	±	11.4	49.962	±	1.749
2364.78	±	1.54	3^+	147.2	±	33.3	23.554	±	0.989
2378.90	±	1.55	3^-	100.0			3.052	±	0.311
2390.87	±	1.55	3^+	101.1	±	4.4	110.302	±	4.081
2408.83	±	1.57	2^+	100.0			102.752	±	3.494
2420.87	±	1.57	3^+	100.0			19.713	±	0.986
2424.63	±	1.58	2^+	100.0			165.300	±	5.620
2433.70	±	1.58	4^-	100.0			3.364	±	0.313
2448.06	±	1.59	2^+	100.0			23.330	±	0.957
2469.48	±	1.61	2^+	118.1	±	14.6	37.520	±	1.388
2476.38	±	1.61	3^+	100.0			110.481	±	8.176
2492.20	±	1.62	3^-	100.0			1.906	±	0.328
2497.30	±	1.62	3^+	100.0			9.642	±	0.665

Energy (eV)			J^π	Radiation width Γ_γ (meV)			Neutron width $g\Gamma_n$ (meV)		
2501.57	±	1.63	3^+	100.0			3.871	±	0.441
2509.51	±	1.63	3^+	100.0			13.796	±	0.662
2519.60	±	1.64	2^-	100.0			3.693	±	0.321
2533.16	±	1.65	2^+	100.0			32.405	±	1.296
2540.99	±	1.65	3^+	158.6	±	14.4	65.855	±	2.305
2552.02	±	1.66	3^+	238.7	±	27.7	48.525	±	1.698
2570.89	±	1.67	2^+	100.0			25.382	±	1.091
2599.00	±	1.69	1^-	100.0			4.707	±	0.612
2603.90	±	1.69	3^+	121.8	±	8.3	44.998	±	1.665
2628.50	±	1.71	4^-	100.0			1.739	±	0.622
2632.10	±	1.71	3^-	100.0			2.072	±	0.644
2637.60	±	1.71	2^-	100.0			1.988	±	0.318
2657.60	±	1.73	3^+	75.1	±	3.5	103.069	±	3.401
2663.73	±	1.73	2^+	100.0			4.684	±	0.539
2668.68	±	1.73	2^+	100.0			4.617	±	0.536
2673.80	±	1.74	4^-	100.0			11.500	±	0.805
2680.80	±	1.74	3^-	100.0			1.125	±	0.194
2688.40	±	1.75	1^-	100.0			2.864	±	0.392
2696.30	±	1.75	3^+	101.9	±	8.4	42.366	±	1.737
2720.10	±	1.77	4^-	100.0			3.059	±	0.330
2732.60	±	1.78	2^+	120.8	±	10.3	61.797	±	2.286
2737.38	±	1.78	3^+	118.5	±	13.3	47.142	±	1.791
2752.80	±	1.79	2^+	100.0			5.403	±	2.096
2756.16	±	1.79	2^+	104.4	±	12.1	80.506	±	4.106
2767.24	±	1.80	2^+	100.0			23.325	±	1.073
2774.40	±	1.80	2^-	100.0			32.473	±	1.364
2794.33	±	1.82	3^+	69.1	±	2.6	301.449	±	9.646
2807.00	±	1.82	3^-	100.0			5.405	±	1.124
2810.19	±	1.83	3^+	100.0			21.267	±	1.595
2827.55	±	1.84	4^-	132.3	±	9.0	92.394	±	3.049
2849.81	±	1.85	3^+	97.9	±	8.8	47.971	±	1.871
2859.94	±	1.86	2^+	100.0			11.965	±	1.005
2863.83	±	1.86	2^+	100.0			4.952	±	0.773
2879.80	±	1.87	2^-	100.0			2.262	±	0.373
2888.86	±	1.88	2^+	100.0			23.981	±	1.966
2893.52	±	1.88	2^+	116.1	±	15.3	413.283	±	14.465
2895.60	±	1.88	3^-	100.0			11.814	±	5.671
2900.66	±	1.89	3^+	100.0			11.012	±	0.969
2921.68	±	1.90	3^+	100.0			15.260	±	0.946
2934.20	±	1.91	1^-	100.0			4.385	±	0.645
2945.62	±	1.91	3^+	101.2	±	3.7	268.376	±	8.856
2969.47	±	1.93	4^-	100.0			5.570	±	3.649
2970.24	±	1.93	2^+	100.0			7.921	±	4.951

Energy (eV)			J^π	Radiation width Γ_γ (meV)			Neutron width $g\Gamma_n$ (meV)		
2975.93	±	1.93	2^+	100.0			5.838	±	0.631
2988.87	±	1.94	2^+	100.0			33.157	±	2.719
2991.65	±	1.94	2^+	100.0			7.632	±	1.778
3006.79	±	1.62	3^+	100.0			20.360	±	0.977
3024.60	±	1.63	3^-	100.0			1.352	±	0.226
3037.60	±	1.64	4^-	100.0			2.809	±	0.315
3050.97	±	1.65	3^+	100.0			11.944	±	1.338
3055.27	±	1.65	3^+	100.0			27.671	±	1.882
3075.15	±	1.66	3^+	100.0			16.576	±	1.011
3091.00	±	1.67	2^-	100.0			3.912	±	1.553
3093.94	±	1.67	2^+	133.4	±	17.6	76.506	±	7.039
3110.50	±	1.68	4^-	100.0			4.856	±	0.447
3122.50	±	1.69	3^-	100.0			3.049	±	0.393
3132.43	±	1.69	2^+	111.0	±	6.3	79.399	±	3.652
3144.82	±	1.70	3^+	102.7	±	19.3	35.298	±	4.906
3147.61	±	1.70	3^+	100.0			19.374	±	3.662
3176.98	±	1.72	3^+	100.0			53.930	±	11.110
3177.08	±	1.72	2^+	100.0			28.087	±	9.325
3181.16	±	1.72	3^+	100.0			5.493	±	2.197
3192.40	±	1.72	1^-	100.0			3.908	±	0.688
3200.56	±	1.73	2^+	100.0			12.340	±	0.864
3207.17	±	1.73	3^+	100.0			16.376	±	1.425
3238.64	±	1.75	3^+	100.0			41.182	±	1.771
3248.30	±	1.75	3^+	100.0			33.729	±	4.115
3270.31	±	1.77	2^+	124.9	±	6.5	164.888	±	6.760
3273.43	±	1.77	3^+	100.0			41.176	±	2.965
3286.10	±	1.77	2^-	100.0			3.153	±	0.337
3298.73	±	1.78	3^+	98.5	±	6.4	83.937	±	3.357
3306.40	±	1.79	4^-	100.0			6.615	±	0.747
3334.59	±	1.80	2^+	100.0			5.312	±	0.999
3339.20	±	1.80	3^-	100.0			5.425	±	0.933
3351.75	±	1.81	2^+	131.4	±	6.4	176.078	±	7.219
3361.81	±	1.82	3^+	100.0			9.146	±	2.716
3366.51	±	1.82	3^+	100.0			18.256	±	8.799
3369.64	±	1.82	3^+	100.0			19.710	±	8.751
3379.80	±	1.83	2^-	100.0			4.133	±	0.393
3394.80	±	1.83	3^+	100.0			6.976	±	1.193
3396.56	±	1.83	3^+	100.0			9.795	±	3.105
3402.50	±	1.84	4^-	100.0			3.301	±	0.845
3418.18	±	1.85	3^+	100.0			15.082	±	6.350
3424.04	±	1.85	2^+	100.0			7.725	±	2.488
3435.60	±	1.86	3^+	100.0			44.117	±	16.500
3435.62	±	1.86	3^+	100.0			37.547	±	19.900

Energy (eV)			J^π	Radiation width Γ_γ (meV)			Neutron width $g\Gamma_n$ (meV)		
3447.95	±	1.86	3^+	100.0			28.464	±	1.651
3452.75	±	1.86	2^+	100.0			7.284	±	1.202
3472.01	±	1.87	3^+	94.5	±	5.0	99.161	±	3.570
3483.98	±	1.88	3^+	100.0			37.517	±	1.613
3496.50	±	1.89	1^-	100.0			6.715	±	3.055
3500.46	±	1.89	2^+	100.0			48.050	±	3.123
3506.10	±	1.89	3^-	100.0			2.680	±	0.670
3525.43	±	1.90	2^+	125.7	±	18.0	89.674	±	9.505
3536.10	±	1.91	4^-	100.0			3.514	±	0.541
3548.10	±	1.92	2^-	100.0			2.348	±	1.603
3561.20	±	1.92	3^-	100.0			63.749	±	4.972
3569.48	±	1.93	3^+	100.0			17.649	±	7.730
3572.68	±	1.93	2^+	100.0			69.006	±	5.934
3580.04	±	1.93	2^+	100.0			6.244	±	0.955
3597.50	±	1.94	4^-	100.0			12.547	±	3.739
3598.50	±	1.94	3^+	100.0			16.889	±	6.452
3612.54	±	1.95	2^+	100.0			15.267	±	3.267
3616.69	±	1.95	3^+	100.0			49.113	±	7.563
3637.13	±	1.96	3^+	100.0			57.819	±	8.384
3648.30	±	1.97	1^-	100.0			4.667	±	0.681
3662.85	±	1.98	2^+	111.4	±	3.9	216.392	±	7.141
3682.64	±	1.99	2^+	156.6	±	5.5	70.839	±	3.896
3693.96	±	1.99	3^+	100.0			11.832	±	0.710
3704.86	±	2.00	3^+	100.0			81.954	±	3.524
3716.78	±	2.01	3^+	100.0			38.123	±	1.868
3734.87	±	2.02	3^+	100.0			10.685	±	0.930
3747.87	±	2.02	3^+	100.0			7.240	±	2.722
3758.59	±	2.03	2^+	121.9	±	6.2	52.519	±	2.258
3767.04	±	2.03	3^+	100.0			11.837	±	0.722
3789.18	±	2.05	3^+	100.0			8.787	±	2.355
3793.39	±	2.05	2^+	100.0			16.994	±	2.379
3811.13	±	2.06	3^+	100.0			8.750	±	0.884
3817.10	±	2.06	3^-	100.0			137.991	±	9.383
3825.55	±	2.07	2^+	100.0			21.693	±	1.735
3849.50	±	2.08	2^-	89.5	±	8.1	89.357	±	3.306
3862.71	±	2.09	3^+	79.6	±	4.0	158.827	±	6.353
3868.50	±	2.09	3^+	100.0			92.499	±	4.070
3873.71	±	2.09	4^-	100.0			8.152	±	2.071
3894.60	±	2.10	3^+	102.6	±	6.3	89.712	±	3.319
3916.75	±	2.12	3^+	92.0	±	3.9	257.644	±	14.686
3928.77	±	2.12	3^+	100.0			61.349	±	2.761
3941.70	±	2.13	3^-	100.0			5.590	±	0.531
3953.07	±	2.13	3^+	100.0			185.781	±	6.874

Energy (eV)			J^π	Radiation width Γ_γ (meV)			Neutron width $g\Gamma_n$ (meV)		
3967.50	±	2.14	2^-	100.0			2.769	±	0.438
3976.25	±	2.15	2^+	100.0			11.678	±	1.051
3984.00	±	2.15	4^-	100.0			3.615	±	0.358
4008.38	±	2.24	2^+	95.3	±	2.0	451.286	±	23.016
4021.93	±	2.25	2^+	100.0			16.995	±	1.309
4033.70	±	2.26	3^+	132.6	±	10.7	76.937	±	3.231
4045.05	±	2.27	3^+	100.0			33.276	±	7.154
4048.86	±	2.27	3^+	100.0			146.122	±	9.644
4054.50	±	2.27	1^-	83.3	±	5.8	309.050	±	12.980
4074.40	±	2.28	2^+	100.0			50.289	±	2.866
4083.10	±	2.29	3^-	100.0			4.367	±	0.747
4090.16	±	2.29	2^+	100.0			10.483	±	1.520
4113.44	±	2.30	3^+	114.9	±	4.3	243.903	±	8.781
4132.87	±	2.31	3^+	100.0			13.789	±	0.965
4154.08	±	2.33	3^+	100.0			120.043	±	5.162
4154.39	±	2.33	3^+	100.0			11.896	±	2.320
4165.08	±	2.33	2^+	100.0			65.965	±	3.298
4183.78	±	2.34	3^+	100.0			7.497	±	1.215
4191.46	±	2.35	4^-	100.0			13.181	±	1.621
4197.65	±	2.35	2^+	100.0			33.540	±	2.616
4218.29	±	2.36	3^+	100.0			15.387	±	1.554
4242.60	±	2.38	3^+	100.0			83.376	±	3.585
4252.83	±	2.38	2^+	100.0			16.146	±	3.536
4255.13	±	2.38	3^+	122.3	±	4.3	650.878	±	24.733
4277.33	±	2.40	3^+	100.0			13.588	±	0.883
4294.90	±	2.41	2^-	100.0			4.932	±	0.651
4304.59	±	2.41	3^+	100.0			58.170	±	2.850
4317.10	±	2.42	3^-	100.0			52.897	±	2.592
4331.50	±	2.43	4^-	100.0			5.835	±	0.519
4333.16	±	2.43	3^+	100.0			39.552	±	3.876
4338.30	±	2.43	1^-	100.0			183.150	±	8.425
4342.78	±	2.43	2^+	100.0			12.563	±	1.432
4364.30	±	2.44	2^-	100.0			5.970	±	1.994
4372.90	±	2.45	3^-	100.0			43.683	±	3.626
4378.73	±	2.45	3^+	100.0			35.336	±	3.039
4400.76	±	2.46	3^+	100.0			94.983	±	3.419
4412.40	±	2.47	4^-	100.0			6.615	±	1.402
4418.10	±	2.47	3^+	100.0			10.114	±	3.378
4430.60	±	2.48	3^+	100.0			58.528	±	10.184
4441.08	±	2.49	2^+	100.0			79.323	±	24.907
4445.63	±	2.49	3^+	90.5	±	10.0	657.938	±	33.555
4450.00	±	2.49	3^-	100.0			6.249	±	0.725
4453.90	±	2.49	4^-	100.0			99.997	±	3.400

Energy (eV)			J^π	Radiation width Γ_γ (meV)			Neutron width $g\Gamma_n$ (meV)		
4457.01	±	2.50	2^+	100.0			12.501	±	1.938
4463.13	±	2.50	2^+	100.0			29.044	±	3.950
4473.13	±	2.50	2^+	100.0			14.876	±	2.737
4502.80	±	2.52	2^+	100.0			13.782	±	1.654
4510.38	±	2.53	2^+	100.0			12.515	±	1.502
4524.64	±	2.53	2^+	100.0			43.443	±	10.383
4528.34	±	2.54	3^+	100.0			201.851	±	17.763
4536.93	±	2.54	2^+	100.0			9.713	±	1.127
4552.42	±	2.55	3^+	100.0			15.479	±	1.641
4558.02	±	2.55	3^+	100.0			19.147	±	1.704
4569.30	±	2.56	2^+	100.0			32.994	±	2.903
4580.20	±	2.56	2^-	100.0			146.362	±	6.147
4588.53	±	2.57	3^+	100.0			50.754	±	3.807
4607.00	±	2.58	2^+	100.0			8.666	±	4.861
4611.60	±	2.58	1^-	100.0			5.330	±	2.777
4625.00	±	2.59	3^-	100.0			4.498	±	2.614
4639.60	±	2.60	2^+	100.0			19.083	±	7.271
4649.60	±	2.60	2^+	100.0			91.709	±	4.035
4657.60	±	2.61	4^-	100.0			4.082	±	2.588
4666.00	±	2.61	2^-	100.0			4.499	±	2.267
4675.51	±	2.62	3^+	100.0			9.134	±	2.402
4684.71	±	2.62	2^+	100.0			13.609	±	2.232
4695.19	±	2.63	2^+	100.0			44.119	±	3.177
4709.18	±	2.64	3^+	100.0			44.277	±	4.472
4723.18	±	2.64	2^+	100.0			16.990	±	3.381
4728.18	±	2.65	2^+	100.0			235.758	±	8.487
4746.18	±	2.66	3^+	100.0			10.446	±	5.756
4754.18	±	2.66	2^+	100.0			8.656	±	3.904
4771.14	±	2.67	2^+	100.0			128.027	±	6.145
4779.22	±	2.68	3^+	100.0			347.071	±	13.189
4786.35	±	2.68	2^+	100.0			12.886	±	1.959
4793.81	±	2.68	2^+	100.0			41.963	±	3.357
4815.55	±	2.70	3^+	124.4	±	11.4	290.914	±	11.346
4822.42	±	2.70	3^+	100.0			39.647	±	3.965
4842.40	±	2.71	3^-	100.0			4.571	±	2.729
4850.42	±	2.72	2^+	100.0			8.738	±	3.469
4859.45	±	2.72	3^+	100.0			54.630	±	3.387
4876.23	±	2.73	3^+	100.0			285.839	±	10.862
4885.23	±	2.74	2^+	100.0			20.850	±	2.127
4896.23	±	2.74	2^+	100.0			16.683	±	1.902
4911.40	±	2.75	4^-	100.0			83.400	±	5.504
4932.60	±	2.76	3^+	100.0			164.733	±	38.218
4937.60	±	2.77	2^+	100.0			8.507	±	0.315

Energy (eV)			J^π	Radiation width Γ_γ (meV)	Neutron width $g\Gamma_n$ (meV)		
4947.60	±	2.77	1^-	100.0	75.300	±	6.175
4962.58	±	2.78	2^+	100.0	26.118	±	5.067
4977.14	±	2.79	3^+	100.0	9.062	±	4.468
4996.44	±	2.80	3^+	100.0	23.061	±	4.013
5004.72	±	2.90	2^+	100.0	10.743	±	2.729
5013.22	±	2.91	3^+	100.0	29.620	±	9.212
5032.20	±	2.92	2^-	100.0	4.492	±	2.295
5039.92	±	2.92	2^+	100.0	10.326	±	4.244
5045.62	±	2.93	3^+	100.0	82.420	±	4.533
5052.62	±	2.93	2^+	100.0	12.626	±	5.151
5064.60	±	2.94	4^-	100.0	2.625	±	1.709
5075.60	±	2.94	3^-	100.0	2.708	±	1.682
5083.62	±	2.95	2^+	100.0	12.626	±	5.656
5092.00	±	2.95	2^+	100.0	92.257	±	5.904
5092.10	±	2.95	3^+	100.0	25.059	±	5.463
5106.80	±	2.96	2^+	100.0	172.514	±	19.322
5117.40	±	2.97	4^-	100.0	4.292	±	2.184
5143.60	±	2.98	3^+	100.0	46.662	±	3.780
5151.08	±	2.99	2^+	100.0	34.111	±	3.513
5173.70	±	3.00	3^+	100.0	117.342	±	4.928
5182.92	±	3.01	2^+	100.0	16.626	±	2.560
5224.00	±	3.03	2^-	100.0	247.720	±	8.422
5249.00	±	3.04	3^+	100.0	64.396	±	3.671
5272.10	±	3.06	3^+	100.0	159.043	±	7.157
5296.78	±	3.07	2^+	100.0	116.218	±	5.462
5313.30	±	3.08	3^-	100.0	165.791	±	14.921
5350.50	±	3.10	3^+	100.0	50.847	±	3.661
5366.52	±	3.11	2^+	100.0	46.212	±	3.697
5374.89	±	3.12	3^+	100.0	14.069	±	9.258
5395.09	±	3.13	2^+	100.0	148.470	±	6.384
5420.50	±	3.14	3^+	100.0	98.245	±	5.109
5429.53	±	3.15	2^+	100.0	123.218	±	6.654
5460.50	±	3.17	3^+	100.0	306.833	±	15.342
5485.80	±	3.18	3^+	100.0	252.837	±	9.861
5496.10	±	3.19	2^+	100.0	30.872	±	3.396
5543.75	±	3.22	3^+	100.0	35.500	±	3.372
5559.20	±	3.22	2^+	100.0	47.495	±	3.895
5591.70	±	3.24	1^-	100.0	121.400	±	5.584
5616.56	±	3.26	3^+	100.0	9.379	±	3.724
5625.30	±	3.26	4^-	100.0	216.750	±	8.670
5626.90	±	3.26	2^+	100.0	64.155	±	38.172
5637.40	±	3.27	3^-	100.0	113.446	±	5.672
5649.10	±	3.28	2^-	100.0	14.936	±	3.361

Energy (eV)			J^π	Radiation width Γ_γ (meV)	Neutron width $g\Gamma_n$ (meV)		
5649.28	±	3.28	3^+	100.0	1.605	±	0.653
5690.80	±	3.30	2^+	100.0	14.176	±	3.842
5716.28	±	3.32	3^+	100.0	28.920	±	3.586
5734.48	±	3.33	3^+	100.0	131.068	±	6.816
5769.20	±	3.35	2^+	100.0	285.573	±	13.422
5821.62	±	3.38	3^+	100.0	67.954	±	4.893
5837.50	±	3.39	2^+	100.0	107.559	±	5.378
5878.75	±	3.41	3^+	100.0	73.321	±	5.279
5953.20	±	3.45	2^+	100.0	18.616	±	3.761
5985.32	±	3.47	3^+	100.0	290.600	±	14.239
6001.20	±	3.66	2^+	100.0	142.161	±	7.108
6010.36	±	3.67	3^+	100.0	552.852	±	20.456
6075.68	±	3.71	3^+	100.0	58.913	±	4.713
6130.80	±	3.74	2^+	100.0	168.864	±	9.625
6138.20	±	3.74	3^+	100.0	48.496	±	6.789
6165.50	±	3.76	2^+	100.0	219.068	±	9.201
6184.54	±	3.77	3^+	100.0	287.742	±	11.797
6216.70	±	3.79	2^+	100.0	551.044	±	35.818
6222.90	±	3.80	3^+	100.0	81.598	±	17.299
6241.50	±	3.81	2^+	100.0	64.855	±	4.864
6253.21	±	3.81	3^+	100.0	446.808	±	21.000
6292.14	±	3.84	3^+	100.0	233.145	±	9.792
6327.95	±	3.86	2^+	100.0	122.343	±	6.607
6371.72	±	3.89	3^+	100.0	123.076	±	6.154
6399.80	±	3.90	2^+	100.0	139.711	±	8.103
6446.57	±	3.93	3^+	100.0	125.468	±	6.273
6493.30	±	3.96	2^+	100.0	67.255	±	4.775
6540.69	±	3.99	3^+	100.0	166.882	±	8.678
6565.10	±	4.00	4^-	100.0	8.990	±	4.585
6577.30	±	4.01	2^+	100.0	190.065	±	8.363
6632.74	±	4.05	3^+	100.0	26.721	±	4.730
6650.90	±	4.06	3^-	100.0	211.236	±	10.562
6662.98	±	4.06	3^+	100.0	89.420	±	6.170
6688.70	±	4.08	1^-	100.0	296.700	±	11.571
6710.30	±	4.09	2^+	100.0	75.256	±	6.623
6733.15	±	4.11	3^+	100.0	130.426	±	7.173
6746.00	±	4.12	2^+	100.0	82.607	±	6.030
6763.24	±	4.13	3^+	100.0	279.167	±	18.425
6770.20	±	4.13	2^+	100.0	366.479	±	21.989
6789.16	±	4.14	3^+	100.0	145.067	±	15.667
6810.30	±	4.15	2^+	100.0	184.215	±	8.842
6827.07	±	4.16	3^+	100.0	32.437	±	4.768
6864.63	±	4.19	3^+	100.0	86.503	±	7.353

Energy (eV)			J^π	Radiation width Γ_γ (meV)	Neutron width $g\Gamma_n$ (meV)		
6936.90	±	4.23	2^+	100.0	485.539	±	17.965
6951.60	±	4.24	2^-	100.0	109.659	±	8.663
6961.10	±	4.25	4^-	100.0	11.125	±	6.274
6978.84	±	4.26	3^+	100.0	10.832	±	2.231
6982.90	±	4.26	2^+	100.0	31.843	±	8.056
6991.80	±	4.26	3^-	100.0	466.273	±	21.449
7002.00	±	4.41	4^-	100.0	26.685	±	6.911
7029.10	±	4.43	2^-	100.0	5.955	±	0.911
7039.57	±	4.43	3^+	100.0	97.761	±	9.678
7051.30	±	4.44	2^+	100.0	80.056	±	8.646
7088.44	±	4.47	3^+	100.0	165.424	±	18.527
7104.90	±	4.48	2^+	100.0	42.928	±	8.500
7120.91	±	4.49	3^+	100.0	58.330	±	9.974
7147.45	±	4.50	3^+	100.0	14.839	±	7.390
7159.60	±	4.51	2^+	100.0	30.517	±	5.493
7197.00	±	4.53	3^+	100.0	39.143	±	21.568
7201.42	±	4.54	2^+	100.0	69.464	±	15.213
7214.70	±	4.55	3^-	100.0	362.632	±	14.143
7240.60	±	4.56	1^-	100.0	296.000	±	11.840
7253.71	±	4.57	3^+	100.0	358.788	±	16.504
7280.10	±	4.59	2^+	100.0	58.605	±	9.260
7296.70	±	4.60	3^+	100.0	122.260	±	25.063
7307.10	±	4.60	2^+	100.0	28.772	±	5.697
7324.70	±	4.61	4^-	100.0	93.353	±	6.908
7348.77	±	4.63	3^+	100.0	23.332	±	4.620
7378.46	±	4.65	3^+	100.0	23.332	±	4.480
7408.30	±	4.67	2^-	100.0	69.256	±	6.372
7456.50	±	4.70	2^+	100.0	101.058	±	23.142
7485.50	±	4.72	3^+	100.0	125.876	±	10.448
7531.00	±	4.74	2^+	100.0	25.697	±	9.611
7542.60	±	4.75	3^+	100.0	87.670	±	7.101
7558.50	±	4.76	2^+	100.0	156.913	±	8.944
7648.08	±	4.82	3^+	100.0	347.530	±	18.419
7659.80	±	4.83	2^+	100.0	153.362	±	10.429
7740.65	±	4.88	3^+	100.0	765.290	±	28.316
7797.30	±	4.91	2^+	100.0	125.210	±	7.888
7848.00	±	4.94	3^+	100.0	26.937	±	6.842
7887.84	±	4.97	3^+	100.0	617.131	±	24.685
7899.10	±	4.98	2^+	100.0	54.204	±	10.570
7927.20	±	4.99	3^-	100.0	32.553	±	22.494
7948.19	±	5.01	3^+	100.0	32.554	±	22.495
7971.00	±	5.02	2^+	100.0	76.306	±	6.944
7996.19	±	5.04	3^+	100.0	32.554	±	22.495

Energy (eV)			J$^{\pi}$	Radiation width Γ_{γ} (meV)	Neutron width $g\Gamma_n$ (meV)		
8033.30	±	5.22	2^+	100.0	75.256	±	9.332
8050.19	±	5.23	3^+	100.0	32.554	±	22.495
8075.90	±	5.25	4^-	100.0	304.650	±	13.709
8099.20	±	5.26	2^+	100.0	31.318	±	7.109
8124.87	±	5.28	3^+	100.0	98.228	±	10.216
8183.65	±	5.32	3^+	100.0	142.092	±	11.225
8208.20	±	5.34	2^+	100.0	504.040	±	20.162
8222.40	±	5.34	3^+	100.0	35.908	±	8.043
8269.30	±	5.38	2^+	100.0	356.279	±	30.640
8284.30	±	5.38	3^-	100.0	1600.400	±	54.414
8316.20	±	5.41	1^-	100.0	477.400	±	19.096
8329.00	±	5.41	3^+	100.0	18.386	±	7.501
8348.80	±	5.43	2^+	100.0	615.549	±	24.006
8361.16	±	5.43	3^+	100.0	37.104	±	8.608
8373.00	±	5.44	2^-	100.0	247.220	±	13.350
8405.50	±	5.46	2^+	100.0	82.057	±	8.616
8420.90	±	5.47	3^+	100.0	470.665	±	27.769
8436.20	±	5.48	4^-	100.0	206.152	±	15.668
8443.90	±	5.49	3^-	100.0	1.986	±	0.953
8445.55	±	5.49	3^+	100.0	59.030	±	11.452
8473.20	±	5.51	2^+	100.0	144.812	±	30.555
8475.33	±	5.51	3^+	100.0	559.268	±	172.814
8503.80	±	5.53	2^+	100.0	188.915	±	12.279
8515.79	±	5.54	3^+	100.0	494.988	±	21.285
8535.50	±	5.55	2^+	100.0	27.012	±	8.239
8658.54	±	5.63	3^+	100.0	62.238	±	8.838
8674.20	±	5.64	2^+	100.0	795.564	±	29.436
8701.13	±	5.66	3^+	100.0	51.575	±	8.665
8713.93	±	5.66	3^+	100.0	874.950	±	33.248
8733.50	±	5.68	2^+	100.0	194.316	±	13.213
8749.60	±	5.69	4^-	100.0	95.948	±	36.940
8766.66	±	5.70	3^+	100.0	41.671	±	9.168
8781.00	±	5.71	2^+	100.0	58.505	±	9.244
8787.80	±	5.71	3^+	100.0	257.410	±	14.158
8814.00	±	5.73	2^+	100.0	181.715	±	12.538
8854.80	±	5.76	2^-	100.0	384.081	±	17.668
8912.68	±	5.79	3^+	100.0	89.128	±	9.537
8945.50	±	5.81	2^+	100.0	322.126	±	15.462
8986.40	±	5.84	3^-	100.0	203.589	±	12.419
9015.33	±	4.24	3^+	100.0	107.969	±	10.257
9038.46	±	4.25	3^+	100.0	136.551	±	10.924
9076.40	±	4.27	1^-	100.0	445.150	±	29.825
9085.10	±	4.27	2^+	100.0	118.609	±	20.164

Energy (eV)			J$^{\pi}$	Radiation width Γ_{γ} (meV)	Neutron width $g\Gamma_n$ (meV)		
9112.16	±	4.28	3^+	100.0	222.354	±	13.119
9140.40	±	4.30	2^+	100.0	61.255	±	9.433
9162.90	±	4.31	4^-	100.0	557.497	±	22.300
9194.60	±	4.32	3^+	100.0	144.600	±	11.423
9221.70	±	4.33	2^+	100.0	63.005	±	9.703
9268.53	±	4.36	3^+	100.0	131.301	±	11.161
9307.40	±	4.37	2^-	100.0	200.316	±	19.431
9317.90	±	4.38	2^+	100.0	245.120	±	28.189
9327.52	±	4.38	3^+	100.0	495.047	±	36.633
9349.35	±	4.39	3^+	100.0	572.684	±	24.625
9404.00	±	4.42	2^+	100.0	249.170	±	76.994
9414.70	±	4.42	3^-	100.0	262.188	±	27.267
9447.06	±	4.44	3^+	100.0	85.862	±	12.364
9459.70	±	4.45	2^+	100.0	753.060	±	27.863
9499.36	±	4.46	3^+	100.0	58.330	±	15.341
9509.90	±	4.47	2^+	100.0	86.257	±	20.184
9535.60	±	4.48	4^-	100.0	67.700	±	9.275
9538.61	±	4.48	3^+	100.0	193.364	±	81.213
9564.20	±	4.50	2^+	100.0	22.972	±	10.636
9586.40	±	4.51	4^-	100.0	138.503	±	11.357
9612.01	±	4.52	3^+	100.0	57.607	±	11.809
9629.58	±	4.53	3^+	100.0	430.592	±	21.099
9656.60	±	4.54	2^+	100.0	669.554	±	27.452
9737.13	±	4.58	3^+	100.0	143.025	±	12.014
9781.60	±	4.60	2^+	100.0	274.222	±	15.356
9809.53	±	4.61	3^+	100.0	139.117	±	14.468
9835.00	±	4.62	2^+	100.0	58.805	±	10.526
9857.38	±	4.63	3^+	100.0	102.486	±	11.581
9909.90	±	4.66	2^+	100.0	320.976	±	17.012
9970.97	±	4.69	3^+	100.0	14.256	±	9.594
10035.47	±	4.72	3^+	100.0	115.435	±	12.467

Table D.2: ^{129}I resonance parameters obtained in this work. The quoted errors for the radiation widths are the statistical uncertainties given by the REFIT code. Those for the neutron widths include also the systematic errors as defined in Table 7.13. The errors for the resonance energies take into account the channel widths as well as the flight path length, the moderation distance and the time delay accuracies.

Energy (eV)	J^π	Radiation width Γ_γ (meV)	Neutron width $g\Gamma_n$ (meV)
-10.76 ± 0.07	4^+	109.3 ± 4.0	25.132 ± 2.513
41.37 ± 0.02	4^+	94.9 ± 6.6	0.069 ± 0.003
72.13 ± 0.03	3^+	90.8 ± 0.6	7.324 ± 0.249
76.15 ± 0.03	4^+	106.0	0.058 ± 0.003
96.36 ± 0.09	4^+	104.9 ± 2.9	0.756 ± 0.026
115.19 ± 0.11	2^-	106.0	0.028 ± 0.002
128.32 ± 0.12	3^+	97.9 ± 1.3	3.832 ± 0.130
140.63 ± 0.13	3^-	106.0	0.055 ± 0.029
146.40 ± 0.14	3^+	108.5 ± 0.9	23.109 ± 0.786
152.57 ± 0.14	3^+	105.4 ± 0.8	12.123 ± 0.424
164.96 ± 0.16	4^-	106.0	0.049 ± 0.004
198.75 ± 0.19	4^+	140.0 ± 4.3	2.037 ± 0.073
202.67 ± 0.15	3^-	106.0	0.026 ± 0.004
259.16 ± 0.19	4^+	106.0	0.884 ± 0.032
265.38 ± 0.20	3^-	106.0	0.234 ± 0.032
284.17 ± 0.21	3^+	107.4 ± 2.4	7.389 ± 0.251
290.65 ± 0.22	3^+	109.8 ± 2.2	8.951 ± 0.304
295.60 ± 0.22	3^+	106.0	1.568 ± 0.055
314.05 ± 0.27	4^-	106.0	0.205 ± 0.020
315.97 ± 0.27	3^-	106.0	0.266 ± 0.020
348.88 ± 0.30	2^-	106.0	0.142 ± 0.011
353.85 ± 0.30	4^+	106.0	0.547 ± 0.051
356.23 ± 0.30	3^+	106.0	0.824 ± 0.037
360.70 ± 0.31	4^-	106.0	0.153 ± 0.024
364.89 ± 0.31	4^+	106.0	1.649 ± 0.221
410.04 ± 0.39	3^+	114.4 ± 1.4	33.565 ± 1.141
423.23 ± 0.40	3^+	123.6 ± 1.2	57.925 ± 1.969
454.28 ± 0.43	3^+	109.6 ± 1.5	28.232 ± 0.960
469.24 ± 0.44	3^+	107.4 ± 1.1	67.331 ± 2.289
489.31 ± 0.46	3^+	127.0 ± 1.8	32.528 ± 1.106
492.73 ± 0.46	3^-	106.0	0.383 ± 0.027
511.64 ± 0.53	3^-	106.0	0.249 ± 0.026
524.45 ± 0.54	2^-	106.0	0.399 ± 0.144
547.98 ± 0.56	3^+	101.1 ± 9.1	31.706 ± 1.078
554.71 ± 0.57	3^+	106.0	0.830 ± 0.091
562.09 ± 0.58	3^-	106.0	0.158 ± 0.027
576.79 ± 0.59	4^-	106.0	0.279 ± 0.045
578.53 ± 0.60	3^-	106.0	0.384 ± 0.036
595.58 ± 0.61	4^+	106.0	6.249 ± 0.219
654.54 ± 0.73	4^+	106.0	1.977 ± 0.087
689.63 ± 0.77	4^-	106.0	0.557 ± 0.056

Energy (eV)			J^π	Radiation width Γ_γ (meV)			Neutron width $g\Gamma_n$ (meV)		
693.26	±	0.77	4^+	110.2	±	1.2	111.600	±	3.794
719.66	±	0.86	4^+	106.0			21.673	±	0.759
725.35	±	0.86	3^-	106.0			0.220	±	0.028
730.17	±	0.87	2^-	106.0			0.175	±	0.068
761.56	±	0.91	4^+	106.0			5.560	±	0.211
797.09	±	0.95	3^+	104.1	±	1.2	90.256	±	3.069
803.65	±	0.43	3^+	122.6	±	2.1	55.737	±	1.895
842.43	±	0.45	3^-	106.0			0.322	±	0.032
845.69	±	0.46	3^-	106.0			0.146	±	0.029
855.25	±	0.46	3^+	106.3	±	1.7	58.319	±	1.983
866.93	±	0.47	4^-	106.0			0.566	±	0.057
879.28	±	0.47	2^-	106.0			0.482	±	0.036
888.46	±	0.48	3^+	106.0			6.055	±	0.224
897.42	±	0.48	3^-	106.0			0.178	±	0.029
915.31	±	0.50	3^+	96.7	±	1.3	116.550	±	3.963
926.06	±	0.51	3^+	106.0			3.658	±	0.172
969.36	±	0.53	4^-	106.0			0.789	±	0.060
991.31	±	0.55	3^-	106.0			0.542	±	0.052
1002.75	±	0.56	3^+	132.9	±	1.6	169.619	±	5.767
1020.90	±	0.57	3^-	106.0			0.708	±	0.046
1038.89	±	0.58	3^+	127.7	±	4.1	36.194	±	1.231
1043.62	±	0.58	4^+	102.4	±	2.8	44.871	±	1.526
1052.00	±	0.59	2^-	106.0			0.242	±	0.029
1098.94	±	0.62	3^-	106.0			0.614	±	0.090
1123.56	±	0.63	3^+	106.0			2.390	±	0.122
1150.90	±	0.64	4^-	106.0			0.519	±	0.156
1154.00	±	0.65	3^-	106.0			0.721	±	0.094
1158.28	±	0.65	4^+	106.0			4.157	±	0.233
1166.70	±	0.65	3^-	106.0			0.681	±	0.062
1185.20	±	0.66	2^-	106.0			0.900	±	0.355
1187.96	±	0.67	3^+	109.0	±	3.6	41.716	±	1.418
1190.71	±	0.67	3^+	85.1	±	3.9	24.220	±	0.872
1203.83	±	0.67	3^+	106.0			4.743	±	0.417
1206.75	±	0.68	3^+	106.0			13.632	±	0.491
1239.00	±	0.69	4^-	106.0			1.782	±	0.159
1242.92	±	0.70	4^+	96.4	±	3.4	36.270	±	1.269
1255.33	±	0.70	3^-	106.0			0.682	±	0.069
1271.13	±	0.71	3^+	111.9	±	5.0	21.687	±	0.759
1281.59	±	0.72	3^+	106.0			4.269	±	0.478
1302.10	±	0.73	4^-	106.0			0.252	±	0.084
1332.84	±	0.75	3^-	106.0			1.445	±	0.085
1340.67	±	0.75	3^+	95.4	±	2.1	61.294	±	2.145
1349.97	±	0.76	3^+	106.0			16.524	±	0.595
1399.00	±	0.78	2^-	106.0			0.229	±	0.040
1414.69	±	0.79	3^-	106.0			1.747	±	0.114

Energy (eV)			J^π	Radiation width Γ_γ (meV)			Neutron width $g\Gamma_n$ (meV)		
1422.47	±	0.80	4^+	106.0			14.912	±	0.582
1428.33	±	0.80	3^-	106.0			2.242	±	0.114
1433.90	±	0.80	4^-	106.0			1.155	±	0.092
1453.64	±	0.81	4^+	114.0	±	2.1	101.812	±	3.462
1475.45	±	0.83	3^+	70.7	±	2.5	24.041	±	0.914
1481.80	±	0.83	3^-	106.0			0.728	±	0.088
1499.40	±	0.84	2^-	106.0			0.570	±	0.055
1506.94	±	0.84	4^+	106.0			14.501	±	0.580
1510.38	±	0.85	3^+	106.0			36.089	±	1.299
1538.40	±	0.86	4^+	106.0			9.703	±	0.378
1547.60	±	0.87	4^-	106.0			1.298	±	0.201
1592.72	±	0.89	3^+	106.0			6.790	±	0.387
1595.87	±	0.89	3^+	101.0	±	2.6	79.450	±	2.860
1606.47	±	0.90	3^+	129.5	±	2.5	117.556	±	4.114
1634.70	±	0.92	3^-	106.0			0.777	±	0.112
1657.00	±	0.93	4^+	106.0			7.341	±	0.411
1661.61	±	0.93	3^+	89.1	±	2.1	126.044	±	4.538
1677.69	±	0.94	3^+	106.0			21.122	±	1.056
1683.05	±	0.94	4^+	99.7	±	2.4	272.700	±	10.090
1700.43	±	0.95	3^-	106.0			0.776	±	0.105
1704.91	±	0.95	3^-	106.0			2.078	±	0.160
1711.69	±	0.96	4^-	106.0			2.211	±	0.159
1726.25	±	0.97	2^-	106.0			2.393	±	0.194
1739.75	±	0.97	3^+	102.1	±	2.1	105.000	±	3.675
1746.63	±	0.98	3^+	138.2	±	3.2	146.037	±	5.111
1753.30	±	0.98	4^-	106.0			1.378	±	0.158
1782.11	±	1.00	3^+	103.8	±	1.6	325.762	±	11.402
1814.24	±	1.02	3^-	106.0			2.788	±	0.332
1818.84	±	1.02	3^+	121.3	±	3.6	85.750	±	3.001
1830.57	±	1.03	3^+	106.6	±	7.0	24.566	±	0.983
1851.44	±	1.04	3^-	106.0			1.986	±	0.145
1868.45	±	1.05	3^+	122.3	±	2.1	371.350	±	12.997
1877.04	±	1.05	3^+	126.0	±	3.0	106.706	±	3.735
1906.63	±	1.07	3^+	106.0			28.459	±	1.138
1918.03	±	1.07	4^+	106.0			7.954	±	0.636
1932.51	±	1.08	3^+	106.0			15.168	±	0.607
1945.40	±	1.09	4^+	106.0			8.601	±	0.525
1957.26	±	1.10	3^+	106.0			7.004	±	0.904
1975.55	±	1.11	2^-	106.0			5.503	±	0.330
1987.64	±	1.11	3^+	120.6	±	3.7	82.688	±	2.894
2021.20	±	1.31	3^-	106.0			5.473	±	0.296
2038.07	±	1.32	4^-	106.0			1.795	±	0.165
2057.82	±	1.34	4^+	106.0			5.426	±	1.112

Energy (eV)			J^π	Radiation width Γ_γ (meV)			Neutron width $g\Gamma_n$ (meV)		
2069.91	±	1.35	3^-	106.0			2.411	±	0.195
2080.02	±	1.35	3^+	89.5	±	4.2	40.092	±	1.884
2117.34	±	1.38	2^-	106.0			2.355	±	0.205
2148.01	±	1.40	4^-	106.0			5.594	±	0.364
2173.22	±	1.41	3^-	106.0			5.049	±	0.298
2188.64	±	1.42	4^+	71.2	±	7.1	24.311	±	1.143
2211.26	±	1.44	3^+	106.0			25.480	±	1.529
2218.99	±	1.44	3^-	106.0			3.316	±	0.259
2256.40	±	1.47	4^+	106.0			9.427	±	0.698
2278.73	±	1.48	3^+	116.9	±	4.2	101.850	±	4.176
2304.60	±	1.50	3^-	106.0			0.698	±	0.157
2324.70	±	1.51	4^-	106.0			4.973	±	1.417
2327.14	±	1.51	4^+	106.0			19.710	±	3.134
2339.64	±	1.52	3^+	106.0			20.772	±	1.309
2363.10	±	1.54	3^-	106.0			2.337	±	0.561
2366.83	±	1.54	4^+	106.0			38.436	±	4.420
2378.30	±	1.55	2^-	106.0			1.293	±	0.727
2381.03	±	1.55	3^+	106.0			32.708	±	1.864
2417.08	±	1.57	4^+	106.0			55.232	±	2.265
2432.49	±	1.58	3^+	106.0			96.338	±	3.661
2458.20	±	1.60	4^-	106.0			5.060	±	0.450
2486.62	±	1.62	3^-	106.0			1.261	±	0.444
2496.79	±	1.62	4^+	106.0			15.036	±	1.654
2511.95	±	1.63	3^+	106.0			10.942	±	0.777
2540.82	±	1.65	3^+	127.0	±	3.4	324.975	±	11.374
2547.15	±	1.66	3^+	106.0			7.219	±	0.736
2562.66	±	1.67	4^+	106.0			6.879	±	2.655
2565.41	±	1.67	3^+	79.4	±	3.5	76.037	±	3.346
2575.30	±	1.67	3^-	106.0			2.230	±	0.234
2587.20	±	1.68	2^-	106.0			1.765	±	0.145
2613.85	±	1.70	4^+	106.0			18.512	±	2.036
2616.93	±	1.70	3^+	106.0			93.188	±	6.523
2620.20	±	1.70	3^-	106.0			3.595	±	0.974
2632.12	±	1.71	4^-	106.0			2.589	±	0.280
2643.62	±	1.72	3^-	106.0			1.499	±	0.273
2650.41	±	1.72	2^-	106.0			3.272	±	0.363
2666.28	±	1.73	4^+	106.0			14.569	±	1.734
2676.51	±	1.74	3^+	106.0			9.988	±	0.709
2699.66	±	1.75	4^+	106.0			7.521	±	1.324
2706.60	±	1.76	4^-	106.0			2.554	±	0.409
2711.36	±	1.76	3^-	106.0			2.486	±	0.428
2718.30	±	1.77	3^-	106.0			1.406	±	0.221
2727.40	±	1.77	4^+	106.0			8.753	±	1.138

Energy (eV)			J^π	Radiation width Γ_γ (meV)			Neutron width $g\Gamma_n$ (meV)		
2737.70	±	1.78	3^+	136.3	±	3.7	340.900	±	12.272
2780.59	±	1.81	4^+	106.0			34.881	±	1.605
2790.65	±	1.81	3^+	106.0			84.000	±	5.124
2798.76	±	1.82	4^+	106.0			8.539	±	1.213
2802.79	±	1.82	3^+	106.0			31.789	±	2.829
2815.21	±	1.83	3^-	106.0			4.319	±	0.410
2841.14	±	1.85	4^-	106.0			4.151	±	0.369
2866.39	±	1.86	2^-	106.0			5.200	±	0.562
2873.32	±	1.87	3^-	120.4	±	10.0	7.223	±	0.592
2881.80	±	1.87	4^-	106.0			3.870	±	1.525
2884.94	±	1.88	4^+	106.0			11.582	±	2.050
2895.77	±	1.88	3^+	92.7	±	2.8	398.606	±	14.350
2909.50	±	1.89	4^+	110.2	±	3.1	257.400	±	9.009
2914.50	±	1.89	3^-	106.0			3.927	±	1.017
2949.16	±	1.92	3^+	106.0			13.383	±	1.004
2971.23	±	1.93	4^+	106.0			10.946	±	0.854
2983.20	±	1.94	3^-	106.0			1.061	±	0.477
2989.55	±	1.94	4^+	121.1	±	4.7	129.938	±	5.197
2993.50	±	1.95	2^-	106.0			4.475	±	1.114
3003.81	±	1.62	4^+	106.0			11.987	±	0.863
3009.80	±	1.63	3^-	106.0			1.457	±	0.351
3080.60	±	1.66	4^-	106.0			3.161	±	0.512
3112.14	±	1.68	3^+	106.0			24.014	±	1.513
3122.36	±	1.69	3^+	91.5	±	3.0	469.438	±	18.308
3125.30	±	1.69	3^+	106.0			10.474	±	3.865
3158.18	±	1.71	3^+	96.1	±	3.0	210.131	±	7.775
3162.00	±	1.71	3^-	106.0			3.853	±	1.306
3172.19	±	1.71	3^+	106.0			43.575	±	3.181
3189.35	±	1.72	4^+	106.0			18.579	±	1.152
3282.68	±	1.77	4^+	110.3	±	3.4	196.312	±	7.264
3291.60	±	1.78	4^-	106.0			3.694	±	0.587
3311.94	±	1.79	3^-	106.0			8.960	±	1.021
3320.14	±	1.79	3^+	113.2	±	4.2	445.375	±	19.151
3324.39	±	1.80	3^+	106.0			126.700	±	13.810
3328.22	±	1.80	4^+	106.0			16.802	±	4.419
3358.95	±	1.81	4^+	106.0			9.951	±	4.438
3374.88	±	1.82	2^-	106.0			3.663	±	1.194
3398.57	±	1.84	4^+	106.0			29.036	±	9.582
3441.64	±	1.86	3^+	106.0			11.344	±	4.322
3446.05	±	1.86	4^+	106.0			13.444	±	5.216
3451.61	±	1.86	3^-	106.0			3.362	±	1.029
3474.67	±	1.88	3^-	106.0			9.166	±	4.977

Energy (eV)			J^π	Radiation width Γ_γ (meV)	Neutron width $g\Gamma_n$ (meV)		
3477.94	±	1.88	4^-	106.0	4.934	±	3.987
3510.84	±	1.90	3^+	106.0	97.825	±	58.499
3528.42	±	1.91	2^-	106.0	9.191	±	0.901
3549.68	±	1.92	3^-	106.0	4.239	±	0.471
3567.57	±	1.93	3^+	106.0	112.875	±	58.582
3568.36	±	1.93	3^+	106.0	220.675	±	174.554
3572.22	±	1.93	4^-	106.0	13.899	±	4.587
3599.97	±	1.94	3^-	106.0	5.701	±	0.656
3618.28	±	1.95	4^+	106.0	74.812	±	29.326
3622.30	±	1.96	3^+	106.0	29.540	±	8.448
3629.77	±	1.96	4^+	106.0	27.523	±	3.550
3635.92	±	1.96	3^+	106.0	235.550	±	53.234
3639.36	±	1.97	4^+	106.0	9.079	±	2.052
3652.15	±	1.97	3^+	106.0	7.166	±	1.792
3657.18	±	1.97	4^+	106.0	154.744	±	35.127
3662.13	±	1.98	2^-	106.0	4.738	±	1.644
3675.68	±	1.98	3^+	106.0	13.930	±	1.087
3689.08	±	1.99	3^-	106.0	5.447	±	0.801
3695.67	±	2.00	4^-	106.0	3.598	±	0.712
3756.72	±	2.03	4^+	106.0	10.862	±	1.662
3762.03	±	2.03	3^+	106.0	317.975	±	27.028
3766.74	±	2.03	4^+	106.0	2.507	±	0.935
3805.61	±	2.06	3^+	106.0	47.206	±	6.939
3812.54	±	2.06	4^+	106.0	50.541	±	6.671
3819.14	±	2.06	3^-	106.0	7.976	±	1.643
3833.79	±	2.07	3^+	106.0	17.522	±	2.050
3841.43	±	2.07	3^-	106.0	4.865	±	0.774
3864.49	±	2.09	4^+	106.0	27.051	±	3.219
3871.30	±	2.09	2^-	106.0	5.153	±	1.257
3882.05	±	2.10	3^-	106.0	4.074	±	0.676
3891.00	±	2.10	4^+	106.0	13.523	±	2.123
3896.99	±	2.10	3^+	106.0	14.109	±	2.286
3913.67	±	2.11	4^-	106.0	7.824	±	0.837
3933.69	±	2.12	4^+	106.0	12.639	±	1.858
3941.08	±	2.13	3^+	106.0	25.174	±	6.948
3946.86	±	2.13	4^+	106.0	31.978	±	5.212
3959.83	±	2.14	3^+	106.0	47.294	±	11.871
3964.98	±	2.14	4^+	106.0	15.469	±	3.310
3977.79	±	2.15	3^+	106.0	20.283	±	2.718
3984.16	±	2.15	3^-	106.0	9.691	±	2.016
3990.71	±	2.15	3^+	106.0	257.163	±	10.801
3995.09	±	2.16	2^-	106.0	11.006	±	2.961
4040.55	±	2.26	3^+	106.0	104.650	±	17.163

Energy (eV)			J^π	Radiation width Γ_γ (meV)	Neutron width $g\Gamma_n$ (meV)		
4047.48	±	2.27	4^+	106.0	15.469	±	1.980
4068.87	±	2.28	4^-	106.0	5.316	±	0.617
4104.61	±	2.30	3^-	106.0	1.418	±	0.529
4119.63	±	2.31	3^+	106.0	30.196	±	4.469
4127.18	±	2.31	3^+	106.0	158.375	±	7.444
4131.39	±	2.31	4^-	106.0	11.250	±	0.979
4144.80	±	2.32	3^+	106.0	30.376	±	2.460
4167.34	±	2.33	4^+	106.0	38.228	±	5.046
4175.72	±	2.34	3^+	106.0	14.223	±	1.394
4194.06	±	2.35	2^-	106.0	3.719	±	0.721
4221.89	±	2.36	3^+	106.0	51.406	±	4.421
4231.92	±	2.37	3^-	106.0	12.057	±	2.134
4238.20	±	2.37	4^+	106.0	395.100	±	15.409
4246.01	±	2.38	4^+	106.0	12.634	±	1.668
4273.80	±	2.39	4^-	106.0	8.257	±	0.991
4281.31	±	2.40	3^-	106.0	3.062	±	0.796
4300.65	±	2.41	3^+	106.0	17.242	±	2.466
4310.62	±	2.41	4^+	106.0	76.275	±	4.653
4343.77	±	2.43	3^+	106.0	56.831	±	7.843
4371.84	±	2.45	4^-	106.0	8.786	±	0.975
4390.29	±	2.46	4^+	106.0	15.424	±	2.329
4394.40	±	2.46	3^+	106.0	380.669	±	81.844
4424.75	±	2.48	4^+	106.0	16.009	±	1.345
4438.04	±	2.49	3^-	106.0	12.132	±	2.596
4444.41	±	2.49	3^+	106.0	162.706	±	23.430
4453.17	±	2.49	2^-	106.0	4.997	±	2.274
4455.68	±	2.50	3^+	106.0	425.294	±	17.862
4472.56	±	2.50	3^-	106.0	4.817	±	2.596
4478.25	±	2.51	3^-	106.0	9.205	±	2.688
4486.57	±	2.51	4^-	106.0	7.673	±	1.442
4494.57	±	2.52	2^-	106.0	11.959	±	2.356
4502.20	±	2.52	3^-	106.0	14.153	±	2.066
4511.41	±	2.53	3^-	106.0	6.269	±	1.016
4532.76	±	2.54	4^+	106.0	15.328	±	2.269
4540.90	±	2.54	4^-	106.0	9.146	±	1.198
4578.30	±	2.56	3^-	106.0	7.626	±	1.121
4607.26	±	2.58	2^-	106.0	6.369	±	1.484
4616.29	±	2.59	3^+	106.0	32.931	±	4.676
4624.08	±	2.59	4^+	106.0	22.314	±	3.392
4632.20	±	2.59	4^-	106.0	8.544	±	1.444
4658.43	±	2.61	3^-	106.0	4.511	±	0.744
4672.70	±	2.62	3^-	106.0	6.672	±	1.401
4680.15	±	2.62	4^-	106.0	6.165	±	1.239

Energy (eV)			J^π	Radiation width Γ_γ (meV)	Neutron width $g\Gamma_n$ (meV)		
4736.32	±	2.65	3^+	106.0	15.439	±	1.667
4748.12	±	2.66	3^+	106.0	452.375	±	17.643
4758.01	±	2.66	3^+	106.0	55.562	±	10.446
4763.13	±	2.67	3^-	106.0	12.967	±	3.903
4778.14	±	2.68	4^+	106.0	25.110	±	2.712
4787.13	±	2.68	2^-	106.0	9.672	±	1.664
4801.07	±	2.69	3^+	106.0	58.888	±	4.829
4806.55	±	2.69	3^-	106.0	10.014	±	2.574
4823.35	±	2.70	4^+	106.0	556.369	±	22.255
4829.35	±	2.70	3^-	106.0	18.939	±	3.125
4842.33	±	2.71	3^+	106.0	658.000	±	24.346
4851.20	±	2.72	4^+	106.0	22.433	±	2.176
4882.18	±	2.73	4^-	106.0	13.472	±	2.681
4887.96	±	2.74	3^+	106.0	237.694	±	10.934
4894.58	±	2.74	2^-	106.0	8.753	±	2.223
4925.58	±	2.76	3^-	106.0	14.468	±	1.505
4961.45	±	2.78	3^+	106.0	25.288	±	2.706
4967.29	±	2.78	4^+	106.0	174.262	±	23.700
4971.99	±	2.78	5^-	106.0	133.444	±	17.081
4978.80	±	2.79	3^-	106.0	13.685	±	2.723
5003.19	±	2.90	4^+	106.0	17.094	±	1.556
5017.03	±	2.91	3^+	106.0	23.100	±	2.310
5031.16	±	2.92	3^-	106.0	13.571	±	1.601
5042.00	±	2.92	4^-	106.0	14.597	±	1.649
5058.22	±	2.93	4^+	106.0	17.381	±	2.034
5067.65	±	2.94	3^+	106.0	21.809	±	2.595
5144.68	±	2.98	4^+	106.0	121.444	±	8.258
5172.14	±	3.00	3^+	106.0	176.750	±	9.368
5204.90	±	3.02	4^+	106.0	340.931	±	18.069
5215.16	±	3.02	3^+	106.0	54.906	±	8.895
5271.75	±	3.06	4^+	106.0	169.369	±	11.856
5296.05	±	3.07	4^+	106.0	41.693	±	4.419
5312.38	±	3.08	3^+	106.0	47.381	±	4.359
5346.65	±	3.10	4^+	106.0	98.944	±	8.509
5545.52	±	3.22	3^+	106.0	444.500	±	17.780
5611.03	±	3.25	4^+	106.0	264.656	±	12.439
5646.55	±	3.27	3^+	106.0	273.962	±	12.876
5720.82	±	3.32	4^+	106.0	404.100	±	16.972
5804.49	±	3.37	3^+	106.0	149.100	±	10.139
5858.72	±	3.40	4^+	106.0	545.962	±	22.384
6018.60	±	3.67	3^+	106.0	111.956	±	19.704
6157.93	±	3.76	4^+	106.0	361.125	±	21.306
6309.11	±	3.85	3^+	106.0	606.375	±	24.255

Energy (eV)			J^π	Radiation width Γ_γ (meV)	Neutron width $g\Gamma_n$ (meV)		
6338.46	±	3.87	4^+	106.0	605.250	±	24.210
6396.67	±	3.90	3^+	106.0	918.750	±	37.669
6477.53	±	3.95	4^+	106.0	199.688	±	12.181
6524.18	±	3.98	3^+	106.0	158.769	±	13.972
6602.10	±	4.03	4^+	106.0	195.525	±	14.469
6660.55	±	4.06	3^+	106.0	226.100	±	13.792
6769.13	±	4.13	4^+	106.0	324.169	±	41.494
6896.43	±	4.21	3^+	106.0	249.769	±	23.728
6996.67	±	4.27	4^+	106.0	179.100	±	14.507
7018.20	±	4.42	3^+	106.0	141.706	±	15.021
7129.49	±	4.49	4^+	106.0	116.100	±	9.985
7147.61	±	4.50	3^+	106.0	134.619	±	12.654
7264.73	±	4.58	4^+	106.0	418.781	±	20.520
7328.18	±	4.62	4^+	106.0	140.400	±	14.882
7333.73	±	4.62	3^+	106.0	122.150	±	13.437
7378.96	±	4.65	4^+	106.0	154.181	±	11.564
7393.47	±	4.66	3^+	106.0	385.438	±	20.428
7432.44	±	4.68	4^+	106.0	385.144	±	18.872
7505.03	±	4.73	3^+	106.0	221.331	±	23.240
7520.71	±	4.74	4^+	106.0	71.269	±	7.626
7532.57	±	4.75	3^+	106.0	672.000	±	32.256
7549.25	±	4.76	4^+	106.0	52.830	±	7.502
7665.31	±	4.83	3^+	106.0	434.919	±	22.616
7871.01	±	4.96	4^+	106.0	296.212	±	19.254
7992.70	±	5.04	3^+	106.0	339.150	±	31.202
8063.29	±	5.24	4^+	106.0	165.488	±	18.369
8107.01	±	5.27	3^+	106.0	259.306	±	18.929
8176.88	±	5.31	4^+	106.0	176.400	±	14.818
8202.88	±	5.33	3^+	106.0	156.406	±	14.546
8309.38	±	5.40	4^+	106.0	247.669	±	29.225
8344.09	±	5.42	3^+	106.0	185.806	±	33.074
8366.46	±	5.44	4^+	106.0	204.131	±	23.475
8532.22	±	5.55	4^+	106.0	904.500	±	38.894
8562.89	±	5.57	3^+	106.0	420.831	±	31.562
8613.24	±	5.60	4^+	106.0	658.688	±	39.521
8630.18	±	5.61	3^+	106.0	124.250	±	11.307
8720.51	±	5.67	4^+	106.0	257.681	±	20.099
8750.38	±	5.69	3^+	106.0	369.994	±	39.589
8761.71	±	5.70	4^+	106.0	251.887	±	26.700
8820.20	±	5.73	3^+	106.0	206.762	±	16.541
8858.72	±	5.76	4^+	106.0	151.312	±	15.737
9018.34	±	4.24	3^+	106.0	141.006	±	13.960
9076.95	±	4.27	4^+	106.0	293.119	±	20.811

Energy (eV)			J^{π}	Radiation width Γ_{γ} (meV)	Neutron width $g\Gamma_n$ (meV)		
9106.40	±	4.28	3^+	106.0	157.588	±	21.905
9190.17	±	4.32	4^+	106.0	735.188	±	39.700
9294.21	±	4.37	3^+	106.0	293.169	±	37.232
9304.35	±	4.37	4^+	106.0	193.050	±	27.992
9345.83	±	4.39	3^+	106.0	191.188	±	18.928
9398.01	±	4.42	4^+	106.0	227.700	±	26.413
9586.98	±	4.51	3^+	106.0	196.262	±	17.271
9642.79	±	4.53	4^+	106.0	239.231	±	24.641
9755.01	±	4.58	3^+	106.0	570.500	±	33.089
9781.37	±	4.60	4^+	106.0	205.594	±	34.745
9801.06	±	4.61	3^+	106.0	162.706	±	16.596
9872.34	±	4.64	4^+	106.0	257.794	±	23.459
10020.64	±	4.71	4^+	106.0	189.281	±	21.200

Bibliography

[1] *Les recherches pour la gestion des déchets nucléaires, les résultats d'aujourd'hui, les solutions de demain*, Clefs du CEA, N^o 46 (2002).

[2] X.L.Hou et al., *Level and origin of iodine-129 in the Baltic sea*, Journal of Environmental Radioactivity 61(2002)331.

[3] C.Gaillard, *Etude de la migration thermique des produits de fission molybdène, technétium et iode dans les apatites*, Thèse de doctorat Université Claude Bernard, Lyon I (2000).

[4] D.W.Wootan et al., *Irradiation test of ^{99}Tc and ^{129}I transmutation in the Fast Flux Test Facility*, Transaction American Nuclear Society 64(1991)125.

[5] E.Gonzales, *Experimental measurements of ^{99}Tc and ^{129}I transmutation in TARC at CERN*, Proc. of the 5^{th} International Information Exchange Meeting, Mol, Belgium (1998).

[6] B.Ya.Galkin et al., *Prospective large-scale transmutation of fission iodine*, Radiochemistry 44(2002)174.

[7] C.De Saint Jean, *Sensibility analysis of profil irradiation experiments*, Internal Note (2000).

[8] A.N.Shmelev, V.A.Apse, G.G.Kulikov, *Some basic advantages of Accelerator-driven transmutation of minor actinides and iodine-129*, American Institute of Physics 345(1995)859.

[9] K.Nishihara, H.Takano, *Transmutation of ^{129}I using an accelerator-driven system*, Nuclear Technology 137(2000)47.

[10] R.J.M.Konings, *Transmutation of iodine: results of the EFTTRA-T1 irradiation test*, Journal of Nuclear Materials 244(1997)16.

[11] A.Gandini, *Time-dependent generalised perturbation methods for burn-up analysis*, Comitato Nationale Energia Nuclear RT/FI(75)4 (1975).

[12] R.C.Block, G.G.Slaughter, A.Harvey, *Thermal neutron cross section measurements of ^{238}U, ^{235}U, ^{240}Pu, ^{234}U and ^{129}I with the ORNL fast chopper Time-Of-Flight neutron spectrometer*, Nuclear Science and Engineering 8(1960)112.

[13] N.J.Pattenden, *Neutron cross section measurements on fission product samarium and iodine*, Nuclear Science and Engineering 17(1963)371.

[14] L.Friedmann, D.C.Aumann, *The thermal neutron cross sections and resonance integrals of ^{127}I, ^{128}I, ^{129}I*, Radiochimica Acta 33(1983)183.

[15] S.Nakamura et al., *Measurement of thermal neutron capture cross section and resonance integral of the $^{129}I(n,\gamma)^{130}I$ reaction*, Nuclear Science and Technology 33(1996)283.

[16] R.L.Macklin, *Neutron capture cross sections and resonances of iodine-127 and iodine-129*, Nuclear Science and Engineering 85(1983)350.

[17] A.M.Lane, R.G.Thomas, *R-Matrix theory of nuclear reactions*, Review of Modern Physics 17(1960)563.

[18] N.Bohr, *Neutron capture and nuclear constitution*, Nature 137(1936)344.

[19] W.Hauser, H.Feshbach, *The inelastic scattering of neutrons*, Physical Review 87(1952)366.

[20] O.Bouland, R.Babut, N.M.Larson, *Samqua - A program for generating all possible combinations of quantum numbers leading to a same compound nucleus state in the framework of the R-Matrix code SAMMY*, JEFDOC-926, ENDF-363 (2003).

[21] B.J.Allen, *Theory of slow neutron - Radiative capture*, Pergamon Press, Oxford (1984).

[22] J.E.Lynn, *The theory of neutron resonance reactions*, Clarendon Press, Oxford (1968).

[23] F.H.Frohner, *Evaluation and analysis of nuclear resonance data*, JEFF Report 18.

[24] C.W.Reich, M.S.Moore, Physical Review 111(1958)929.

[25] G.Breit, E.Wigner, *Capture of slow neutron*, Physical Review 49(1936)519.

[26] M.C.Moxon, J.B.Brisland, *GEEL REFIT, a least square fitting program for resonance analysis on neutron transmission and capture data*, Technical report Harwell laboratory, CBNM/ST/90-131/1 (1990).

[27] N.M.Larson, *RISC peripheral shielding routine collection, SAMMY-M6*, Oak Ridge National Laboratory, ORNL/TM-9179/R6 (2003).

[28] F.H.Frohner, O.Bouland, *Treatment of external levels in neutron resonance fitting: application to the non-fissile nuclide ^{52}Cr*, Nuclear Science and Engineering 137(2001)70.

[29] A.Foderaro, *The elements of neutron interaction theory*, The mit press, Massachusetts, US (1971).

[30] E.Melkonian, W.W.Havens, L.J.Rainwater, *Slow neutron velocity spectrometer studies. V, Re, Ta, Ru, Cr, Ga*, Physical Review 3(1953)702.

[31] F.G.P.Seidl et al. *"Fast Chopper" Time-of-flight measurement of neutron resonances*, Physical Review 95 (1954) 476.

[32] A.Gilbert, A.G.W.Cameron, *A composite nuclear-level density formula with shell corrections*, Canadian Journal of Physics 43(1965)1446.

[33] E.P.Wigner, International Conference on Neutron Physics by Time of Flight, Gatlinburg, Tennessee, ORNL report, ORNL-2309 (1957).

[34] T.A.Brody et al., *Random-Matrix physics: spectrum and strength*, Reviews of Modern Physics 53(1981)385.

[35] J.A.Harvey, D.J.Hughes, *Spacing of nuclear energy levels*, Physical Review 109(1958)471.

[36] J-Ch.Sublet, P.Ribon, M.Coste, *CALENDF-2002: user manual*, Rapport CEA-R-6020 (2003).

[37] M.Herman, G.Reffo, *Realistic few-quasiparticule level densities in spherical nuclei*, Physical Review C 36(1987)1546.

[38] C.E.Porter, R.G.Thomas, *Fluctuations of nuclear reaction widths*, Physical Review 104(1956)483.

[39] E.Fort, J.P.Doat, *ESTIMA: a code to calculate average parameters from sets of resolved resonance parameters*, NEANDC-161 (1983).

[40] M.Gyulassy, R.J.Howerton, S.T.Perkins, *Experimental data, indexes, and techniques of obtaining a selected set of neutron resonance parameters*, University of California UCRL-50400, vol.11 (1972).

[41] S.Y.Oh, J.Chang, L.C.Leal, *Statistical assignment of neutron orbital angular momentum to a resonance*, PHYSOR 2002, Seoul, Korea (2002).

[42] J.M.Verbaarshot, H.A.Weidenmuller, M.R.Zirnbauer, Physical Reports 129(1985)367.

[43] N.T.Koyumdjieva, N.B.Janeva, *Unresolved resonance region - Neutron cross sections presentation*, INT.Conf. Nuclear Data for Science and Technology, Bologna, Italy (1997).

[44] N.T.Koyumdjieva, N.B.Janeva, *Validation of the characteristic function model for the unresolved resonance region*, Nuclear Science and Engineering 137(2001)194.

[45] P.Moldauer, *Theory of average neutron reaction cross section in the resonance region*, Physical Review 123(1961)968.

[46] P.Moldauer, *Why the Hauser-Feshbach formula works*, Physical Review C 11(1975)426.

[47] F.H.Frohner, *Evaluation of the unresolved resonance range of* ^{238}U, Nuclear Science and Engineering 103(1989)119.

[48] P.A.Moldauer, *Statistics and the average cross section*, Nuclear Physics A344 (1980)185.

[49] G.R.Satchler, *Average compound nucleus cross sections in the continuum*, Physics letters 7(1963)55.

[50] C.Ingelbrecht, J.Lupo, K.Raptis, T.Altizouglou, G.Noguere, *Iodine-129 targets for nuclear waste transmutation studies*, Nucl. Inst. Meth. in Physics Research, A480 (2002) 204.

[51] H.Postma et al., *Neutron-resonance capture analysis of materials*, Journal of Radioanalytical and Nuclear Chemistry, Vol.248 No.1 (2001).

[52] A.Borella, A.Antonio, P.Schillebeeckx, K.Volev, *High resolution cross section measurements at GELINA in support of ADS and P-T*, International Workshop on P-T and ADS Development, SCK·CEN, Mol, Belgium (2003).

[53] P.Mutti, F.Corvi, *^{207}Pb capture measurements at the GELINA facility*, private communication.

[54] P.Mutti, *s-Process implication of* ^{136}Ba, ^{208}Pb *and* ^{209}Bi *stellar capture rates*, Phd Thesis, University of Gent (1996).

[55] K.J.R.Rosman, P.D.P.Taylor, *Isotopic composition of the elements 1997*, Pure & Appl. Chem., Vol.70, No.1 (1998) 217.

[56] S.F.Mughabghab and al., *Neutron cross sections, neutron resonance parameters and thermal cross sections* vol 1., Academic Press (1981).

[57] A.Plompen et al., *Recent neutron activation cross section measurements*, International Conference on Nuclear Data for science and technology, Tsukuba, Japan (2001).

[58] C.R.Quetel, I.Tresl, *Correcting ICP-MS isotope ratio measurements for mass discrimination effects: an art in its own*, Oral communication FACCS meeting, 29th edition, Providence, USA (2002).

[59] G.Molnar et al., *Iodine-129 thermal capture cross section determination* private communication (2003).

[60] J.E.Leiss, *The NBS linac*, Proc. Linear Accelerator Conf., Los Alamos, New Mexico (1966).

[61] J.W.T.Dabbs, *Neutron cross section measurements at ORELA*, Proc. Int. Conf. On nuclear cross section for technology, Knoxville, Tenesse (1979).

[62] K.H.Bockoff et al. *Electron linear accelerators for fast neutron data measurements in support of fusion energy applications*, Nucl. Sci. Eng. 106 (1990) 192.

[63] M.Drosg, *Sources of variable energy monoenergetic neutrons for fusion-related applications*, Nucl. Sci. Eng. 106 (1990) 279.

[64] S.Cierjacks, *Neutron sources for basic physics and applications*, Pergamon Press (1983).

[65] A.Bensussan, J.M.Salome, *GELINA: a modern accelerator for high resolution neutron time of flight experiments*, Nucl. Inst. Meth. 155 (1978) 11.

[66] J.M.Salome, R.Cools, *Neutron producing targets at GELINA*, Nucl. Inst. Meth. 179(1981)13.

[67] D.Tronc, J.M.Salome, K.H.Bockoff, *A new pulse compression system for intense relativistic electron beam*, Nucl. Inst. Meth. In Physics Research 228(1985)217.

[68] M.Flaska et al., *Study of properties of the GELINA neutron target*, Int. Conf. on Nuclear Mathematical and Computational Science, Gatlinburg, Tennessee (2003).

[69] G.Fioni, *Resonance Neutron Capture in ^{56}Fe and ^{60}Ni below 300 keV*, Phd Thesis, University of Gent (1990).

[70] V.Gressier, *Nouvelle détermination expérimentale des paramètres de résonances neutroniques de ^{237}Np en dessous de 500 eV*, Phd Thesis, Université de Paris Sud (1999).

[71] C.Brienne-Raepsaet, *Nouvelle détermination expérimentale des paramètres de résonances neutroniques de ^{99}Tc*, Phd Thesis, Université de Provence Aix-Marseille I (1998).

[72] A.Brusegan, *Transmission measurements of the natural xenon*, private communication (2000).

[73] J.L.Tain et al., *Accuracy of the pulse height weighting technique for capture cross section measurements*, J. Nucl. Science and Technology, Suppl. 2, 689 (2002).

[74] D.B.Gayther, R.B.Thom, *Prompt gamma-ray detectors for the measurement of neutron capture cross-sections*, Proc. of the NEA-NDC/NEA-CRP Specialist's meeting on fast neutron capture cross section, Illinois (1982).

[75] K.Wisshak, F.Voss, F.Käppeler *Neutron capture cross section of ^{232}Th*, Karlsruhe (1999).

[76] F.Corvi, C.Bastian, *Neutron capture in the 1.15 keV resonance of ^{56}Fe using Moxon-Rae detectors*, Nucl. Sci. Eng. 93(1999)348.

[77] F.Rau, Nukleonik 5(1963)191.

[78] R.L.Macklin, J.H.Gibbons, *Capture-cross-section studies for 30-220 keV neutron using a new technique*, Phy. Rev. 4(1967)159.

[79] N.Yamamuro et al., *Reliability of the weighting function for the pulse height weighting technique*, Nucl. Inst. Meth. 133(1975)531.

[80] F.Corvi, A.Prevignano, H.Liskien *An experimental method for determining the total efficiency and the response function of a gamma-ray detector in the range 0.5-10 MeV*, Nucl. Inst. Meth. A265(1987)475.

[81] R.L.Macklin *Gamma flash supression for the ORELA Pulsed neutron source*, Nucl. Inst. Meth. 91(1971)79.

[82] A.Lepretre, A.Brusegan, N.Herault, G.Noguere, P.Siegler, *Détermination des paramètres des résonances neutroniques du Neptunium 237, en dessous de 500 eV, et obtention des matrices de covariances statistiques et systématiques entre les paramètres de ces résonnances*, DAPNIA-02-374 (2002).

[83] F.Corvi, G.Fioni, F.Gasperini, P.B.Smith *The weighting function of a neutron capture detection system*, Nucl. Sci. Eng. 102(1991)272.

[84] T.Z.Kowalski *The influence of the concentration of the quench gas on the count rate effect in proportional counters*, Nucl. Inst. Meth. A239(1985)551.

[85] J.Liglou *Introduction au génie nucleaire* Presse polytechniques et universitaires romandes (1997).

[86] *DATA acquisition system manual CMTE-FAST*, Daten System, Gmbh, Munich, Allemagne (1990).

[87] J.Gonzales, C.bastian, S. de Songe, K.Hofmans, *MMPM, Hardware description and user guide*, IRMM internal report GE/R/INF/06/97 (1997).

[88] J.Gonzales, C.bastian, S. de Songe, K.Hofmans, *TBM, Hardware description and user guide*, IRMM internal report GE/DE/R/03/94 (1994).

[89] S. de Songe, *Fast Time Digitizer, type 8514A*, IRMM internal report GE/DE/R/24/87 (1987).

[90] C.bastian, J.Gonzales, *A user's guide to MPA/TP, Multi-Parameter Acquisition with transputer*, IRMM internal report GE/DE/R/01/94 (1994).

[91] J.Gonzales, *Routing Extender, hardware description and user guide*, IRMM internal report GE/R/INF/07/97 (1997).

[92] R.L.Macklin, N.W.Hill, B.J.Allen, *Thin ^{6}Li(n,α)T transmission flux monitor*, Nucl.Inst.Meth. 96(1971)509.

[93] G.F.Knoll, *Radiation detection and measurement*, John Wiley and Sons, New York (1979).

[94] C.Bastian, *AGS, a set of UNIX commands for neutron data reduction*, Proc. Int. Conf. on Neutrons in Research and Industry, Crète, Grèce (1979).

[95] G.Aerts, F.Gunsing, *Weighting functions for the neutron capture measurements performed at nTOF-CERN in 2002*, internal report DAPNIA-03-95 (2003).

[96] S.Boyer et al., *Efficiency and response of a C_6D_6 detector used for (n,γ) capture reaction cross section measurements*, International Conference on Applications of High Precision Atomic and Nuclear Methods, HIPAN2002, Neptun, Romania (2002).

[97] M.Moxon, *The effect of dead time*, http://www.nea.fr/lists/ueval.

[98] M.Moxon, *Notes on the background determination in the Doppler measurements*, IRMM internal report, GE/R/ND/01/93 (1993).

[99] G.Lobo, F.Corvi, P.Schillebeeckx, N.Janeva, A.Brusegan, P.Mutti, *Measurement of the ^{232}Th neutron capture cross section in the region 5 keV-150 keV*, Int. Conf. on Nuclear Data for Science and Technology, Tsukuba, Japan (2001).

[100] R.L.Macklin, J.Halperin, R.R.Winters *Absolute neutron capture yield calibration*, Nulc. Inst. Meth. 164 (1979) 131.

[101] O.Bouland, H.Derrien, *Variance-covariance matrices of resonance parameters and average cross sections at low energy for ^{239}Pu, ^{240}Pu and ^{235}Pu calculated with the Bayesian R-matrix fitting code SAMMY after a semi-empirical estimate of the experimental covariance matrices*, Internal Note (1997).

[102] F.H.Frohner, *Assigning uncertainties to scientific data*, Nuclear Science and Engineering 126 (1997) 1.

[103] *Nuclear Data Covariance Workshop*, ORNL/TM-2000/19.

[104] F.Gunsing, *Uncertainty propagation in AGS*, Internal Report DAPNIA/SphN-98-37, Internal Report CEC-JRC-IRMM GE/R/ND/02/98.

[105] D.L.Smith, *Examination of various roles for covariance matrices in the development, evaluation, and application of nuclear data*, Int. Conf. on Nuclear Data for Science and Technology, Jaeri, japan (1988).

[106] R.Von Mises, *Mathematical theory of probability and statistics*, Academic Press (1964).

[107] W.Solbrig, Am.Journal of Physics 29 (1961) 257.

[108] H.A.Bethe, G.Placzek, Physical Review 51 (1937) 450.

[109] W.E.Lamb, *Capture of neutrons by atoms in a crystal*, Physical Review 55 (1939) 190.

[110] A.Meister, A.Santamarina, *The effective temperature for doppler broadening in UO_2 lattices*, JEFF/DOC-706 (1997).

[111] D.G.Naberejnev, C.Mounier, R.Sanchez, *The influence of crystalline binding on resonant absorption and reaction rates*, Nucl. Sci. and Eng. 131 (1999) 222.

[112] V.Gressier, D.G.Naberejnev, C.Mounier, *The impact of the harmonic crystal model on the neutron resonance parameters of ^{237}Np*, Annals of Nuclear Energy 27 (2000) 1115.

[113] M.C.Moxon, *Doppler effects*, IRMM internal report GE/R/ND/0**/95.

[114] J.A.Young, *Neutron scattering from uranium dioxide*, Nukleonik 12. Bd., Heft 5 (1969).

[115] G.R.Stewart, *Measurement of low-temperature specific heat*, Rev. Sci. Instr. 54 (1983) 1.

[116] I.D.Feranchuk, A.A.Minkevich, A.P.Ulyanenkov, *Estimation of the Debye temperature for crystals with polyatomic unit cell*, Eur. Phys. Journal Applied Physics 19 (2002) 95.

[117] C.Coceva, M.Magnani, *Resolution rotary target*, Internal Report IRMM, GE/R/ND/06/96 (1996).

[118] B.E.Moretti, *Molybdenum neutron transmission measurements and the development of an enhanced resolution neutron target*, PhD Thesis, Rensselaer Polytechnic Institute (1996).

[119] P.Mutti, H.Beer, A.Brusegan, F.Corvi, *Reinvestigation of* ^{85}*Kr branching ratio in the light of new* ^{82,84,86}*Kr neutron capture cross section measurements*, International Conference on Nuclear Data for science and technology, Tsukuba, Japon (2001).

[120] C.Coceva, M.Frisoni, M.Magnani, A.Mengoni, *On the figure of merit in neutron time of flight measurements*, Nuclear Instruments and Methods A 489 (2002) 346.

[121] K.M.Case, F.Hoffman, G.Placzek, *Introduction to the theory of neutron diffusion*, Los Alamos Scientific Laboratory (1953).

[122] F.G.Perey, *private communication* to N.M.Larson (1990).

[123] N.M.Larson, K.N.Volev, *Validation of multiple-scattering corrections in the analysis code SAMMY*, PHYSOR 2002, Seoul, Korea (2002).

[124] MCNP^{TM} - A general Monte-Carlo N-Particle transport code, version 4C, ORNL, USA, LA-13709-M (2000).

[125] L.Dresner, *Resonance self-shielding in the measurement of radiative capture cross sections*, Nuclear Instruments and Methods 16 (1962) 176.

[126] M.C.Moxon, *REFIT, A least square fitting program for resonance analysis on neutron transmission and capture data*, Technical Report Harwell Laboratory, AEA-IN Tec=0470 (1991).

[127] R.L.Macklin, J.Halperin, R.R.Winters, Nuclear Instruments and Methods 96 (1971) 509.

[128] N.M.Larson, F.H.Froehner, *Worshop SAMMY*, NEA, France (2002).

[129] V.P.Alfimenkov et al., *Parity violation in neutron resonances*, Nuclear Physic A398(1983)93.

[130] Y.Matsuda et al., *Parity violation in neutron resonances of antimony and iodine*, Physical Review C, 64(2001)1.

[131] E.I.Sharapov et al.,*Parity violation in p-wave neutron resonances*, Physics of Particles and Nuclei 32(2001)129.

[132] J.B.Garg, J.Rainwater, W.W.Havens, *Neutron resonance spectroscopy. V, Nb, Ag, I and Cs.*, Physical Review 137(1965)547.

[133] G.Rohr, R.Shelley, A.Brusegan, *Neutron resonances studies of* ^{127}I, Int. Conf. on interaction neutrons with nuclei, Lowell, Massachusetts 11(1976)1249.

[134] D.D.Wilkey, J.E.Willard, *Isomer of* ^{130}I, Journal of Chemical Physics 44(1966)970.

[135] BNL 325, *2nd edition*, Brookhaven National Laboratory (1958).

[136] F.H.Frohner, D.C.Larson *Cross section fluctuations and self-shielding effects in the unresolved resonance region*, Report NEA/WPEC-15.

[137] F.H.Frohner, *SESH - A fortran code for calculating the self-shielding and multiple scattering effects for neutron cross section data interpretation in the unresolved resonance region*, Report Gulf General Atomic GA-8380 (1968).

[138] F.H.Frohner, *Evaluation of the unresolved resonance range of* ^{238}U*+n, Part II: differential data tests*, Nuclear Science and Engineering 111(1992)404.

[139] R.L.Macklin, *Resonance self-shielding in neutron capture cross section measurements*, Nuclear Instruments and Methods 26 (1964) 213.

[140] A.Lukyanov et al., *Neutron capture of* ^{232}Th *in the unresolved resonance region-Data corrections and analysis*, Int. Conf in Nuclear Mathematical and Computational Sciences, Gatlinburg, Tennessee (2003).

[141] K.K.Seth, R.H.Tabany, E.G.Bilpuch, H.W.Newson, Bull. Am. Phys. Soc 9(1964)167.

[142] J.H.Gibbons et al, *Average radiative cross section for 7- to 170-keV Neutrons*, Physical Review 122 (1960) 182.

[143] H.S.Camarda, *p-wave neutron strength function measurements and the low energy optical potential*, Physical Review C 9(1974)28.

[144] Yamamuro et al., *Neutron capture cross section measurements of Nb-93, I-127, Ho-165, Ta-181 and U-238 between 3.2 and 80 keV*, Nuclear Science and Technology 17(1980)582.

[145] R.E.MacFarlane, D.W.Muir, *The NJOY nuclear data processing system*, version 97-99, Los Alamos National Laboratory (1998).

[146] M.D.Ricabarra et al., *Neutron activation resonance integrals of* ^{74}Se, ^{78}Se, ^{80}Se, ^{81}Br, ^{127}I, ^{130}Te, ^{138}Ba, ^{140}Ce *and* ^{142}Ce, Canadian Journal of Physics 46(1968)2473.

[147] L.Moens et al., *Comparative study of measured and critically evaluated resonance integral to thermal cross section ratios (Part I)*, Journal of Radioanalytical Chemistry 54(1979)377.

[148] L.Dresner, *Resonance absorption in nuclear reactor*, Pergamon Press, Oxford, England (1960).

[149] T.Katoh et al., *Measurement of thermal neutron capture cross section and resonance integral of the reaction* $^{127}I(n,\gamma)^{128}I$, Nuclear Science and Technology 36(1999)223.

[150] D.Cano-Ott, M.Embid, E.Gonzales, *Monte-Carlo simulations of the photon and neutron background in the n-TOF experimental area produced by a high energy neutron source hitting its walls*, n-TOF Internal Note 2001-2.

[151] A.Brusegan, *Experimental determination of the structured background*, Private communication.

[152] G.Noguere, A.Brusegan, A.Lepretre, *Resolution function of the Geel facility GELINA*, Note Technique (2002).

[153] F.Gunsing, A.Brusegan, *The resolution function of GELINA modelled in REFIT*, Internal Report DAPNIA/SPhN-00-33 (2000).

[154] A.Brusegan, G.Noguere, F.Gunsing, *The resolution function in time-of-flight experiments*, International Conference on Nuclear Data for science and technology, Tsukuba, Japan, 2001.

[155] H.J.Groenewold, H.Groendijk ,Physica 13 (1947) 141

[156] A.Michaudon, *Contribution à l'étude par des méthodes du temps de vol de l'interaction des neutrons lents avec l'*^{235}U, Université de Paris (1964) Rapport CEA R2552.

[157] C.Coceva, R.Simonini, *Calculation of the ORELA neutron moderator spectrum and resolution function*, Nuclear Instruments and Methods 211 (1983) 459.

[158] S.Ikeda, M.Carpenter, *Wide energy range, high-resolution measurements of neutron pulses shapes of polyethylene moderators*, Nuclear Instruments and Methods in Physics Research A239 (1985) 536.

[159] *Reactor physics constants*, Argonne National Laboratory, ANL-5800 second edition (1963) 277.

[160] E.J.Fairley, A.R.Spowart, *Neutron scintillating glasses partIII, pulse decay time measurements at room temperature*, Nuclear Instruments and Methods 150 (1977) 159.

[161] A.Bignami, C.Coceva, R.Simonini, *Monte-Carlo calculations for the moderator of the pulsed neutron target of the Geel LINAC*, Report CNEM, EUR 5157 e (1974).

Résumé :

Les études expérimentales sur l'interaction des neutrons avec la matière ont principalement été focalisées sur les matériaux de structure liés à la physique des réacteurs. Parallèlement, les données disponibles relatives aux actinides mineurs et produits de fissions à vie longue sont limitées. Une forte demande concernant l'amélioration des sections efficaces neutroniques de ces isotopes a émergé suite aux études sur la transmutation des déchets nucléaires. Avec 400 kg d'iode-129 produits chaque année en Europe et une période radioactive de $1{,}57\times10^{7}$ ans, l'iode nécessite un stockage qui l'isolerait de l'environnement pendant une très longue période. Aussi, l'iode-129 est potentiellement un bon candidat pour les études de transmutation, puisque après capture d'un neutron, la période du noyau composé (^{130}I) n'est plus que de 12.36 h. Par suite, l'optimisation des scénarios de transmutation requiert une bonne connaissance de la section efficace neutronique de capture radiative.

Dans ce contexte, une campagne de mesures par temps de vol a été réalisée auprès de la source pulsée de neutron GELINA de l'Institut des Matériaux et des Mesures de Référence (IRMM). Deux types d'expériences ont été réalisées. Une série de mesures de capture d'une part et de transmission d'autre part nous ont permis de déterminer la section efficace de capture radiative et la section efficace totale de l'iode-129 de 0.5 eV à 100 keV. Les échantillons de PbI_2 nécessaires à la réalisation de ces mesures contiennent de l'iode naturel et de l'iode radioactif. Aussi, une étude complète des réactions ^{127}I(n,γ) et ^{127}I(n,tot) a été réalisée dans les mêmes conditions expérimentales que celles de l'iode-129. La réduction des données a été réalisée avec le système AGS, et les paramètres de résonance ont été analysés avec les codes d'analyse de forme REFIT et SAMMY. Les paramètres de résonance obtenus ont été convertis en format ENDF-6 . Nous avons utilisé le code NJOY afin de produire les sections efficaces ponctuelles et multigroupes associées ainsi que les bibliothèques des codes MCNP et ERANOS.

Abstract :

Most of the experimental work on the interaction of neutrons with matter has focused on materials important to reactor physics and reactor structures. By comparison, the corresponding data for minor actinides or long-lived fission products are poor. A significant demand has developed for improved neutron cross-section data of these little-studied nuclides due to the surge of interest in the transmutation of nuclear waste. With 400 kg of ^{129}I produced yearly in the reactors of the EU countries and a very long β^- half-life of 1.57×10^{7} years, iodine requires disposal strategies that will isolate this isotope from the environment for long periods of time. Therefore, ^{129}I is potentially a key long-lived fission product for transmutation applications, since ^{129}I transmutes in ^{130}I after a single neutron capture and decays to ^{130}Xe with a 12.36 h half-life. Accurate capture cross sections would help to reduce uncertainties in waste management concepts.

For that purpose, Time-Of-Flight measurements covering the [0.5 eV-100 keV] energy range have been carried out at the 150 MeV pulsed neutron source GELINA of the Institute for Reference Materials and Measurements (IRMM). Two types of experiments have been performed at the IRMM, namely capture and transmission experiments. They are respectively related to the neutron capture and total cross sections. Since the PbI_2 samples used in this work contain natural and radioactive iodine, extensive measurements of ^{127}I have been carried out under the same experimental conditions as for the ^{129}I. The data reduction process was performed with the AGS system, and the resonance parameters were extracted with the SAMMY and REFIT shape analysis codes. In a last step, the parameters have been converted into ENDF-6 format and processed with the NJOY code to produce point-wise and multigroup cross sections, as well as MCNP and ERANOS libraries.